Improving Aesthetics and Energy Performance of Photovoltaics for the Building Environment

Modeling and Experimental approaches

Ortiz Lizcano, J.C.

DOI
10.4233/uuid:10e12e34-47b9-4c45-832b-ed2289cf1e99

Publication date
2025

Document Version
Final published version

Citation (APA)
Ortiz Lizcano, J. C. (2025). *Improving Aesthetics and Energy Performance of Photovoltaics for the Building Environment: Modeling and Experimental approaches.* [Dissertation (TU Delft), Delft University of Technology]. https://doi.org/10.4233/uuid:10e12e34-47b9-4c45-832b-ed2289cf1e99

Important note
To cite this publication, please use the final published version (if applicable).
Please check the document version above.

Improving Aesthetics and Energy Performance of Photovoltaics for the Building Environment

J.C. Ortiz Lizcano

IMPROVING AESTHETICS AND ENERGY PERFORMANCE OF PHOTOVOLTAICS FOR THE BUILDING ENVIRONMENT

MODELING AND EXPERIMENTAL APPROACHES

IMPROVING AESTHETICS AND ENERGY PERFORMANCE OF PHOTOVOLTAICS FOR THE BUILDING ENVIRONMENT

MODELING AND EXPERIMENTAL APPROACHES

Proefschrift

ter verkrijging van de graad van doctor
aan de Technische Universiteit Delft,
op gezag van de Rector Magnificus prof. dr. ir. T.H.J.J. van der Hagen,
voorzitter van het College voor Promoties,
in het openbaar te verdedigen op dinsdag 29 april 2025 om 10:00 uur

door

Juan Camilo ORTIZ LIZCANO

Master of Science in Sustainable Energy Technology,
Technische Universiteit Delft, Delft, Nederlands,
Geboren in Málaga, Colombia

Dit proefschrift is goedgekeurd door de

promotor: Em.prof.dr. M. Zeman
promotor: Prof.dr.ir. O. Isabella

Samenstelling promotiecommissie:

Rector Magnificus,	voorzitter
Em.prof.dr. M. Zeman,	Technische Universiteit Delft
Prof.dr.ir. O. Isabella,	Technische Universiteit Delft
Onafhankelijke leden:	
Prof.dr. M. Topič,	University of Ljubljana
Prof.dr. M. Schmid,	University of Duisburg-Essen
Dr. B. Bläsi,	Fraunhofer Institute for Solar Energy Systems ISE
Prof.dr.ir K. Hooman,	Technische Universiteit Delft
Prof.dr.ir A.A.J.F van den Dobbelsteen,	Technische Universiteit Delft
Prof.dr.ir A.W. Weeber	Technische Universiteit Delft, reservelid

Printed by: Print&Bind | www.printenbind.nl
Front & Inside: Images created using Microsoft Bing Image Creator.

ISBN 978-94-6522-201-1

An electronic version of this dissertation is available at
http://repository.tudelft.nl/.

There is no book so bad...
that it does not have at least one good thing in it

Miguel de Cervantes Saavedra

CONTENTS

SUMMARY

With an estimated global share of greenhouse emissions of 35%, the building sector must be the target of significant transformation. These next decades represent one of the best opportunities for a giant energy consumer to become an efficient energy *prosumer*. Of the many technical possibilities available that can help in this objective, building integrated photovoltaic systems is becoming one of the most salient because of their versatility of application and simplicity of operation. However, to achieve their projected market growth, BIPV products must overcome technical, financial, and social barriers.

The interrelationship between these barriers creates requirements that are sometimes in conflict with each other. Research suggests that the most important parameters for the financial viability of a BIPV system (studied in North America) are its electrical performance and its effective lifetime. However, the social acceptance of BIPV systems, among architects and other consumers, increases when photovoltaic modules are provided with a variety of colors, resulting in losses in their electrical output. Furthermore, a BIPV system can present an installation layout in which its modules operate at high values of temperature, which hinders their useful lifetime.

Significant research has been done to tackle these requirements, striving to find a balance in which each, however contradictory, is met. This thesis seeks to add to this body of research through modeling and experimental efforts focused on creating techniques and concepts to improve the aesthetics and thermal behavior of photovoltaic modules.

After an introductory chapter, **Chapter 2** presents an overview of the efforts done so far to improve aesthetics and passively cool photovoltaic modules. The challenges and barriers that remain from a technical perspective are outlined, and the base modeling approach deployed to tackle them is introduced. **Chapter 3** presents how this model can be complemented by auxiliary algorithms to find ways to provide color directly to c-Si solar cells by using interference optical filters. The chapter also provides insight into ways of stabilizing color and the beneficial impact that a color optical filter has on the operating temperature of a c-Si solar cell.

Chapter 4 expands on the findings of **Chapter 3** and discusses that the application of the color optical filter on the front glass of a PV module provides better benefits, particularly in terms of better color saturation and more vivid hues. In addition, it provides guidelines for how colorimetry can be added to the modeling effort to improve the quality of color matching and color stability of a color photovoltaic module based on optical filters. Furthermore it demonstrates that it is possible to achieve colorful designs with relative DC energy losses below 10%.

Chapter 5 argues that optical filters can also be designed to provide thermal control to photovoltaic modules. Furthermore, this thermal control can be achieved by taking advantage of the harmonic reflectance produced by simple designs. It shows that the analysis of a thermal management solution must always consider their benefits related

to extended lifetime. A simple optical thermal filter, despite its lossy nature (in terms of electrical output), can still provide a net benefit in terms of energy yield when this benefit is accounted for.

Chapter 6 presents the huge cooling potential provided by phase change material (PCM). This work is entirely experimental and demonstrates that a single type of PCM can be used in different locations, with different installation layouts, to provide substantial temperature reductions and increase the electrical output of photovoltaic modules with great consistency, even during the winter months.

Chapter 7 presents the novel concept of a photovoltaic chimney, developed with the purpose of studying the potential use of the thermal energy produced by photovoltaic modules. The concept was analyzed using common modeling approaches to calculate mass flow and heat production, offering quick ways to create sensitivity analysis for earlier stages of design. These initial stages of the model can be used to have insight into the quality (or lack thereof) of the heat produced and its potential use to improve the ventilation of buildings.

Chapter 8 completes this dissertation, highlighting its main conclusions and providing details on potential areas that can drive future research.

SAMENVATTING

Met een geschat wereldwijd aandeel van 35% in de uitstoot van broeikasgassen, moet de bouwsector het doelwit worden van een significante transformatie. De komende decennia vormen een van de beste kansen voor een gigantische energieverbruiker om een efficiënte energie *prosumer* te worden. Van de vele technische mogelijkheden die beschikbaar zijn om dit doel te bereiken, worden gebouwgeïntegreerde fotovoltaïsche systemen een van de meest in het oog springende vanwege hun veelzijdige toepassingsmogelijkheden en eenvoudige bediening. Om de verwachte marktgroei te bereiken, moeten BIPV-producten echter technische, financiële en sociale barrières overwinnen. De onderlinge relatie tussen deze barrières zorgt voor eisen die soms met elkaar in strijd zijn. Onderzoek suggereert dat de belangrijkste parameters voor de financiële levensvatbaarheid van een BIPV-systeem (onderzocht in Noord-Amerika) de elektrische prestaties en de effectieve levensduur zijn. De sociale acceptatie van BIPV-systemen, onder architecten en andere consumenten, neemt echter toe wanneer fotovoltaïsche modules worden voorzien van een verscheidenheid aan kleuren, wat resulteert in verliezen in hun elektrische output. Bovendien kan een BIPV-systeem een installatielay-out hebben waarbij de modules bij hoge temperatuurwaarden werken, wat hun nuttige levensduur belemmert. Er is veel onderzoek gedaan om aan deze eisen te voldoen, waarbij gestreefd is naar een evenwicht waarin aan elk van deze eisen, hoe tegenstrijdig ook, wordt voldaan. Deze dissertatie probeert iets toe te voegen aan dit onderzoek door modellering en experimenten gericht op het creëren van technieken en concepten om de esthetiek en het thermisch gedrag van fotovoltaïsche modules te verbeteren.

Na een inleidend hoofdstuk geeft **hoofdstuk** 2 een overzicht van de inspanningen die tot nu toe zijn gedaan om de esthetiek te verbeteren en fotovoltaïsche modules passief te koelen. De uitdagingen en barrières die vanuit een technisch perspectief overblijven worden geschetst en de basismodelbenadering die wordt gebruikt om ze aan te pakken wordt geïntroduceerd. **Hoofdstuk** 3 laat zien hoe dit model kan worden aangevuld met hulpalgoritmen om manieren te vinden om rechtstreeks kleur te geven aan c-Si zonnecellen door gebruik te maken van optische interferentiefilters. Het hoofdstuk geeft ook inzicht in manieren om kleur te stabiliseren en de gunstige invloed die een optisch kleurenfilter heeft op de bedrijfstemperatuur van een c-Si zonnecel.

Hoofdstuk 4 gaat verder in op de bevindingen van **hoofdstuk** 3 en bespreekt dat de toepassing van een optisch kleurenfilter op het glas aan de voorkant van een PV-module betere voordelen biedt, met name op het gebied van betere kleurverzadiging en levendigere tinten. Daarnaast geeft het richtlijnen voor hoe colorimetrie kan worden toegevoegd aan het modelleren om de kwaliteit van kleurafstemming en kleurstabiliteit van een kleuren fotovoltaïsche module op basis van optische filters te verbeteren. Verder wordt aangetoond dat het mogelijk is om kleurrijke ontwerpen te maken met relatieve DC energieverliezen van minder dan 10%.

Hoofdstuk 5 stelt dat optische filters ook kunnen worden ontworpen om thermische

controle te bieden aan fotovoltaïsche modules. Bovendien kan deze thermische controle worden bereikt door gebruik te maken van de harmonische reflectie die door eenvoudige ontwerpen wordt geproduceerd. Hieruit blijkt dat bij de analyse van een oplossing voor thermisch beheer altijd rekening moet worden gehouden met de voordelen van een langere levensduur. Een eenvoudig optisch thermisch filter kan, ondanks zijn verlieslatende aard (in termen van elektrische output), nog steeds een netto voordeel opleveren in termen van energieopbrengst als dit voordeel wordt meegerekend.

Hoofdstuk 6 presenteert het enorme koelpotentieel van faseveranderingsmateriaal. Dit werk is volledig experimenteel en toont aan dat een enkel type PCM op verschillende locaties, met verschillende installatie lay-outs, kan worden gebruikt om de temperatuur aanzienlijk te verlagen en de elektrische output van fotovoltaïsche modules met grote consistentie te verhogen, zelfs tijdens de wintermaanden.

Hoofdstuk 7 presenteert het nieuwe concept van een fotovoltaïsche schoorsteen, ontwikkeld om het potentiële gebruik van de thermische energie geproduceerd door fotovoltaïsche modules te bestuderen. Het concept werd geanalyseerd met behulp van gangbare modelbenaderingen om de massastroom en warmteproductie te berekenen, wat snelle manieren biedt om gevoeligheidsanalyses te maken voor eerdere ontwerpfasen. Deze eerste fasen van het model kunnen worden gebruikt om inzicht te krijgen in de kwaliteit (of het gebrek daaraan) van de geproduceerde warmte en het potentiële gebruik ervan om de ventilatie van gebouwen te verbeteren.

Hoofdstuk 8 rondt dit proefschrift af door de belangrijkste conclusies te benadrukken en details te geven over potentiële gebieden die toekomstig onderzoek kunnen stimuleren.

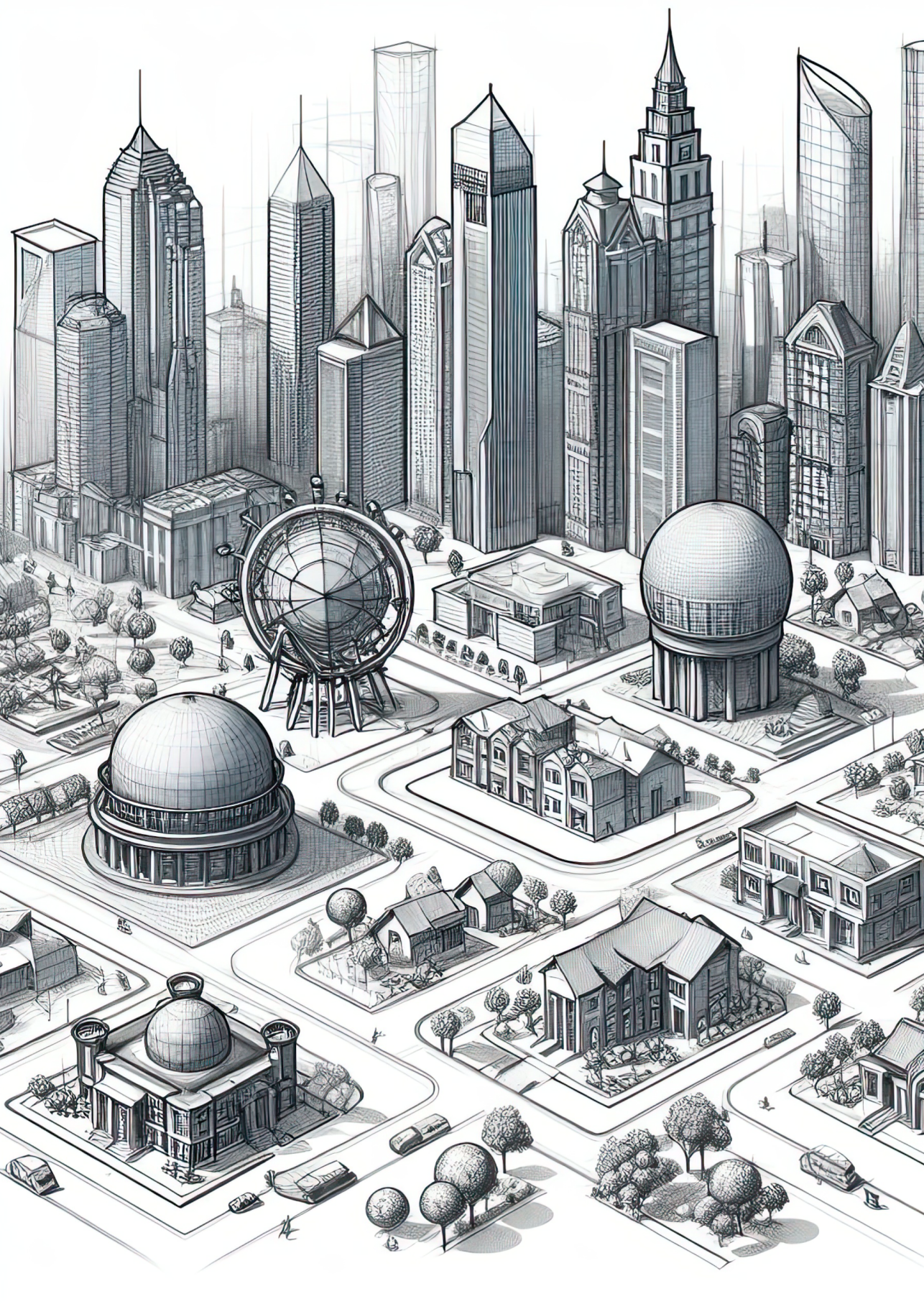

1

INTRODUCTION

1.1. RESHAPING THE BUILDING SECTOR

A paramount goal toward a sustainable future is to transform our urban landscapes from energy consumers to energy producers. The construction sector is one of the most significant contributors to greenhouse gas emissions (GHG), with an estimated global share of 35% [1]. The International Energy Agency (IEA) reports that by 2060, projected population growth will require an additional 240 million square meters of built area, representing the largest increase in human history [2]. This also presents a unique opportunity to transform the urban environment from an energy consumer to an efficient *prosumer*. Efforts in policies around the world aim to produce buildings with near-zero energy in the near future and are currently underway. For example, Europe aims to produce zero energy housing by 2030, the United States is looking to retrofit half of its commercial building sector and transform them into net zero projects, and similar efforts are starting to take hold in Australia, China and Japan, to name a few [3]. The achievement of a near-zero energy infrastructure includes reducing the carbon footprint of materials used in the construction sector, improving the energy performance of residences and office buildings, and the production of energy on site [4].

The installation of photovoltaic systems (PV) on site is becoming a common way to improve the energy performance of buildings. Photovoltaic systems are versatile and straightforward, as their basic layout is consistent in small, medium, and large-scale topologies that require very moderate maintenance [5]. Their implementation in buildings is usually classified into two categories: Building-added (or attached) photovoltaics (BAPV), where modules are installed on existing building surfaces (such as roofs) and building-integrated photovoltaics (BIPV), where PV modules act as the building envelope, replacing conventional materials used for this purpose, such as facades, rooftiles, and skylights [6].

BIPV systems are considered an excellent alternative for renewable energy production in densely populated areas where land use is limited and needs to be reserved for other human activities, such as farming and preservation. By 2022, the BIPV market was

valued at USD 19.82 billion with a projected compound annual growth rate (CAGR) of 21% until 2030, reaching USD 89.80 billion [7]. However, the acceptance of BIPV projects increases when their application is considered from the design stage of new building developments, particularly considering their aesthetic appeal [8]. In this regard, shape, texture, and color have been proven to be essential characteristics in accepting BIPV products, both for architects and homeowners [9][5]. Color, in particular, has been shown to be a critical factor in adoption, brand recognition, and purchasing decisions [10]. Furthermore, studies indicate that potential customers are willing to pay premium prices for a colored BIPV system, and are preferred to standard BAPV systems based on standard dark blue and black colors [11]. Discrete integration of photovoltaic energy is essential in heritage buildings [12][13], and stakeholders in rural and urban areas prefer to harmonize the color of photovoltaic modules with their surroundings [14].

The integration of photovoltaics into buildings has diverse meanings. The Photovoltaic Power Systems Division of the International Energy Agency (IEA PVPS Task 15) categorizes the integration of photovoltaic modules in buildings by three main functions; roofs, facades and integrated external devices [15]. Each of these functions can be divided into different categories of applications. For example, roofs can be divided into discontinuous, continuous, and atrium / skylights. Facade applications include rain screens, double skin, curtain walls, windows, and masonry walls. External devices can be parapets and balustrades or canopies and shading structures. One of the most challenging aspects of BIPV products is that each application has specific technical requirements. These requirements range from fire safety certification, mechanical resistance, hygrothermal performance, and electrical insulation, among others [16]. Regarding the color appearance, Figure 1.1[1] presents the main technical requirements for BIPV modules for every integration application. Depending on their applications, color photovoltaic modules can be required to be completely opaque, such as when replacing masonry facades, roofs, and specific external devices, or they can require certain levels of transparency.

This work focuses on opaque BIPV products. One of the main requirements for these solutions is to conceal their active area and mimic a wide variety of colors commonly used in the construction sector, such as those defined by the RAL [2] system [17]. Color matching is essential for renovation projects that involve heritage buildings, where the aesthetic of the building must be maintained [18]. If photovoltaic modules replace masonry, architects are reluctant to implement them due to their glass-pane appearance and feel, so trying to match the texture of the material is also important for this application [19]. Replacement of large facades and roofs can involve the use of a large number of photovoltaic modules, making color consistency essential. Therefore, color photovoltaic products must ensure color stability not only in their manufacturing process but also in any installation layout and size. The availability of bright colors is also preferred by architects and consumers, but glare should be avoided as it reduces visual comfort and can become a safety hazard [20].

[1] The image was generated using the following query: *A colored 3D model of a European heritage apartment building with a portion of its roof as a glass ceiling*

[2] From the german acronym *Reichsausschuß für Lieferbedingungen und Gütesicherung*, the RAL system defines colors using four digits. The code is commonly used in civil and military projects

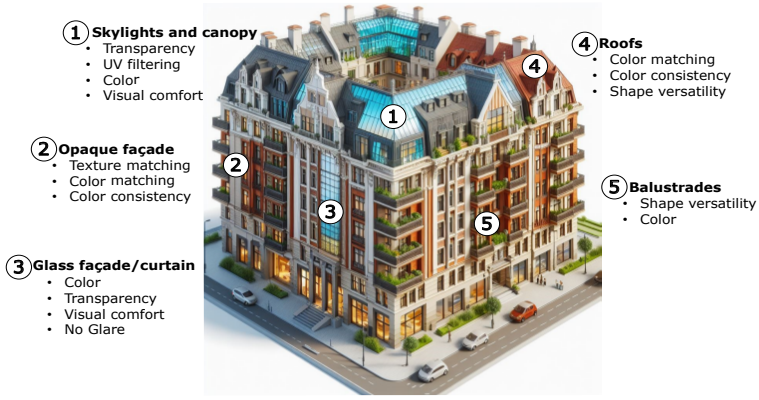

Figure 1.1: Different integration applications within the building environment. **1** Canopy or skylight. **2** Opaque facade. **3** Glass facade / glass curtain. **4** Roofs. **5** Balustrades or external devices. Each application has its particular technical challenges. Image generated via Microsoft Designer: Image creator (Dall·E3 engine)

In addition, the technological and economic evaluation of a BIPV system requires a complete understanding of the expected electrical performance, available financial incentives, social and environmental benefits, and other regulatory frameworks required for its installation. Gholami *et al.* [21] found that a life cycle analysis evaluation that considers these aspects can demonstrate that BIPV systems have the potential to be economically feasible. The authors expanded the methodology from the European scenario [22] to other places, such as Brazil, China, and Bahrain, obtaining similar conclusions. From a performance point of view, Zimmerman *et al.* [23] found that module efficiency and lifetime were critical parameters to verify whether a vertically mounted photovoltaic system could achieve levelized cost of electricity (LCOE) values similar to grid prices in the United States.

In terms of reliability and lifetime, research suggests that the reliability of photovoltaic modules (PV) seems very sensitive to their operational temperature [24]. Modules that consistently perform at high temperatures throughout the year can have a significantly shorter lifespan [25]. Therefore, improving reliability is instrumental for BIPV products, as they typically operate at temperatures higher than a standard rack mounted configuration [26]. Long lifetimes are required on BIPV modules, so they can match the building materials they are replacing. Thus, thermal management is another important technical challenge in the development of photovoltaic solutions targeted at the building sector.

1.2. AIM AND OUTLINE OF THIS WORK

The main objective of this thesis is to explore the way in which to improve both the aesthetics and the thermo-electrical performance of photovoltaic modules. Using comprehensive experimental and computational efforts, this work seeks to understand optimal and practical ways to overcome the barriers mentioned above, providing pathways to develop products that can achieve a reasonable balance between aesthetics, performance,

and reliability. To this end, this thesis is divided into two main sections. The first is centered on ways to improve the aesthetics of photovoltaic cells and modules. The second discusses approaches to their thermal management.

Given the scope of both topics, **Chapter 2** presents a literature overview of different approaches to provide color to photovoltaic modules and improve their thermal performance. It argues that despite the substantial amount of research developed so far, some challenges remain. Finally, the chapter discusses the foundational performance model developed in this thesis work with the purpose of meeting these challenges.

Chapter 3 studies ways of providing color directly to c-Si solar cells. Advanced TCAD simulations were deployed to understand how color affects the performance of a solar cell. The chapter demonstrates that the effect on the electrical parameters produced by the application of a color filter can be accurately predicted by the use of two scaling factors. The first accounts for the additional optical loss produced by the color filter at normal incidence and the other that accounts for its optical behavior at different angles of incidence of light. The chapter also explores how a wide range of colors is possible by tailoring the thickness of the most basic optical filter (based on two commonly used materials). The chapter also provides valuable insight into ways of stabilizing color and the beneficial impact that a color optical filter has on the operating temperature of a c-Si solar cell.

Chapter 4 expands on the findings of **Chapter 3** by studying the application of the color optical filter on the front glass of a PV module. The chapter argues that this approach provides better benefits, particularly in terms of better color saturation and more vivid hues. The chapter provides pathways for design optimization, by the application of colorimetry principles that allow simplifying the design of the color filter without loss in color appearance, thus avoiding unnecessary optical losses. Furthermore, these same colorimetry principles are used to study how different surface textures can be used to stabilize the color appearance at different angles of observation, which is one of the main drawbacks of using optical filters to provide color. The optimization process also considers spectral thermal effects, making it one of the most comprehensive modeling approaches for color photovoltaics to date.

Since optical filters offer great versatility of application, due to their spectral flexibility, **Chapter 5** explores how these devices can provide thermal control to photovoltaic modules based on c-Si solar cells. It is argued that, for the most advanced architectures of c-Si solar cells, the rejection of near-infrared (NIR) radiation provides limited cooling. An alternative approach, which focuses on reduction of thermalization losses, has a better cooling potential, albeit with an induced optical loss. One of the main conclusions of this chapter is that the thermal gain cannot compensate for the optical loss. However, when the effect of the temperature reduction provided by the optical filter on the lifetime of the photovoltaic module is taken into account, the thermal filter has the potential to improve the electrical output of the photovoltaic module. This chapter highlights the importance of including lifetime effects when studying the benefits of devices or systems aimed at improving the thermal behavior of photovoltaic modules.

Chapter 6 explores the potential of thermal control provided by phase change materials (PCM). These devices can be applied on the backside of photovoltaic modules, making them suitable to be used alongside the spectral approaches presented in previ-

ous chapters. The chapter presents a multi annual, multiple location experimental effort to study how much thermal control of a photovoltaic module is provided by a given phase change material under different climatic conditions. The chapter offers analysis of how the cooling provided by the PCM is increased or reduced by different environmental factors. Furthermore, it provides guidelines for data filtering and analysis that can help optimize the thermal properties of the PCM with the aim of improving its cooling capabilities for different photovoltaic applications.

Chapter 7 introduces a novel concept of a photovoltaic chimney, designed with the aim of utilizing the heat produced by the photovoltaic modules to increase air flow inside the chimney cavity. A simplified model is used to study the different configurations of the chimney and how it can be optimized either for thermal energy generation or electrical energy generation. The study concludes that the concept has a significant potential to provide adequate ventilation on large facades and sets the groundwork for further thermal modeling efforts.

Finally, **Chapter 8** presents the main conclusions of this dissertation and provides potential areas for future research on the topics discussed.

1.3. MAIN CONTRIBUTIONS TO THE FIELD

The works contained in this thesis were developed to expand existing modeling and experimental approaches aimed at improving the aesthetic appeal and performance of photovoltaic modules that operate as building integrated systems. The results obtained provide the following contributions to the field of photovoltaic system modeling and performance assessment.

- The development of **Spectrally resolved models** that allow accurate simulation of the effect that a color filter (by means of interference effects) has on both the electrical output and the operating temperature of c-Si solar cells. In addition, TCAD simulations were implemented to find simple and accurate ways to model these effects. This work demonstrates that the performance of a colored solar cell is accurately predicted by using two scaling factors that account for the induced optical losses of any given color and its respective angular behavior. These scaling factors are applied to the plane of the array irradiance. The resulting irradiance (called effective irradiance) is used on a standard two-diode equivalent circuit.

- Introduction of **design guidelines** for color photovoltaic modules using color filters. These design guidelines provide ways to analyze how surface texture can be engineered to reduce glare. Additionally, the model framework provides suitable ways to analyze aesthetic potential (color hues, saturation, and luminance that can be produced via optical filters), reduce unnecessary optical losses, and optimize performance based on color appearance, color stability, and thermal performance.

- A practical approach to designing an optical filter for the **spectral thermal management** of photovoltaic modules. The efforts focused on the practicality and ease of manufacturing, highlighting the potential benefits that cooling has on the lifespan of the module. The modeling presented highlights the importance of consid-

ering this effect when analyzing the viability of any given cooling solution. This work is one of the first attempts to unify these aspects of thermal management.

- An extensive **long-term** experimental work on the cooling potential provided by the attachment of phase-change materials to photovoltaic modules. In-depth analysis of how environmental factors, installation layout, and location solar resource enhance or hinder the cooling ability provided by a single-phase change material.
- An innovative **photovoltaic chimney concept** was developed to replace standard double skin facades, highlighting the potential improvement in terms of ventilation for large installations.

2

IMPROVING AESTHETICS AND ENERGY PERFORMANCE OF BIPV MODULES

This chapter is partially based on the following publication:

J.C. Ortiz Lizcano[1] , O. Isabella, B. Bläsi, M. Schmid *Chapter 11: Color and aesthetics of photovoltaic modules*, from *Optics for Terawatt-Scale Photovoltaics: Review and Perspectives* by K. Jäger *et al.* Advances in Optics and Photonics, (2025).

Understanding the effect of coloring a photovoltaic device requires a combination of colorimetry, optical, and electrical models. Human color perception of a non-illuminant object is modeled based on the CIE standard observer [27], which quantifies the chromatic response of human vision [28] [29] to stimuli from a given light source and the observed object reflectance. The result of these calculations is the three-dimensional XYZ color space, which is the basis for deriving various alternatives using transformation matrices [30]. The most commonly used color spaces are sRGB, CIE La*b*, and Hue, Chroma, and Luminosity (HCL). The last one is beneficial, as it is the basis of the formula for color difference [31]. This factor, denoted ΔE_{00}, quantifies the difference between two colors and represents a valuable figure of merit for computational validation models and the analysis of color consistency. Theoretically, studies have estimated the maximum efficiency achievable in a colored photovoltaic device. Peharz and Ulm [17] and Halme and Mäkinen [32], for example, calculated that colors can induce relative power losses between 5% - 20 % compared to a perfectly absorbing device. Both authors concluded that the most impactful colorimetry parameter is the luminosity (brightness) of the color, and the most impacted performance parameter was the photogenerated current on the solar cells due to the reflectance loss needed to provide color.

[1] Candidate's contribution: literature overview, writing, editing and image creation

The main challenge in modeling the electric yield of color BIPV systems is to accurately calculate the irradiance that effectively reaches the solar cells. Since the relationship between the output power of a photovoltaic module is nearly linear with the irradiance it receives, inaccuracies in estimating this parameter can lead to important errors in the obtained energy yield. Although several studies have focused on finding ways to reliably estimate this power output under the complex surrounding conditions of urban installations for standard modules [33]–[37], the same is not currently available for color modules. The additional reflectance loss and its spectral dependence on the coloring technique increase the complexity of accurately estimating the expected electrical efficiency. Furthermore, coloring a photovoltaic module has the potential to reduce its operating temperature [38], which can have a significant impact on its reliability [24]. A modeling tool that considers color perception, color stability, accurate energy yield, accurate operating temperature, and expected lifetime is instrumental in studying the feasibility of color BIPV products.

2.1. APPROACHES FOR COLORING BIPV PRODUCTS

Several techniques have been developed to provide color to photovoltaic modules. This roadmap presents the techniques that have reached, or have the potential of reaching, large-scale production. Substantial information on all different coloring approaches can be found in the review work by Meddeb *et al.* [39], Sehati *et al.* [40], Basher *et al.* [5], and Li *et al.* [41].

In practice, the coloration of photovoltaic modules is done using a wide variety of techniques. These techniques can be applied directly to solar cells or at the module level by adding or coloring a layer of the photovoltaic module, such as the front glass, the encapsulant, or the back sheet. Examples of these different levels of application are found in the work of Pelle *et al.* [42], Kutter *et al.* [43], and Lisco *et al.* [44].

For opaque photovoltaic modules, four techniques have industrial terawatt-scale potential given their large-area feasibility, high industrial throughput, and minimal impact on the standard manufacturing process of solar cells and photovoltaic modules. These techniques are summarized in Figure 2.1 and are presented starting from those based on readily available industrial methods to those with potential for industrial production.

2.1.1. *Intermezzo* OR ADDED COLOR LAYER

Refers to retrofitting existing commercial photovoltaic modules to change their color. These approaches are based on techniques available in other industrial sectors, but are tailored to photovoltaic modules. An example is presented by Gewohn *et al.* [45] who developed imprinted textiles that can be laminated to existing photovoltaic modules using an inkjet hybrid printer using a halftone technique. The results show that the technique can effectively change the color of a standard photovoltaic module with current losses in the range of 15%.

Another example of intermezzo layering is the work of Morlier *et al.* [49], who proposes a way to provide standard photovoltaic modules with the look and feel of stone veneer sheets using different stone laminates. The main drawback of this method is its significant power loss. Relative losses for stone-shaped samples ranged from 47% to

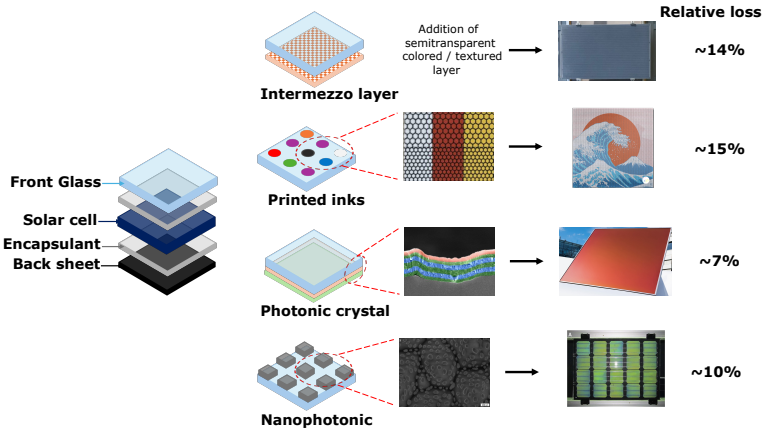

Figure 2.1: Coloring techniques for opaque photovoltaic modules. These techniques aim at concealing the active area (solar cells). From top to bottom: Color textiles or layers can be added to any of the front layers of the module to change its color appearance. (Photograph used with permission of The Institute of Electrical and Electronics Engineers, Incorporated (IEEE) taken from [45]). Digitally printed inks (Photographs reprinted with permission from Kameleon Solar [46]). Interference structures that selectively reflect light via interference effects (Image and photograph reprinted from [47]). Nanostructures that produce wavelength specific light scattering (Photographs reprinted from [48] with permission from Elsevier) . The last column indicates the reported average relative efficiency loss compared to a standard photovoltaic module

76%. However, the successful integration of these aesthetic options is a promising starting point for future research.

Masuda *et al.* [50] carried out experiments to understand the feasibility of using automotive paints in photovoltaic modules. The aim was to investigate which of the best painting techniques commonly used in the automotive industry was suitable for manufacturing potential lightweight photovoltaic modules. The study concluded that mica pigments could confer a rich color to the module while maintaining a relatively high level of light transmittance, with relative efficiency losses around 20%.

2.1.2. MICROSCOPIC INK PATTERN

on the front glass consists in creating patterns (like dots or hexagons) separated in such a way that, at a distance, it is impossible to discern by the human eye. Basher *et al.* [51] present a concept that consists of creating a 50 μm spearated dot pattern printed on glass using a UV-sensitive white ink (UV-curable technique). The area of glass covered by the ink transmits light within the ultraviolet and near-infrared (NIR) regions, while the gaps transmit the whole light spectrum. The result, from a distance, is a fully concealed photovoltaic module. Shin *et al.* [52] tested the screen printing method to create single-color photovoltaic modules. The technique prints the dotted pattern directly onto low iron glass and then fires it at high temperature to ensure adhesion. Riedel *et al.* [53] found that for ceramic inks applied via digital printing, the optical and electrical performance was almost independent of the geometry of the microscopic pattern. The aesthetic potential of this technique is essentially limitless, since any high-resolution image can be

used to create any design of the photovoltaic module. The most commonly used techniques to apply color, silk screen printing, digital UV-printing, and digital ceramic ink printing all reach industrial scale status for large-scale production. In addition, digital ceramic ink printing has proven reliability. Kameleon Solar, for example, claims that this technique provides coloring with a useful life of close to fifty years [46].

Despite its aesthetic potential, the colors obtained through this technique have comparatively limited saturation values [43]. Furthermore, the absorptive nature of inks can produce significant relative losses, some colors almost halving the electrical output [53]. Modeling the impact of this technique is time consuming and complex, and care must be taken in the design of the pattern as excessive irradiance inhomogeinity on the solar cells can lead to performance and reliability problems.

2.1.3. INTERFERENCE STRUCTURES (IS)

are one of the most studied techniques for coloring photovoltaic modules. These devices offer the advantage of producing color without absorbing dyes, thus reducing unnecessary optical losses. Additionally, color saturation can be maximized by creating reflectance spectra that can be similar to those of a monochromatic source. They are manufactured by depositing thin dielectric layers in a given sequence (alternating high and low refractive indices). The width of reflectance around the created peak depends to some extent on the difference in the refractive index of the materials used [54]. Macleod [55] provides an in-depth mathematical approach to the engineering possibilities of these optical systems.

The materials most commonly used, given their suitable optical properties, are titanium dioxide TiO_2, silicon nitride SiN_x, silicon dioxide SiO_2, and magnesium flouride MgF_2. Soman and Antony [56], Røyset *et al.* [57], Wessels *et al.* [58], Ingenito *et al.* [59], Ortiz Lizcano *et al.* [38], and Bläsi *et al.* [47] present comprehensive examples of the aesthetic potential of this approach. Furthermore, this approach has reached commercial status, due to manufacturing techniques readily available within the photovoltaic industry, such as sputtering and atomic layer deposition. Products such as those offered by LOF Solar [60], Soluxa [61], Kromatrix™[62] and Megasol [63] are based on this technique. Similarly to the case of nanostructures, the relative losses reported using this technique are among the lowest. Bright colors can have relative losses as low as 5%.

One of the main drawbacks of ISs is poor color stabilization and the potential to create significant glare. However, several studies have provided approaches to ameliorate these obstacles. Stabilizing color perception at different angles of observation represents an essential challenge for these devices. Bläsi *et al.* proposed the deposition of these optical systems on textured glass surfaces. This layout creates a 3D interference structure named MorphoColor [47], which improves the stability of the color at different angles of observation. Furthermore, the use of second-harmonic designs made with materials with a high refractive index (such as TiO_2) can help create bright and stable colors. Similarly, a glass-based texturization layout with inverted pyramids on the front side and random texturing on the back, where the structure is deposited, provides excellent color stability for observation angles up to 80 °[38]. Jolissaint *et al.* [64] also provide insight into how texturing the front glass helps reduce unwanted glare effects and helps conceal the solar cells.The above-mentioned works are only a few examples of approaches

to coloring photovoltaic modules based on ISs; other contributions using this approach are Rudzikas *et al.* [65] and Xu *et al.* [66].

2.1.4. NANOSTRUCTURES

exploit the effects of wavelength-specific light absorption and scattering and have been shown to be successful in the coloration of photovoltaic devices and modules. Perharz *et al.* [48] demonstrated the potential of this technique by applying metallic nanoparticle structures based on silver (Ag). The authors deposited thin Ag films on a commercial monocrystalline surface using DC sputtering, followed by an annealing process at 300 °C, thus creating a coating based on Ag nanoparticles. The second row of Figure 2.1 presents scanning electron microscope images of Ag nanoparticles deposited on the surface of the pyramidal-textured solar cell with sizes ranging from 50 to 150 nm. These nanoparticles create plasmonic scattering that produces a reflectance peak at 500 nm. This shift in reflectance changes the perceived color from blue to green. Similarly, Neder *et al.* [67] demonstrated that green colors could be produced by using c-Si nanocylinders that scatter light at a wavelength value around 540 nm. Other colors have also been proven by Uleman *et al.* [68] with the design of semitransparent meta-grating based on silicon nanowires. The layout allowed control of light scattering over a wide range of angles by modulating the pitch of the structures, the final design provided a red-mated appearance that emulates roof materials. Zhou *et al.* [69] also studied the aesthetic potential of using a poly (methyl methacrylate) matrix that contains nanoparticles based on Si @ SiO_2 core shells. In general, the reported relative efficiency losses of nano-structural approaches ranged from 2% [70] to 13% [68]

The use of metal-based nanostructures has the disadvantage of inducing absorptive losses that hinder the electrical output of the photovoltaic module; however, alternative dielectric-based structures could reduce this problem. The main advantage of this approach is its unique ability to modulate light in a wavelength-dependent manner using a single layer. In this respect, the fundamental principles of obtaining colors using these structures is well known,[71] as it is their application in photovoltaic devices [72]. However, to date, only single-module demonstrators or small area devices have been showcased. The technique is still in its infancy when it comes to mass production, with no clear method that could be translated into a large area, reliable, and cost-effective industrial application. However, some recent approaches, such as that presented by Das Gupta *et al.* [73], offer promising results in terms of versatility and potential scalability.

For integration layouts that require transparency, such as glass facades, skylights, and canopies, thin-film-based photovoltaic modules have reached a significant level of maturity at the industrial level. The same approaches discussed for opaque photovoltaic modules can be applied to provide color to semitransparent modules. As stated in the previous section, the challenge is to provide the transmitted spectra required according to the application. For indoor office lighting, semitransparency and color must comply with health and safety requirements [74].

Kim *et al.* [75] demonstrate that nanostructures made with SiO_2 and TiO_2 in hexagonal patterns can create colorful CIGS solar cells. Yoo *et al.* [76] presented coloring concepts for CIGS solar modules based on a triple layer photonic crystal made with SiO_2 and TiO_2. The authors focused on semitransparent modules and presented designs for

a blue, yellow, and red photovoltaic module for window applications.

Amorphous silicon (a-Si:H) is an extremely versatile technology with respect to customized modules with different levels of transparency. Lee *et al.* [77] created semi transparent colored solar cells based on thin films of a-Si:H and cuprite Cu_2O. Myong and Jeon [78] discuss ways to produce colored and semitransparent glass-to-glass (GTG) photovoltaic modules based on a-Si:H solar cells, including the use of colored materials used for encapsulation and transparent contacts. Given the transparency achievable in solar cell fabrication, the colored layer is placed on the back side of the active area, thus avoiding optical losses. Neugebohrn *et al.* [79] focused on the use of oxide-metal oxide stacks made of aluminum-doped zinc oxide ZnO:Al and silver in Cu(In, Ga)Se_2 solar cells (CIGS). Adjusting the physical properties of this stack changed the color produced.

Products based on this solar cell technology have an outstanding level of maturity and development. Onyx Solar [80] is one of the largest BIPV manufacturers in the world, with a significant portfolio of projects, many of which are based on semi-transparent and even colored a-Si:H photovoltaic glass. Their main drawback, compared to potential new alternatives (semi-transparent c-Si-based products, perovskite approaches), is their lower power conversion efficiency, which, depending on their level of transparency, can range between 4% and 10%.

2.2. PASSIVE COOLING OF PHOTOVOLTAIC MODULES

In recent years, research has been driving the efficiency of crystalline silicon (c-Si) solar cells to such an extent that it almost reaches its theoretical limit. The focus of increasing the electrical output of photovoltaic modules has changed to its efficiency dependence on its operational temperature. c-Si solar cells have temperature coefficients related to output power in the range of -0.2% [81] to -0.4% [82]. If operating at 60 °C, a c-Si solar cell can lose between 11% and 14% of its power measured under standard test conditions due to its increased temperature. Moreover, research suggests that the reliability of photovoltaic modules (PV) seems very sensitive to their operational temperature [24], [83], [84]. Modules that consistently perform at high temperatures throughout the year can have a significantly shorter lifespan. As discussed earlier, improving reliability is instrumental in bolstering the economics of photovoltaic systems and is essential, more specifically, for building integrated photovoltaics (BIPV). A module installed on an integrated system usually presents an operational temperature higher than a standard rack mounted configuration [26]. Long lifetimes are required on BIPV modules, so they can be competitive in this aspect with the building materials they are replacing. Thus, thermal management is an increasingly important aspect of the design of photovoltaic modules. In recent decades, researchers have studied many options to reduce the operating temperatures of photovoltaic modules [85]–[87]. Although widely varied, the proposed solutions fall into two main categories: passive and active approaches [88].

Active approaches utilize auxiliary systems, usually to significantly improve convective cooling, and utilize the heat produced on PV modules for other applications, such as residential or commercial water heating [89]. The active system provides more predictable cooling power than the passive approach, but demands an external energy source. Passive approaches rely on environmental factors (such as wind speed) or installation layouts (e.g., non-insulating PV module backside) to provide observable benefits [85].

A passive approach utilizes devices that take advantage of physical principles that can increase cooling effects, such as those driven by radiation or convection, and require no additional energy to function. Notable examples of passive cooling are phase change materials (PCM) [90], [91]. Spectral cooling approaches are interesting because they can work alongside other cooling technologies, given their unique nature. These solutions can also be divided into thermal radiative approaches and full spectrum management approaches, as presented in the review work by Zhao *et al.* [92].

2.2.1. SPECTRAL APPROACHES FOR COOLING PHOTOVOLTAIC MODULES

Thermal radiative approaches refer to the improvement of the emissivity of solar cells and modules at wavelengths in the so-called atmospheric window wavelength band (8-13 μm) where the heat from a photovoltaic device can be dissipated through dry clear air into outer space. The seminal work of Zhu *et al.* [93] numerically demonstrated the cooling potential of this mechanism for bare silicon solar cells, with potential temperature reductions of 18.3 K. However, when this approach is applied to conventional photovoltaic modules, Zhao *et al.* [94] argued that its cooling potential was 1.75 K, mainly because conventional photovoltaic modules already have a suitable emissivity in the range of interest due to the front glass. The authors argued that the approach is much more suitable for extraterrestrial applications, a similar conclusion reached by Safi and Munday [95], who demonstrated, through the detailed balance method, that for space applications, radiative cooling approaches could provide an absolute efficiency increase of up to 2.60%, compared to a 0.87% when applied on a terrestrial application. Further studies by Zhao *et al.* [96] proved the radiative cooling potential of photovoltaic modules, particularly at night, estimating temperature reductions up to 12 °C. In addition, the authors also discussed the negative effect that environmental factors (increased relative humidity, wind speed, and ambient temperature) have on this potential. Further examples of radiative cooling approaches can be found in the aforementioned review by Zhao *et al.* [92] as well as in the works of Sato *et al.* [97] and Hu *et al.*[98]

Full-spectrum management approaches also consider the rejection of sub and above-bandgap radiation that contributes to temperature increases in photovoltaic modules. Khorrami *et al.* created numerical models of spectral shields [99] to assess performance gains obtained by rejecting 40% and 80% of solar irradiation at wavelength values from the sub-bandgap range of 1 to 2.4 μm. The authors state that under high irradiance conditions (above 1025 $W \cdot m^{-2}$), a shield with 80% reflectance provides a relative improvement of electrical efficiency of up to 5.72%. Vaillon *et al.* [100] also demonstrated that sub-bandgap reflection and improved radiative cooling were interesting options for thermally managing PV modules. Sun *et al.* [101] performed an opto-electro-thermal simulation of the potential cooling provided to photovoltaic modules by the ideal rejection of sub-bandgap irradiance and the enhancement of emissivity in the atmospheric window range. The authors demonstrated temperature reductions as high as 10 °C. Similarly, Heideier *et al.* [102] used numerical models and estimated a potential energy yield increase of 6.8% by ideally reflecting light at wavelengths above 1000 nm for an equatorial location.

Other research efforts focus on feasible alternatives to achieve spectral management. Lu *et al.* [103], for example, presented a technique that uses broadband textured im-

printed glass that provides high emissivity within the atmospheric window combined with high transmittance within the visible spectrum, resulting in increased short circuit current (5.12%) and power conversion (3.12%) compared to a standard case. Lin *et al.* [104] reported a relative increase in efficiency of 3.23% on a c-Si photovoltaic module by using flexible photonic architectures on polydimethylsiloxane. Cui *et al.* [105] studied the effect of thermal regulation coatings used on the front or back of a glass / glass photovoltaic module. The authors found that an optimized polymer matrix TPX (polymethyl pentene) mixed with SiO_2 particles located on the back side of the module provides radiative coating with temperature reductions of 1 °C, which results in an absolute increased efficiency of 0.21%. However, they also argue that, from an ideal standpoint, front-side spectral management has better cooling potential.

From this perspective, photonic crystals represent one of the most promising technologies. These devices affect the propagation of electromagnetic waves, allowing the reflectance and transmittance to be tuned to a surface via interference effects. This versatility makes them suitable for a variety of applications in solar cells and modules, such as optional back reflectors [106],[107] coloring technology [38], [47], [66], [108] and light management in thin film solar cells [54]. Regarding thermal management, An *et al.* [109] studied the use of a combination of a one-dimensional (1D) photonic crystal based on ten layers of nine different materials with a two-dimensional (2D) photonic crystal based on grated SiO_2. The combination provided high sub-bandgap reflection and high emissivity in the atmospheric window, providing potential cooling on a c-Si solar cell of 10°C with an absolute increase in power conversion efficiency of 0.43%. Akerboom *et al.* [110], studied a 2D photonic crystal based on silicon cylinders that provided a cooling potential of 3 K to a c-Si module, representing a potential increase in relative efficiency of 1. 35%. Other examples of 2D photonic crystals can be found in the works of Zhao *et al.* [111] which presented a combination of a 1D and 2D photonic crystal to enhance diurnal PV performance and nocturnal radiative cooling, and Perrakis *et al.*. [112] which simulated a 2D photonic crystal implemented in a photovoltaic module based on an interdigitated back contact solar cell (IBC), which provided a cooling potential of 0.63 °C and a relative efficiency increase of 3% due to a better optical behavior within the useful wavelength range (0.3-1.1 μm).

Perrakis *et al.* [113] compared the effects of cooling performance on a commercial photovoltaic module of implementing a 2D photonic crystal (radiative cooling) versus the implementation of a 1D photonic crystal (spectral management). Their results conclude that a 1D photonic crystal that rejects UV and sub-bandgap radiation while providing high transmittance in the useful range for c-Si solar cells outperforms the 2D device. 1D photonic crystals are simpler to manufacture but present some technical challenges. Achieving high reflectance over a wide range of wavelengths demands the use of several different materials and a high number of layers. In addition, they are required to have stable angular behavior, which can increase the complexity of the design. Fan *et al.* [114], for example, designed a 1D photonic crystal based on ZnS and MgF_2 for a concentrated photovoltaic application in space. A total of 247 layers were required to meet the requirements mentioned above (reflectance at UV / IR, transmittance between 0.4 and 1.1 μm, and angular stability). The simulation results predicted a temperature reduction of 30 °C and an absolute efficiency increase of 1.4%. Slauch *et al.* [115] designed and optimized

several 1D photonic crystals with the purpose of cooling a photovoltaic module working in the climatic conditions of Golden, Colorado. The authors demonstrated that achieving angular stability and good optical performance required designs with 34 layers and four materials for a photonic mirror located at the air / glass interface and 35 layers and two materials for one placed between the front glass and the EVA. The simulation results predicted an increase in energy output of up to 3.4% for the selected location.

Li *et al.* [116] also introduced a comprehensive study on the thermal management of solar cells using a 1D photonic crystal that rejects light at wavelengths that only contribute to the temperature increase of an encapsulated cell without any contribution to its electrical output. The device presents a near ideal performance and consists of alternating layers of four materials (TiO_2, Al_2O_3, SiN and SiO_2) with a total count of 45 layers. The proposed filter provides a solar cell temperature reduction of 5.7 K compared to a standard uncoated encapsulated solar cell under the same illumination conditions.

High layer counts imply complexity in manufacturing, and simplified designs could contribute to widespread implementation. This work explores the experimental implementation of simple 1D photonic crystals (henceforth referred to as optical filters) to be used as thermal PV management devices and the related modeling to simulate the energy yield and the degradation rate of PV modules endowed with such filters. This work shows that it is possible to produce a reflectance profile containing two high reflectance peaks with a low layer count by following basic optical filter design rules. These reflectance peaks are tailored to partially reflect unwanted infrared (IR) irradiation and light at wavelength values where a c-Si solar cell presents high thermalization losses. Reducing thermalization also entails reducing electrical output, which produces designs with a lower performance compared to more sophisticated alternatives such as those presented before. Such comprehensive designs are preferred, provided adequate economic feasibility of their implementation.

The main contribution of this study is the implementation of a full simulation framework that considers not only the impacts of temperature on the instantaneous performance of a PV module but also its expected lifetime, thus allowing the analysis of when these simplified optical filters can provide a net positive benefit when implemented on PV systems.

2.2.2. PHASE CHANGE MATERIALS

Recent research has produced promising results on the potential thermal management of photovoltaic modules by using phase-change materials (PCMs). PCMs have the potential to provide temperature reductions of tenths of degrees for extended periods of time [90], making them among the most promising techniques for improving the electrical performance of photovoltaic systems. PCMs are usually classified into four main categories: Organic, Inorganic, Eutectic, and Composite PCM [117]. A significant amount of research has focused its attention on solid-to-liquid PCMs because of their technical advantages, particularly volume stability, as reviewed by Zhang *et al.* [118]. PCM materials can be manufactured with a wide range of latent heat (in kJ/l) and melting temperature values, from salt solutions with melting temperatures below 0 °C and latent heat values ranging from 50 to 200 kJ/l to fluorides, exhibiting melting temperatures up to 800 °C and very high latent heat values (in the range of 900 – 1000 kJ/l). Such a wide

span of values means that PCMs are extremely versatile and can be deployed in many applications.

Research focused on the incorporation or attachment of PCMs into PV modules has provided valuable information on their cooling potential. Upon reaching its melting temperature, heat produced by the photovoltaic module goes into the PCM, and it is used for the phase change (e.g. solid to liquid), a process that occurs at constant temperature. The PCM acts as a heat sink and thermally manages the photovoltaic module, thus reducing its operating temperature and delaying its increase rate. For PV applications, key physical properties are the chemical stability of the material, high thermal conductivity, high latent heat, low supercooling effect, in which the PCM maintains a liquid state even at temperatures lower than its solidification threshold [119]. From a safety and reliability perspective, low leakage, low flammability, and volume stability are among the most important aspects of selecting a PCM for photovoltaic applications.

Properly selected, a PCM can provide substantial cooling potential, as evidenced by a substantial amount of experimental work. Some examples of research using PCM to reduce the operating temperature of modules include the work of Japs *et al.* [120] that mechanically attached bags filled with different PCMs on the backside of 30 W PV panels and measured their temperature for one month in the summer of 2013 in Germany, finding differences of 10 °C and 7 °C depending on the PCM utilized. Maiti *et al.* [121] used metallic enclosures filled with paraffin wax, measuring reductions of between 17 °C and 20 °C. Sharma *et al.* [122] used the Rubitherm (RT) 42 (melting temperature of 42 °C) alongside metallic fins on the backside of a PV module with different installation layouts, including building integrated concentrated applications (BICPV). Indoor measurements showed a temperature reduction of up to 10.7 °C. A full year experiment carried out in the United Arab Emirates by Hasan *et al.* [123] implemented PCMs based on RT 42 on a 40 W PV module, finding maximum temperature reductions of 13 °C and increased power output of around 5.9% compared to a standard module. Stropnik and Stritih [124] tested using RT 28 during seven days of October in Ljubljana using a 250 W PV module. The authors observed a PV surface temperature reduction of 35 °C and an average increase in electrical efficiency of 2.8%. Elavarasan *et al.* [125] developed a cooling system based on PCM (HS29), fins and a water reservoir (3.3 *L*) and applied it to a PV module (5 W). The measurements took place during two days of October in Madurai, India. They measured temperature reductions of up to 16.7 °C, and a relative increase in power output of 9%. Kumar *et al.* [126] used a phase change material fabricated from a mixture of copper, silicon carbide and paraffin wax. The authors measured temperature reductions of up to 4.5 °C under the environmental conditions of Coimbatore, India, during February 2020. Karthick *et al.*[127] investigated the cooling provided by a eutectic PCM based on Zinc Nitrate Hexahydrate and Sodium Sulfate Decahydrate on a tailored semitransparent PV module in Kovilpatti, India, during the year 2018. Measurements showed that incorporating the PCM resulted in instantaneous temperature reductions up to 12 °C, which, over the course of the year, resulted in a relative increase in the electrical yield of 8%. Furthermore, Singh *et al.* [128] investigated the effects on the operational temperature of a PV module by attaching one or more conductivity enhancing containers with PCM material (Calcium chloride hexahydrate) on its backside. The authors found that covering the backside of the module with five containers provided much better cooling

homogeneity compared to using one single large container. In the experiment, carried in Chennai, India, the authors measured temperature reductions up to 23.3 °C in the month of June. A two-day experiment in China, carried out by Waqas *et al.* [25] using RT 24 with limited contact area (0.3 m^2) showed a maximum temperature reduction of 9 °C in case of a 50 W PV module. Wongwuttanasatian *et al.* [129] used palm wax on containers with different layouts (grooved, finned and tubed), finding that the finned option provided the best cooling performance.

The promising potential of thermally managing the temperature of the PV module with PCM has also expanded to PVT systems. Choubineh *et al.* [130] focused on an air-cooled PVT system, Rajaee *et al.* [131] who studied the combination of PCM with thermoelectric generators to cool PVT systems using paraffin wax with alumina powder, demonstrating a 12.3% increase in electrical efficiency compared to a water-cooled PVT system. Klugmann-Radziemska and Wcislo-Kucharek [132] conducted a comprehensive set of experiments consisting of testing three different PCM materials (Paraffin, RT22 and Ceresin) on PV and PVT modules under both laboratory and natural conditions. The authors concluded that the combination of paraffin and water cooling provided the best results but argued that the use of PCM alone was a suitable solution to provide significant cooling.

The literature mentioned above is only a fraction of the amount of experimental and computational research carried out to investigate the implementation of PCM in photovoltaic systems. For a broader overview, the readers are referred to the review work of Ali [91], Biwolde *et al.* [133], Dutil *et al.* [134], Huang *et al.* [135], Kant *et al.* [136], Khanna *et al.* [137], Tao *et al.* [138], and Preet [139].

2.3. ADVANCES NEEDED TO MEET FUTURE CHALLENGES

Pelle *et al.* [42] highlighted the need for more comprehensive and accurate models for color BIPV modules. The main challenge is that the modeling needed usually requires detailed optical characterization of all the layers within the module. Any change in the layout or properties of these materials can produce a change in the behavior of the final product. For interference structures, modeling textured surfaces usually requires a complex combination of ray tracing techniques [140]–[143] and models based on the transfer matrix method [58], [144]. A change in the textured pattern implies a reconfiguration of the model input. Furthermore, useful optimization algorithms that could reduce unwanted optical losses, such as the needle technique [145], are not yet available when working on texture surfaces with roughness in micrometers. For the case of ceramic inks, the transmittance of each of the materials and dyes used must be characterized to estimate their induced optical loss. Comprehensive CAD tools that address these aspects could reduce the time and costs required to develop new products.

More efforts are needed to include the impact that any coloring technique can have on the operating temperature of a photovoltaic module. The published performance loss is usually estimated under laboratory conditions, where temperature effects are not taken into account. This may lead to an underestimation not only of the power output of a color photovoltaic module but also of its potential lifetime, both extremely important parameters in life-cycle and LCOE analysis. It is also important to agree on a standard way of assessing color matching and color stability, particularly for applications in which

these aspects are critical, such as heritage buildings or seamless integration into open environments. Some works utilize the CIEDE2000 color difference standard ΔE_{00}, which is defined in the HCL color space, while others use the CIE76 color difference standard ΔE_{76}, based on CIELAB. There are important differences between these two approaches, especially in terms of perceptual uniformity. Standardizing these approaches, as well as the limiting values of perceived color differences according to different hues, is essential to guarantee excellence in the final product. In this sense, Borja Block *et al.* [146] proposes the use of an innovative large-area colorimeter that allows to accurately characterize the color of BIPV products.

There is also a need to create thermal models that can be used to understand and optimize Spectral Thermal Management adapted cooling techniques. Given the importance of extending the lifetime of photovoltaic products aimed toward building integrated systems, all approaches to achieve lower operating temperatures must be carefully studied to analyze their suitability for a specific or a general application. Most of the thermal models available in commercial software packages do not consider any spectral effect, which greatly limits the modeling options in the design of BIPV products.

A substantial body of experimental research has focused on the potential of phase-change materials (PCMs) as passive cooling devices to increase the electrical output of photovoltaic modules. However, long-term experimental work is still needed to understand the suitability of a given PCM working under different local environmental conditions to fully understand the parameters that need to be optimized on these materials for specific installation layouts.

2.4. PERFORMANCE MODEL OVERVIEW

Each of the following chapters will provide details on the modeling approach used to estimate the performance of a photovoltaic module when specific aesthetic and thermal approaches are present in their layout. However, these specific modeling algorithms are based on the same basis: the calculation of two parameters, the effective irradiance reaching the solar cell, denoted in this work as G_{cell}, and the operational temperature of the solar product of this irradiance parameter and other environmental conditions, T_{cell}.

The modeling framework is divided into three main pillars: Optical, thermal, and electrical. Auxiliary functions are added to these pillars according to the specific modeling needs, for example, by adding color perception models or accounting for spectral effects to the optical model. Figure 2.2 presents the flow chart of the optical pillar. The spectral behavior of the photovoltaic module is estimated using GenPro4 [140], which combines ray tracing techniques and wave optics (more details on this can be found in Chapter 3). The specific optical properties of all components of the photovoltaic module (front glass, encapsulating material, etc.) are used to calculate the wavelength-dependent reflectance ($R(\lambda)$), transmittance ($T(\lambda)$) and absorptance ($A(\lambda)$).

The specific operating conditions of the photovoltaic module are accounted for using two independent inputs. First, the overall installation layout of the system, namely orientation, tilt angle, and configuration of the installation, which is either integrated in the building or mounted in an open rack. From these inputs, the model estimates the mass of air at each specific time instant according to the position of the sun. The Simple

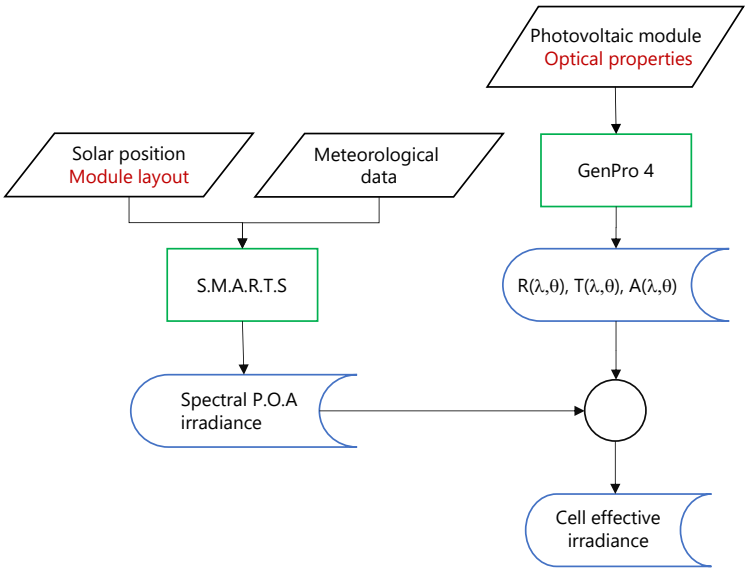

Figure 2.2: Flow chart of the base optical model upon which specific auxiliary functions are added according to specific simulation requirements (e.g. color perception, spectral thermal management).

Model of Atmospheric Radiative Transfer of Sunshine (SMARTS) [147] provides the spectral nature of the irradiance at each of these values of air mass, under the assumption of clear skies. The software provides spectral direct beam, circumsolar, and hemispherical diffuse irradiance at any given plane, and each of them is normalized by their highest value. Parallel to this, the model uses the specific meteorological data of any given location and estimates each component of the plane of the array irradiance using the Perez [148] transposition model. Each component of G_{POA} is multiplied by their respective normalized spectra, resulting in a spectral plane of the array irradiance. Finally, adjusting for the optical behavior of the module ($R(\lambda)$, $T(\lambda)$, $A(\lambda)$), the effective irradiance reaching the solar cell $G_{cell(\theta)}$ is calculated, where θ denotes the angle of incidence.

Chapters 3 and 4 argue that, for the case of the selected solar cell architecture (IBC solar cell), $G_{cell(\theta)}$ can be estimated using:

$$G_{cell(\theta)} = \tau_0 \cdot G_{POA} \cdot j_{SC(\theta)} \tag{2.1}$$

τ_0 represents an optical loss that considers the absorption and reflectance losses produced by the different components of the photovoltaic module, using the implied photocurrent calculated by GenPro4. Finally, $j_{SC(\theta)}$ represents an angular optical loss due to the increase in reflectance at the air | front glass interface, which has a high spectral dependence and therefore is specifically calculated in each of the following chapters. This parameter is commonly referred to in the literature as the incidence angle modifier (IAM). In this book, $j_{SC(\theta)}$ and IAM are equivalent.

Similarly to $G_{cell(\theta)}$, the value of T_{cell} has a strong spectral dependence. Solar cell architectures have different spectral responses and operative temperature as discussed

by Xu *et al.* [149], who demonstrated that most of the heat comes from thermalization, recombination and resistive losses. However, other mechanisms such as sub-bandgap absorption and infrared absorption also contributed to architectures such as passivated emitter and rear cell (PERC), mono-c-Si back surface field (BSF). Infrared parasitic losses, the authors argue, occur at wavelengths up to 1200 nm, whereas sub-bandgap absorption losses are associated with wavelength values larger than 1200 nm.

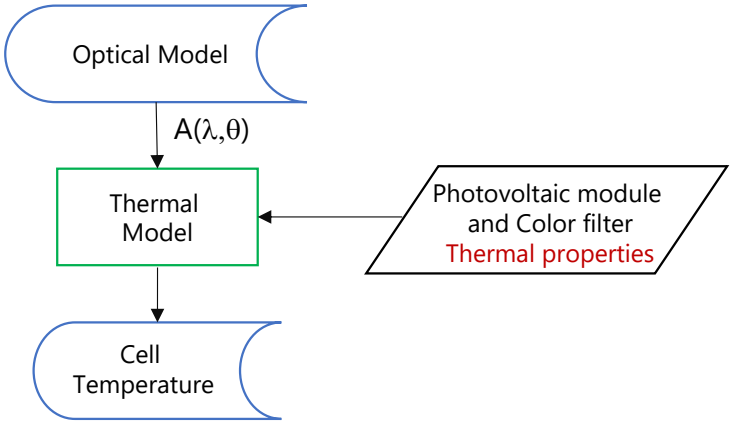

Figure 2.3: Flow chart of the thermal model used to account for the spectral nature of the devices studied in this thesis work.

Figure 2.3 presents the basic flow chart that summarizes the spectral model approach. Although much simpler than in the case of the optical pillar, the thermal pillar represents a more comprehensive set of algorithms. The calculated spectral absorptance $A(\lambda)$ in each layer is used to estimate the volumetric heat generated by the different materials in the module. The range of wavelength values considered for this model is 300 nm to 1800 nm, which will be shown later on to be sufficient for accurate temperature prediction. In summary, the method for the estimation of the operating temperature of the module is a two-dimensional finite-volume transient thermal approach. The photovoltaic module is divided into finite volumes and each volume is represented by a node. By applying the following energy balance:

$$\dot{E}_{in} + \dot{E}_{gen} = \dot{E}_{st} \tag{2.2}$$

Where $\dot{E}_{in}$ is the energy flow that enters (or exits) each node, $\dot{E}_{gen}$ is the energy generated at each node, and $\dot{E}_{st}$ represents the energy at each node, a set of linearized equations can be created based on the heat transfer mechanisms associated with each finite volume. Figure 2.4 exemplifies how the photovoltaic module can be divided into twelve different relevant nodes. The division can be customized to any number of nodes distributed horizontally or vertically.

In general, the thermal model operates under the following assumptions:

- The space between the solar cells is not taken into account. Cells are modeled as a

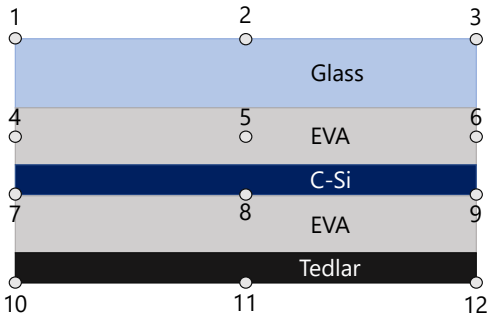

Figure 2.4: Example of the division of a photovoltaic module into finite volumes, each of them associated to a node by a number. Each node is analyzed based on the energy balance presented by equation 2.2

continuous layer over the entire module geometry.

- The effect of radiation and convection on the narrow sides of the module is neglected. Only the nodes at the top and bottom surfaces are analyzed considering these heat transfer mechanisms. Aly *et al.* [150] demonstrated that this assumption incurs only a small error.
- The frame of the module is not considered in any calculation
- the thermal generation due to thermalization are calculated considering a bandgap of the solar cell that is temperature independent.

The modeling follows the approach presented by Aly *et al.* [150], which begins from the heat equation derived with respect to time:

$$\rho_{mat} C_{mat} \frac{\partial}{\partial t} T(x,y,t) = k_x \frac{\partial^2}{\partial x^2} T(x,y,t) + k_y \frac{\partial^2}{\partial y^2} T(x,y,t) + Q \tag{2.3}$$

in which ρ represents the density of a given material (mat), C_m its specific heat capacity, t represents time, Q is the heat generated within the material, and $T(x,y)$ is the temperature distributed throughout the area analyzed. It is important to note that the above equation applies for the case where conduction is the only heat transfer mechanism at work, and hence only the thermal conductivity k applies. Second, the first-order term of equation 2.3 is expressed as a finite difference of the form:

$$\frac{\partial}{\partial t} T(x,y,t) \approx \frac{T(x,y,t+\Delta t) - T(x,y,t)}{\Delta t} = \frac{T_{m,n}^{p+1} - T_{m,n}^{p}}{\Delta t} \tag{2.4}$$

Here $p+1$ is the new time step, p represents the previous one, and Δt its increment. m and n indicate the position of the node under analysis. The second-order terms of equation 2.3 are approximated as:

$$\frac{\partial^2}{\partial x^2} T(x,y,t) \approx \frac{T_{m+1,n} - 2T_{m,n} + T_{m-1,n}}{\Delta x^2} \tag{2.5}$$

and

$$\frac{\partial^2}{\partial y^2} T(x,y,t) \approx \frac{T_{m,n+1} - 2T_{m,n} + T_{m,n-1}}{\Delta y^2} \tag{2.6}$$

respectively, thus allowing for the linearization of the set of equations required to analyze the nodes presented in Figure 2.4. For the case of node 1, the following diagram depicts its interaction to establish the energy balance.

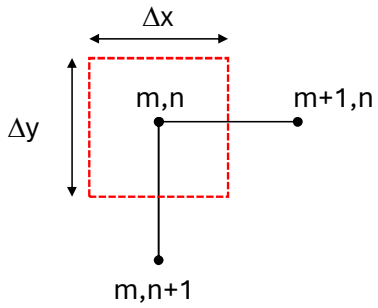

Figure 2.5: Schematic of the interactions associated with node 1 from Figure 2.4

The final equation for this node is as follows:

$$\frac{Q_{gen}\Delta_t}{\rho C_p} + T^p_{m,n} + 2Bi_c Fo_y T_a + 2Bi_R Fo_y T_s = T^{p+1}_{m,n}\left(1 + 2Fo_y + 2Fo_x + 2Bi_c Fo_y + 2Bi_R Fo_y\right) - 2Fo_y T^{p+1}_{m,n+1} - 2Fo_x T^{p+1}_{m+1,n} \tag{2.7}$$

Given that this node belongs to the front glass, the values of ρ and C_p belong to the thermal properties of this material. Additionally:

$$Fo_y = \frac{\alpha\Delta_t}{\Delta_y^2} \quad Fo_x = \frac{\alpha\Delta_t}{\Delta_x^2} \quad Bi_c = \frac{h_c\Delta_y}{k} \quad Bi_R = \frac{h_R\Delta_y}{k} \tag{2.8}$$

where $Fo_{x,y}$ is the Fourier number which represents the degree of change in temperature inside a body due to heating or cooling phenomena. $Fo_{x,y}$ depends on the thermal diffusivity α and the geometry of the node. In this case, half of the volume represents the external air and the other half represents the glass. Bi_c and Bi_R are the Biot numbers of the convection and radiation mechanisms, since this node is subject to both. They represent the ratio of convection/radiation to conduction in the material. In this case, the term h_R is taken from the approximation presented by Incropera *et al.* [151]:

$$h_R = \varepsilon_{\text{sur}}\,\sigma\,(T_s + T_{\text{sur}})\left(T_s^2 + T_{\text{sur}}^2\right) \tag{2.9}$$

where ε_{sur} is the emissivity of the material, σ is the Stefan-Boltzmann constant, T_s is the temperature of the sky, and T_{sur} is the temperature of the surface. The equations for the remaining nodes are presented in the appendix of this document. These equations are grouped into matrix form:

$$[A]\{C\} = \{T\} \tag{2.10}$$

where $[A]$ is the matrix filled with the temperature-dependent variables of the heat transfer mechanisms at each node at the instant analyzed time, C is the vector of the temperature independent constants and T is the vector of known temperatures, belonging to the previous time step. Finally, Equation 2.10 can be solved using the Gauss-Seidel method. The result of this calculation is a temperature distribution across the photovoltaic module for any environmental condition. For example, under nominal operating cell conditions (NOCT), once the module reaches steady state, the temperature profile obtained is presented in Figure 2.6. The physical and thermal properties considered for this (and all the subsequent simulations) are presented in Table 2.1

Layer	$d\ (m)$	$k\ (W/m^2)$	$\rho\ (kg/m^3)$	$C_p\ (J/kg \cdot K)$
Glass	3.2 x 10^{-3}	1.8	3000	500
EVA (x2)	580 x 10^{-6}	0.35	960	2090
Solar cell	210 x 10^{-6}	148	2330	677
Backsheet	200 x 10^{-6}	0.2	1200	1250

Table 2.1: Physical and thermal properties of each layer of the photovoltaic module, with d being the physical thickness, k the thermal conductivity, ρ the density and C_p the specific heat capacity. These properties were used in all the simulations presented in the following chapters. The thermal properties were obtained from [150].

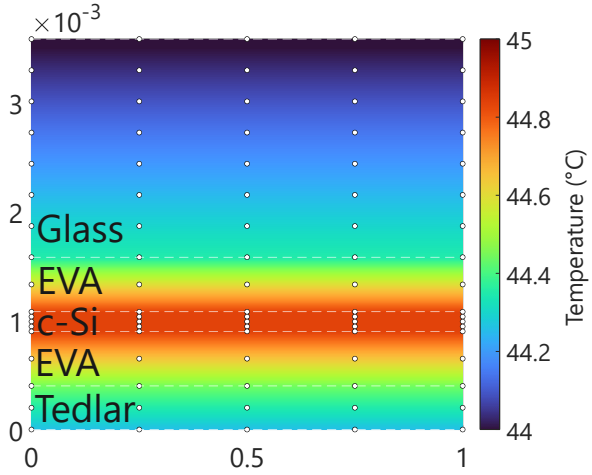

Figure 2.6: Steady state temperature profile of a photovoltaic module operating under NOCT (800 W/m^2 of irradiance, 20 °C ambient temperature and 1 m/s wind speed) conditions. The x and y directions denote distance, in m

For field validation, a setup consisting of six mini modules, each equipped with 16 Al-BSF cells (4 x 4) were manufactured and connected in series to achieve a total peak power of 250 W_p. The mounting of the setup closely represents a BIPV condition, with

very low convection on the backside and negligible effects of the wind on the sides. The measurement station, located on the roof of a selected building on the campus of Delft University of Technology, was equipped with all the necessary sensors to measure irradiance components, wind speed, ambient temperature, and plane of array irradiance. The time resolution used to obtain the data was one minute. T-type thermocouples were attached to the back of the module (see the arrows in Figure 2.7b) and connected to a PicoLog TC-08 data logger. The average temperature values were taken every minute and used for validation. The comparison between the temperature values obtained by the thermal model and those measured directly in the module are shown in Figure 2.8. For simplicity of viewing, all the data for a measured irradiance below 10 W/m^2 was omitted; hence the simulated temperature value at the end of the day was used as the first iteration value for the following day (notice the straight red lines).

(a) (b)

Figure 2.7: **(a)** Photovoltaic mini modules connected in series and used for the validation of the thermal model **(b)** Arrows indicating the placement of the thermocouples at the backside of two mini modules.

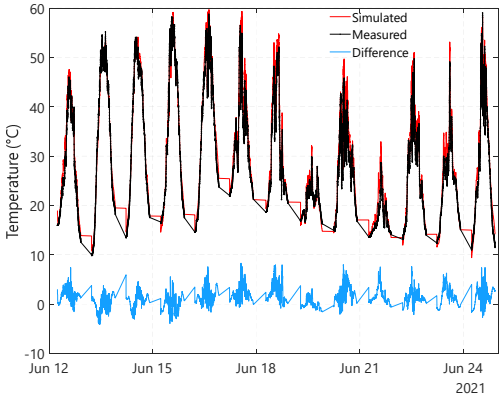

Figure 2.8: Simulated *vs* measured operational temperature of a 250 W_p c-Si module. The thermal model was calculated for a raw data resolution of 1 minute and compared to the average value of the 4 thermocouples installed on the module. The model can mimic the behavior of the model even for such low time resolution

Taking into account the entire measurement period of 13 days, the value of RMSE was found to be 2.10 °C, while the MBE was estimated at 0.89 °C. Overall, the model accurately predicts the temperature behavior under transient conditions (considering the low time resolution) and was deemed appropriate for testing with spectral devices added to a photovoltaic module.

With the model able to estimate G_{cell} and T_{cell}, the third pillar is added: the electrical model. The works presented in subsequent chapters make use of a two-diode equivalent circuit model developed by Calcabrini [35]. For a specific photovoltaic module, the parameters required for the two-diode model are extracted using the photovoltaic lighthouse calculator [152]. With the parameters found, a batch of simulations is deployed to estimate the IV curve of the module for a combination of irradiances (G_{cell}) and operating temperatures (T_{cell}). The values of both of these factors are then matched from the pool IV curves, and the maximum power point and other electrical parameters are extracted. Each of the works utilized a particular sample of the PV module, so the details of this approach and its validation are presented when appropriate.

3

IMPROVING AESTHETICS OF C-SI SOLAR CELLS

This chapter is partially based on the following publication:

J.C. Ortiz Lizcano[1] , P. Procel, A. Calcabrini, G. Yang, A. Ingenito, R. Santbergen, M. Zeman, O. Isabella, *Colored optic filters on c-Si IBC solar cells for building integrated photovoltaic applications*, Progress in Photovoltaics Research and Applications, **30**(4), 401-435 (2021).

This chapter seeks to provide insight on how color filters can be used to provide aesthetic flexibility to BIPV systems based on crystalline silicon (c-Si) modules. The selected architecture is based on interdigitated back-contacted (IBC) c-Si solar cells. This technology currently has the highest conversion efficiency (η) not only at the cell level at the laboratory scale [153] but also at the module level among all commercially available technologies [154]. Moreover, since both metallic contacts are on the back of the cells, modules based on such an architecture result in a pleasant and homogeneous aesthetic. Combining our internal developed ray-tracing software coupled with the device physics modeling platform, the cell-to-module (CTM) losses model, and the energy yield model, we can predict not only the appearance of colored IBC c-Si modules but also their angular and location-dependent energy yield performance for BIPV applications.

3.1. MODELING FRAMEWORK

The following is an overview of the modeling framework used in this chapter. First, a study on how the implementation of an optical filter affects the performance of a c-Si solar cell. It is essential to note that any potential effect that the manufacturing process might have on the cell when the color filter is deposited is not considered in this study.

[1] Candidate's contribution: Writing, coding work, simulation work, experimental work, results analysis

Mostly, it focuses on how the behavior can be modeled using standard electrical models.This is later extrapolated to fully encapsulated cells and examine the effect that the color filter deposited on cells has on the direct current (DC) energy yield and operational temperature of PV modules installed in two different locations.

As stated in the previous chapter, the starting point is the optical calculation of the amount of irradiance reaching the solar cell. Estimating this parameter requires understanding the OF's optical effect on surface appearance and optical performance. The main interest lies in simulating the impact of the color-tuning OF on the conversion efficiency of the selected solar cell structure when the OF covers the cell itself and for different angles of incidence (AOI), to this end, the TCAD Sentaurus is used to predict the effect of the filter on the electrical quality of the cell. From this knowledge, this chapter demonstrates that it is accurate to model the optical losses introduced by the OF using color-specific and angle-dependent modifying factors. These factors scale the effective irradiance that is reaching the cell. In addition, the models show that the open-circuit voltage (V_{OC}) and the fill factor (FF) of the colored cells are primarily independent of the OF in place.

3.1.1. BASIC THEORY OF OPTICAL FILTERS

Optic filters (OFs) are multilayered systems designed to deliver a desired reflection or transmission of light at a given wavelength. With proper design, these optical devices can provide very high transmittance / reflectance values (reaching 99%) at a given wavelength [55], the so-called Bragg wavelength (λ_0) and exhibit a so-called reflectance width (Δ_g) [54]. This is the width of the reflectance peak produced by the design of the filter.

The working principle of an OF is based on light interference. Consider the schematic of Figure 3.1a that depicts *one* thin layer of a material with a given refractive index (n_L) and thickness d_L deposited between an incident medium and a substrate. The refractive index of the incident medium and the substrate are indicated as n_0 and n_s, respectively. For this case, it is assumed that $n_0 < n_L < n_S$. The rays reflected at point A (depicted by the black arrows) of the first interface defined by the medium n_0 and the thin layer n_L can interact with the one reflected at point B of the second interface between the layer and the substrate, at point C. The effective distances through which light travels through the optical system (in Figure 3.1a, the paths AD and ABC) are called *optical paths.* Destructive interference, which is a reduction in the reflected light at a given wavelength, can occur at a given combination of optical paths and phase shifts that are related to the refractive index of the materials [155].

The optical paths shown in Figure 3.1a are expressed by the following equations.

$$\overline{AB} = \overline{BC} = \frac{d_L}{\cos(\gamma)} \cdot n_L \tag{3.1}$$

and

$$\overline{AD} = 2 \cdot d_L \tan \cdot (\theta) \cdot \sin(\gamma) \cdot n_0 \tag{3.2}$$

Using Snell's law, it can be demonstrated that the optical path difference OPD (defined as $\overline{AB} + \overline{BC} - \overline{AD}$) can be expressed as:

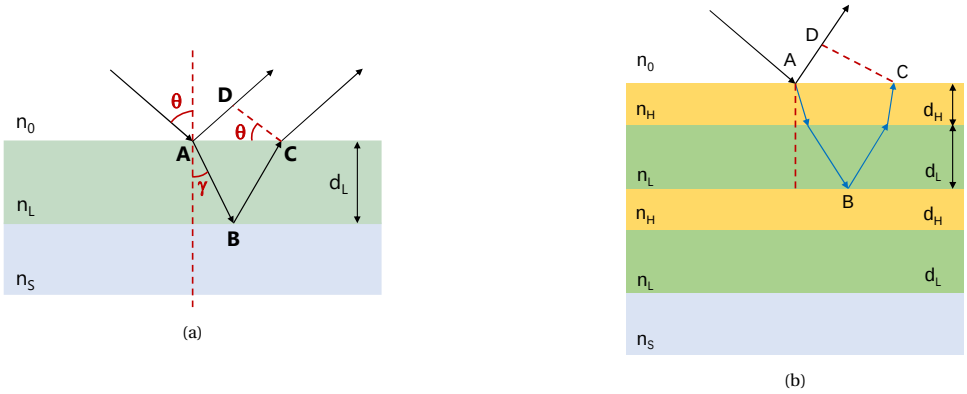

Figure 3.1: **(a)** Optical system comprising a thin film layer ($n = n_L$) of thickness d_L in between an incident medium ($n = n_0$) and a substrate ($n = n_s$). A ray of a given wavelength λ_0 (black line) is reflected both on the surface of the layer (A) and the surface of the substrate (B), their optical paths AD and ABC respectively are dependent of the layer thickness d_L. For a thickness $d_L = \lambda_0/(4 \cdot n_L)$, known as a QWOT layer, the optical path difference is equal to $\lambda_0/2$, leading to destructive interference. **(b)** Alternatively, high reflectance can be achieved by interleaved QWOT layers with refractive index n_H and n_L. For this case, the optical path difference is equal to λ_0, which produces constructive interference

$$OPD = 2 \cdot n_L \cdot d_L \cdot cos(\gamma) \tag{3.3}$$

Equation 3.3 can be used to analyze the conditions of destructive or constructive interference. For conditions $n_0 < n_L < n_S$ and $\theta = 0°$ of Figure 3.1a, destructive interference occurs when the following condition is met:

$$2 \cdot n_L \cdot d_L = \left(m - \frac{1}{2}\right) \cdot \lambda_0 \tag{3.4}$$

For values of m that are integers greater than 0.

Destructive interference at λ_0 is achieved when $d_L = \lambda_0/4n_L$, commonly known as a quarter-wavelength optical thickness layer (QWOT). Replacing this value of d_L in equation 3.4 yields a value of $m = 1$, confirming that such a layer will reduce reflection at λ_0.

Constructive interference occurs when the following condition is met:

$$2 \cdot n_L \cdot d_L = m \cdot \lambda_0 \tag{3.5}$$

For values of m that are integers, including 0. This second condition becomes important when designing an optical filter that seeks to increase reflectance at λ_0. To achieve this, consider the optical system shown in Figure 3.1b, where an additional layer with refractive index n_H (which meets the condition $n_H > n_L$) is introduced. The OF consists of pairs of $n_H|n_L$ layers (called periods p), both of them with thickness equal to a quarter wavelength. For this case, the optical path difference $\overline{ABC}$ when $\theta = 0°$ is calculated as

$$OPD = 2 \cdot n_L \cdot d_L + 2 \cdot n_H \cdot d_H \tag{3.6}$$

Solving Equation 3.6 for the case of two QWOT layers, the value of OPD is equal to λ_0, which means that the condition of constructive interference is met (with $m = 1$ in Equation 3.5), leading to high reflectance.

To achieve a desired reflectance (R) profile, the pattern of the two media that make up the OF can be varied in different ways (thicknesses, position and number of periods of n_L and n_H). For example, an OF which delivers high reflectance in a narrow wavelength range can be obtained by using many periods in the multilayer stack. An OF with a period based on two materials (n_L, n_H) can provide high reflectance by deposition of an even number of layers on a n_L/n_H sequence or an odd number of layers for a n_H/n_L one [55]. For these setups, their reflectance is given by [55]:

$$R = \left(\frac{1 - \left(\frac{n_H}{n_L}\right)^{2p} \cdot \frac{n_H^2}{n_s}}{1 + \left(\frac{n_H}{n_L}\right)^{2p} \cdot \frac{n_H^2}{n_s}} \right)^2 \tag{3.7}$$

while their width of reflectance Δ_g, can be estimated as follows [26]

$$\Delta_g = \frac{4}{\pi} \cdot \sin^{-1}\left(\frac{n_H - n_L}{n_H + n_L}\right) \tag{3.8}$$

Since the purpose of the OF is to provide aesthetic flexibility with minimum optical losses, the following design guidelines were considered for study.

- The materials composing the filter must have an energy bandgap equal to or greater than 2.75 eV (i.e. less than 450 nm) to mitigate parasitic losses due to photon absorption. Furthermore, as expressed in Equation 3.8, this study analyzes two potential design options. **Option 1** is a filter with a low refractive index difference ($n_H - n_L$), and **Option 2** with a higher value of this same difference. These two options are used to analyze how color saturation and brightness can be tuned by slight modifications of the optical properties of a given material.

- The filter design should provide flexibility in installation. It could be deposited on the encapsulating glass of a photovoltaic module or on the cell itself. For the former application, fabrication and installation of the filter need to be decoupled. See Appendix 9 for more details.

The color tuning OF used in this work was designed based on two dielectric layers: silicon dioxide (SiO_2) and silicon nitride (SiN_x). The first reason for selecting these materials is related to the deposition method. Using plasma-enhanced chemical vapor deposition (PE-CVD), both materials can be quickly deposited. The deposition rates for SiO_2 and SiN_x in this study were 26.4 nm/min and 18.2 nm/min, respectively, more information on the manufacturing process can be found in the Appendix 9 at the end of this book. The second reason is that SiO_2/SiN_x layers significantly improve color purity, brightness, and exhibit low parasitic losses [156]. In a potential upscale scenario, a single-sided, low-CAPEX, high-throughput [157] physical vapor deposition technique, such as sputtering [158], could be suitable to manufacture these devices.

By tuning the bandgap of SiO_2 and SiN_x, achieved by adjusting the deposition parameters during fabrication, the first abovementioned guideline is met (see Appendix 9).

Filter **Option 1** was based on using a refractive index value of SiN_x of $n_H = 1.73$. Whereas **Option 2** uses a SiN_x with a refractive index value $n_H = 2.10$). To produce bright colors, a stack of ten pairs of SiO_2/SiN_x was used for both filter options.

The reflectance profile of a multi-stack OF is not independent of the angle of incidence of light, as Figure 3.2a shows. Increasing the angle of incidence, the high reflectance region of an OF applied to a polished surface tends to shift toward shorter wavelengths compared with the one designed for normal incidence. This effect is related to the change in the optical light path through the layers of the filter, which was designed only considering the normal incidence. This leads to a wavelength shift of constructive interference [55].

For textured surfaces, the angular behavior of the OF is different compared to flat surfaces. As Figure 3.2b shows, when the angle of incidence increases, the width Δ_g expands. The wavelength at which R has a peak remains constant at least for angles between 0° and 40°. At larger angles of incidence, the peak of R shifts slightly towards longer wavelengths. This behavior is highly dependent on the type of texture the device has. Figure 3.2b reports the simulated reflectance change for a c-Si wafer coated with OF and textured pyramidally (slope of 54.7°). This is the reason why, as the angle of incidence approaches this value, the reflectance spectra present a larger photonic bandgap and reflectance peak.

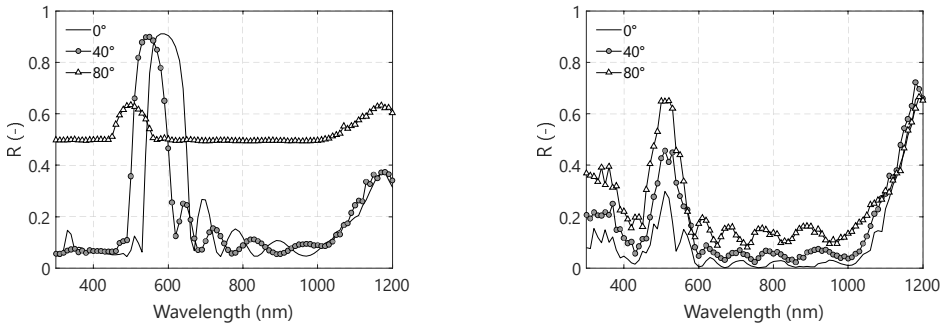

Figure 3.2: **(a)** Simulated effect of increasing the angle of incidence on the reflectance profile of a color filter deposited on a flat glass surface. Such a filter is formed by 10 pairs (p) of SiN_x/SiO_2 (90 nm and 110 nm, respectively). **(b)** Simulated effect of increasing the angle of incidence on the reflectance profile for the same filter layout as in **(a)** but deposited on a pyramidally textured solar cell surface. The wavelength at which R is maximum remains within a small range up until 40°; then the reflectance across all wavelengths starts to increase.

Given their ability to modify the way a surface reflects light, OFs have been studied for various applications on photovoltaic devices. For example, studies have been performed to assess their suitability as metal-free back reflectors [106], [107], [159]. In addition, other works focus on their use to produce colored cells [160]. However, color filters require a specific modeling approach to reasonably assess their impact on the performance of colored cells, particularly considering their spectral nature.

3.1.2. OPTICAL MODEL

The optical model allows the calculation of the reflectance, absorptance and transmittance spectra of a colored solar cell (both bare and encapsulated); these values are then used as inputs on a color perception model to predict the color produced by the filter. The backbone of this modeling step is the in-house developed MATLAB-based ray tracing software named GenPro4 [140].

GenPro4 (GP4) combines raytracing and wave optics in a single package. The core of the software is the extended net-radiation method. In incoherent layers, GP4 uses the Lambert-Beer and Fresnel law equations. In multi-stack optical systems with coherent layers, GP4 implements a different algorithm based on the characteristic matrix method described by Mcleod [55]. The output of the software is the wavelength-dependent absorptance $A(\lambda)$, the reflectance $R(\lambda)$, and the transmittance $T(\lambda)$ of the modeled optical system. Furthermore, GP4 uses the AM1.5 spectrum to estimate a photogenerated current density ($mA \cdot cm^{-2}$) by assuming that every photon effectively absorbed in the cell yields an electron-hole pair. In this work, this implied photocurrent density will be defined as J_{ph}.

3.1.3. COLOR PERCEPTION MODEL

The colors perceived by humans from non-luminous objects depend on how they are illuminated and how they reflect light [161]. The way to model this phenomenon has been extensively studied in the last century [[162]–[164]. GP4 is used to design the OF pattern required to deliver the desired R spectrum. The model then converts such generated spectrum into Red, Green and Blue [R_{RGB}, G_{RGB}, B_{RGB}] color coordinates to render the color as perceived by humans on a computer screen. A common standard for evaluating color perception is the Comission Internationale de l'Eclairage (CIE) system [164].

The CIE model uses a standard observer that is represented by three mathematical functions called color matching functions [155]. These functions, denoted by x, y, and z, are wavelength dependent. The functions $x(\lambda)$ and $z(\lambda)$ represent an approximation of the spectral response of the cones of the human eye to light, while $y(\lambda)$ models human perception of luminosity. Once each of their values is normalized with respect to $y(\lambda)_{max}$, namely $\bar{x}(\lambda)$, $\bar{y}(\lambda)$ and $\bar{z}(\lambda)$; they become scaling factors called tri-stimulus values and can be seen as mathematical constructs that depict a unique hue [160]. The CIE model also provides several theoretical light sources, called illuminants. Each illuminant represents the spectral power distributions of a certain illumination source such as daylight, fluorescence, incandescent lamps, etc. They are categorized in letters and can be found elsewhere [165]. The selected illuminant for this work is called D65. This source emulates natural daylight conditions at noon and is the standard source used in simulations to render colors on a computer monitor [166]. From the spectral power distribution of the source $S(\lambda)$, the reflectance profile of the surface $R(\lambda)$ obtained with GP4, and the color matching functions $\bar{x}(\lambda)$, $\bar{y}(\lambda)$ and $\bar{z}(\lambda)$, it is possible to calculate the following three coordinates:

$$X = \frac{1}{N} \int_{380}^{780} \bar{x}(\lambda) \times R(\lambda) \times S(\lambda) d\lambda \tag{3.9}$$

$$Y = \frac{1}{N}\int_{380}^{780} \bar{y}(\lambda) \times R(\lambda) \times S(\lambda) d\lambda \tag{3.10}$$

$$Z = \frac{1}{N}\int_{380}^{780} \bar{z}(\lambda) \times R(\lambda) \times S(\lambda) d\lambda \tag{3.11}$$

Where:

$$N = \int_{380}^{780} \bar{y}(\lambda) \times S(\lambda) d\lambda \tag{3.12}$$

Since the values obtained X, Y and Z are based on models of human perception of light, they are used to produce a three-dimensional space in which every color a human perceives can be represented [167]. This space is called the CIE XYZ color space. To transform the X, Y and Z coordinates into color coordinates used by computer monitors, a transformation matrix is needed. The values of this matrix depend on the illuminant used as reference and the target color space coordinates (e.g., sRGB, AdobeRGB, etc.). These matrices can be found in [168]. For the D65 illuminant and sRGB color space (the one chosen for this project), the transformation matrix is.

$$\begin{bmatrix} R \\ G \\ B \end{bmatrix} = \begin{bmatrix} 3.2406 & -1.5372 & -0.4986 \\ -0.9689 & 1.8758 & 0.0415 \\ 0.0557 & -0.2040 & 1.5070 \end{bmatrix} \begin{bmatrix} X \\ Y \\ Z \end{bmatrix} \tag{3.13}$$

Since these values of R, G, and B are linear, the so-called *gamma correction* must be performed to increase the accuracy of the color rendering. This is achieved by replacing each color coordinate into an equation of the following form:

$$R_{SRGB} = \begin{cases} 12.92R & \text{if } R \leq 0.0031308 \\ & \text{or} \\ (1.005)R^{\frac{1}{2.4}} - 0.005 & \text{if } R > 0.0031308 \end{cases} \tag{3.14}$$

Equation 3.14 shows the gamma correction for the R coordinate, and the same procedure must be performed for the G and B coordinates. With this, the color rendering on a screen that uses sRGB becomes accurate.

sRGB coordinates can be transformed into other color spaces that serve as a basis for colorimetry analysis. The hue, saturation and value (HSV) color space, for example, is a cylindrical representation of RGB coordinates, whose coordinates are obtained by simple mathematical transformations [169]. The usefulness of the HSV color space is that it is a perceptual representation of a given color. The hue and saturation coordinates provide information about the visual sensation (color perception) and the colorfulness of those stimuli relative to their own brightness. To find its position in the cylindrical coordinate of the color space, the value of H can be represented on a polar graph. The color space starts with red (0°), and is followed by orange, yellow, green, cyan, blue, and magenta at every 60°, respectively, as shown in Figure 3.3.

The saturation value can be maximum for both dark and bright colors (coordinate S). The explanation for this is outside the scope of this paper, but more information can

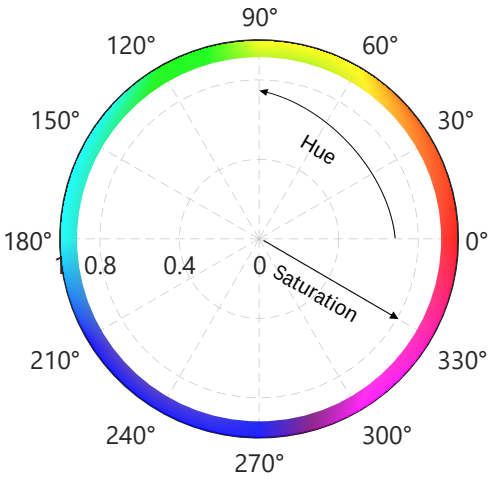

Figure 3.3: Graphical representation of fully saturated colors depicted by the hue and saturation coordinates from the HSV color space

be found at [170]. A comprehensive explanation of the different definitions regarding colorimetry (Hue, Chroma, Brightness, etc.) can be found in [171].

In this chapter, the HSV color space is used to assess the aesthetic potential provided by color filters. However, the HSV color space has perceptual inaccuracies since it is based on the cubical RGB color space, which is symmetric, placing pure red, green and blue colors at the same distance of a neutral axis. Absolute color spaces are required for analysis that requires a more accurate modeling of human color perception, such as color difference. Chapter 4 will discuss the alternatives that can be used to this end.

3.1.4. SELECTED SOLAR CELL ARCHITECTURE

The inset of Figure 3.4a shows an interdigitated back-contacted (IBC) architecture based on carrier selective passivating contacts of poly-Si [172]. This device, designed, manufactured, and characterized in facilities of the Delft University of Technology [173], was used as a reference case for performance assessment. The external quantum efficiency (EQE) spectrum and current density-voltage ($J-V$) curve of the selected device are reported in Figures 3.4a and Figure 3.4b, respectively. The conversion efficiency of this device is 21.36%.

The opto-electrical performance of the reference cell is the starting point for assessing how the implementation of a colored filter affects device performance. To this end, 10 pairs of SiO_2/SiN_x with different thickness combinations were modeled on the reference cell architecture using TCAD Sentaurus [174], [175]. Device considerations include random pyramidal texturing on the front side. The pyramids have a maximum height of 5.6 μm and a fixed base angle of 54.7°. The thickness of the wafer is 280 μm. The simulation considered a 650-μm wide rear pitch. Further details of the complete modeling, simulation and optimization study of this structure can be found elsewhere [174], [175].

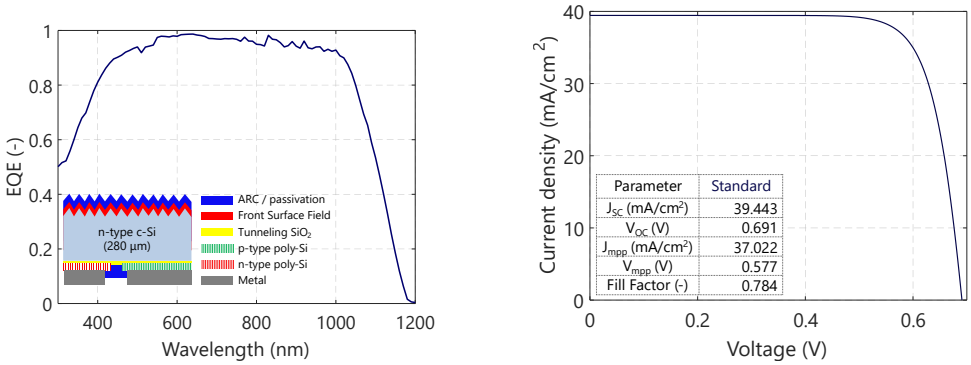

(a) (b)

Figure 3.4: **(a)** External Quantum Efficiency (EQE) spectrum and **(b)** current density-voltage (J-V) curve of the selected reference IBC solar cell. Insets: (a) solar cell sketch, (b) external parameters of the reference solar cell.

3.1.5. EFFECT OF ENCAPSULATION

For the case of a module, the effective irradiance reaching the solar cell is also affected by the reflectance and absorptance spectra of the glass, the encapsulant ethylene vinyl acetate (EVA), the colored filter, and the cell's antireflective coating. Using GenPro4 simulations, it is possible to estimate the transmittance factor τ_0 for normal incidence. This parameter is defined as the ratio between the light intensity that reaches the silicon (I_{cell}) and the light intensity that reaches the front surface of the module (I_{POA}).

$$\tau_0 = \frac{I_{cell}}{I_{POA}} \tag{3.15}$$

The properties of the encapsulant glass and EVA used in this chapter are shown in Table 3.1. For the case of a module without filter (standard case), τ_0 was found to be equal to 0.903.

Material	Thickness	Optical Properties
Glass	3.20 cm	See [48]
EVA	0.58 cm	See [49]
SiN_x layer	Variable (0-200 nm)	See Appendix 9
SiO_2 layer	Variable (0-200 nm)	See Appendix 9
Anti-reflective layer (SiN_x)	78 nm	See [38]

Table 3.1: Physical and optical properties of the layers that contribute to front side optical losses.

3.1.6. PERFORMANCE MODEL

As stated in the previous chapter, the model selected to assess the electrical performance of a colored cell is the equivalent two-diode circuit model [176], [177]. As inputs, this model requires the effective irradiance reaching the c-Si solar cell (G_{cell}), after considering all the optical effects mentioned above, and the temperature of the device (T_{cell})

under these conditions. G_{cell} is calculated using factors to scale the plane of the array irradiance G_{POA}. Estimation of T_{cell} is done by using the thermal model explained in the previous chapter.

To estimate the power produced by the photovoltaic module, the main performance parameters of the two-diode model were found, for the case of the standard device, using the $J-V$ curve obtained for normal incidence as shown in Figure 3.4b. The cell area was assumed equal to 153 cm^2, which is the area of the commercial IBC cell of SunPower, the Maxeon generation III [178].

The fitting method used to find these values was the calculator devised by [152] assuming a cell temperature of 298.15 K. The result of this fitting can also be found in Appendix 9. Different $I-V$ curves were obtained for a large combination of irradiances and temperatures using the equivalent electrical circuit of two diodes. The selected irradiance range ranged from 1 $W \cdot m^{-2}$ to 1200 $W \cdot m^{-2}$ with a resolution of 1 $W \cdot m^{-2}$, combined with cell temperatures ranging from -10 °C to 120 °C every 2 °C. In total, 77935 different IV curves were produced. In the calculation, both the series and shunt resistances were considered to be temperature independent.

3.2. SIMULATION WORK AND VALIDATION

3.2.1. COLOR PERCEPTION RESULTS

It was established that variation in the thicknesses of the layers inside an optical stack changed the wavelength value at which the reflectance reached a maximum value. With an OF Option 1 as the base, the thickness values of both SiO_2 and SiN_x varied from 0 to 200 nm in steps of 10 nm. The color perception model was used to build color matrices, which depict the predicted color appearance at normal incidence. Two matrices were considered, one for the case of a color filter deposited on glass (as in Figure 3.5a), the other for the case of a filter deposited on a bare cell. Figure 3.5b shows the different colors obtained for all thickness combinations. Although this chapter focuses on a color filter applied to solar cells, due to technical limitations, the matrix belonging to the color filter deposited on glass was used for the validation of the optical model. The matrices show that the deposition of the filter on the textured surface of a bare solar cell produces colors with lower brightness compared to that in the case of a color filter deposited on flat glass.

It was established in Section 3.1.1 that the deposition of layers with a thickness equal to $d = \lambda_0/(4 \cdot n)$ creates a high reflectance peak at λ_0. The color obtained by varying the thickness values of SiN_x and SiO_2 and shown in Figure 3.5a does not always follow this condition. Take, for example, the reflectance profile of the orange color obtained by the combination of SiO_2 = 90 nm and SiN_x = 110 nm, shown in Figure 3.6a. For these thickness values, the wavelength at which SiO_2 will be a QWOT layer is 533 nm, while SiN_x will be 792 nm. There are no peaks present at these wavelengths. Similar behavior is observed in the case of the green filter (SiO_2 = 50 nm and SiN_x = 110 nm) shown in Figure 3.6b, where the reflectance peak appears at a wavelength equal to 540 nm, which does not belong to any λ_0 values of each of the layer thickness. The reason for this is related to the way that optical paths and reflectance phase shifts impact the performance of a complex optical system. Macleod [55] establishes that a multilayer filter made with

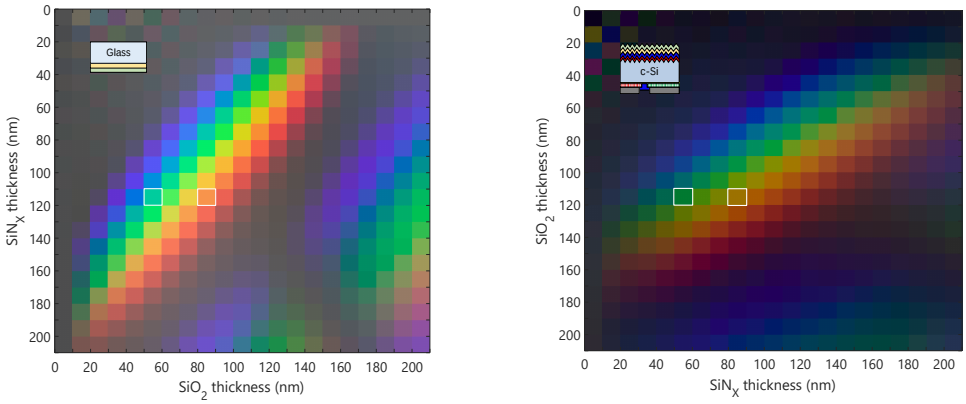

(a) (b)

Figure 3.5: Differences in color perception according to the placement of the Color filter: **(a)** color matrix for 10 pairs of SiO_2/SiN_x layers deposited behind a **flat glass substrate**, **(b)** color matrix for 10 pairs of SiO_2/SiN_x layers deposited directly on the c-Si solar cell. Placing the filter on the front of an non-encapsulated **textured surface of a solar cell** produces color with a brightness lower than placing it on the flat surface of the glass. The white squares represent the selected colors used to compare the colors on the HSV color space.

QWOT layers can present reflectance peaks not only at λ_0, but also at $\lambda_0/3$, $\lambda_0/7$, $\lambda_0/9$, and other odd integers. In contrast, layers with an optical thickness of $\lambda_0/2$ can act as absentee layers, in which case the filter will not produce reflectance at such a wavelength. Consider the following equation.

$$d = \frac{\lambda}{X \cdot n} \tag{3.16}$$

When solving for X, it can be quickly assessed if the multilayer stack will reflect light at wavelength λ if both materials have a value equal to 4. If *at least* one of them has a value of X equal to 2, the filter will not have an effect and the reflectance value at that wavelength will be that of bare glass. If the value of X is none of the values mentioned above, modeling the spectral behavior of the filter requires a much more involved method. Calculating the wavelengths at which reflectance occurs in a multilayer optical filter requires the application of the concept of optical admittance, in which the optical layer is replaced by a single surface with admittance Y. This admittance is mathematically expressed as the ratio of the total tangential magnetic field B and the total tangential electrical field C. Calculating this transmittance is done using the matrix transfer method, in which each layer of the optical system is represented as a matrix, and their multiplication provides the values of both B and C. The complete mathematical approach is beyond the scope of this chapter, and the interested reader is directed to Section 2.9 of Macleod [55]. GenPro4 implements other methods depending on the nature of the surfaces in which the filter is applied (flat, sub-wavelength textures and large textures), more information is available in the work of Santbergen *et al.* [140]

In conclusion, it is important to note that not all the colors presented in Figure 3.5a are QWOT stacks, but a product of an iterative process of thickness combinations that

could produce reflectance peaks at wavelengths within the visible spectrum.

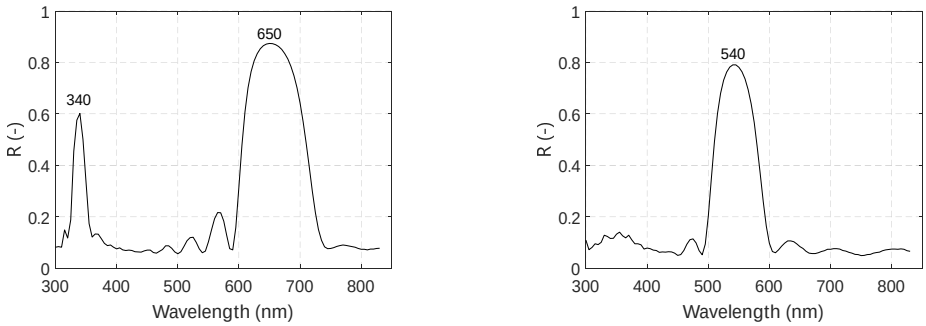

(a) (b)

Figure 3.6: **(a)** Reflectance profile of an orange color filter that consists of 10 pairs of SiO_2 = 90 nm and SiN_x = 110 nm layers deposited on glass, following the optical system depicted in the insert of Figure 3.5a **(b)** Reflectance profile of a green color filter that consists of 10 pairs of SiO_2 = 50 nm and SiN_x = 110 nm layers deposited on glass, following the optical system depicted in the insert of Figure 3.5a.

As stated in Section 3.1.3, color analysis requires that the RGB color coordinates be translated into the coordinates in the Hue Saturation Value (HSV) color space. The two selected combination of thicknesses: (90 nm of SiO_2, 110 nm of SiN_x) and (50 nm of SiO_2, 110 nm of SiN_x) will be used for this purpose. These combinations produce a bright orange and a bright green color, respectively, when deposited on flat glass, as shown in Figure 3.5a. Similarly, they produce a dark brown and a dark green color when deposited on the solar cell. The conversion from RGB to HSV is relatively simple via the MATLAB image processing tool. The HSV values for the selected colors for each case can be found in Table 3.2.

Surface	SiO_2/SiN_x thickness (nm)	*RGB* coordinate	*HSV* coordinate
Flat glass	90/110	204 077 077	0.00 0.62 0.80
Texture cell	90/110	170 089 000	0.08 1.00 0.66
Flat glass	50/110	125 221 025	0.25 0.88 0.86
Texture cell	50/110	000 121 049	0.40 1.00 0.47

Table 3.2: RGB coordinates and HSV coordinates of two different color filters: One deposited on flat and another on non-encapsulated colored solar cells.

Table 3.2 shows that a specific color filter deposited on flat glass produces higher brightness compared to deposition on a textured solar cell (denoted by the third coordinate V of the HSV values). The calculation of HSV helps to analyze the effect of encapsulation on a colored solar cell.

3.2.2. VALIDATION OF OPTICAL AND ELECTRICAL MODELS

OPTICAL MODEL

It is important to note that the colors perceived in the color matrix presented in Figure 3.5a can be misleading. Since the optical system is an OF on glass, gray must be taken as a transparent or non-perceived color rather than an opaque gray surface. From this color matrix, three colors were selected for fabrication as summarized in Figure 3.7a. Three OFs (based on the design Option 1) that show a red, yellow, and green color appearance were designed and implemented on glass. The thicknesses of the layers that make up the different colored OFs are also indicated in Table 3.3. The photographic evidence of the fabricated samples is in good agreement with the colors predicted by our model, as shown in Figure 3.7a. The R spectra exhibited by the fabricated filters deposited on glass were measured by placing the glass samples on a PerkinElmer Lambda 950 spectrophotometer. The spectrophotometer was equipped with an integrated 150 mm diameter sphere, which is entirely covered by Spectralon, a highly reflective material that exhibits Lambertian behavior. The glass samples were placed at the reflectance port. This port is sealed with a removable cap whose interior is completely covered by a perfect absorber material (more information about this measurement setup can be found in [54], [179].) They are compared in Figures 3.8a to 3.8c with the simulated results, showing good agreement in the wavelength range between 380 and 1180 nm.

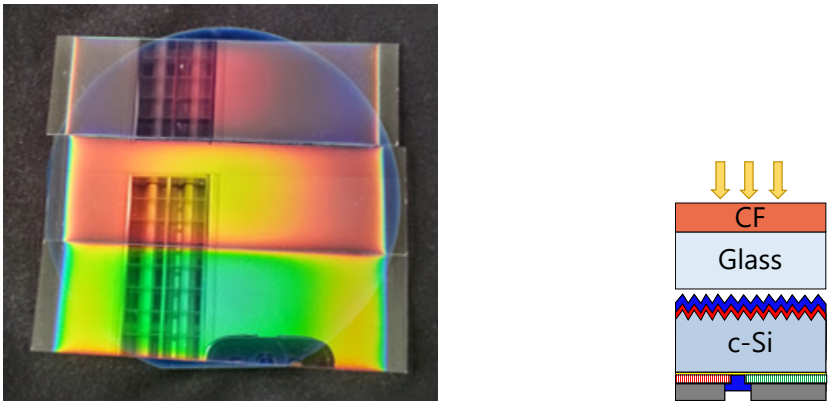

(a) (b)

Figure 3.7: **a** Perceived colors of the chosen OFs. Notice that the three samples are placed above a double textured c-Si solar cell with standard anti-reflective coating (ARC). The colors perceived by placing the filter above a solar device are not altered by the device. Note that the deposition area of the layers is not homogeneous, so the desired thicknesses were only achieved in the middle of each glass sheet. **b** Sketch of the optical system photographed in **a**. Notice that the color filter deposited on the glass is simply placed above the solar cell without optical coupling

The mean average error (MAE) and the mean bias error (MBE) of the measurements were calculated as follows:

$$MAE = \frac{\sum_{i=1}^{n} |y_i - x_i|}{n} \tag{3.17}$$

	SiO_2 = 100 nm SiN_x = 100 nm
	SiO_2 = 90 nm SiN_x = 100 nm
	SiO_2 = 40 nm SiN_x = 110 nm

Table 3.3: Thicknesses and perceived color of the filters.

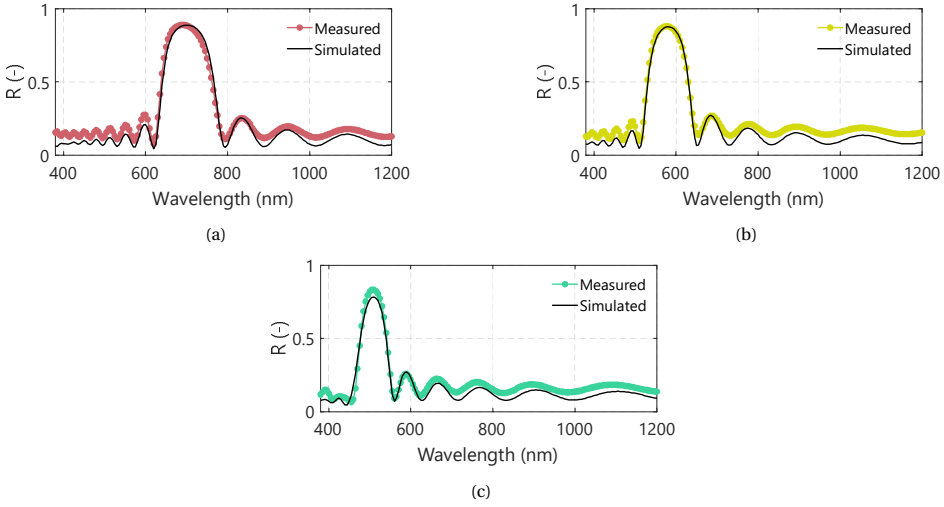

Figure 3.8: Measured and simulated reflectance spectra of the **(a)** red, **(b)** yellow, and **(c)** green samples. The reflectance spectra were measured from the glass side of the samples.

$$MBE = \frac{\sum_{i=1}^{n} (y_i - x_i)}{n} \tag{3.18}$$

where y_i is the predicted value, x_i is the measured value and n represents the number of measured points. The results are presented in Table 3.4. Overall, the color model can accurately predict the resulting surface color once it is deposited on a flat glass.

	MAE = 5.10% MBE = 2.80%
	MAE = 5.30% MBE = 3.92%
	MAE = 4.00% MBE = 3.57%

Table 3.4: Mean absolute error and mean bias error of the reflectance spectrum for each selected color.

The deposition of a multi-stack colored filter on the textured surface of a solar cell can be accurately translated from the planar model. In their work, Ingenito *et al.* [59] demonstrated that by increasing the deposition time on the PECVD machine by a factor of 1.7, the thickness calculated for a planar surface could be obtained in the direction orthogonal to the pyramid facet of a textured solar cell.

ELECTRICAL MODEL

The main objective of this work is to find ways to accurately model the effect of implementing a color filter on a solar cell in a simplified way. From an electrical point of view, it was decided to test whether the use of a standard two-diode model could be suitable to this end. The two-diode model can be described as an analytical expression to describe the behavior of a solar cell. The model assumes (i) low injection level conditions, (ii) infinite thickness on the cell, (iii) uniform generation rate, (iv) superposition principle, and (v) ideal behavior on its diodes and resistances. However, TCAD Sentaurus describes the working principles of a solar cell by using the fundamental equations of a semiconductor. It makes no assumptions and uses as input the properties of the layers and the materials involved in the cell structure. For this reason, TCAD Sentaurus was deployed as a validation step of our approach of how to electrically model a colored cell with a two-diode model.

To monitor the impact of the color filter on the value of η of the IBC c-Si solar cell, if the color filter covers the textured front side of the device, several SiO_2/SiN_x stacks were adapted onto the reference solar cell and modeled. Like the flat case on glass, the thickness of every material was varied from 0 to 200 nm at 10 nm steps. The color matrix of the colored filters applied to the textured IBC c-Si solar cell is reported in Figure 3.5b. As stated before, the obtained colors are less bright with respect to those deposited on glass because of the front texturing of the device. However, the front texturing yields lower R values at the wavelength of design and therefore lower optical losses. The EQE spectra obtained by placing the OF color adjustment on the textured device prior to the encapsulation of a dark green cell and a brown cell are shown in Figure 3.9a. The impact of the dark green and brown OFs on the $J-V$ curves is shown in Figure 3.9b.

The EQE spectra of the colored solar cells show a slight increase at a wavelength value of 400 nm. Since Sentaurus simulations are carried out in bare solar cells, the refractive indices of the materials that make up the filter improve the optical performance of the cell's front surface. From a value of n in the ARC layer ($n = 2.4$), the tuned SiN_x ($n = 1.73$) and SiO_2 ($n = 1.50$) can reduce light reflection at wavelengths outside the interference range. Additionally, for the brown cell, the dip in the EQE occurs on a wavelength range in which the standard device absorbs better. Because of this, the impact of this color on the performance of the cell is greater than the effect produced by the green filter. In addition, while J_{SC} changes significantly for the presence of the color filter, V_{OC} and FF remain largely color independent, as reported in Figure 3.9b. This is demonstrated by optoelectrical modeling of colored IBC c-Si solar cells within the thickness space of both SiO_2 and SiN_x. The values of V_{OC}, FF, J_{SC}, and η are found through these simulations. The trends of η and J_{SC} as a function of the thickness pairs of SiO_2/SiN_x for the filter Option 1 are reported in Appendix 9.

From the similarity of both trends, the variation in J_{SC} as a function of the different color filter is the main driver of the variation in η. Compared to the color matrix reported

in Figure 3.5b, it is also noticeable that the lowest values J_{SC} are obtained for colors that reflect light in wavelength ranges in which the IBC solar cell utilizes light better. Taking into account the reference value J_{SC} and the values in Figure 3.9b, a color-specific map $\Delta_{JSC} = J_{SC_{ref}} - J_{SC_{color}}$ could be generated. Such a map would help predict the impact that each color has on the value of η of a non-encapsulated colored IBC c-Si solar cell by derating its J_{SC} from the reference value. That is, without accounting for any potential manufacturing issues, the implementation of a color OF is not expected to negatively impact the electrical quality of the device itself.

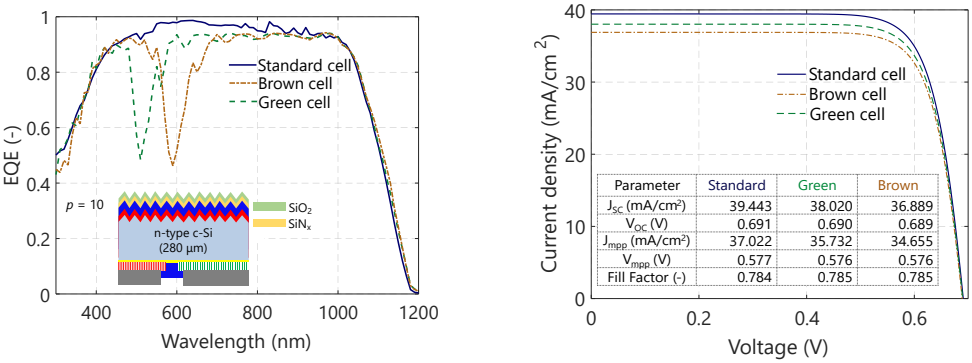

(a) (b)

Figure 3.9: Simulated effect of a dark green (dashed) and brown (dash-dotted) color tuning OF on **(a)** the EQE and **(b)** the J-V curve of a non-encapsulated IBC c-Si solar cell endowed with the color tuning OF (see inset) compared to a standard cell (blue line).

To evaluate the effects that values of AOI larger than 0° have on V_{OC}, V_{MPP}, J_{MPP} and FF, Sentaurus simulations were carried out to calculate these performance parameters on both the standard cell and the green and brown solar cells. The selected values were 0°, 20°, 40°, 60° and 80°. The results of these simulations are presented by the $J-V$ curves found in Appendix 9 and the numeric values shown in Table 3.5.

	Standard			Green			Brown		
Parameter	0°	40°	80°	0°	40°	80°	0°	40°	80°
$J_{SC}(mA/cm^2)$	39.443	29.197	6.045	38.020	26.956	5.255	36.889	25.942	4.958
$\Delta_{JSC}(mA/cm^2)$	0.000	-10.246	-33.399	-1.423	-12.487	-34.188	-2.554	-13.501	-34.485
V_{OC} (V)	0.691	0.682	0.634	0.690	0.680	0.630	0.689	0.679	0.628
J_{mpp} (mA/cm^2)	37.022	27.480	5.686	35.732	25.316	4.948	34.655	24.378	4.661
V_{mpp} (V)	0.577	0.572	0.531	0.576	0.572	0.526	0.576	0.571	0.525
Fill Factor (-)	0.784	0.789	0.787	0.785	0.790	0.787	0.785	0.790	0.786
Efficiency (%)	21.362	15.719	3.019	20.582	14.481	2.603	19.961	13.920	2.447

Table 3.5: External parameters of non-encapsulated standard, dark green and brown colored IBC c-Si solar cells for different angles of incidence. The value of Δ_{JSC} refers to the difference with respect to the standard cell at normal incidence.

The simulations from Sentaurus concluded that even at different angles of incidence, the main driver in power loss on both the colored and standard solar cells is the reduction of current generation. From Table 3.5, the voltage variation for all three cases re-

mains reasonably similar. The biggest difference is found to be 6 mV between the standard cell and the brown solar cell at an incidence angle of 80°. This voltage difference represents a deviation of less than 1%. For lower AOI values, the differences are on the order of 2 mV or less. Regarding the fill factor, the maximum difference is 0.001. These two findings conclude that the addition of a color filter produces negligible effects on the values of V_{OC} and FF, even at higher angles of incidence.

In their work, Balenzategui and Chenlo [180] state that the angular effect on the short-circuit current density can be approximated by the following cosine relation:

$$J_{SC(\theta)} = J_{SC(0°)} \cdot \cos(\theta) \tag{3.19}$$

According to Equation 3.19, the ratio between J_{SC} at any angle of incidence with respect to its value at normal incidence equals the cosine of the angle. For the case of colored cells, this approach can be inaccurate. To study this, the values of J_{SC} obtained from the simulations for all cases were used to calculate a short circuit current angular factor j_{SC}, mathematically defined as:

$$j_{SC(\theta)} = \frac{J_{SC(\theta)}}{J_{SC(0°)}} \tag{3.20}$$

Notice that according to Equation 3.19, the value of j_{SC} always equals the cosine of the angle of incidence. The trends obtained from Equation 3.20 for the standard and the colored cells are shown in Appendix 9. The approximation used in Equation 3.19 is sensible for the case of the standard solar cell, but not for the colored cells, as their angular behavior deviates significantly. The suitability of the two-diode model was analyzed by keeping all parameters except the light-collected current density (J_L) constant. The value of (J_L) was changed to the values previously found with Sentaurus. The calculated factors j_{SC} were used to modify the effective normal incidence irradiance G_{cell} as follows:

$$G_{cell(\theta)} = G_{cell(0°)} \cdot j_{SC(\theta)} \tag{3.21}$$

The objective is to verify that if the intensity of light is reduced without changing the angle of incidence, a similar behavior is produced (see Figure 3.10). The factor j_{SC} used for each cell is presented in Table 3.6. Figure 3.10 shows that modeling the angular behavior of a cell using the angular factor j_{SC} to modify the value of effective irradiance at normal incidence produces very accurate results. The prediction of the maximum power point for each angle of incidence, for a standard and a colored cell, produces very little error, as shown in Table 3.7.

The complete data for the case of colored cells can be found in Appendix 9

Calculating the plane of the array irradiance modifying factor j_{SC} in both GenPro4 and TCAD Sentaurus allows assessing the suitability of using the implied photocurrent density J_{ph} obtained in the former as a means of estimating this factor. The results provide evidence of the suitability of this approach, as presented in Figures 3.11a and 3.11b for the case of a standard and a colored solar cell, respectively.

AOI	Standard	Green	Brown
0°	1.000	1.000	1.000
20°	0.947	0.925	0.916
40°	0.740	0.709	0.703
60°	0.461	0.414	0.401
80°	0.153	0.138	0.134

Table 3.6: Values of the j_{SC} angular factors for a non-encapsulated standard, a green and a brown colored solar cell.

AOI	Standard	Green	Brown
0°	-0.151	-0.086	-0.028
20°	-0.066	0.061	0.152
40°	0.329	0.445	0.525
60°	0.819	0.921	0.927
80°	1.251	1.328	1.409

Table 3.7: Relative error (in %) of the estimated maximum power point (mpp) using a two-diode model compared to TCAD Sentaurus for both a standard, a green and a brown non-encapsulated solar cell at different angles of incidence of light.

THERMAL MODEL

The validation of the spectrally resolved thermal model for the case of a colored photovoltaic device is presented in Section 4.7. The validation was carried out for a color PV module, as it was not technically feasible to fabricate colored solar cells at the university facilities.

VALIDATION FOR THE CASE OF ENCAPSULATED DEVICES

Figure 3.12a shows that the trend of the value of j_{SC} obtained with GenPro4 closely follows those of the literature for a standard module. Similar findings were observed by Sjerps-koomen *et al.* [181]. In addition, Knisely *et al.* [182] found that even for modules with different photovoltaic technologies, the relative optical response factor for different AOIs was remarkably equal in those using flat glass as the front layer. Figure 3.12b shows the value of j_{SC} also for the green and brown modules. The effect of the optical filter is noticeable for incidence angles ranging from 20° to 60°. At values higher than 60°, the reflectance produced by the air/glass interface dominates and the difference between the standard and the colored modules practically disappears. On a textured glass, the value of j_{SC} is different than for the case of a flat glass. The results for this case are shown later in this chapter.

3.3. MODELING ENCAPSULATED COLOR SOLAR CELLS

Figure 3.5b showed that a color filter deposited on a textured solar cell could produce colors with saturation similar to but lower brightness than when deposited on flat glass. However, the appearance of a colored cell can change significantly as a result of encap-

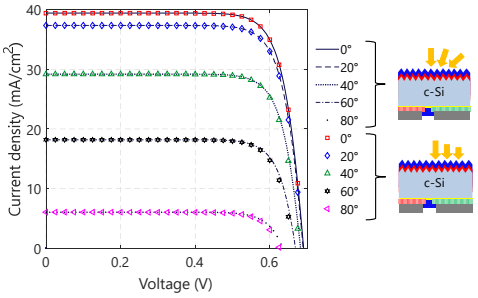

Figure 3.10: Comparison between the $J-V$ curves of a standard IBC solar cell obtained by Sentaurus simulation (lines) and those obtained by the two-diode model (markers). The effect on performance for different angles of incidence of light can be modelled with great accuracy by adjusting the value of irradiance at normal incidence with the angular factor j_{SC}.

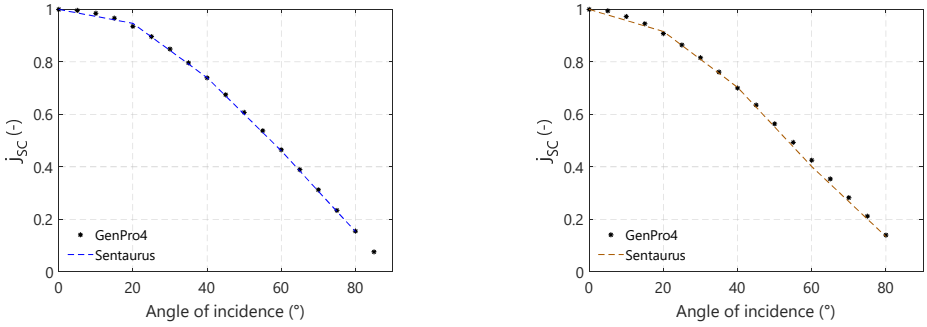

Figure 3.11: Comparison between the angular factor j_{ph}. obtained from GP4 simulations to those obtained with Sentaurus (j_{SC}) for **(a)** a Standard solar cell and **(b)** a Brown colored solar cell.

sulation. Analysis of this effect is performed by calculating the HSV color coordinates of the selected brown and green solar cells after encapsulation.

Table 3.8 shows the effect of encapsulation on the saturation value of a colored cell. For both brown and green solar cells, encapsulation with flat glass significantly reduces the perceived saturation of colors. Moreover, the brown solar cell shows a significant change in its hue, which means that it will no longer appear brown. For the case of the green solar cell, the effect on the perceived hue is lower, and the cell could still be perceived as a dark green, although with poor saturation and brightness. Evidently, good color saturation should be an important aspect on a module with encapsulated colored solar cells. For this reason, it was decided to study different ways to improve this aspect. An approach was to consider the front glass of the PV module with a random micro-textured pattern. These patterns can be produced by wet etching, as shown in [185]–[188]. The effect produced by texture on the perceived color of the cell is presented in Section (c) of Table 3.8. For the brown cell, neither the hue nor the saturation can be restored. There is a slight improvement in the saturation, but its value remains low. For

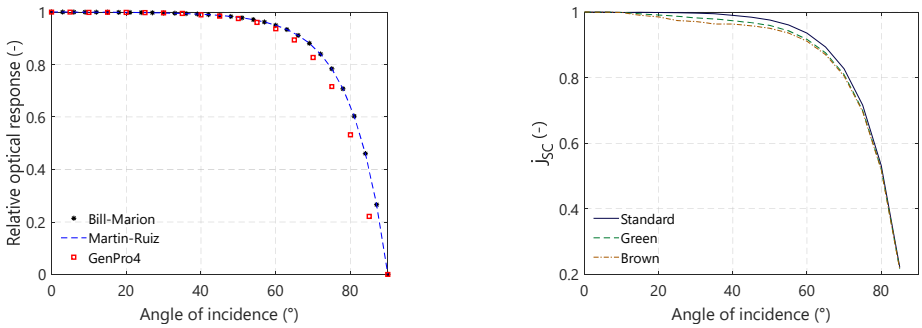

Figure 3.12: **(a)** Comparison of the relative optical response (a concept similar to j_{SC} used in this work) between the computational model produced in this work and the Martin-Ruiz [183] and Bill-Marion [184] models to account for the effect of different AOI on the performance of a standard dark-blue module. **(b)** Change in the j_{SC} factor for 153-cm^2 wide, encapsulated standard and colored solar cells.

the case of the green cell, the front texturing significantly improves the saturation, albeit with an important change on the hue. In both cases, the brightness of the color itself remains lower than in the case of the bare cell. The calculation of the color saturation was performed for all combinations of thicknesses shown in Figure 3.5b. Considering encapsulation with textured front glass (as shown in Table 3.8 (c)), a very small number of colors achieve a saturation value higher than a selected threshold (S = 0.5). Further ways to improve the S and V values of encapsulated colored cells involve, for example, modeling a different front glass texture. If a very high color brightness is required, the best approach is to deposit the filter on glass. This last solution will be explored in the next chapter. Increasing the difference between the refractive indices of the materials that make up the filter has profound effects on the color saturation, as shown by Equation 3.7. However, Equation 3.8 also states that increasing this difference also affects the width of the reflectance, which can lead to greater performance losses. However, given that the color saturation produced by a filter with a SiN_x of $n = 1.73$ (Option 1) is limited, it was explored how changing this property can produce a better color appearance. By implementing Option 2, the color saturation of the encapsulated cell is significantly improved. Figures 3.13a and 3.13b highlight this improvement.

The angular factors j_{SC} (as defined by Equation 3.20) were calculated for a range of incidence angles from 0 to 85°, with a resolution of 5°. This was repeated for all colors shown in Figure 3.14a. Since these factors already consider the effect of absorptance and reflectance from the glass/EVA/Filter, the irradiance reaching an encapsulated cell at any AOI is defined as:

$$G_{\text{cell}\,(\theta)} = \tau_0 \cdot G_{POA} \cdot j_{SC(\theta)} \tag{3.22}$$

where G_{POA} is the irradiance in the plane of the array of the module.

As explained previously and presented in Figure 3.9a, the implementation of a color produces changes in the EQE of the cell. Even for a similar peak reflectance, the brown cell presents a larger J_{SC} degradation compared to the green cell. This spectral behavior

Perceived color	Brown	Green	Encapsulation effect		Front glass texturing effect	
HSV Coordiantes	0.08 1.00 0.66	0.40 1.00 0.47	0.84 0.15 0.31	0.45 0.34 0.32	0.23 0.31 0.34	0.54 0.80 0.31
Structure	(a)		(b)		(c)	

Table 3.8: Effect of the encapsulation on the saturation of colored solar cells ((**a**)). When the cells are encapsulated with a flat glass layer ((**b**)), the saturation value of the bare cell drops dramatically. When the front surface of the glass is textured ((**c**)), in some cases, the saturation value increases to high values, but the hue changes.

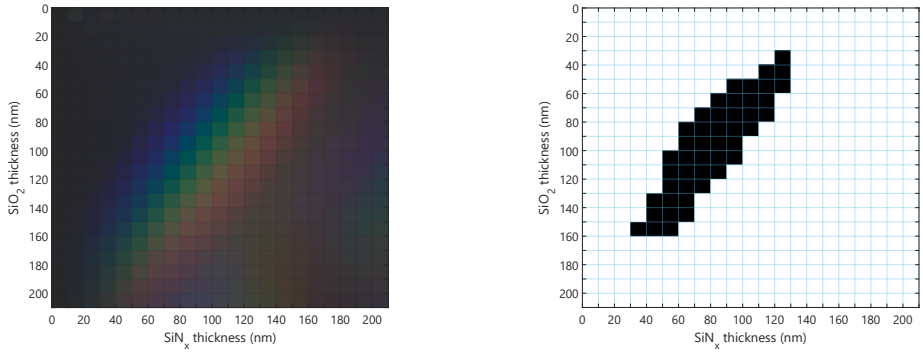

(a) (b)

Figure 3.13: **(a)** Effect of encapsulating colored solar cells with a textured front glass. The overall effect is that of low saturation and low brightness. This color matrix belongs to the optical filter **Option 1**, with SiN_x with a value of $n = 1.73$. **(b)** The black squares indicate the encapsulated colored cells that still present saturation values higher than 0.5 in the HSV color space.

must be taken into account when performance calculations are performed with scalar values of G_{POA}. To account for the spectral sensitivity of a colored cell, the following color factor (CF) is introduced:

$$CF = \frac{J_{\text{PHcolor}}}{J_{\text{PHstd}}} \tag{3.23}$$

CF is then defined as the ratio of the photogenerated current density of a colored cell ($J_{PHcolor}$) to that of a standard device (J_{PHstd}) for the same spectrum. In this work, the AM1.5 spectrum was used to calculate this factor for each color. As the relationship between J_{PH} and irradiance can be considered linear [180], CF modifies Equation 3.22 as follows:

$$G_{\text{cell}\,(\theta)} = \tau_0 \cdot CF \cdot \left[j_{SC(dir,c)} \cdot (G_{dir} + G_c) + j_{SC(id,hb)} \cdot (G_{id} + G_{hb}) + j_{SC(gr)} \cdot G_{gr} \right] \tag{3.24}$$

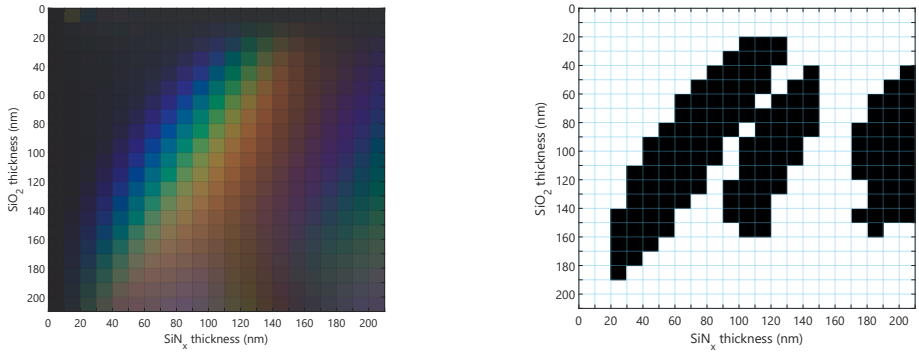

(a) (b)

Figure 3.14: **(a)** Color matrix produced by deposition of ten periods of SiO_2 / SiN_x on a solar cell encapsulated with a textured glass. In this case, the value of the refractive index of SiN_x is ($n = 2.1$) (**Option 2**). The use of a higher refractive index improves color saturation substantially. **(b)** The number of colors whose saturation value is above 0.5 increases when compared to a filter with SiN_x with a value of $n = 1.73$.

with all the respective angular modifiers being consigned for each component of irradiance.

3.4. IMPACT ON THE DC ENERGY YIELD OF AN ENCAPSULATED CELL

The validated optical, thermal, and electrical models allow one to calculate the DC energy yield of a colored solar cell. To this end, five different encapsulated solar cells are studied. One standard device, without any color filter, and two colored cells with filters made with SiO_2/SiN_x, for both filter options. Two different locations were selected for this study: Delft, in the Netherlands, and Alice Springs, in Australia. The former is a location with an average annual diffuse to global ($D2G$) factor of 0.531 [189]. This means that on average, because of environmental conditions, the diffuse component of irradiance dominates over the direct normal component. The latter, on the contrary, has an average annual $D2G$ factor of 0.211, making it a location with a more frequent occurrence of clear skies. For both locations, the weather data was extracted from Meteonorm software [190]. The selected time resolution was ten minutes. The modeling framework calculates the effective irradiance reaching the silicon of the cell, estimating its temperature under the ambient conditions at the given time instant, and, via iteration, calculating its power production.

3.4.1. EFFECT ON OPERATIONAL TEMPERATURE

Since the additional reflectance produced by the optical filter can produce a reduction in the temperature of the solar cell, the effect of this temperature difference was studied under NOCT conditions. For this, the case of encapsulation with a textured front glass surface was selected. For the standard device, the operational temperature calculated

under NOCT was 47.20 °C. Thermalization losses were estimated with a wavelength resolution of 10 nm. Figure 3.15b shows the amount of energy thermalized by the c-Si cell and the power extracted for a wavelength range of 300 nm to 1800 nm. Notice that the bandgap was considered temperature-independent and equal to 1100 nm.

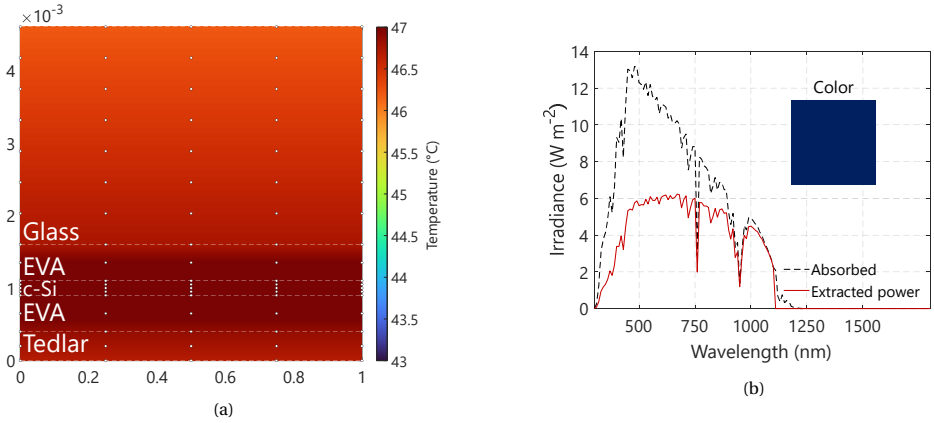

Figure 3.15: **(a)** Temperature profile of the encapsulated standard solar cell without color filter. **(b)** representation of the thermalized power on the c-Si cell for a wavelength range from 300 nm to 1800 nm. For this calculation, the bandgap of the cell was assumed independent from the temperature and equal to 1100 nm.

For the case of an encapsulated colored solar cell based on a color produced by the deposition of a filter based on Option 2. The thicknesses selected in this example were SiO_2= 110 nm and SiN_x = 80 nm. Figure 3.16a shows that the colored solar cell reaches a steady state temperature under NOCT conditions of 44.10 °C, which is 3.10 °C lower than the standard cell under the same conditions. This temperature reduction is driven by a reduction in thermalization losses close to 600 nm, as shown in Figure 3.16a. The effect also negatively affects the amount of power that can be extracted from the cell, which is translated into lower electric energy.

The same calculation of the steady state temperature under NOCT conditions was performed for all combinations of thicknesses (ranging from 0 – 200 nm). **Option 1** produces a maximum temperature reduction of 2.5 °C under NOCT conditions. However, most colors with high saturation did not show reductions beyond 2.0 °C. For Option 2, the temperature reduction produced is higher, reaching a maximum of 5.2 °C. Bright and saturated colors presented reductions ranging from 2.0 °C to 5.0 °C. The results for all color combinations can be found in Appendix 9.

3.4.2. EFFECT ON ENERGY YIELD

Finally, calculations of the DC energy yield for the five encapsulated solar cells. In all cases, the encapsulated front surface was textured glass. This case was selected because it yields a better saturation and brightness of colors for both filters options compared to the case of encapsulation with a flat-front glass. The chosen colors from both options of the color filter can be found in Table 3.9. Notice that the colors were selected for high saturation as obtained with Option 2, and a comparison is made with the filter produced

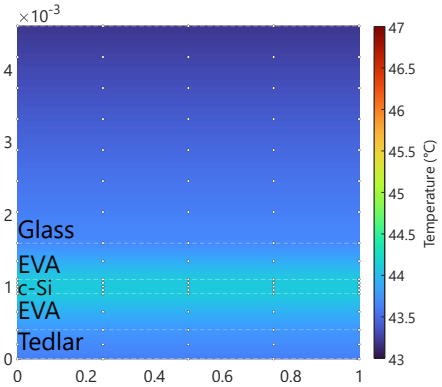

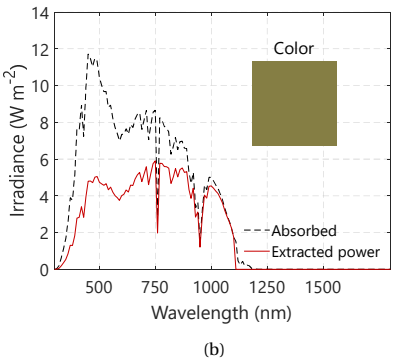

Figure 3.16: **(a)** Temperature profile of an encapsulated colored cell with an optic filter with ten pairs of SiO_2 = 110 nm and SiN_x = 80 nm (Option 2) under NOCT conditions. At steady state, the encapsulated cell reaches a temperature of 44.10 °C, nearly 3 °C lower than an encapsulated standard solar cell under the same conditions. **(a)** Thermalization losses are reduced due to the additional reflectance required to change the color appearance of the solar cell.

by Option 1 with the same thickness combination.

Filter	Thickness 1	Perceived color 1	Thickness 2	Perceived color 2
Option 1 SiO_2/SiN_x ($n = 1.73$)	110 nm / 180 nm		130 nm / 100 nm	
Option 2 SiO_2/SiN_x ($n = 2.10$)	110 nm / 180 nm		130 nm / 100 nm	

Table 3.9: Selected colored cells for DC energy yield assessment. The perceived colors account for the effect produced by the encapsulation.

The installation layout assumed that the encapsulated cell is tilted 35°from the horizontal, oriented toward the optimal azimuth according to the location (ie, south for Delft and north for Alice Springs). In addition, the backside of the encapsulated cell does not have forced convection on its backside (BIPV condition). All simulation parameters can be found in Figure 3.17. The simulation results for each of the selected colors and the standard devices are summarized in Table 3.10. For the case of the color filter with SiN_x with a value of $n = 1.73$ (Option 1), the green cell installed in Delft presents a relative loss in DC yield of 2.25% compared to the standard cell. The dark brown color has higher relative losses of 3.93%, despite its poor saturation. In Alice Springs, the relative energy loss for the green cell is slightly lower compared to Delft, with a value of 2.23%. A similar case is found for the dark brown cell, which in the Australian city presents a relative annual yield loss of 3.57% compared to the standard case.

Of all the colors that can be produced from this filter option, the maximum relative DC energy yield loss for Delft was of 11.3%, whereas on Alice Spring it was found to be of 10.9% (see appendix 9 for a full overview of all color combinations). In Alice Springs the losses were slightly lower than in Delft, due to a slightly better thermal performance of

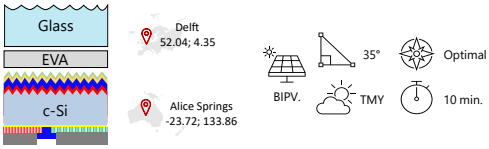

Figure 3.17: Simulation parameters for the DC energy yield calculation. The simulated structure was an encapsulated IBC solar cell with a textured front glass. All the colors produced by the combination of the different thicknesses from each color filter were simulated by using Typical Meteorological Year (TMY) data obtained from Meteonorm. The selected time resolution was 10 minutes.

Solar cell					
	Standard	Green option 1	Brown option 1	Green option 2	Brown option 2
RGB Value		23 88 72	101 70 64	93 140 83	139 92 60
HSV Value		0.46 0.74 0.34	0.02 0.37 0.40	0.30 0.41 0.55	0.07 0.57 0.55
Efficiency at STC (%)	19.54	18.88	19.01	17.50	17.65
Delft					
Energy yield (KWh/yr)	3.56	3.48	3.42	3.27	3.17
Relative loss (%)	-	2.25	3.93	8.15	10.95
$T_{mod_{max}}$ (°C)	60.30	60.20	60.10	57.10	57.00
Alice Springs					
Energy yield (KWh/yr)	6.73	6.58	6.49	6.21	6.02
Relative loss (%)	-	2.23	3.57	7.73	10.55
$T_{mod_{max}}$ (°C)	75.00	73.60	73.40	71.40	71.30

Table 3.10: Energy yield for the selected colors on the chosen locations. The installation conditions considered were 35°of tilt, optimum orientation and a BIPV layout (no forced convection on the backside).

the colored cell.

When the refractive index of SiN_x is increased to $n = 2.1$ (Option 2), the increase in saturation is followed by a decrease in the relative annual DC energy loss compared to a standard solar cell. For Delft, the green cell has an 8.15% relative loss of DC yield, while the brown cell presents a relative loss of 10.95%. In Alice springs, the relative loss was 7.73% for a green cell, while the brown cell presented relative losses of 10.55%. For Option 1, colors with a saturation value above 0.5 yield relative DC yield losses in Delft that range from 1.20% to 2.70%. However, the color with the least relative loss (1.2%) is a green color that despite presenting a relatively high saturation color, has a very low brightness. This is a general trend observed on all the colors produced with this filter. Alice Springs losses share a similar trend to relative yield losses that range from 1.10% to 2.20%.

Option 2 offers much better results not only in terms of saturation, but also in terms of brightness. For Delft, relative yield losses range from 0.50% to 12.90% for colors with saturation values above 0.6. Like in Option 1, colors with low losses lack brightness. A combination of both is desirable from an aesthetics perspective. To produce such a combination, losses increase in rage from 7.00% to 12.90%, this is consistent with findings from the work of Kutter *et al.* [43].

Notice that a color can have poor saturation, poor brightness and still present high losses, which is the case for the brown color produced with Option 1 for the thickness

combination shown in Table 3.9. This is due to the relatively high reflectance produced outside the visible spectrum, which increases losses without affecting color perception.

3.5. CONCLUSIONS

A computational model was created to aid the design of a color-tuning optical filter (OF) for photovoltaic solar cell applications. The model uses (i) the standard proposed by the International Committee of Illumination (CIE) to predict color perception, and (ii) advanced models validated via the TCAD software platform and experimental data that help predict the impact on the optoelectrical performance when applied on a c-Si IBC solar cell. The materials selected for the OF proposed in this work are SiO_2 and SiN_x. Such materials were chosen because of their non-absorptive nature, their availability for industrial-scale application, and their adequate refractive index values over the entire visible spectrum. Samples manufactured and measured by spectrophotometry show that the optical model accurately predicts reflectance spectra for different colored OF.

Performance-wise, optoelectrical simulations deployed on TCAD Sentaurus showed that the application of the filter is expected to not influence the electrical quality of the cell, as the values of V_{OC}, FF, and V_{MPP} remain relatively unaffected. However, OF can have a significant impact on the current generation of the device.

Sentaurus simulations were deployed to opto-electrically assess the effect of the color filter. Two selected colors, green and brown, were studied. The results showed that, for the normal incidence of light, the green color reduces the efficiency of the cell by 0.78% absolute, while the brown color presented a reduction of 1.40% absolute, mainly driven by current loss. For angles of incidence greater than 0°, the current density of the standard changes closely to a cosine relationship. However, colored cells have a significant deviation from this behavior. By means of a two-diode equivalent electrical circuit, the angular behavior of the cells was modeled by modifying the effective irradiance with scaling factors. These factors were equal to the ratio of photogenerated current at a given angle of incidence with respect to the value at normal incidence. The approach was proven to be very accurate, producing absolute errors in the prediction of the maximum power point of less than 0.2% for normal incidence and less than 2% for an angle of incidence of light equal to 80°.

Since filters operate by selectively reflecting light within the visible spectrum, a two-dimensional finite-volume thermal model was developed to study the effect on the cell temperature produced by a color filter. The model considers the absorption on every layer of the module for a wavelength range from 300 nm to 1800 nm. The validation of the model was carried out in two ways. First, by studying its behavior under NOCT conditions and second, by comparing its estimated temperature against measurements taken during twelve days. The errors produced under constant environmental conditions were below 2% absolute. Compared with measurements with a resolution of 1 minute, the model produced MBE and RMSE of 0.89 °C and 2.10 °C, respectively, when considering the entire measurement period. The daily values of MBE and RMSE are significantly higher because of the low time resolution.

With validated optical and thermal models, an analysis of the effect that encapsulation has on color saturation highlighted the influence of the value of the refractive index n_H. The use of SiN_x with a relatively low refractive index (n = 1.71, Option 1) was first

studied given its good results in terms of color saturation and brightness in bare solar cells. However, once the effect of encapsulation was taken into account, these properties were negatively impacted. In some colors, the encapsulation eliminated almost entirely the saturation and brightness of a bare colored cell.

The use of front glass texture and increasing the value of the refractive index of SiN_x to $n = 2.1$ (Option 2) were shown to significantly increase both the brightness and the saturation of color. This second option was also selected to study its effects on the performance of an encapsulated cell.

Temperature calculations under NOCT conditions showed that the deposition of Option 1 could have temperature reductions of up to 2.20 °C. The use of Option 2, given its better reflectance, produces significant reductions of up to 5.20 °C. This reduction in temperature was discussed because of the additional reflectance produced by the colored filter, which reduces the thermalization losses.

However, the reduction in operational temperature does not bridge the gap in electrical performance between an encapsulated colored solar cell and an encapsulated standard solar cell. It is important to note that this temperature reduction can have potential benefits. Research has shown that thermal cycling degradation rates can significantly reduce the lifetime of photovoltaic modules, particularly in a very warm climate [24].

The model was used to study the effect of the colored filters on the energy yield of an encapsulated cell. The installation layout selected was a tilt of 35°with the optimal orientations for Delft in the Netherlands and Alice Springs in Australia.

Calculations of DC energy yield showed that using color filters can produce low relative yield losses compared to an encapsulated standard device. For selected colors with high saturation values (a value of S in the HSV color space greater than 0.5), the losses presented by using Option 1 were up to 6.40% for Delft and 5.9% for Alice Springs. Despite the high saturation, the brightness was still poor. However, this filter option is still a valid approach for installation looking for dark tones with minimal impact on performance.

If highly bright and highly saturated colors are desired, Option 2 is a promising alternative, but the relative DC yield losses will increase to 13.70%. However, there are color options that meet both high saturation and high brightness with relative losses below 7.00%. In general, colored filters produced by deposition of multilayer optical systems are a promising alternative to improve the aesthetics of photovoltaic modules.

4

IMPROVING AESTHETICS OF PHOTOVOLTAIC MODULES

This chapter is partially based on the following publication:

J.C. Ortiz Lizcano[1], S. Villa, Y. Zhou, G. Frantzi, K. Vattis, A. Calcabrini, G. Yang, M. Zeman, O. Isabella *Optimal Design of Multilayer Optical Color Filters for Building-Integrated Photovoltaic (BIPV) Applications*, Solar RRL, **7**, 2300256 (2023).

This chapter presents an application of a comprehensive modeling framework that can help optimize the design of multilayered optical filters for coloring photovoltaic (PV) modules based on crystalline silicon solar cells. To overcome technical issues related to the implementation of color filters on PV modules, like glare and color instability, we have extensively deployed colorimetry metrics, such as the Hue, Chroma, Luminance (HCL) color space and the quantitative concept of difference between two colors. Our work showcases that designing colored modules with high hue and chroma stability is possible by using a front-side texturing with edged geometry, like V-shaped grooves and inverted pyramids, while obtaining colors with relatively high luminance values, indicating good brightness. Furthermore, it is argued that adapting the rear surface of the front glass with a random textured layout where the color filter is applied can improve color and luminance stability without significant loss of chroma while eliminating glare. Finally, the models can be used to optimize the number of layers for a given color filter, reducing unnecessary optical losses. Compared to a standard photovoltaic module, the performance simulation of optimized brightly colored photovoltaic modules predicts relative energy yield losses ranging from 7% to 25%.

[1] Candidate's contribution: Writing, coding work, simulation work, experimental work, results analysis

4.1. MODELING FRAMEWORK

This work expands on the research presented in the chapters 2 and 3, where the entire computational model framework is presented in detail. In summary, the framework is divided into three main pillars: optical, thermal, and electrical models. GenPro4 [140] is the basis for the optical model. The software uses the transfer matrix and net radiation method approaches to calculate the optical behavior of multilayer systems. The outputs used from the optical model are the following: The values per wavelength of reflection (R (λ)), transmission (T (λ)), and absorption (A (λ)), as well as the total optical current densities (J_{opt}) based on the AM1.5 spectrum for each layer of the optical system. Color perception [30], the effective irradiance reaching the solar cell (G_{cell}) and the operating temperature of the solar cell (T_{cell}) are estimated based on these outputs. The thermal model is based on the finite-volume method, with a two-dimensional mesh with nodes distributed throughout the different layers of the photovoltaic module. The different thermal properties considered in this study are the same as those presented in Table 2.1. Estimation of the heat generated on the solar cell is performed per wavelength, so that the spectral effects that color filters have on the temperature of the solar cell can be accurately modeled. Other absorptions present on the remaining module layer are also taken into account. The Gauss elimination technique allows for the estimation of T_{cell} for every time instant.

Lastly, both G_{cell} and T_{cell} are used in a two-diode electrical model [191] to estimate the power output at any time instant. The complete validation of these models can be found in the Experimental methods section at the end of this chapter.

4.1.1. COLOR FILTER (CF) CONSIDERATIONS

Optical filters produce color by reflecting light at wavelengths within the visible spectrum. Given that these filters can produce reflection values close to unity, there is great potential to produce bright colors. This work focuses on very simple optical filter structures that have a good potential for large-scale production without incurring significant costs. The simplest way to increase the reflection via optical filters is to utilize two dielectric materials with a mismatch in their refractive indexes. The materials selected here are silicon dioxide (SiO_2), which is the material with the lowest refractive index (n_L), and silicon nitride (SiN_x), as that with the highest refractive index (n_H). The optical properties of each material and details of their deposition conditions can be found in the appendix 9 section of this document. Both materials are considered to be deposited in pairs (p) on a ($n_L|n_H$) sequence right below the front glass sheet of the photovoltaic module. A value of $p = 10$ was selected as a starting point as it was found to ensure a reflection value on flat glass above 0.9 (see Figure 4.1a). Graphically, the optical filter (hereafter called a color filter or CF) is represented in this work as shown in Figure 4.1b.

4.1.2. EFFECTS OF THE COLOR FILTER ON THE PERFORMANCE OF A PHOTOVOLTAIC MODULE

As demonstrated in chapter 3, the only effect a color filter has on the performance of a photovoltaic module is the reduced light absorption in the solar cell due to light reflection. It was also demonstrated that, for the case of an interdigitated back-contact (IBC)

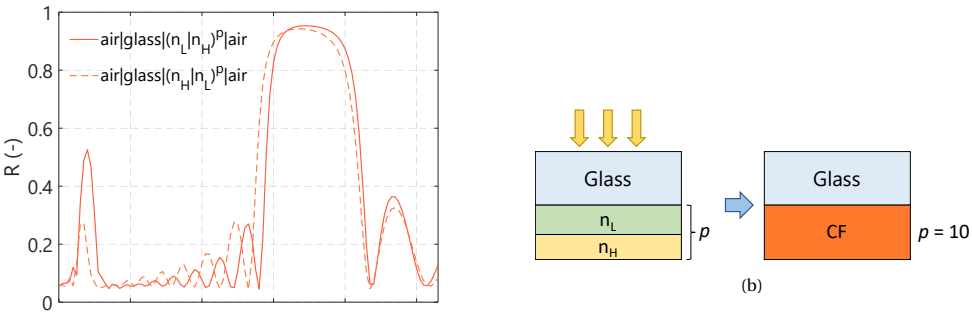

Figure 4.1: **(a)** In this work, the sequence of the materials of the color filter (CF) follows the $air|glass|(n_L|n_H)^p$ layout. When analyzed on flat glass, the sequence produces a slightly narrower reflection band compared to the $(n_H|n_L)^p$ alternative, which helps reduce optical losses. **(b)** For simplicity, the color filter is graphically represented as a single-colored layer representing the $(n_L|n_H)^p$ sequence from the top glass downwards.

cell, this effect could be very accurately modeled using scaling factors that are applied on the calculated plane of array irradiance. These scaling factors are denoted as θ_0 and j_{CF}, the first mathematically defined as

$$\tau_0 = \frac{I_{cell}}{I_{POA}} \tag{4.1}$$

Here, I_{cell} and I_{POA} are the light intensities calculated in the cell and the front glass of the photovoltaic module, respectively. And the latter estimated by:

$$j_{CF} = \frac{J_{Optcolor}}{J_{OptStd}} \tag{4.2}$$

j_{CF} is the ratio between the optical current density produced after taking into account the color filter and the optical current density of a standard module without the filter, both estimated at normal incidence of light.

Both scaling factors depend not only on the color filter design but also on the surface morphology of the different layers of the photovoltaic module that interact with light before reaching the solar cell, as will be shown later. A third scaling factor, $j_{opt(\theta)}$, accounts for the angular optical losses produced by additional reflectance losses due to light reaching the module at an angle of incidence different from 0°(normal incidence). $j_{opt(\theta)}$ is the ratio between the optical current density of a module illuminated at angle of incidence equal to θ and the optical current density of the same module under normal incidence. Mathematically, this is expressed as follows:

$$j_{Opt(\theta)} = \frac{J_{Opt(\theta)}}{J_{Opt(0°)}} \tag{4.3}$$

The reflective behavior of optical filters is very sensitive to the angle of incidence at which they are studied. Thus, $j_{opt(\theta)}$ is characteristic of every module.

4.2. COLOR FILTERS: AESTHETIC POTENTIAL AND TECHNICAL CHALLENGES

In his seminal work, Macleod [55] demonstrates that, for an optical filter with only two different materials, the width of reflectance depends on the difference between their refractive indexes. The wavelength at which this reflectance occurs depends on the physical thickness of the layers. Finally, the height of the reflectance depends on the number of pairs deposited. It was established that for a number of pairs p equal to ten, a color filter deposited on a flat glass surface presents reflection values at a given wavelength greater than 0.9. The thickness values of both materials, defined as d_L and d_H, ranged from 0 nm to 200 nm with a resolution of 10 nm. It was found that, for combinations above this range, the color patterns become repetitive, producing similar colors with significantly thicker filters, which was considered not practical. The reflectance produced by each combination of thickness values was then used in a color perception model [30] to estimate the R, G, and B coordinates using the mathematical transformation provided within the MATLAB image processing toolbox for a standard Illuminant D65. These were then used to build color matrices as a graphical representation of the expected color for that given combination. An example of a color matrix for a color filter deposited on the backside of a flat glass sheet (as presented in Figure 4.1b) is presented in Figure 4.2a. Since the matrix is based on RGB values, a gray hue represents a transparent perception, not a color. The gray hues indicate that for that combination of thickness values from the materials, the reflectance peak is within the visible spectrum but is insufficient for color perception, or it is located outside the visible spectrum, at the ultraviolet (UV) or infrared (IR) region. Notice that when the value of one of the materials in the filter is 0 nm, no significant color can be produced, unlike the case of a CF applied directly on a c-Si solar cell, where the variation of the SiN_x layer alone can produce a different color of the cell. When the thickness value of one of the materials is below 30 nm, a higher value of thickness (>100 nm) is needed in the other material to produce a good color brightness. In general, for a flat surface, the layout of the selected color filter can produce a wide variety of bright colors, ranging from purple to red.

The utility of the color matrix is to be a guide for matching a particular color to a combination of thicknesses for a given filter layout. However, it is limited as an analytical tool for optimizing its design. A quantitative way of color analysis is the use of color spaces such as the RGB, or, in particular, the hue, chroma, and Luminance (HCL) color space. The HCL color space has recently been advocated over others because it is a perceptual-based color space that does not have the saturation bias issues of other alternatives [192]. Each color is depicted by triplets: The Hue value describes the dominant wavelength and is represented as a polar coordinate in the range [0°360°]. In this coordinate, 0°depicts red hues, going toward yellows (90°), cyans (180°), blues (270°) and magenta. The Chroma coordinate depicts the intensity of the color (also known as colorness) compared to a gray hue under the same conditions of luminosity. Lastly, Luminance itself, which defines the brightness of the color. Figure 4.2b depicts all the colors found in the color matrix of Figure 4.2a in the HCL color space. Representing the colors that can be produced by a filter in this way allows one to see the aesthetic potential of a given layout, both in terms of the hues that can be achieved and their intensity. Another

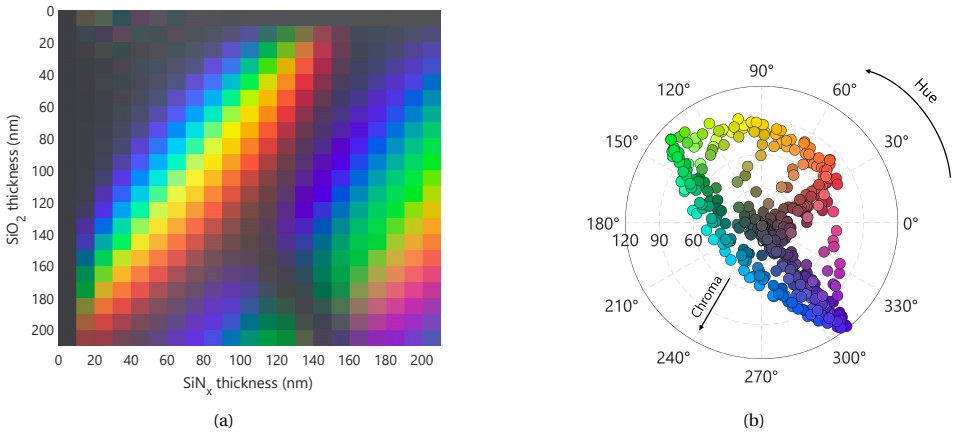

(a) (b)

Figure 4.2: **a** Color matrix for different combinations of thickness values for the color filter materials selected in this study. The filter is located beneath a flat glass as shown in Figure 4.1b, with a total number of pairs $p = 10$. The color perception is modelled for the case of an angle of incidence equal to 0°. **b** Representation of the colors depicted on the matrix on the Hue, Chroma, and Luminance (HCL) color space, which is used in this study as an analytical tool for design.

way in which a color space could be used as an analytical tool for color filter design lies in the ability to estimate, quantitatively, the difference between two colors. The CIEDE2000 color difference standard is defined within the HCL color space (polar) by estimating the differences between two colors from their respective CIE L*a*b* color space (cartesian) coordinates. The mathematical derivation of this standard can be found in the work of Sharma *et al.* [31], whose main formula is

$$\Delta E^*_{00} = \sqrt{\left(\frac{\Delta L'}{k_L S_L}\right)^2 + \left(\frac{\Delta C'}{k_C S_C}\right)^2 + \left(\frac{\Delta H'}{k_H S_H}\right)^2 + R_T \frac{\Delta C'}{k_C S_C}\frac{\Delta H'}{k_H S_H}} \tag{4.4}$$

Here $\Delta L'$, $\Delta C'$, and $\Delta H'$ are the differences in luminance, chroma, and hue estimated from the two selected colors based on their CIE L*a*b* coordinates. S_L, S_C and S_H are compensation values for each color coordinate that correct the non-uniformity of the CIE L*a*b* color space. R_T is a rotation term that reduces inaccuracies in perceived differences in hue and chroma, particularly in the blue region. Finally, k_L, k_C, and k_H are factors that explain the influence of illumination on the perception of color differences. A full explanation of their meaning is outside the scope of this work, and interested readers can find further information on the work by Sharma *et al.* [31]. In this work, the estimation of ΔE^*_{00} was done using the MATLAB image processing toolbox.

The lower the value of ΔE^*_{00}, the less is the discernible difference perceived by the human eye between one color and another. In this work, we explore how the estimation of ΔE^*_{00} can be used to analyze the optimization of a color filter, particularly to overcome one important drawback of the technology: its color instability. At different angles of incidence, the optical thicknesses of the different layers within an optical filter change. This change means that the wavelength at which constructive interference (high reflectance) occurs differs. Consequently, the perceived color at different angles of

observation is not the same as that perceived at normal incidence, as will be explained in the following section.

4.2.1. TECHNICAL CHALLENGES OF COLORED FILTERS ON FLAT SURFACES

(a) (b)

Figure 4.3: **(a)** Colored coated glass on a vertical facade of a building located in the campus of TU Delft. The color shift from window to window is very perceptible, and sometimes undesired. **(b)** The coated glass produces substantial glare, which can cause discomfort and must be avoided in critical areas where it could be a potential safety hazard.

Figures 4.3a and 4.3b show the decorative potential of utilizing color filters. The result can be a very bright color that can effectively "hide" any object that might be located behind the coated glass. This is particularly attractive for designers who wish to prevent solar cells within a photovoltaic module from being visible to any passing observer. However, the photographs also showcase two aspects of the color filter that can be considered undesirable.

As the observer moves, the perceived color on the coated glass changes significantly. The deviation from the color observed at normal incidence is very noticeable, and, on a large façade arrangement, a continuous change in color can be perceived throughout the glass structure. This phenomenon occurs because, at higher angles of incidence, there is a change in the optical thickness in which light travels through the layers within the filter. This causes a shift in the wavelength at which they produce constructive interference and, therefore, the observed color changes [193]. Another potential issue is glare, which is produced due to the specular nature of the reflectance produced by the color filter. Glare is an undesirable aspect of photovoltaic modules, particularly those installed in dense urban areas or close to airports, where it can cause safety concerns [20]. These drawbacks have been ameliorated by depositing the color filter on a textured surface, as explained in the work by Jolissant, *et al.* [64] Textured surfaces can produce a diffuse light reflection, significantly eliminating glare. S. Villa [179] studied how the deposition of a color filter on a random texture surface, produced by Loef [188], could help improve both the issue of glare and color stability. Results showed that when using a color filter deposited at the top of a random textured glass as the top layer of a mini-PV module, the glare was completely reduced (see Figure 4.5a and 4.5b for details).

As mentioned above, depositing the filter on textured surfaces also improves color stability, as demonstrated by A. Wessels, *et al.*[58]. Using the HCL color space and the

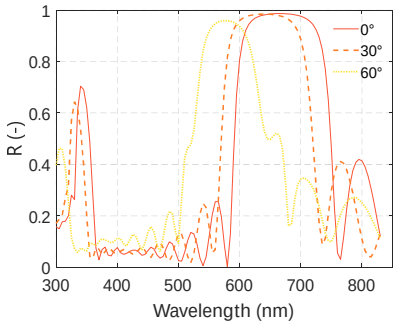

(a)

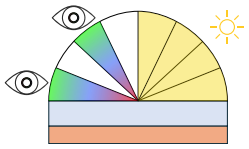

(b)

Figure 4.4: **(a)** Change in the wavelength of high reflectance due to change in the angle of incidence of light, the simulated structure is the one shown in Figure 4.5a. **(b)** Schematic of the simulation of angle of observation (AoO) with isotropic illumination conditions for the different angular divisions used for simulation. a total of 30 divisions were used, meaning a range from 0° to 90° in steps of 3°.

ΔE^*_{00} color difference formula can help analyze how texturization improves color stability. Figure 4.6a shows the HCL coordinates of the color perceived at different angles of observation for the colored mini-PV module shown in Figure 4.5a. At normal incidence, a bright orange color is perceived; as the angle of observation changes, a shift on the perceived color occurs, driven by the changes on the optical paths, as explained before. Notice that the main change is in the hue coordinate rather than the chroma coordinate, which indicates that the selective reflection is still high. However, as the angle of observation increases toward large angles (> 60°), the hue stabilizes and the chroma becomes smaller. This means that the selective reflection is lost and the color disappears. Figure 4.6b shows how the factor ΔE^*_{00} changes at different angles of observation. For this case, the color stability is limited to only low angles of observation (< 20°).

When the color filter is deposited on the randomly textured glass, the color stability partially improves compared to that for the filter deposited on flat glass. Figure 4.7a shows how the hue coordinate remains remarkably stable, with only a few degrees of variance between normal incidence and an angle of observation of 87°. Significant change in the color occur on the chroma coordinate, however, meaning a loss in color brightness as a result of increased front-surface reflection. This is evident in the estimation of the value ΔE^*_{00}, as shown in Figure 4.7b. Note that, to highlight color differences graphically, in Figures 4.6a and 4.7a, the markers are filled with the colors perceived at any given angle of observation. In contrast, the outline lines are colored with the perceived color at normal incidence.

Random textures are therefore a promising surface modifying technique for color filter implementation when glare effects need to be removed; moreover, as shown in Figure 4.8a, the range of hues and chromas is quite variable and appealing. Compared to a filter deposited on a flat glass, there are losses in purple and blue hues, but not by a considerable amount. However, positioning the filter at the top of the front glass of a photovoltaic module not only can lead to problems with the integrity of the filter itself, which might reduce its usefulness, but it does not guarantee color stability.

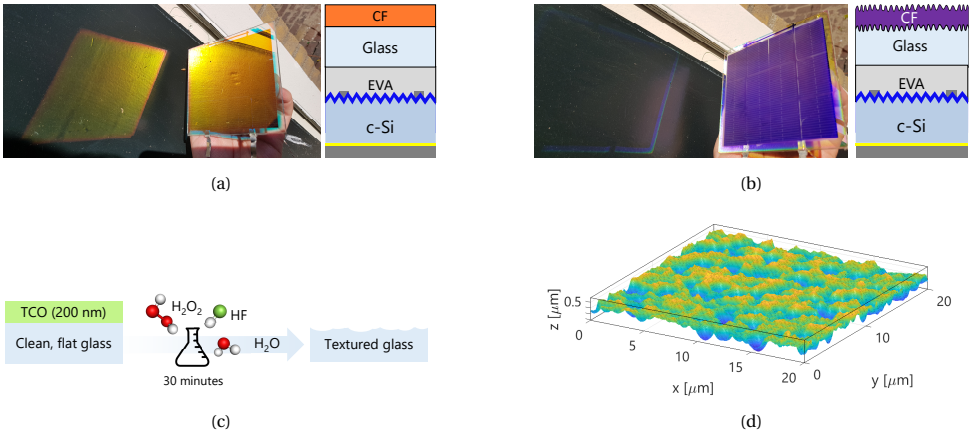

Figure 4.5: Two different colored mini-PV modules (10 cm x 10 cm) based on aluminium back surface field (Al-BSF) laser-cut solar cells. **(a)** An orange color filter deposited at the top of flat glass (p = 10, SiO_2 = 90 nm, SiN_x = 100 nm) which produces significant glare. **(b)** The glare is completely reduced by deposition of the color filter on a randomly textured glass (p = 10, SiO_2 = 68 nm, SiN_x = 164 nm). More information about these results can be found in the work of S. Villa [179]]. **(c)** Wet-chemical etching procedure of glass mediated by transparent conductive oxide (TCO) [188]. **(d)** Atomic force microscope image of a typical etched glass used for improving color stability (statistical data of the randomly textured surface can be found in the work by Loef [188]). This graph depicts just a section of the textured surface, a more detail graph can be found on Figure 9.12

Figure 4.6b and Figure 4.7b also present changes in luminance values in relation to the angle of observation of a color filter deposited on a flat glass surface and a randomly textured glass surface, respectively. At normal incidence, the color filter deposited on a flat glass presents a higher luminance value than the deposition on a random textured glass, which translates into a brighter perception of the color from the flat sample. As the angle of observation increases, the luminance of both colors follows the same trend. For the flat sample, at high angles of observation, the reflectance from the front glass increases in a broader range of wavelengths, decreasing the color strength and making its perception closer to a white color. Thus, even when the chroma coordinate decreases rapidly, the luminance increases, almost reaching its limit. The observed behavior on the textured sample is similar. However, in this case, the reflectance peak shifts from the blue region to the UV outside of the visible spectrum, producing a color loss. The luminance value at high angles of incidence is significantly lower than in the case of the flat sample, meaning that the perceived color is closer to a gray color than to white.

4.3. OPTIMAL DESIGN OF COLORED FILTERS BASED ON COLORIMETRY PARAMETERS

Placing the color filter underneath a thick glass layer protects it from environmental hazards, but could potentially change its overall behavior. To study this effect, an optical system, as described in Table 4.1, was modeled. The selected c-Si cell structure was based on the Maxeon® III IBC solar cell from SunPower [194]. The cell was measured in-house, and the optical model was fitted to its behavior (see Experimental Methods).

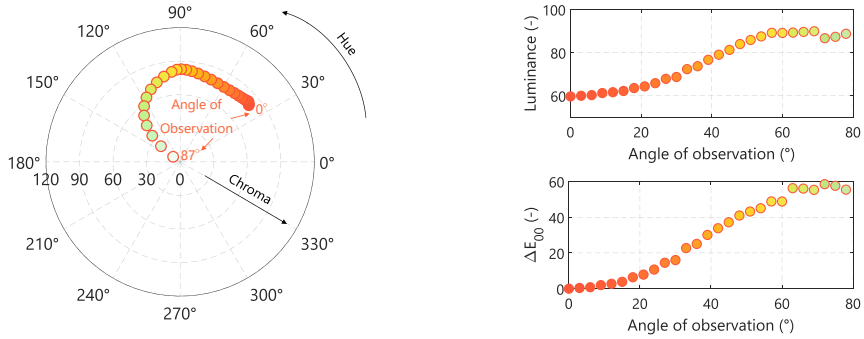

(a) (b)

Figure 4.6: **(a)** HCL color space representation of the change in color perception as a function of angle of observation for a colored mini-PV module based on the structure shown in Figure 4.5a. On flat surfaces, color stability is limited. **(b)** Change on the value of luminance L (top) and ΔE^*_{00} for increasing angles of observation.

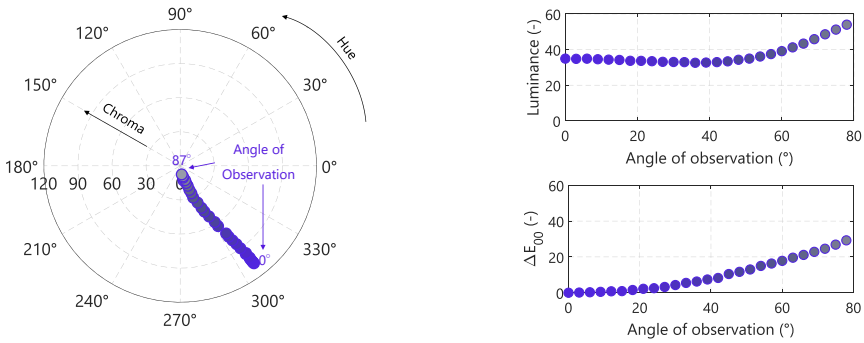

(a) (b)

Figure 4.7: **(a)** HCL color space representation of the change in color perception as a function of angle of observation for a colored mini-PV module based on the structure shown in Figure 4.5b. The texture surface provides impressive color stability while maintaining high values of chroma. **(b)** Change on the value of luminance L (top) and ΔE^*_{00} for increasing angles of observation.

To study the effect that the texture of the front glass has on the color stability, the HCL coordinates were calculated for the case of a color filter with SiO_2 = 90 nm and SiN_x = 100 nm for a value of p = 10. The angle of observation (AoO) ranged from 0°to 87° with a resolution of 3°. Different types of front-side texture were analyzed and compared with those of flat glass. Three types of texture were analyzed: An inverted pyramidal structure with depths up to 250 μm and a steepness of 45°. A rounded groove like Saint-Gobain's Albarino P [197] with depths equal to 250 μm and a V-shaped texture with an angle of 45° and a depth of 500 μm that mimics the Saint-Gobain Albarino G series [197]. These front-side layouts were paired with one of two options for the backside, where the color filter is placed: A flat surface and the random textured surface used by S. Villa [179]. These two layouts were selected because the optical behavior of the color filter could be experimentally validated. The selected structures are shown in Table 4.2, and a graphical

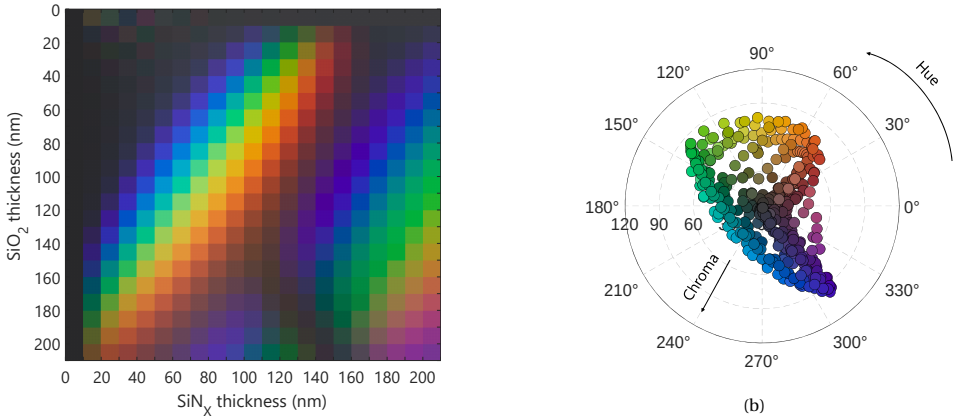

Figure 4.8: **(a)** Matrix of the perceived colors produced by different combinations of thicknesses of SiO_2/SiN_x, $p = 10$ of a CF deposited on a randomly textured glass similar to that reported on Figure 4.5d. The simulated optical system is that shown in Figure 4.5a **(b)** HCL representation of all the color reproduced on the color matrix.

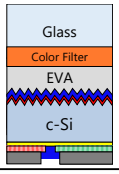

Layer	Thickness	Optical properties
Glass	3.2 mm	[195]
Color filter	Varied (0 - 0.2) μm $p = 10$	See Appendix 9
EVA	0.5 mm	[196]
Solar cell	0.18	Fitted

Table 4.1: Selected optical system for color filter design. Fitted refers to a simulated structure with the same optical performance than the measured sample, see the experimental section of this chapter for more information

description of these geometries is presented in Appendix 9.

Analysis of other structures on which the color filter can be deposited is outside of the scope of this chapter, as some of them require specific and complex additional optical modeling to accurately predict the growth of the color filter layers and the correct optical paths resulting from their manufacturing. An example of the additional modeling required can be found in the work by Wessels *et al.* [58] Figure 4.9a summarizes the effect of texturing on perceived color for the same combination of thicknesses ($SiO_2 = 80$ nm and $SiN_x = 80$ nm and $p = 10$). Structures 2 and 3, which feature rounded grooves on the front side of the glass and flat (Figure 4.9b) or random texture (see Appendix 9) on the rear side of the glass, respectively, only slightly improve color stability at different angles of observation. Color stability only improves when the geometry of the front glass consists of edge geometry. V-shaped grooves significantly improve color stability at the expense of loss of chroma. At different viewing angles, the green color produced with a V-groove glass has only marginal changes in the chroma coordinate, and the hue coordinate can be contained within the green region (Figure 4.9c). Compared to a V-shaped geometry, an inverted pyramidal texture improves color stability over a wider range of

	Glass texture layout		
Structure number	Front	Rear	Symbol
1	Flat	Flat	□
2	Rounded grooves	Flat	○
3	Rounded grooves	Random textures	○
4	V-Shaped grooves	Flat	△
5	V-Shaped grooves	Random textures	△
6	Inv. Pyramids	Flat	★
7	Inv. Pyramids	Random textures	★

Table 4.2: Structures simulated to study the efect on color stability of different texturization layouts. Details of these geometries are explained in Figures 9.9 to 9.12

observation angles, as seen in Figure 4.9d. The hue coordinate remains stable with a slight gain in chroma. Only at values of AoO greater than 60°does the hue coordinate change. The deposition of the color filter on a randomly textured surface provides better color stability, as Figure 4.9e shows. Moreover, the random texture does not reduce the luminance but stabilizes it (see Figure 4.9f).

In summary, texturing the front side of the module's glass with edge geometries provides good color stability, even when the color filter is on a flat backside surface. Inverted pyramids are the best front surface configuration for luminance stability. Deposition of the color filter on a random texture surface presents the best luminance stability and slightly improves the color stability. Figure 4.10a to 4.10d showcases the aesthetic potential of all the structures analyzed in this work. Color filters deposited on flat surfaces have a wider range of chroma, particularly in the case of glass with front V-shape grooves. This structure can produce bright yellows, but not reds. Green and purple colors can achieve chroma values close to their respective limits. A front texture based on inverted pyramids with a steepness of 45°presents a more limited chroma range. Bright yellow colors are not possible for these texture configuration and thickness combinations. However, highly saturated purples, blues, and greens are still possible.

The above-mentioned does not mean that brighter colors, including yellow, cannot be obtained with an inverted pyramid texturing surface. Reducing the angle and depth of the pyramid steepness can improve the hue, chroma, and luminance, as the surface will behave closer to that in the case of flat glass. However, doing this also means that the color stability will decrease. Further investigation of the potential of this geometry is underway. With respect to luminance, the textured layouts studied cannot produce the wide range of bright colors obtained by the double flat glass. V-shaped grooves and inverted pyramid layouts can produce colors with high luminance but are usually limited to green, blue, and brown hues (see Appendix 9). Another example of a texture layout that can produce vibrant colors is the Morpho Color concept [47].

4.3.1. OPTIMIZED NUMBER OF LAYERS FOR COLOR PERCEPTION

Stabilizing the color is, from a PV module performance point of view, stabilizing the value of $j_{opt(\theta)}$. A stable color means that the peak of reflectance remains close to its

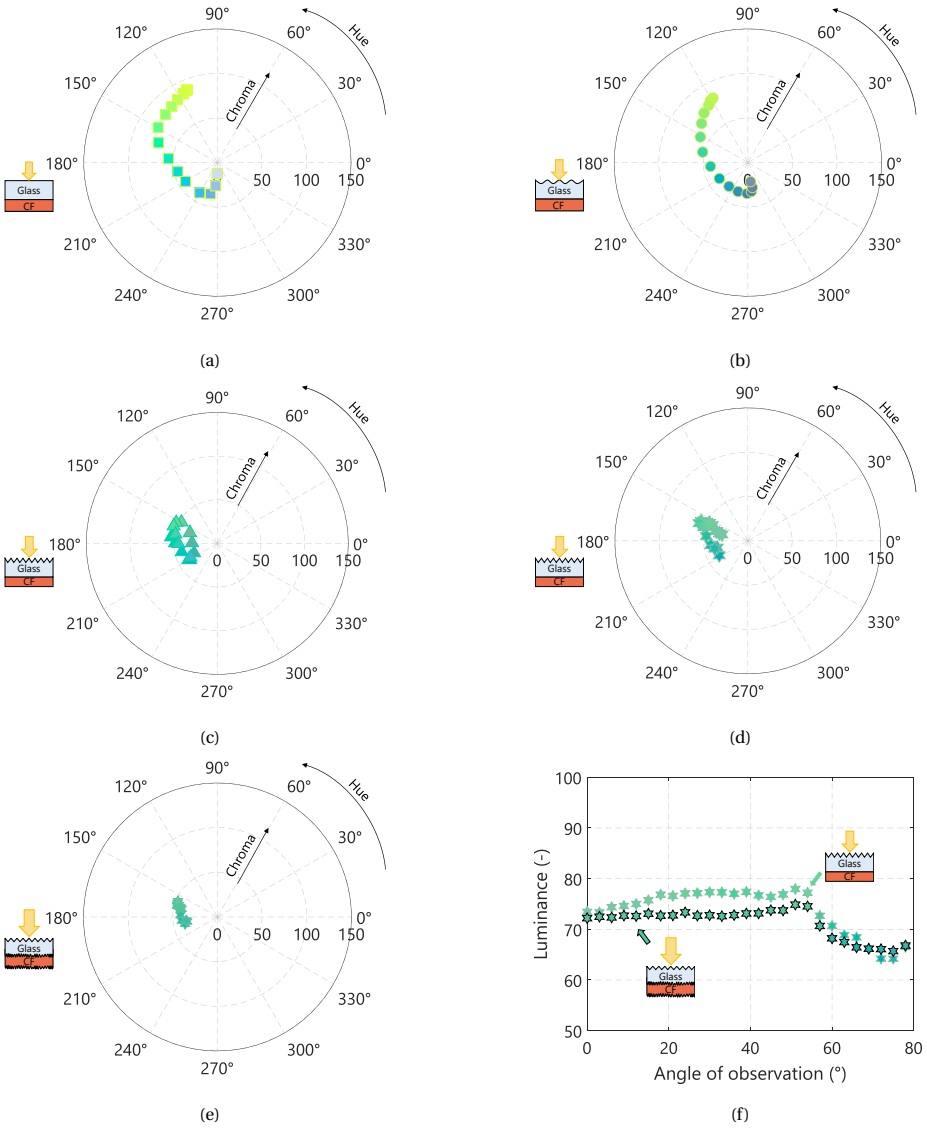

Figure 4.9: Color stability for five of the different structures presented in Table 4.2. Namely **a** Structure 1 (Flat | Flat). **b** Structure 2 (Rounded grooves | Flat). **c** Structure 4 (V-Shaped grooves | Flat). **d** Structure 6 (Inverted pyramid | Flat). **e** Structure 7 (Inverted pyramid | random textures). **(f)** A CF with $p = 10$ deposited on the flat back surface of a front textured glass (inverted pyramids) presents values of luminance that slightly increases at different observation angles (hexagrams without black edges) Deposition of the CF on a random textured surface improves luminance stability (hexagrams with black edges). On all cases, as depicted by the sketches, the color filter is placed on the back surface of the glass. The results presented here are obtained by simulating the complete optical system depicted in Table 4.1

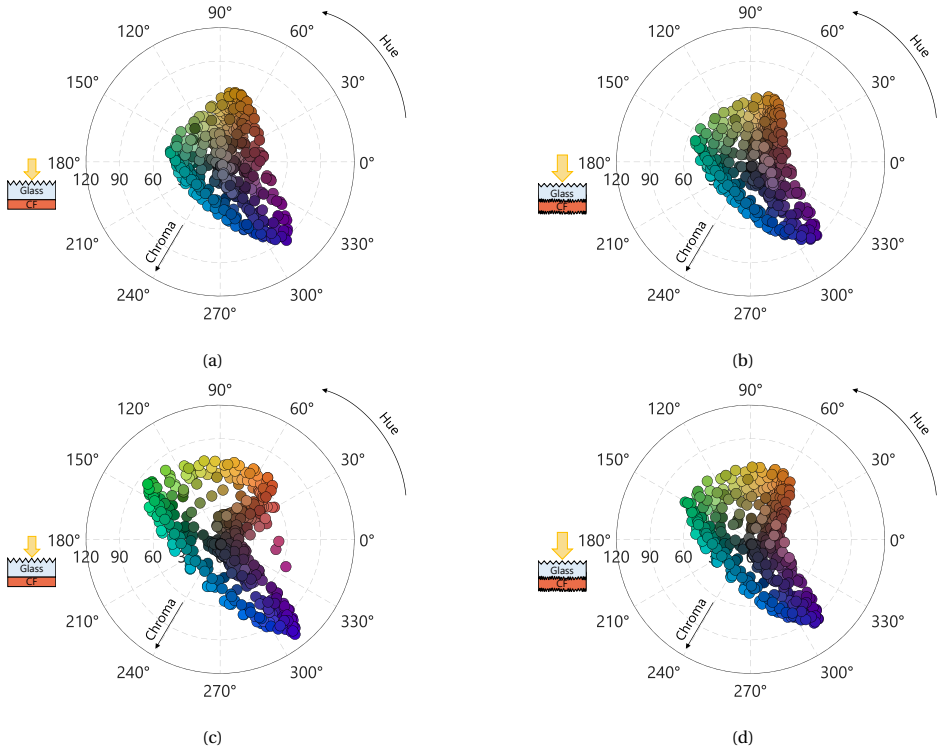

Figure 4.10: Hue and chroma variations for different PV module glass texturing (topside | backside) layouts:**(a)** Inverted pyramids | Flat (Structure 6). **(b)** Inverted pyramids | random textures (Structure 7). **(c)** V-shape | Flat (Structure 4). **(d)** V-shape | Random textures (Structure 5). More details of these layouts is presented in Table 4.2. For all cases, the colors are those obtained from a CF with a number of pairs $p = 10$. The sketches depict the differences between glass layouts. These results are obtained by simulating the full optical system depicted in Table 4.1

wavelength value at normal incidence, thus the value of $j_{opt(\theta)}$ at various angles of observation becomes close to unity. Also, designs that involved thin color filters with small layer counts are preferred due to their ease of manufacture. The color difference formula can be used to determine if the initial number of pairs (p) considered for a given design can be reduced without any loss in color perception. **Structure 7** was selected because it showed the best combination of chroma, hue, and luminance stability among all samples studied. The three selected colors, which belong to different hue coordinates, are presented in Table 4.3.

Given that the number of pairs had an initial value of 10, the color produced by this color filter design was considered as a reference. The value of p was increased to 13 and reduced to a value of 4. For each iteration, the value of ΔE^*_{00} is calculated with respect to the color produced with $p = 10$. Figure 4.11a shows how the value of ΔE^*_{00} changes for different values of p for Color 1. For the sake of clarity, the squares in the inset in the graph depict the color perceived based on the number of pairs. This was done to

Color 1	Color 2	Color 3
$p = 10$	$p = 10$	$p = 10$
$SiO_2 = 80$ nm	$SiO_2 = 100$ nm	$SiO_2 = 90$ nm
$SiN_x = 80$ nm	$SiN_x = 140$ nm	$SiN_x = 100$ nm

Table 4.3: Selected color filters for the optimization of number of pairs without perceivable color change

demonstrate that for a value of $p = 6$, a change in color can be perceived and becomes evident at lower values of p. For optimization of the number of pairs, the limit $\Delta E^*_{00} = 2$ was selected as the maximum allowed value ΔE^*_{00}. The results indicate that, to produce Color 1, the filter can be reduced from 10 pairs to 7 with just a slight loss on the perceived color. $\Delta E^*_{00} = 2$ is only used as a limiting value for the case of normal incidence of light to optimize the value of p. When analyzing the color stability at different angles of observation, ΔE^*_{00} serves only as an analytical metric, without selected limiting value.

The same process of optimization is used to find the value of p for Color 2, Color 3 and all combinations of thicknesses presented in this work. For the selected limit value of $\Delta E^*_{00} = 2$, the optimal value of p for the different colors is shown in Figure 4.12

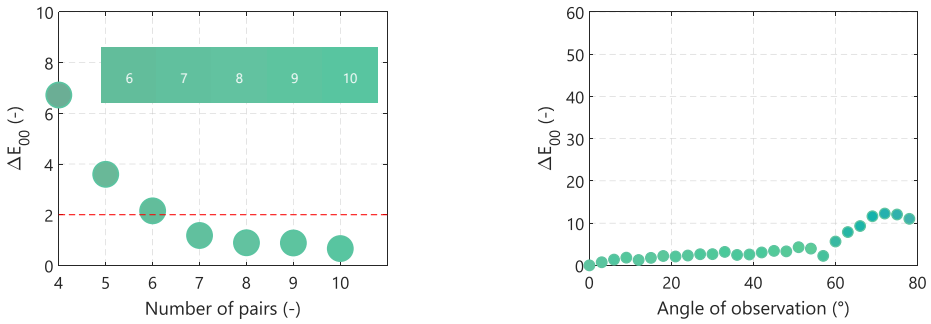

(a) (b)

Figure 4.11: **(a)** Changes on the value of ΔE^*_{00} by modifgying the number of pairs for Color 1. **(b)** Value of ΔE^*_{00} for different AoO to study the color stability of the final design based on $p = 7$. Notice that the selected limit value for ΔE^*_{00} to optimize the value of p only applies for the optimization of color perception at normal incidence. ΔE^*_{00} at different AoO is only used as an analytic metric for color stability. These results belong to an optical system with the layout depicted by Structure 7 (see Table 4.2).

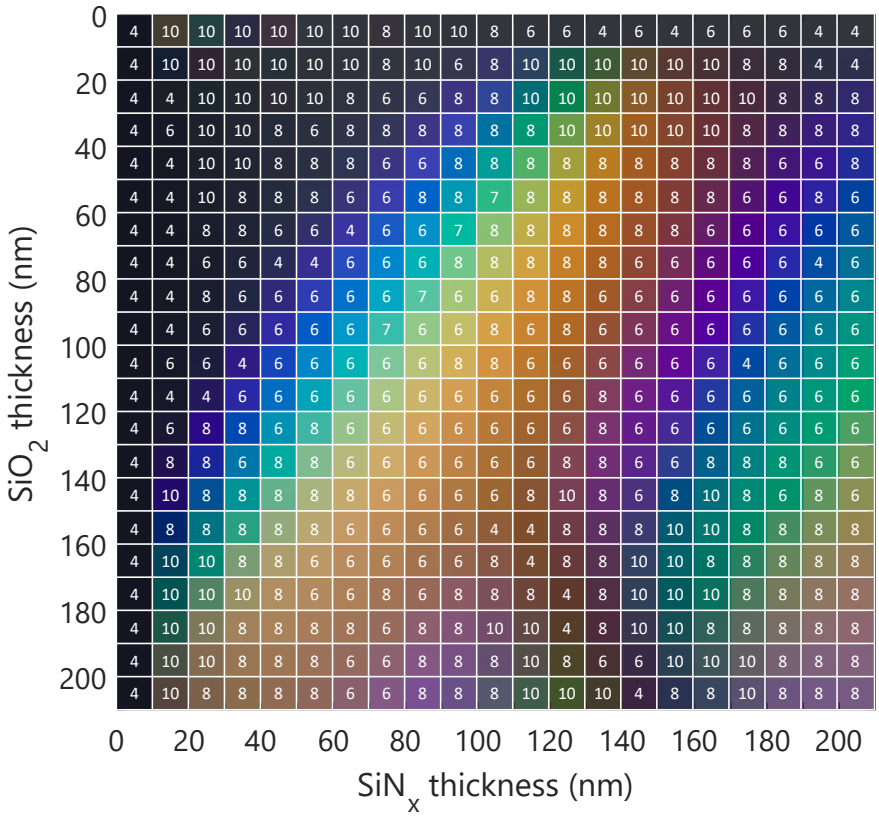

Figure 4.12: Optimized number of pairs for the different color filters wihtout significant loss in color perception

4.4. EFFECT OF THE COLOR FILTER ON THE PERFORMANCE OF C-SI PHOTOVOLTAIC MODULE

Implementing a color filter on a photovoltaic module, as described in the previous chapter, has two main effects that affect the overall performance of the solar cell. The additional optical loss reduces the current generated in the cell, which lowers the electrical efficiency of the colored module. However, the same reflection loss reduces the operating temperature of the cell, which is beneficial for performance. Estimating both G_{cell} and T_{cell} is essential in accurately modeling the effect that a color filter has on the performance of a photovoltaic module. The measured reflectances from both mini modules at different angles of incidence were compared to those obtained via the optical model. The results indicate a good agreement for the case of a flat color filter ($RMSE$ = 2.36%) and a reasonable agreement for the color filter deposited on random textured glass ($RMSE$ = 5.65%). Due to technical constraints, creating a fully functional textured sample was impossible. For this reason, the thermal and electrical models were validated by measuring the orange mini module (flat sample). The comparison between the simulated and measured temperatures for twelve days produced a $RMSE$ value of

1.15 °C. Lastly, the simulated IV curves had a $RMSE$ below 1% for the power generated once the value of the scaling factor j_{CF} was applied to the two-diode model of the standard module. Detailed information on the experiments is presented at the end of this chapter. Figures 4.13a and 4.13b show the difference in absorbed and extracted irradiance power on a c-Si solar cell for (a) the standard module compared to (b) a color module under nominal operational cell temperature (NOCT) conditions. The latter case shows a reduction in thermalization losses, which reduces not only the operating temperature but also the extracted power.

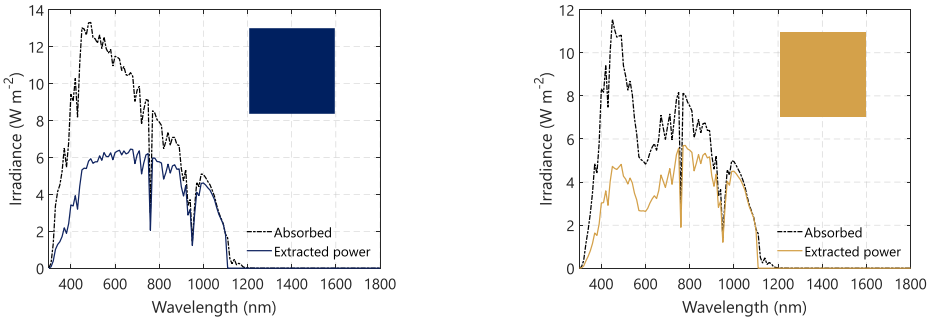

Figure 4.13: Absorbed and extracted power of **(a)** A Standard module under nominal operational cell temperature (NOCT) conditions and **(b)** Module with a filter that produces Color 3, under the same conditions. Reflection of light to create the color produces a dual effect on the overall performance of a PV module. Reduction of extracted power, which reduces electrical performance, and a reduction of the total absorbed irradiance, which reduces the cell's operational temperature. Overall, the optical loss created by the color dominates and it is never compensated by a reduced operational temperature

	Standard	Color 1	Color 2	Color 3
$J_{opt}(mA \cdot cm^{-2})$	42.26	35.22	31.84	33.19
$J_{CF}(-)$	-	0.83	0.75	0.78
$J_{opt}(mA \cdot cm^{-2})$ p optimized	-	35.63	32.30	33.69
$J_{CFopt}(-)$	-	0.84	0.76	0.79
$T_{cellNOCT}$ (°C)	47.32	40.01	40.10	39.51
$T_{cellNOCT}$ (°C) p optimized	-	43.07	43.22	42.78

Table 4.4: Effect of the layer optimization on the optical current density ($J_{opt}@STC$), the irradiance scaling factor j_{CF} ($@STC$), and the operational cell temperature ($T_{cell}@NOCT$) for the three selected colors

The optimization carried out in the previous section focused on reducing the number of pairs within the filter without a significant loss in color perception. Lowering the number of pairs translates, as demonstrated by Macleod [55], into a reduced reflection

peak. This means a lower value of the factor j_{CF} and an increase in optical current in the optimized design, but could also translate into increased operational temperature. The effect of this optimization is presented in Table 4.4, with optical currents estimated under standard test conditions (STC).

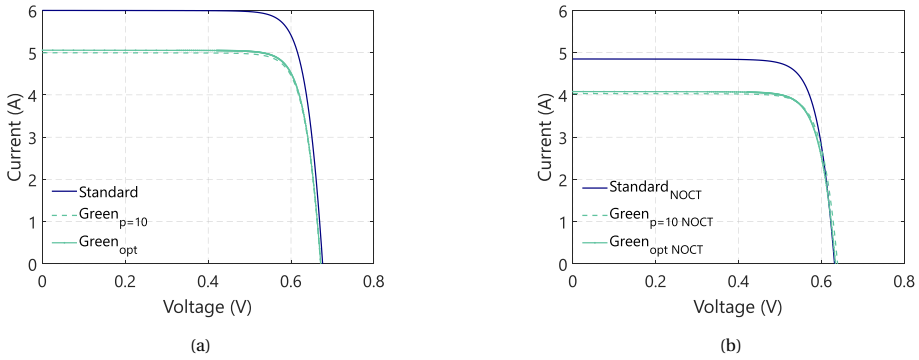

Figure 4.14: **(a)** Current density-voltage ($J-V$) curves of a single solar cell under a standard module layout, or a module with a Color 1 filter with $p = 10$ layout, or a module with an optimized Color 1 filters under standard test conditions (STC). **(b)** $J-V$ curves of a single solar cell under standard module layout and optimized Color 1 module layout under NOCT conditions.

Color 1 with a value of $p = 10$ presents a relative loss in optical current density of 16.65% compared to a standard module. Optimizing the number of pairs reduces this loss to 15.69% without incurring noticeable losses in color perception. For the case of Color 2, the optimization causes the relative loss in optical current density to go from 24.65% to 23.56%. For Color 3, the optimization produces a relative loss change from 21.47% for $p = 10$ to 20.28% for $p = 6$. With respect to operational temperature, Table 4.4 shows that Color 1 production reduces operational temperature by almost 7.31 °C, while Color 2 and Color 3 present reductions of 7.22 °C and 7.81 °C, respectively. Optimizing the number of pairs increases the temperature under NOCT conditions of Color 1 by 3.06 °C. Optimization of Color 2 and Color 3 produces higher temperatures under NOCT conditions of 3.12 °C and 3.27 °C.

In general, optimizing the number of layers contributes to a better electrical performance of colored modules. The two-diode model was used to estimate the JV curves of a single solar cell operating under the different module layouts studied. Equation 4.2 was deployed to scale the effective irradiance that reaches the solar cell. The results are presented in Figures 4.14a and 4.14b for the case of Color 1 and Table 4.5 for all colors under STC and NOCT conditions.

Under NOCT conditions, a cell inside a color module, due to its reduced operational temperature, closes the difference in power produced compared to a similar cell in a standard module layout, as shown in Table 4.5. In general, the gains produced by the reduction in operating temperature do not compensate for the loss produced by the additional reflection loss. For all the thickness combinations discussed in this work, the color filter always produces less electrical energy than a standard module. Annual yield calculations were performed to assess the overall effect of the implementation of a color

	Standard	Color 1	Color 2	Color 3
$P_{STC}(W)$	3.31	2.76	2.47	2.60
$P_{STC}(W)$ optimized	-	2.79	2.53	2.64
Relative loss (%)	-	15.69	23.56	20.28
$P_{NOCT}(W)$	2.45	2.09	1.87	1.97
$P_{NOCT}(W)$ optimized	-	2.09	1.89	1.98
Relative loss (%)	-	14.69	22.85	19.18

Table 4.5: Power produced (W) by a single solar cell under the module layouts depicted by the colors and its relative power loss for the optimized color cases compared to a standard layout

filter on the performance of a solar cell. The selected locations were, as in the case presented in the previous chapter, Delft in The Netherlands and Alice Springs in Australia. The higher frequency of clear skies in Australia proved to be slightly more beneficial due to the lower operating temperatures of the color modules. At both locations, two different installation layouts were analyzed, a module tilt of 35 °C, for a rooftop photovoltaic system, and a façade layout, with a tilt equal to 90 °C. In both cases, the optimal azimuth was considered. The annual yield of a single IBC solar cell in Delft under a standard module layout was estimated at **3.65** $kWh/year$ for the case of a rooftop photovoltaic system and **2.38** $kWh/year$ for the case of a photovoltaic façade. In Alice springs, these values were found to be **6.81** $kWh/year$ and **3.22** $kWh/year$, respectively. The color matrix for the optimized filter designs is presented below for both locations, with the relative loss indicated, as a percentage, when compared to the values mentioned above.

Figure 4.15 shows that there is the possibility of producing colored modules with blue, green, purple, maroon, and gold with relative losses below 14%. Some combinations of thicknesses can produce similar hues with significantly higher relative losses (> 20%). Furthermore, the relative losses of a few colors are lower in a location with higher frequency of clear skies, such as Alice Springs, as presented in Figure 4.16. Relative DC yield losses also remain remarkably stable for the case of the PV façade, with comparative changes below 2% compared to the case of the PV on the roof, as presented in Appendix 9. As mentioned earlier, one of the main benefits of color stabilization, from a perspective of energy yield, is that the value of $j_{opt(\theta)}$ (Equation 4.3) remains very stable for a wide range of angles of incidence. The main loss comes from the reflectance provided to create the color, and its stability translates into similar relative performance under different installation layouts.

4.5. INDUSTRIAL APPROACHES OF DESIGNING COLOR MODULES USING OPTICAL FILTERS

As discussed in Section 3.2, the color matrices obtained here and in Chapter 3 are based on an iterative process of values of thin film thickness for a given stack. The optimiza-

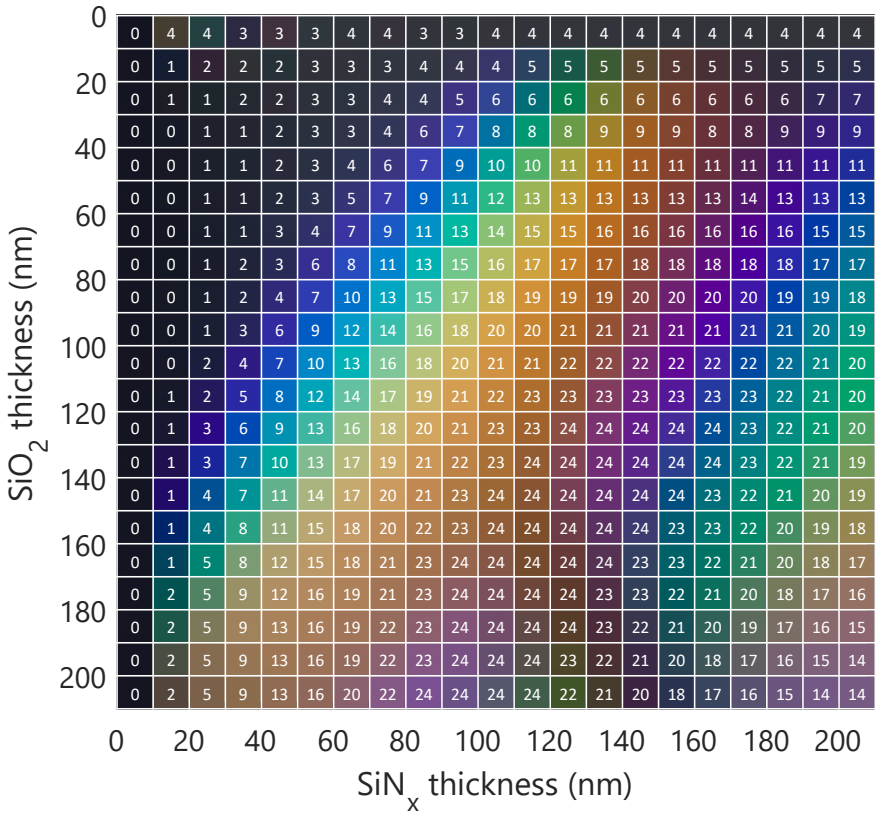

Figure 4.15: Relative DC energy yield (EY_{DC}) loss (in percentage) for different colored modules when compared to a standard modue ($EY_{DC} = 3.65 kWh \cdot year^{-1}$) for a system installed on a rooftop in Delft (module tilt = 35 °, oriented south)

tion of the number of layers is done using colorimetry analysis. This approach has the advantage of exploring the aesthetic potential that can be produced by a given color filter layout. However, there are some important caveats to this approach. First, the range of thicknesses studied was limited between 0 and 200 nm. As depicted in Figure 4.12, this can lead to designs that require a large number of layers to produce the color. Second, some colors can present additional reflectance peaks that can reduce color purity or induce additional losses without contributing to color perception.

Figure 4.17a presents two examples of these drawbacks. The color filter that produces a green hue has additional reflectance peaks at 640, 695, and 800 nm that reduce the purity of the color and induce more optical losses. A similar case is shown for an orange filter, in which the relative peaks at both sides of the high-reflectance area reduce the color purity.

Bläsi *et al.* [47] argue that color filter designs with a high layer count are not manufacturing friendly. The authors also provide better alternatives to designing these color filters using one of the harmonic reflectance peaks, which appear at $\lambda_0/3$, $\lambda_0/5$, and any

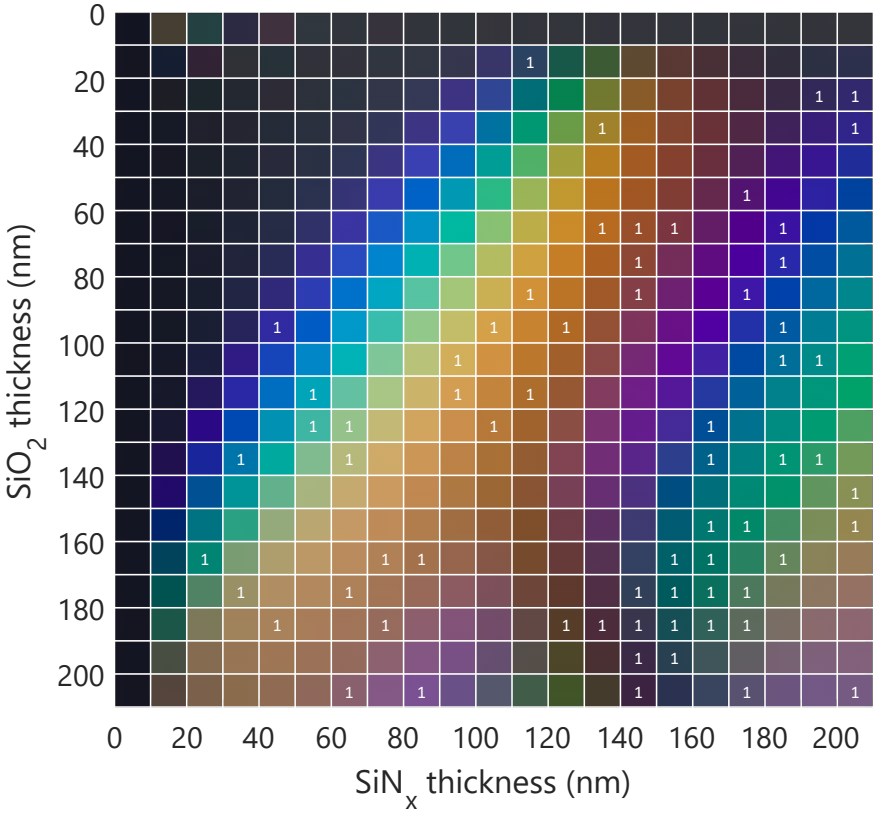

Figure 4.16: Difference on the relative DC energy yield losses at Alice Springs for the different color modules compared to the case of Delft (see Figure 4.15). The positive numbers indicate a *reduction* in the relative energy yield loss. Meaning that the modules perform better comparatively to Delft. For most colors, this difference is negligible (no number provided). On the exceptions, the improvement is always below 2 %.

other odd integer of this sequence. The authors suggest using the 3rd harmonic to produce the color, as shown in Figure 4.17b. The filter consists of 7 QWOT layers based on TiO_2 ($n = 2.48$ at 550 nm) and SiO_2 with $\lambda_0 = 1650nm$. The filter produces a reflectance peak at $\lambda = 550$ nm, which is perceived as a bright green color. Note that despite having less than half the number of layers compared to the green in Figure 4.17a, the reflectance peak is only marginally lower. Eliminating the ripples also increases the purity of the color and reduces unwanted optical losses.

Selecting TiO_2 as the material with the highest refractive index (H) also helps decrease the number of layers needed to achieve high reflectance, as argued by He *et al.* [198]. In their work, the authors present approaches to tailoring the reflectance peak either at λ_0 or one of its harmonics by the combination of different materials. The authors show that using a large refractive index mismatch (for example, using SiO_2 with $n = 1.46$ and TiO_2 with $n = 2.32$), the designer can achieve high values of reflectance in the 3rd harmonic, but also a higher reflectance width Δ_g. Narrower and lower reflectance

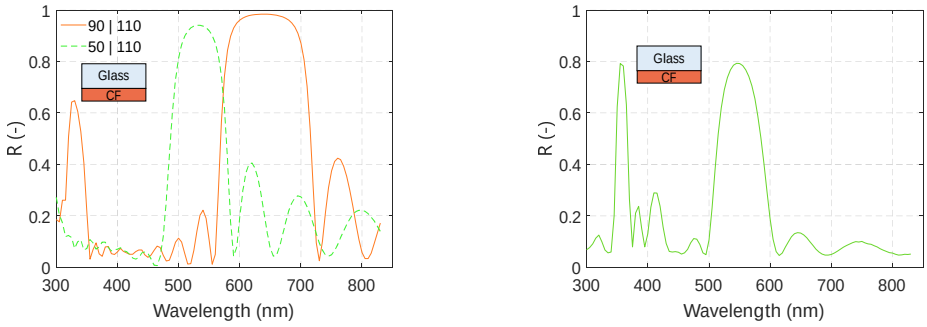

(a) (b)

Figure 4.17: **(a)** Orange (based on 10 pairs of SiO_2 | SiN_x) and green color filters obtained via the iterative process used on Chapter 3 and Chapter 4. This iterative process can lead to designs that 1. require a significant number of layers and 2. can present reflectance peaks that reduce color purity and induce optical losses **(b)** A green color obtained following the approach by Bläsi *et al.* [47] using the third harmonic of $\lambda_0 = 1650$ nm to produce the green color ($\lambda = 550$ nm) using only 7 layers of SiO_2 and TiO_2 on a LHLHLHL sequence

is achieved using a lower mismatch (SiN_x with $n = 2.02$ and TiO_2 with $n = 2.32$), which reduces optical losses and increases color purity.

The approaches mentioned above are very effective for creating highly efficient colors that require narrow wavelengths, such as blue, red, and green. The relative performance loss obtained from this technique can be quite consistent for these three hues, with values around 5%. Compared to the results shown in Table 4.5 in which the green color presents relative losses of 14%, it shows the advantages of the approach taken by Bläsi and He. Further adjustments to the optical system include the addition of two layers of the lower refractive index material at the end of the stack with a thickness equal to half a wavelength (here denoted 0.5L). Macleod [55] showed that the addition of these layers eliminates the ripple between the main reflectance peak (λ_0) and its lower harmonics (like $\lambda_0/3$).

The next step is to study the effect that the glass texture layout has on the color stability of a filter design with this approach. To this end, a green filter was designed using TiO_2 as the high refractive index material (H) and SiO_2 as the low refractive index material (L). The design wavelength was selected as $\lambda_0 = 1650$ nm. which will produce a 3rd harmonic at $\lambda = 550$ nm. In total, the filter consists of 5 layers in the following sequence: 0.5LHLH0.5L. Figures 4.18a to 4.18d present the behavior at different angles of observation and the color consistency for the case of the green filter deposited on the backside of a flat glass substrate. Note that these results belong to the complete optical system depicted in the sketch in Figure 4.1.

Note that, compared to Figure 4.9a, the color stability provided by a filter with thicker layers and a lower layer count is improved. In this new filter layout, the hue remains within the green region, and the loss of chroma at high values of angles of observation is due to the increased reflectance of the front side of the glass.

Applying a random texture to the backside of the glass slightly changes the hue coordinate, without losing its green appearance, as shown in Figures 4.19a to 4.19d. The

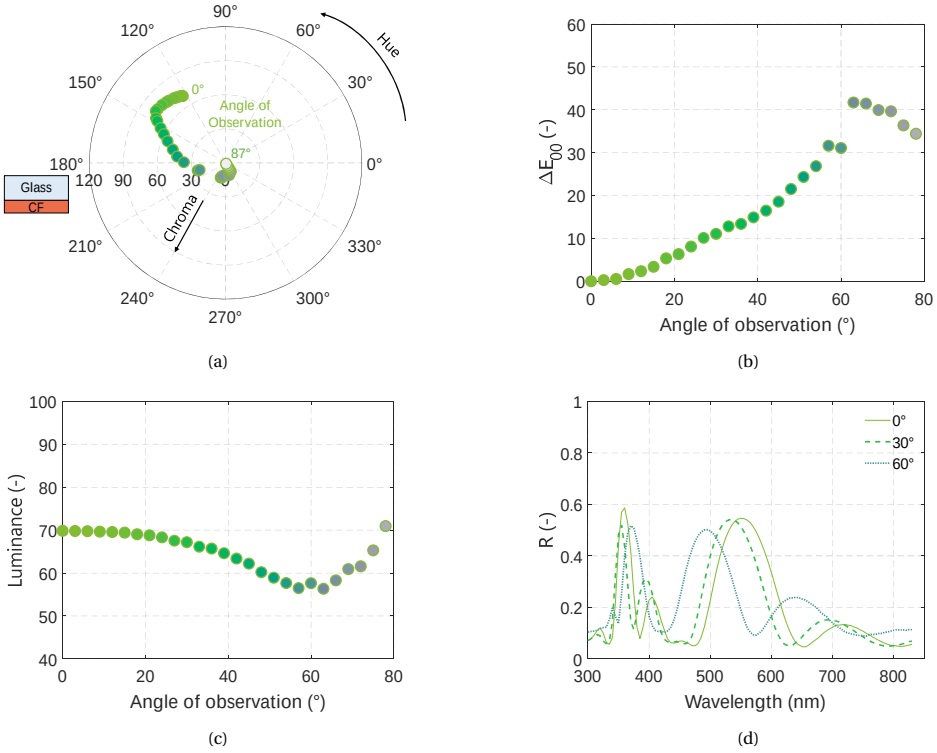

Figure 4.18: Color consistency for a green filter made with TiO_2 and SiO_2 following the 0.5LHLH0.5L sequence and deposited on a flat glass substrate. **(a)** Change in hue and chroma for different angles of observation. **(b)** Change of the ΔE_{00} for different angles of observation **(c)** Change in the luminance coordinate and **(d)** change in the reflectance spectrum for different AoO. These results are obtained by simulating the full optical system depicted in Table 4.1

color stability improves for higher values of the angle of observation. The luminance coordinate is slightly decreased, but not significantly, compared to the case of a complete flat glass substrate.

When the inverted pyramidal texture at the front of the glass is combined with a random texture at the back, the color is significantly more stable even at very high values of angle of observation (see Figures 4.20a to 4.20d). However, this layout reduces the chroma of the color, which now appears as a dark green rather than the bright one of the previous layouts.

Using the harmonic approach has substantial advantages in terms of ease of manufacturing, improved color purity, and reduction of ripples that do not contribute to color and can produce additional unnecessary optical losses. This approach will be studied in depth in future research, where all the modeling framework will be deployed to optimize these designs not only in terms of color perception but also with a focus on thermal and electrical performance. In this latter aspect, the following chapter will provide more insight on how the harmonic approach can help to improve the thermal performance of a

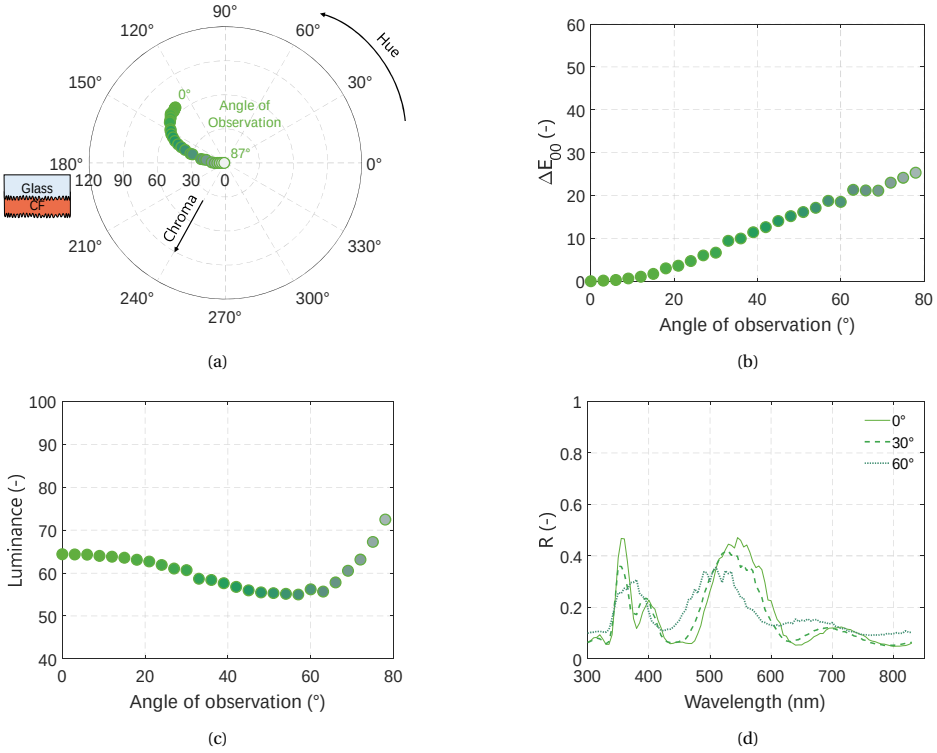

Figure 4.19: Color consistency for a green filter made with TiO_2 and SiO_2 following the 0.5LHLH0.5L sequence and deposited on a flat | random textured glass substrate. **(a)** Change in hue and chroma for different angles of observation. **(b)** Change of the ΔE_{00} for different angles of observation **(c)** Change in the luminance coordinate and **(d)** change in the reflectance spectrum for different AoO. These results are obtained by simulating the full optical system depicted in Table 4.1

photovoltaic module.

4.6. CONCLUSIONS

The proposed modeling framework presented in our previous publication, in combination with colorimetry concepts, is used in this work as computational aiding tools for the design of colored modules for building integrated photovoltaics based on c-Si technologies. The models can help find the optimal texturing layout for color stability, assess the hue chroma and luminance losses of a given color filter layout, and estimate the simplest filter design for a desired color. Experimental activities were conducted to validate the accuracy of the spectrally resolved models, producing good agreement on all three main pillars. Optical, thermal, and electrical. The calculated error *RMSE* for the case of a color filter deposited on flat glass was 2.36%. For the case of a color filter deposited on random textured glass, the value of *RMSE* was 5.65%. The angular behavior of the textured sample was measured and compared with the simulation results. The optical model presents high *RMSE* values at angles of observation above 70 °C. A possible ex-

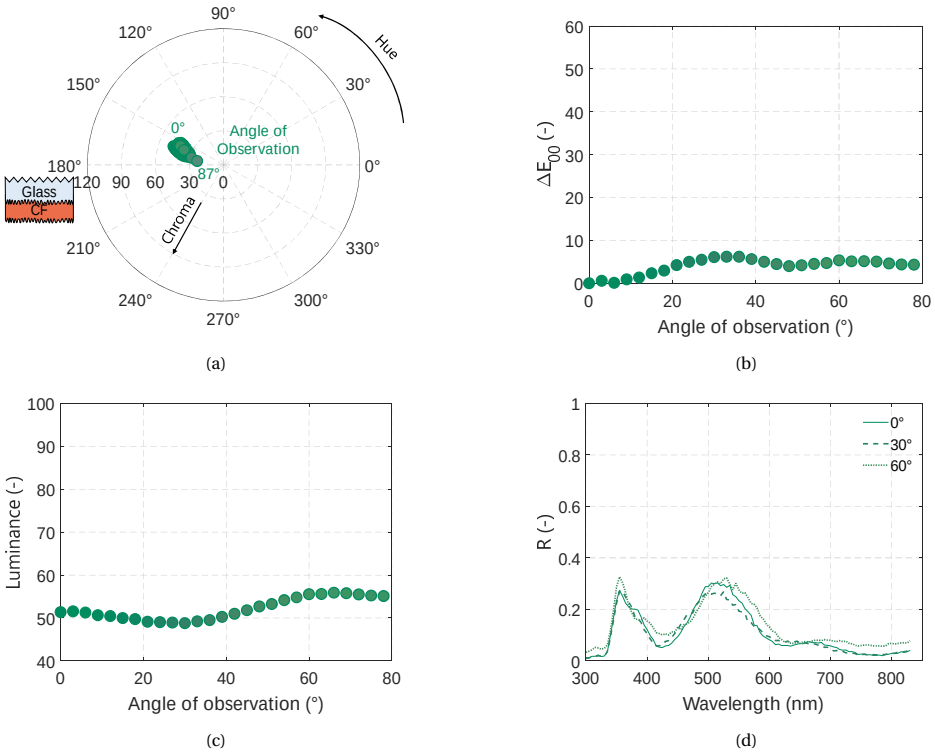

Figure 4.20: Color consistency for a green filter made with TiO_2 and SiO_2 following the 0.5LHLH0.5L sequence and deposited on a inverted pyramid | random textured glass substrate. **(a)** Change in hue and chroma for different angles of observation. **(b)** Change of the ΔE_{00} for different angles of observation **(c)** Change in the luminance coordinate and **(d)** change in the reflectance spectrum for different AoO. These results are obtained by simulating the full optical system depicted in Table 4.1

planation for this lies in the assumption of the optical model that the growth of the filter layers during deposition is homogeneous in all directions of the texture. Improvements in this matter will continue in future work.

The thermal model showed *RMSE* values of 1.15 °C for both a standard and a colored module (flat glass) with a time resolution of ten seconds for a period of 11 days. The accuracy of the electrical model is highly dependent on the accuracy of the optical model, with low error on the latter, the former can produce highly accurate results. The use of the color difference factor ΔE^*_{00} and the HCL color space is key to producing high-performance designs in terms of both electrical output and aesthetic approaches. ΔE^*_{00} can be used to evaluate the color stability of a given color filter layout. Seven structures were studied using ΔE^*_{00}, from the combination of three texture geometries on the front side of the PV glass and two layout options on the backside: random texture and flat. The results showed that hard edged geometries, such as V-shaped grooves or inverted pyramids, substantially improve color stability. HCL color space analysis indicates that texturing the backside of the module, where the color filter is to be deposited, improves

luminance stability with the bonus of eliminating any potential glare. Overall, the simulation results indicate that a combination of inverted pyramidal texture on the front glass and the color filter deposited on a randomly textured surface (structure 7) showed greater color stability compared to other alternatives. Analysis of ΔE^*_{00} also helps reduce unnecessary optical losses by reducing the number of layers of a given color filter, without a significant sacrifice in color perception. The optical current densities resulting from the three selected color filters deposited on a random textured glass were increased to 1.2% using this approach.

When other effects on performance are analyzed, the additional reflection produced by the color filter has a dual effect on a solar c ell. The additional optical loss causes a reduction in the current generation. However, this same loss produces a lower operating temperature than in the standard case. Electrical calculations performed under STC and NOCT conditions lead to the conclusion that the optical loss is not fully compensated for by the thermal gain; however, at higher operating temperatures, the relative electrical loss on a colored module is lower than in the case of STC.

Calculations of the expected annual DC energy yield for two installation layouts (Roof photovoltaic and PV façade) showed that the overall losses produced by the color filters are almost independent of the location in which they operate. Locations with a high frequency of clear skies have slightly lower relative energy yield losses than locations with more frequent overcast days. These findings indicate that the benefits of lower operating temperatures do not translate into significant gains in electrical p erformance. Furthermore, the differences in relative DC yield losses between the two installation layouts studied were also small due to efforts to stabilize the color. This stabilization results in very small additional angular losses.

Generally, a large number of hues can be produced with relative energy yield losses below 20%, with some color filters showing losses as low as 7 %. Further improvements can be made by designing the filters using the harmonic approach, a method that will be studied in detail in future work.

4.7. EXPERIMENTAL WORK AND VALIDATION

The electrical models presented in [38] were validated on first instance via comparisons between the two-diode model approximation with simulations carried out on Sentaurus TCAD. The thermal model was validated by comparing the predicted temperature of a standard PV module with measurements carried out on non-colored solar modules. For this work, both the thermal and the electrical models have been validated by making direct comparisons with colored mini modules. The mini modules were manufactured by encapsulating two SunPower Maxeon Gen III solar cell. One of the solar cells was encapsulated on a standard glass | EVA | cell | EVA | Tedlar layout, whilst the other one had the glass | CF | EVA | cell | EVA | Tedlar. The selected color filter was made of 6 pairs of SiO_2 | SiN_x layers, with thicknesses of 90 nm and 100 nm, respectively. For the case of the color filter deposited on a random textured glass, the demonstrator manufactured by S. Villa [179] was used. The results from the measured and simulated reflectance for each color filter are shown below.

For both cases, the metrics used to assess the accuracy of the prediction were the mean bias error (MBE), the mean absolute error (MAE), and the root mean square error

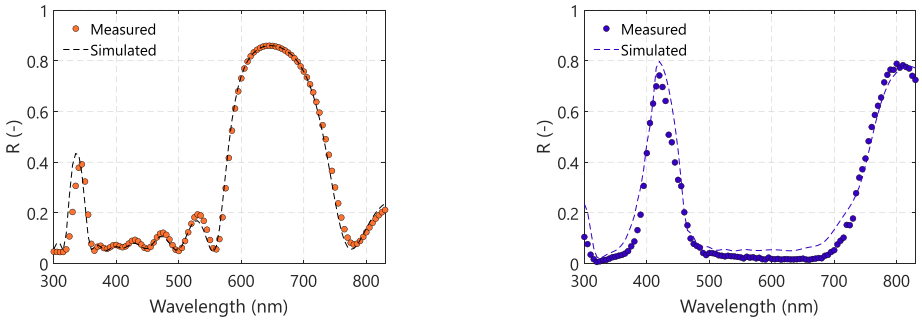

Figure 4.21: Measured and Simulated reflectance of a color filter deposited on the front glass of a PV mini module: **(a)** an IBC solar cell encapsulated with a flat glass and the color filter deposited below the glass (Orange); **(b)** a set of Al-BSF laser cut solar cells encapsulated with a random textured front glass with the color filter deposited on top (Purple), see Figure 4.5b.

(RMSE). The results of these calculations are summarized in Table 4.6. Results indicate a particularly good agreement for the case of the flat color filter (RMSE = 2.36%), and a good agreement for the color filter deposited on the random textured glass (RMSE = 5.65%).

	Orange	Purple
MAE	1.24%	4.53%
MBE	-0.42%	-3.54%
RMSE	2.36%	5.65%

Table 4.6: Values of MAE, MBE and RMSE for the assessment of the accuracy of the optical model for both colored mini modules

The optical model was also validated for angles of incidence greater than 0°for the case of the textured surface. The measurements of the purple module (based on randomly textured glass) were carried out with a PerkinElmer Lambda 950 spectrophotometer equipped with an ARTA accessory [199] [200] The measurement obtained is known as the angular intensity distribution (AID) [201]. It was not possible to validate the optical model by direct comparison of the predicted reflectance but rather by comparing the normalized reflection with the AID values obtained experimentally. Figures 4.22a and 4.22b present the results for angles of observation of 50° and 70°.

Table 4.7 presents the calculated accuracy metrics. The value of the RMSE error is significant at angles of observation of 70°and above. A probable explanation for this deviation is that GenPro4 considers a uniform layer growth on the textured surface. The growth of layers on such surfaces does not follow this trend, as explained by Wessels et al.[58] and reported by other studies that analyzed this trend on non-flat surfaces [202] [106]. So, for larger optical paths, the deviation between the predicted behavior differs more than for the case of normal incidence.

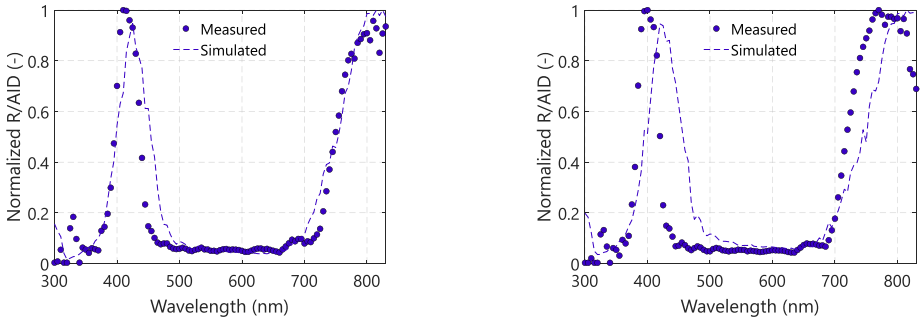

Figure 4.22: Simulated normalized reflectance compared con the measured angular intensity distribution (AID) obtained with the spectrophotometer with an ARTA device for two angles of observation of **(a)** 50° and **(b)** 70°.

	50°	70°
MAE	6.72%	14.84%
MBE	-2.65%	-1.90%
RMSE	11.30%	23.80%

Table 4.7: values of MAE, MBE and RMSE to assess the accuracy of the predicted angular behavior of a purple color filter deposited on a randomly textured surface

The orange mini module was taken for temperature measurements under the environmental conditions of Delft, The Netherlands. The measurements took place from the third through the 14th of September 2022. T-type thermocouples were attached to the mini modules with aluminum tape and thermal tape for proper insulation. The time resolution of the measurements was 10 seconds. The mini modules were tilted 30° and oriented towards the south.

Figure 4.23: Temperature measurements of a colored mini module (Orange, left), a mini module with an experimental filter (middle, outside of the scope of this work) and a standard mini module (right)..

The predicted temperature from the thermal model was compared with the temper-

ature measurements obtained for the same time resolution. The results show that for both cases the thermal model predicts with great accuracy the thermal behavior of the mini modules. It is also observed that the color module operates at lower temperatures compared to the standard module. The thermal model, which estimates the spectral behavior of the solar cell and its thermalization losses, predicts very well the impact of color on the operational temperature of the cell (see Table 4.8).

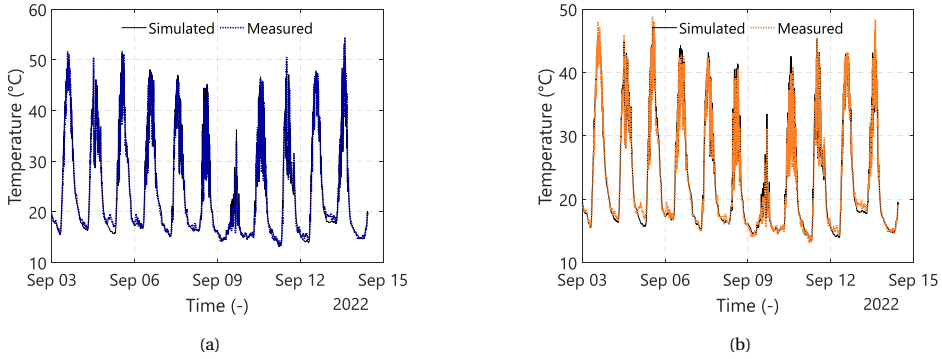

Figure 4.24: Predicted and measured mini module temperature for (a) the standard layout and (b) the color layout.

	Standard	Orange
MAE	0.82 °C	0.77 °C
MBE	0.22 °C	0.36 °C
RMSE	1.15 °C	1.15 °C

Table 4.8: values of MAE, MBE and RMSE to assess the accuracy of the predicted angular behavior of a purple color filter deposited on a randomly textured surface

For the validation of the electrical model, the optical behavior of the IBC solar cell from SunPower was measured. The resulting fit with the optical model is presented in Figure 4.25a. The electrical behavior of the solar cell was measured (already encapsulated with a 3-mm thick flat glass) on an AAA solar simulator. From these measurements, the parameters for the two-diode model were extracted using the tool provided by the PV lighthouse website [152]. The resulting parameters are shown in Table 4.9. The parameters were kept constant, except for the light collected current, which was scaled down according to the value of j_{CF} defined in Equation 4.2 and estimated using GenPro4. The resulting $J-V$ curve was then compared to the measured JV of the colored mini module. The results show great agreement, as shown in Figure 4.25b. The RSME error for the case of the colored mini module was below 1%.

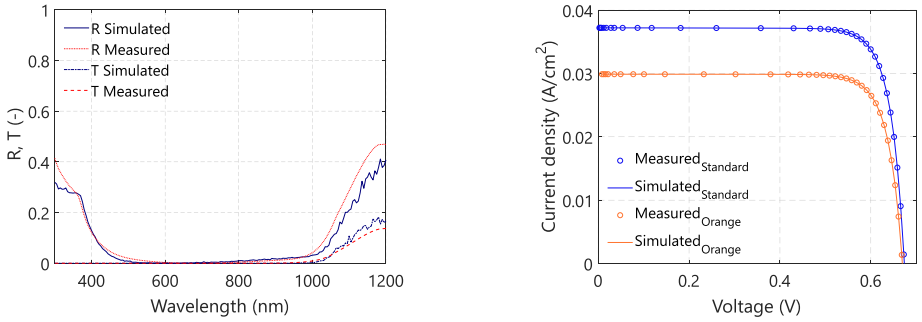

(a) (b)

Figure 4.25: **(a)** optical fit based on measurements carried out using the Perkin Elmer Lambda 950 spectrophotometer of A 5-inch wide SunPower IBC solar cell **(b)** Measured and simulated JV curved of an encapsulated IBC solar cell with a standard flat glass and a colored flat glass.

Parameter			Value
Light collected current	(J_L)	$(mA \cdot cm^{-2})$	37.204
Saturation current 1	(J_1)	$(pA \cdot cm^{-2})$	0.14
Ideality factor 1	(m_1)	(-)	1
Saturation current 2	(J_2)	$(nA \cdot cm^{-}2)$	3.74
Ideality factor 2	(m_2)	(-)	2
Shunt resistance	(R_{SH})	$(k\Omega cm^2)$	18
Series Resistance	(R_S)	(Ωcm^2)	0.6

Table 4.9: Estimated two-diode parameters for the SunPower IBC solar cell

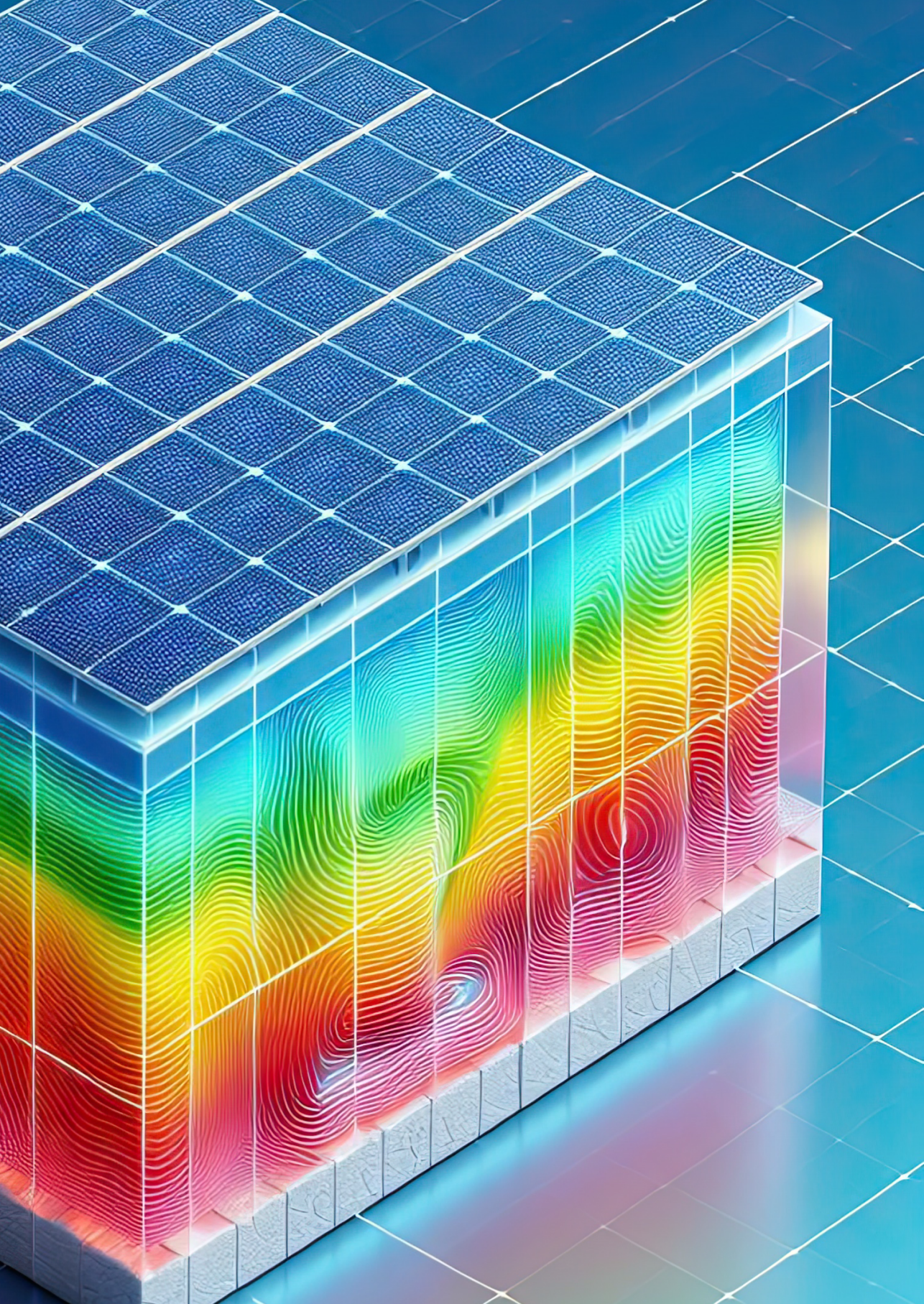

5

THERMAL CONTROL: OPTICAL FILTERS

This chapter is partially based on the following publication:

J.C. Ortiz Lizcano[1], I. Kaaya, H. Ziar, P.S da Silva, Y. Zhou, M. Zeman, O. Isabella *Practical Design of an Optical Filter for Thermal Management of Photovoltaic Modules*, Progress in Photovoltaics Research and Applications, **32**(11), 753-773 (2024).

This work presents a practical approach to designing an optical filter for thermal management of photovoltaic modules. The approach emphasizes the practicality of manufacturing over optical performance. Simulation work demonstrates that, for an interdigitated back-contact solar cell architecture, complete rejection of infrared radiation offers limited thermal benefits that require highly complex optical filter designs. An alternative approach consists of reducing thermalization losses by providing reflectance at lower wavelength values. An optical filter design that fulfills this requirement is possible using simple structures based on two materials and taking advantage of the harmonics present in quarter-wavelength optical thickness designs. The filter is later optimized for angular performance via second-order algorithms, resulting in a device consisting of only 15 thin-film layers. Performance simulations in two locations, Delft (the Netherlands) and Singapore, estimate a temperature reduction of 2.20 °C and 2.45 °C, respectively. In a single year, the optical loss produced by the filter is not compensated for by reducing the temperature. However, improvements in the annual degradation rate show that in Singapore, the overall effect of the filter on the lifetime DC energy yield is positive.

5.1. MODELING FRAMEWORK

The computational model framework follows the same approach presented in our previous work [203] The models consist of spectrally resolved algorithms that estimate the ef-

[1] Candidate's contribution: Writing, coding work, simulation work, experimental work, results analysis

fective irradiance reaching the solar cell, its operating temperature and its electrical energy output at any instant. The Simple Model of Atmospheric Radiative Transfer of Sunshine (SMARTS) [147] allows estimation of the solar spectrum. These spectra are used for optical, thermal, and electrical assessments. The optical pillar utilizes two software packages: GenPro4 [140] and OptiLayer® [204]. The former produces four main outputs: First, it matches the spectral behavior of the chosen solar cell optically. The SunPower Maxeon II interdigitated back-contacted solar cell (IBC) [194] is the structure selected in this work. Second, it computes the optical current densities J_{opt} (in $mA \cdot cm^{-2}$) of each layer within a photovoltaic module, which are the basis of the irradiance scaling factors τ_0 and i_{opt}, mathematically defined as

$$\tau_0 = \frac{J_{opt(c-Si)}}{\sum J_{opt(lay)} + J_{opt(c-Si)}} \tag{5.1}$$

$$i_{opt(\theta)} = \frac{J_{opt(\theta)}}{J_{opt(0°)}} \tag{5.2}$$

In equation 5.1, $J_{opt(c-Si)}(mA \cdot cm^{-2})$ represents the optical current density of the c-Si solar cell. $J_{opt(lay)}$ $(mA \cdot cm^{-2})$ is the optical current density of each layer within a PV module that contributes to losses (reflectance or absorptance), such as glass, encapsulant, antireflective coating, emitter, and optical filter. τ_0 is a factor that accounts for the optical losses at normal incidence. Equation 5.2 defines the factor that accounts for the optical loss at different angles of incidence (AOI). It is calculated by dividing the optical current density at any given AOI $J_{opt(\theta)}$ by the optical current density at normal incidence $J_{opt(0°)}$. Notice that, at normal incidence, $J_{opt(0°)} = J_{opt(cSi)}$. The effective irradiance reaching the solar cell G_{cell} depends on these two factors as they scale the plane of array irradiance G_{POA} as follows:

$$G_{cell} = \tau_0 \cdot i_{opt(\theta} \cdot G_{POA}) \tag{5.3}$$

Third, GenPro4 helps in the first stage of the design, which aims to find an adequate range of wavelengths at which thermal management produces as low an optical loss as possible at normal incidence. OptiLayer® allows for the discovery of potential design candidates that ensure low optical losses at different angles of incidence through second-order optimization methods. Lastly, GenPro4 provides the spectral absorptance of all layers within a photovoltaic module, which are fed into the thermal model. This model uses a two-dimensional finite-volume transient approach that estimates the volumetric heat produced within each layer as a function of wavelength. The model provides the operating temperature of the solar cell (T_{cell}) as output, which serves as a guide for the design of the thermal filter. T_{cell} and G_{cell} are the inputs for a two-diode equivalent circuit electrical model. After an iterative process (given the direct relationship between electrical power and thermal power in the cell), the maximum electrical output power is obtained at each instant in time.

5.2. THERMAL FILTER DESIGN AND OPTIMIZATION

Optical filters reflect light by depositing thin layers of dielectric materials with a mismatch in their refractive indices n. As mentioned above, the optical filter structure se-

lected in this study consists of two materials, one with a high refractive index (n_H) and the other with a low refractive index (n_L). These materials are deposited sequentially in pairs, and, depending on the wavelength value (λ_0, in nm) at which high reflectance is desired, the thickness of the layers (d, in nm) is calculated using the formula for the quarter-wavelength optical thickness (QWOT) [55].

$$d_{L|H} = \frac{\lambda_0}{4 \cdot n_{L|H}} \tag{5.4}$$

In the literature, it is common practice to notate a QWOT layer as the capital letter of its refractive index hierarchy. Thus, H refers to a layer with refractive index n_H and thickness d_H (nm) given by Equation 5.4, and L is the corresponding value for a layer with a lower refractive index. This work follows the same notation scheme. When a layer does not have a thickness value equal to that given by Equation 5.4, the presented notation is a fraction of it. For example, $0.5H$ represents a layer of high-refractive index material with a thickness that is half that of the QWOT value. When stacks of several pairs of layers are involved in the design, the notation utilized here follows the form$(LH)^p$, where p is the number of pairs of LH layers. More detailed information on the designs presented is available in [205]. The selected materials are Silicon Nitride (SiN_x), represented henceforth as H, and silicon dioxide (SiO_2), which is represented as L. These materials were selected due to their optimal optical properties and ease of manufacturing, as explained in chapter 3. The appendix 9 at the end of this thesis document provides details on the optical properties of these materials. The design of the thermal filter starts with studying the optical behavior of the selected IBC solar cell structure. Figure 5.1a presents the measured data. It is noticeable that the cell either transmits or rejects a significant portion of the near-infrared (IR) spectrum (from 1200 nm to 1800 nm). This IR behavior is due to the architecture of the IBC solar cell itself, and different topologies will show different behaviors in this region [206]. Optical simulations of a photovoltaic module help to analyze its spectral absorbed irradiance (see Figure 5.1b). It is noticeable that most of the spectrum in the near-infrared region range mentioned above is not absorbed.

5.2.1. INFRARED REJECTION

Previous studies have shown that the high rejection of the near-infrared region could have potential cooling benefits in photovoltaic modules [206]. Rejection of light in this wavelength range eliminates thermal gain without producing an optical loss. Therefore, it is interesting to see the potential cooling effect on the selected solar cell. The optical filter must provide high reflection for a wavelength range of 1200 to 1800 nm and high transmittance of 300 to 1200 nm. Fulfillment of these requirements usually results in very complicated structures.

Figure 5.2a presents an example of such a complex filter. The initial design of the filter consisted of layers arranged as 0.5A|(AB)20|B|0.5A, based on the work by Seoane da Silva [207], where A and B refer to the QWOT layers of MgF_2 and TiO_2, respectively. OptiLayer® allowed the optimization of this starting design using the needle technique [204], [145], [208]. The resulting design consists of 81 layers, whose simulated reflectance at normal incidence is presented in Figure 5.2b. After optimization, the final thickness values of the materials differ from their starting QWOT value, and Figure 5.2a only shows

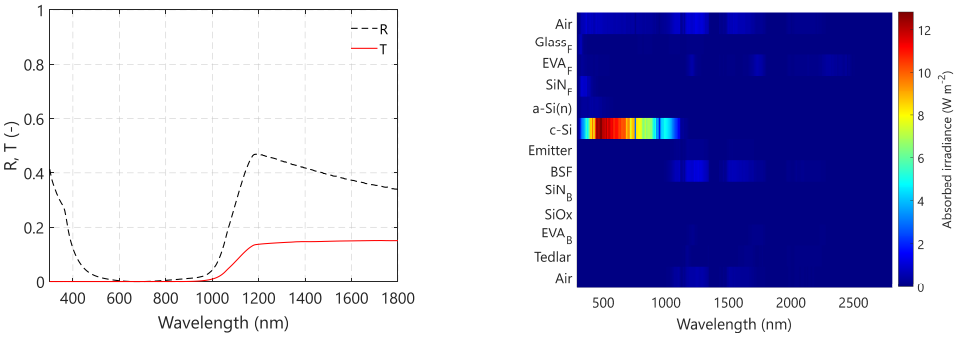

(a) (b)

Figure 5.1: **(a)** measured reflectance (R) and transmittance (T) for a SunPower Maxeon II IBC solar cell (non-encapsulated) using a PerkinElmer Lambda Spectrophotometer. **(b)** Heatmap of the simulated absorbed irradiance of a PV module endowed with an IBC solar cell. The heatmap showcases that most of the irradiance on the near-infrared does not affect the PV module. The subscripts F and B refer to the front and back layers of the module with respect to the c-Si cell.

Parameter	Standard	IR Filter
τ_0	0.93	0.92

Table 5.1: Simulated value of τ_0 for both PV module layouts

their order. The complete details of this design can be found in [205].

The complete optical model of a PV module with this implemented IR filter (see Figure 5.2a) aimed to study the predicted effect on the operational cell temperature. The module was considered to operate at maximum power point under NOCT conditions. The optical, physical and thermal properties are presented in Table 2.1. The results were then compared with the case of the same PV module without the filter implemented. The steady-state temperature on the solar cell obtained for the standard PV modules was estimated at 45.2 °C. Figure 5.3a shows the temperature profile of the entire module for this case. A PV module with the optical filter implemented presents a steady state temperature of 41.6 °C, representing a reduction of 3.6 °C. The profile for this case is shown in Figure 5.3b.

Implementing such a complex filter design for this cell architecture does not provide a significant temperature reduction. Moreover, optical filters have markedly different behavior at different angles of incidence (AOI) (see Figure 5.2b). Estimating the scaling factors τ_0 and i_{opt}, defined by Equation 5.1 and Equation 5.2, allows analysis of the optical losses produced by the filter. The absolute optical loss produced by the infrared filter at normal incidence is 1%, as presented in Table 5.1.

The angular optical loss is significantly higher for the case of the PV module with an IR optical filter compared to the standard, as presented in Figure5.4. The filter will substantially reduce the effective irradiance reaching the solar cell for values of AOI greater than 20°. At 50°, for example, the scaling factor iopt of a standard photovoltaic module has a value of 0.94. Implementing the IR filter will reduce the value of this factor to 0.8,

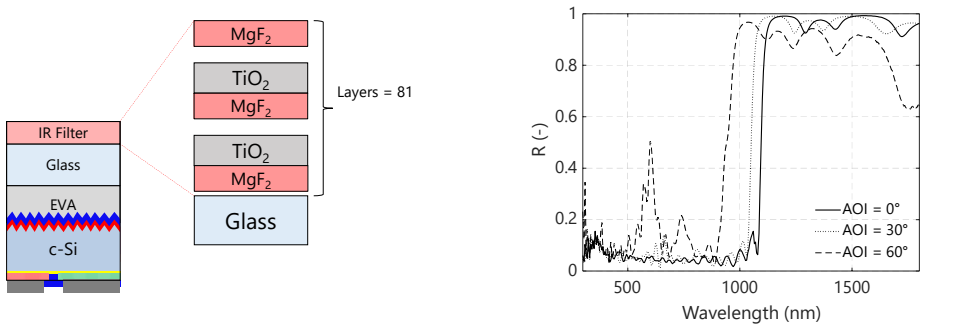

(a) (b)

Figure 5.2: **(a)** Final design layout of a near-ideal optical filter with high reflection in the near-infrared region and high transmittance from 300 nm to 1200 nm. **(b)** Simulated Reflectance profile of the complete optical model of the PV module, with the optimized IR optical filter deposited on the front surface of the glass, for three different angles of incidence (AOI). At higher values of AOI, the reflectance of the filter shifts towards lower wavelength values. Moreover, additional reflectance peaks appear between 500 nm to 700 nm, increasing the optical loss.

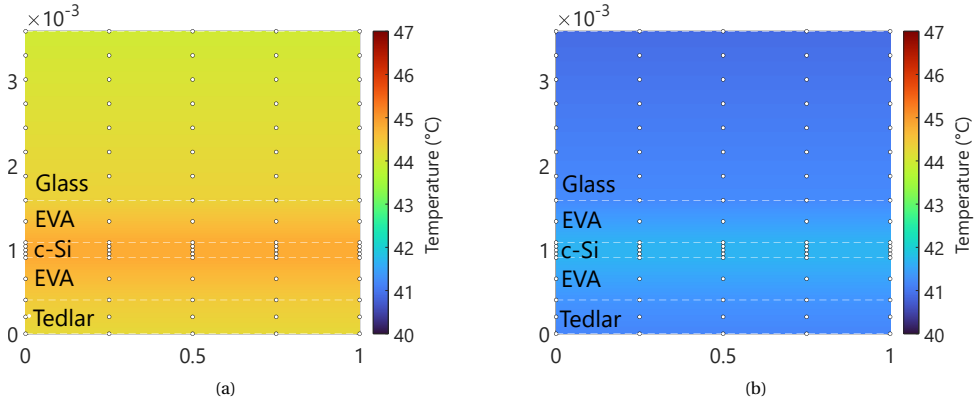

(a) (b)

Figure 5.3: Thermal profile as a function of a PV module's width (x-axis, in meters) and depth (y-axis, also in meters) depicting: **(a)** The steady-state temperature profile of a PV module under NOCT conditions, with a cell temperature value of 45.2 °C. **(b)** The steady-state temperature profile of a PV module with the optical filter is presented in Figure 2(a). The filter reduces the cell's operating temperature by 3.6 °C to a value of 41.6 °C.

an additional loss of 15%. Improving the angular behavior of the filter will only increase its complexity. With its high layer count and limited thermal benefits, this design has no practical application for a PV module made with IBC solar cells.

5.2.2. REDUCTION OF THERMALIZATION LOSSES

Another option to provide thermal management on the solar cell is by reducing its thermalization losses. Thermalization is one of the primary sources of heat within a solar cell. Simulations of the photovoltaic module under NOCT conditions help highlight the

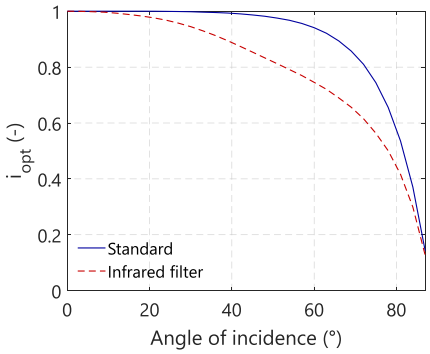

Figure 5.4: Simulated value of i_{opt} as a function of the angle of incidence for a standard and an IR filter PV module.

wavelength range at which the difference between absorbed irradiance and extracted power is the largest. The optical model selected for the PV module, in this case, differs from that of Figure 5.2a. To ensure protection from environmental damage, the filter is placed on the back of the front glass, as shown in Figure 5.5. Figure 5.6a highlights this difference. The selected wavelength of interest was 400 to 500 nm. Although the difference between absorbed and extracted power is the highest at 470 nm, lower wavelength values allow thermal management with lower optical losses.

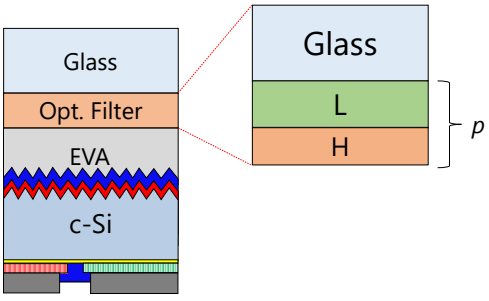

Figure 5.5: Optical model of a PV module with an optical filter deposited on the backside of the front glass. The filter is made of p pairs of LH layers and is the basis for the optimization presented in this section. In the experimental work, the filter was deposited into a glass substrate via plasma-enhanced chemical vapor deposition (PECVD). Afterward, the glass was used as the front layer of an encapsulated solar cell, creating a mini-module. The mini-module was manufactured using a vacuum laminator with a curating temperature of 140°C. In the optical model, no air layer is considered at any interface within the mini-module.

Equation 5.4 allows finding the thickness values of the H and L layers for λ_0 = 450 nm. The higher the number of pairs p, the higher the reflectance of the filter at λ_0. However, as established by Macleod [55], a high layer count produces an equal amount of reflectance ripples around the central reflectance peak. These ripples, along with the wider reflection range, translate into significant optical losses. Furthermore, at higher angles of incidence, the reflection peak shifts towards lower wavelength values, mean-

ing that the angular stability of the optical filter must be guaranteed to maintain the cooling potential. This work suggests and implements the use of a more straightforward design strategy, that is, using a harmonic peak produced by a filter with a high value of λ_0. These peaks appear at $\lambda_0/3$, $\lambda_0/5$, $\lambda_0/7$, and lower harmonics for the case of filters with a $(LH)^p$ layout. Their maximum reflectance value decreases as the harmonic order increases, meaning that the harmonic with the highest reflectance peak will be at $\lambda_0/3$.

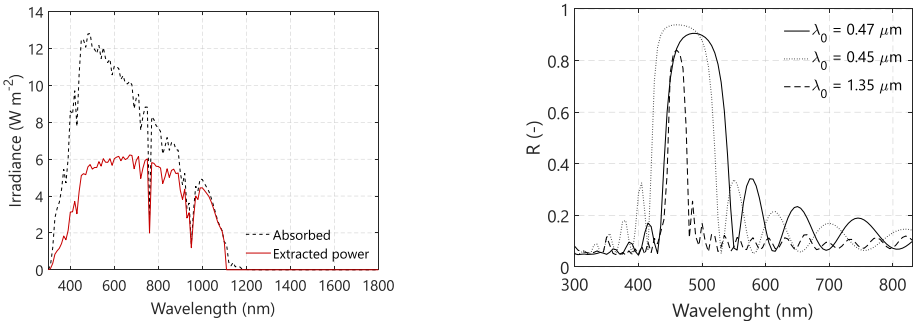

(a) (b)

Figure 5.6: **(a)** Absorbed and extracted power of a PV module based on IBC solar cells by simulating the behavior of the PV module at maximum power point under NOCT conditions. (b) **(b)**Reflectance profile of three different optic filter designs that provide high reflectance at the wavelength range of interest (400 nm – 500 nm, focused towards 470 nm) based on their value of λ_0.

Figure 5.6b presents the reflectance profile of three different filters that guarantee a peak in the wavelength range of interest for different values of λ_0. The practical advantage of the design with a value of λ_0 = 1350 nm lies in three main aspects. First, the filter produces a reflectance width of around 60 nm, less than the other options, which in both cases exceeds 100 nm, thus reducing optical losses. Second, the ripples around the 450 nm reflectance peak are significantly lower than their counterparts, improving optical performance. Lastly, the central reflectance peak at 1350 nm has an additional cooling contribution that its alternatives lack.

Narrow reflectance peaks across the wavelength range of interest (400 nm – 500 nm) can be achieved simply by shifting the value of λ_0 from 1200 nm to 1600 nm. The number of pairs p that achieved near unity reflectance is 11, as presented in Figure 5.7a. Notice that, for the sake of clarity, the units of λ_0 are expressed in μm on the graphs.

The models of the different filter candidates were obtained by changing λ_0 from 1200 to 1600 nm. The right axis of Figure 5.7b shows the calculated difference (ΔJ_{opt}) between the optical current density of a module without an optical filter and the possible candidates in STC. On this axis, the greater the value of ΔJ_{opt}, the greater the optical loss. Notice that a filter with λ_0 = 1200 nm presents a more significant loss than a filter with λ_0 up to 1450 nm. This higher loss is because part of the high reflectance width around 1200 nm falls at wavelengths at which a c-Si solar cell still produces current, such as 900 nm. Once λ_0 increases, this reflectance range shifts more and more toward the IR region, where it does not produce any optical loss.

Examination of the steady-state solar cell temperature under NOCT conditions also

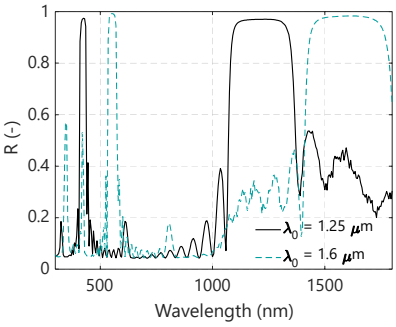

(a)

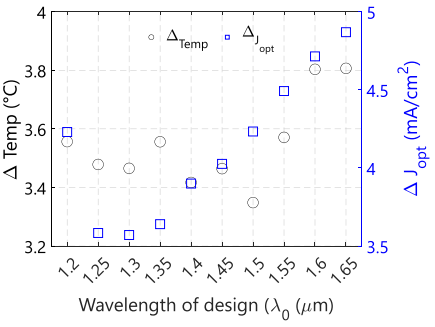

(b)

Figure 5.7: **(a)** Reflectance profile of the two limits of λ_0 studied (1200 nm and 1600 nm) that produces narrow reflectance peaks ranging from 400 nm to 533 nm. **(b)**Solar cell temperature difference ($\Delta Temp$ in °C) and optical current density difference (ΔJ_{opt} in $mA \cdot cm^{-2}$) between an encapsulated solar cell with and without a deposited thermal filter. The greater the value of temperature difference, the better the cooling provided by the filter. On the contrary, higher values of current density difference represent higher optical losses, leading to reduced electrical output.

5

provides insight into the optimal value of λ_0. The temperature difference (ΔT_{cell}) compared to a PV module without the filter is presented on the left axis of Figure 5.7b. This parameter represents the potential cooling power, so the higher the value of ΔT_{cell}, the better the performance of the filter. A filter should have relatively good cooling performance and low optical loss. The left axis of Figure 5.7b shows that the behavior of ΔT_{cell} differs from that of ΔJ_{opt}. From the starting value of λ_0 = 1200 nm, the temperature difference decreases slightly to λ_0 = 1300 nm. The differences are marginal and driven mainly by the shift of the high reflectance band and its ripples at around 900 nm towards higher values. At λ_0 = 1350 nm, the peak of harmonic reflectance coincides with the differences in peak between absorbed and extracted power. Once that peak shifts towards higher wavelength values, the temperature difference drops again for 1400 < λ_0 < 1500 nm. The temperature difference then increases to λ_0 = 1600 nm, caused by harmonics at λ_0 / 5 and λ_0 /7 that contribute to the cooling effect and produce higher optical losses (see the dashed reflectance profile in Figure 5.7a). A suitable value of λ_0 lies between 1300 nm and 1350 nm. At normal incidence, a filter with a λ_0 value of 1300 nm produces lower optical current losses, although with a slight reduction in cooling potential compared to a filter with λ_0 = 1350 nm. However, at higher angles of incidence, the shift of the reflectance peaks toward lower wavelength values on the filter with λ_0 = 1300 nm presents higher optical losses than the one with λ_0 = 1350 nm, as depicted in Figure 5.8a. The relative optical loss, calculated via Equation 5.2 for both filters, indicates that at values of AOI greater than 20°, the filter with λ_0 = 1300 nm presents higher optical losses, reaching a maximum of 4% around AOI = 60°, compared to the filter with λ_0 = 1350 nm (see Figure 5.8b). This relative optical loss was estimated using the following Equation:

$$Relativeloss(\%) = -\frac{i_{opt\lambda=1300} - i_{opt\lambda=1350}}{i_{opt\lambda=1350}} \tag{5.5}$$

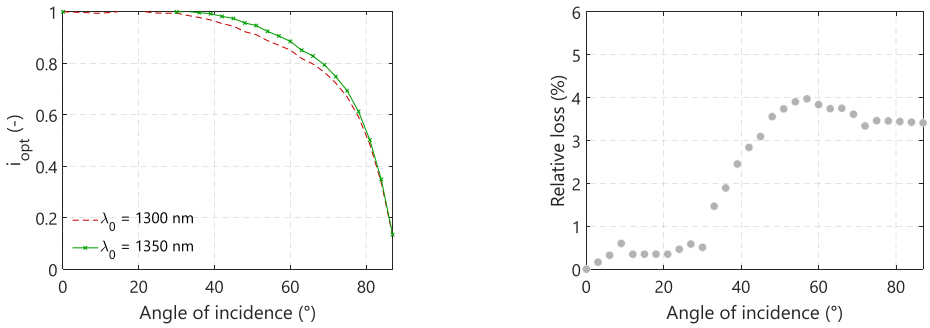

(a) (b)

Figure 5.8: **(a)** Simulated angular factor iopt for a thermal filter with λ_0 = 1300 nm (dashed line) and λ_0 = 1350 nm (line with cross markers). The trend of the filter with λ_0 = 1350 nm indicates a better optical performance. **(b)**Relative loss produced by a filter with λ_0 = 1300 nm compared to one with λ_0 = 1350 nm for different angles of incidence. Notice that the negative sign in Equation 4 transforms the calculated relative loss into a positive number for easier understanding.

Since simplicity is at the core of this work, a filter with λ_0 = 1350 nm was considered to be the best to provide a sensible combination of thermal and optical performance.

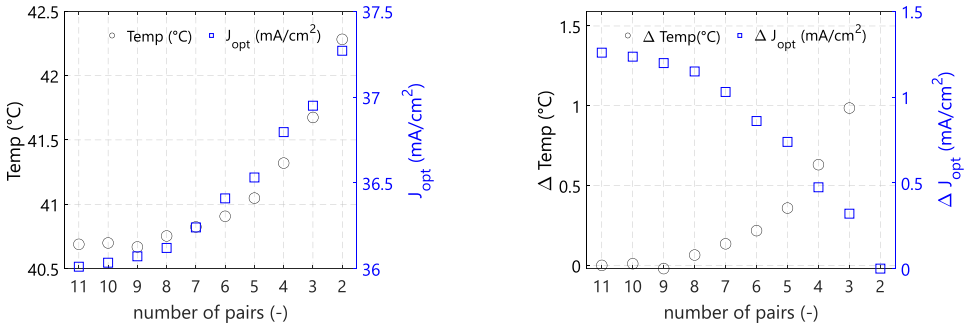

(a) (b)

Figure 5.9: **(a)** (right) Simulated optical current density in $mA \cdot cm^{-2}$ (under STC conditions) and (left) steady state temperature in °C (under NOCT conditions) as a function of the number of pairs for an optical filter with an λ_0 = 1350 nm. **(b)** (right) Differences in optical current density ($mA \cdot cm^{-2}$) with respect to the filter with the highest current density ($p = 2$). (left) Differences in steady-state temperature with respect to the filter that provides the lowest cell operating temperature ($p = 11$)

Optical losses are reduced by lowering the value of p. As with λ_0, the optimization involves a trade-off between optical loss and cooling improvement. Figure 5.9a shows how reducing the value of p affects both the optical current density J_{opt}, estimated at STC, and the steady-state solar cell temperature T_{cell}, estimated at NOCT. This difference in scenario (STC versus NOCT) was selected to optimize the optical effect produced by the different filter layouts separately, for the same value T_{cell}, and later study its effect on the steady-state temperature reached by the cell under the environmental conditions of

the NOCT scenario. The practical value of p was found by comparing the different values of p with the designs that provide the best performance in terms of J_{opt} ($p = 2$) and T_{cell} ($p = 11$). Figure 5.9b presents the trends obtained. Reducing the number of pairs to $p = 4$ causes a gain in the optical current density J_{opt} of 0.82 $mA \cdot cm^{-2}$ while increasing the value of T_{cell} by 0.55°C, compared to the best-performing designs mentioned above. Reducing the number of pairs decreases the optical loss depicted by λ_0. An additional strategy for reducing the optical loss consists of eliminating the ripples produced between the two main reflectance peaks. These ripples appear at wavelengths lower and higher than the central reflectance peak (determined by λ_0). They can be suppressed by placing layers with half QWOT at both ends of the filter. If the layer belongs to material H, the ripples for wavelengths greater than λ_0 are suppressed. In contrast, placing material L at each end eliminates the ripples below λ_0. The latter option is applied in this case. Figure 5.10a shows how going from an $(LH)^4$ design to a $0.5L|(HL)^3|H|0.5L$ design significantly eliminates ripple without significant effects on the reflectance peak at 450 nm.

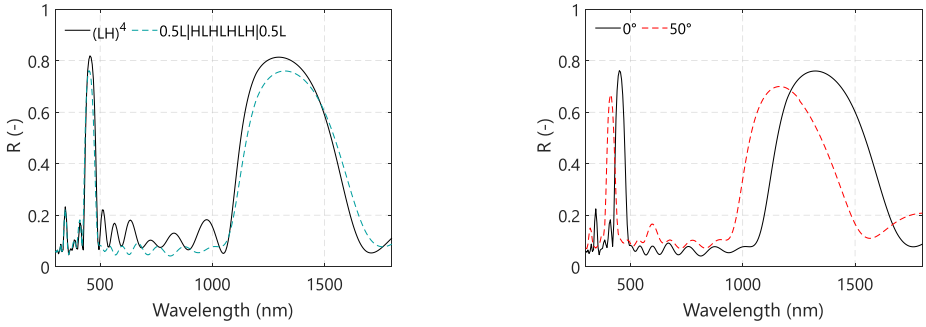

(a) (b)

Figure 5.10: **(a)** Reduction of ripples by changing the layout of the filter from $(LH)^4$ to $0.5L|(HL)^3|H|0.5L$. **(b)** Even though the ripple is substantially reduced, the angular behavior still presents shifts that produce significant optical losses on the PV module.

As presented in the case of the IR filter, it also represents an essential optical loss that needs optimization. The angular behavior of the simplified filter based on $0.5L|(HL)^3|H|\ 0.5L$ still presents important losses. Figure 5.10b shows the behavior of this filter at two dif-ferent angles of incidence, 0° and 50°. At 50°, the high reflectance peak shifts to lower wavelength values. For example, at 1000 nm, the filter presents a reflectance value of 0.4, which translates into substantial optical losses on the PV module. Notice that the results presented in both Figures 5.10a and 5.10b belong to an optical system of air|glass|filter|air. This simplified optical system is easier to optimize in OptiLayer®. OptiLayer® was used to improve the angular stability of the filter by using its second-order optimization algo-rithm, the so-called needle technique [204], [145], [208]. The main inputs for the deploy-ment of the needle technique are the initial filter design, the desired final reflectance, and, for each wavelength value of reflectance, the accepted tolerance in percentage. The selection of the target reflectance and the allowed tolerance per wavelength plays an im-portant role in the complexity of the filter design. Figure 5.11a gives an example of a potential reflectance target.

The target aims to eliminate the remaining ripples to fur-ther reduce optical losses while keeping both areas with high reflectance. The blue and green areas depict the upper and lower tolerance limits. These target and tolerance val-ues allow the algorithm to accept any value of reflectance that falls within the colored areas. However, with this target, the algorithm also forces the elimination of the small ripples. Reduction of these ripples will have a less significant impact on the incurred optical losses compared to the improvement of angular stability. Figure 5.11b presents a more appropriate reflectance target. The ripples are considered acceptable, and the effort in the optimization procedure focuses on a slight reduction of the reflectance at 450 nm (notice the difference between the blue and green areas, which forces the algorithm to reduce the peak) and to maintain angular stability. The target is fed into OptiLayer® as the same for normal incidence, 20° and 50°.

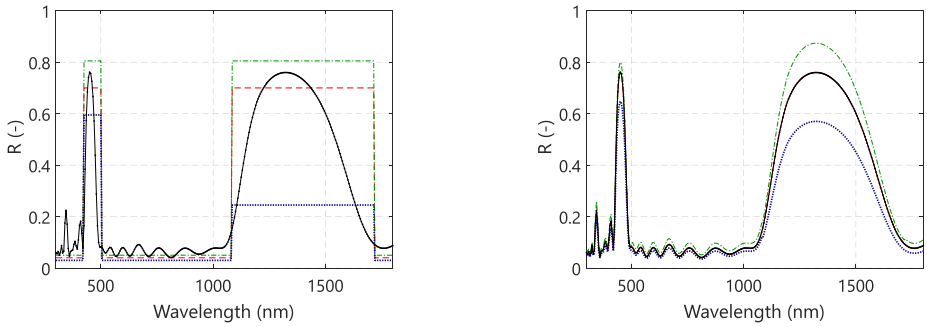

Figure 5.11: **(a)** Original reflectance (continuous dotted line), target reflectance (red dashed line), and tolerance ranges (delimited by the dash-dotted green and dotted blue lines) for a highly optimized filter design. Such strict target leads to highly complex and thick filter designs **(b)** A more practical approach is to use a target reflectance that mimics the reflectance behavior of the initial design and set tolerance limits to the algorithm that also follows the reflectance pattern. Acceptable losses from small ripples force the algorithm to focus mainly on reducing the peak at 450 nm and improving angular stability, keeping the design of the optical filter practical.

OptiLayer® has different options to automate the optimization process. An explanation of the different approaches can be found in the developer's work [204]. However, the automation process is extremely fast, allowing quick insertion of new layers. The filters obtained by this approach quickly reach a layer count that easily exceeds twenty layers. The aim of this work is to obtain filters that have a relatively low layer count. To achieve this, the layer insertion was done manually according to the value of a merit function [209]. The merit function estimates, according to the position where a new layer is added, if the resulting reflectance gets closer (negative value) or further (positive value) from the target. The resulting filter (hence referred to as a Thermal filter) consists of 15 layers with no repetitive thickness values. The main objective of the optimization was to improve the angular behavior while limiting the number of layers to a practical value. Easy manufacturing was deemed preferable to near-ideal optical behavior. For comparison, Figure 5.12b presents the reflectance profile of this thermal filter at the same angle

of incidence values as its base design once it is implemented in a PV module. Notice that at 1000 nm, the thermal filter has a reflectance value of 0.23, which reduces optical losses (comparing Figure 5.12a and Figure 5.12b). The trend depicted by the scaling factor i_{opt} of this thermal filter showcases the improvement with respect to the filter with $0.5L|(HL)^3|H|0.5L$. Moreover, the peak at 450 nm was reduced to improve the value of τ_0.

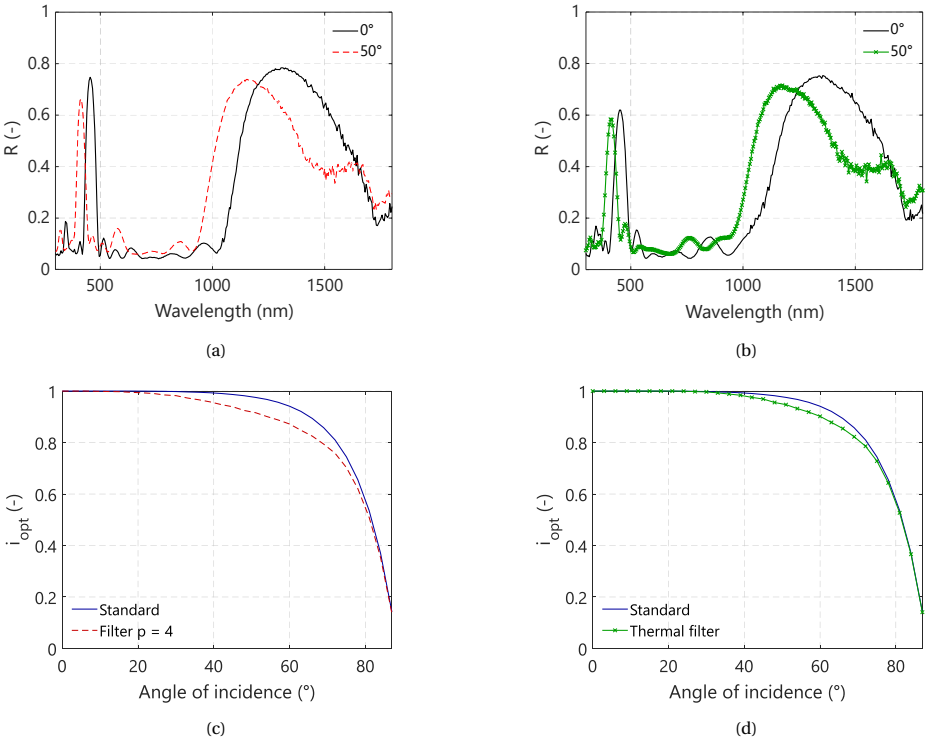

Figure 5.12: **(a)**Simulated reflectance at normal incidence and an angle of incidence equal to 50° for a filter with a $0.5L|(HL)^3|H|0.5L$ layout implemented on a full PV module. **(b)** Simulated reflectance of the improved thermal filter under the same angle of incidence conditions. Notice the reduced value of (R) at 1000 nm for the case of AOI = 50°. The optimization technique shifted the high reflectance zone towards higher wavelengths while keeping the peak at the desired value of 450 nm. **(c)** The simulated trend of the angular scaling factor iopt for the filter with $p = 4$ compared to a standard module without the filter. **(d)** The same trend simulated for the thermal filter highlights the results from the optimization process, reducing the gap with respect to the standard module

The optimization procedure increased the value of τ_0 from 0.80 to 0.85. An increased solar cell temperature follows this reduction of the optical loss at normal incidence. Simulations at NOCT predict that this increase amounts to 0.54 °C compared to the baseline design $(0.5L|(HL)^3|H|0.5L)$. The overall results from the simulations are presented in Table 5.2.

Filter $0.5L\|(HL)^3\|H\|0.5L$		Thermal filter	
τ_0 (-)	T_{cell} (°C)	τ_0 (-)	T_{cell} (°C)
0.80	41.32	0.85	41.86

Table 5.2: Simulated values of τ_0, estimated under STC conditions, and T_{cell}, estimated under NOCT conditions for the baseline filter design ($0.5L|(HL)^3|H|0.5L$) and the final thermal filter design after optimization (15 non-QWOT layers) via needle technique.

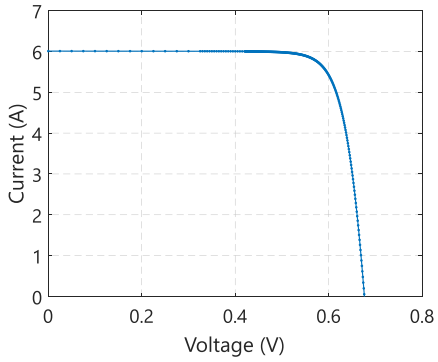

Figure 5.13: IV curve of a single encapsulated SunPower IBC solar cell utilized for the simulation work

5.3. EFFECT ON PV PERFORMANCE AND DEGRADATION RATE

A study of the overall effect of adding a thermal filter to a photovoltaic module was carried out by simulating the DC energy yield obtained from two modules, one with the thermal filter and a standard module. The chosen locations for the study were Delft (in the Netherlands) and Singapore City State. Weather data was extracted from the PVGIS database [210] for five consecutive years (2015 – 2020). The photovoltaic modules were set to their optimal tilt and azimuth for each location. The measured data obtained from the SunPower IBC solar cell was used to model the PV modules. The resulting curve of current (I) versus voltage (V) was obtained experimentally and is presented in Figure 5.13. Each module is considered to have 96 solar cells connected in series. Even though the IBC solar cells under test are bifacial, we consider that the transmitted light through them is lost. Therefore, current losses and the effect of the back sheet were not considered for the simulations. The total DC power was obtained by estimating the individual contribution of each cell, which operated under the same conditions. The data for the module under STC conditions are presented in Table 5.3. The temperature coefficients were taken from the data sheet published by SunPower for their Maxeon® Gen II solar cell.

The simulations had a time resolution of hours. Estimation of the hourly DC yield and operating cell temperature for each module was used to analyze the overall effect of the thermal filter implementation. The results show that thermal gain cannot compensate for the optical loss. In Delft, a PV module with a thermal filter presents a relative loss in DC energy yield compared to a standard module of 10.01%. The 98^{th} percentile

Parameter	Value
I_{SC} (A)	6.01
V_{OC} (V)	64.93
I_{MPP} (A)	5.71
V_{MPP} (V)	55.66
P_{max} (W)	317.82
$\delta V_{MOC}/\delta T$ (mV/°C)	-1.84
$\delta I_{SC}/\delta T$ (mA/°C)	2.60
$\delta P_{max}/\delta T$ (%/°C)	-0.35

Table 5.3: PV module parameters. The values belong to a module containing 96 solar cells without the thermal filter installed.

	Standard PV module			PV module + thermal filter			
	DC Yield (kWh)	$T_{cell}avg$	$T_{cell}max$	DC Yield (kWh)	$T_{cell}avg$	$T_{cell}max$	ΔT_{p98}
Delft, NL	1876.30	18.73	43.22	1688.40	17.91	41.02	2.20
Singapore	2749.80	36.11	51.83	2481.40	35.02	49.38	2.45

Table 5.4: Simulation results of the 5-year DC energy yield for two 96 IBC solar cell PV modules. One standard PV module and another with a thermal filter implemented beneath the front glass. Hourly simulations were run for five consecutive years using weather data from the PVGIS database.

value of the instantaneous temperature difference between the standard module and the thermal filter module was estimated at 2.20 °C. The estimated relative energy loss in Singapore was 9.76%, with a 98th percentile temperature difference of 2.45 °C. The module with the thermal filter presented maximum and mean values of T_{cell} lower than those obtained for the standard module. Table 5.4 presents the main results from the simulation work for both locations and modules. No degradation mechanism was taken into account at this first stage of the simulations.

To evaluate the yearly degradation rates/lifetime of the modules, a physics-based approach was used that considers various aspects that could influence the reliability of the photovoltaic modules [211]. In this approach, the electrical model is modeled as time and climate/stress factors (i.e., module temperature, relative humidity, UV dose) using the degradation rate and reliability models presented by Kaaya *et al.* [84]. The output of the degradation model is the time series of electrical parameters (power, short circuit current, open circuit voltage) with degradation. The five years of weather data were replicated to estimate the annual degradation rates of both locations (DR). The UV component was estimated to be a 5% fraction of the plane of array irradiance components obtained from the weather data. The calculated normalized performance ratio (PR) serves as the key performance indicator to determine the useful lifetime of a module. The limiting value is a normalized PR of 0.8. The time it takes a module to reach this limit is considered its useful lifetime (LT), expressed in years. The lifetime energy yield was defined as the total energy produced by the module until it reached the normalized PR limit. In the case of Singapore, the thermal filter increases the lifetime of the PV module by two years. A standard photovoltaic module reaches its limit in 22 years ($DR = 0.98\%/year$), while the thermal filter module does it in 24 years ($DR = 0.89\%/year$), as shown in

Figure 5.14a. During its lifetime, the standard photovoltaic module produces 8934.09 kWh. The PV module with the thermal filter produces 9212.85 kWh, representing a relative energy yield gain of 3.12%. This gain means that the net effect of the thermal filter on the DC energy production of a photovoltaic module, despite the initial optical loss, is ultimately positive. However, the benefits produced by the filter depend greatly on the location. For Delft, the benefits provided in terms of a lower annual degradation rate did not compensate for the initial optical loss. At this location, the lifetime energy yield of the standard PV module (9153.57 kWh) was greater than that of the PV module with thermal filter (8925.29 kWh). The lifetime of a standard PV module was estimated at 34 years ($DR = 0.57\%/year$). The thermal filter extended this lifetime to 35 years ($DR = 0.55\%/year$). Implementing a thermal filter will cause a relative loss in the energy yield of 2.49%. Figure 5.14b presents the trend of the renormalized power ratio (PR) for the Delft case for both PV modules. The overall results of the degradation study are presented in Table 5.5. The mean, maximum, and 98th percentile values of operational cell temperature used for the study are those presented in Table 5.4.

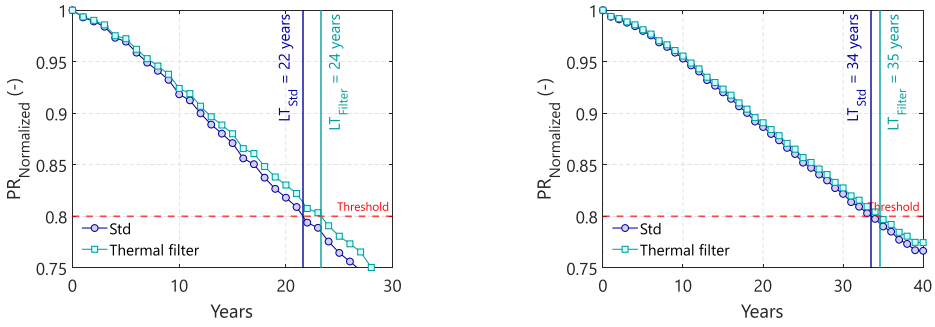

Figure 5.14: **(a)** Renormalized performance ratio (PR) of a standard PV module and a PV module with a thermal filter installed in Singapore.**(b)** The renormalized PR of both modules is located in Delft.

	Singapore		Delft	
	Standard	PV + T Filter	Standard	PV + T Filter
RH (%)	84.45	84.48	83.11	83.11
UV dose ($kWh \cdot a^{-1} \cdot m^{-2}$)	79.74	79.74	52.56	52.56
DR (%)	0.98	0.89	0.57	0.55
LifeTime (years)	22.00	24.00	34.00	35.00
DC lifetime (kWh)	8934.09	9212.85	9153.57	8925.29

Table 5.5: Simulated degradation rate results for a standard PV module and a PV module with a thermal filter. Values of ultraviolet light and relative humidity (RH) were extracted from the weather data. For the case of UV light, the values were estimated as a 5% fraction of the irradiance components.

5.4. OUTLOOK

The findings of this work indicate that the annual degradation rate may be the critical performance parameter of optimization. The main limitation of this work lies in the detachment of the different optimization algorithms, particularly the second-order optimization stage aimed at improving the angular stability while maintaining a simplified structure. Creating a single comprehensive modeling framework that includes this latter algorithm in the overall design would be desirable. The best approach to optimizing the benefit of the optical filter is to find a good balance between τ_0 and DR. τ_0 is proven to be the main driver of optical loss and an essential contributor to lower operational temperature. Therefore, an optimal thermal filter is one whose value of τ_0 optimizes DR such that the DC energy yield exceeds that of a standard module. Another important aspect of this work is the selected solar cell architecture. As stated before, the selected IBC solar cell has a specific behavior in the near-infrared wavelength range. Since most of the light at these wavelengths is being transmitted or reflected, the effect on the temperature produced by reflection in the near-IR range is rather limited. However, this is different for other c-Si solar cell architectures. In aluminum back-surface field solar cells (Al-BSF), for example, the contribution of sub-bandgap absorption losses can be significant [149], leading to operational solar cell temperatures higher than those of PERC architectures [206]. For Al-BSF cases, a practical design can be focused on producing rejection only on the sub-bandgap range. In general, creating a practical design is dependent on the target cell architecture. The findings produced in this work will be adapted to a wider range of commercially available solar cells in the future.

5.5. CONCLUSIONS

This work presented a practical approach to the design of an optical filter that provides passive thermal management to PV modules. The filter was tailored to an IBC solar cell architecture. It was proven that for this architecture, rejection of just IR radiation provides a limited level of thermal management and requires an extremely complex optical filter design. Therefore, another approach was proposed consisting of finding a wavelength range that ensures the best reduction of thermalization losses. The simulation framework indicated that a narrow rejection of light in a wavelength range of 400 to 500 nm provided the best cooling potential. It is demonstrated that a practical way to achieve this is to use the harmonic reflection peak created by an optical filter based on the QWOT approach with a design wavelength of λ_0 in the IR region. The optimization of the optical filter was done by finding, through simulations, the design that provided the lowest optical loss with a reasonable temperature reduction. From an initial design of 11 pairs (p) of SiO_2 $(L)|$ SiN_x (H), the value of λ_0 was changed from 1200 to 1600 nm. A value of λ_0 = 1350 nm was shown to provide the best trade-off. Later, the number of pairs p was optimized to a value of 4, reducing optical losses without significantly sacrificing the cooling potential. Angular stability was improved using the second-order optimization algorithm of OptiLayer, establishing the final number of layers as 15. Simulating the effect of the thermal filter on PV modules predicted a cooling potential of 2.20 °C for a module located in Delft, NL, and 2.45 °C for a module located in Singapore. If degradation effects are not taken into account, the implementation of a thermal filter in a

photovoltaic module translates into a loss of DC energy yield. For Delft, the relative loss of DC energy yield was found to be 10.01%, while for Singapore, this value was estimated at 9.76%. The optical losses are not compensated for by the cooling provided to the PV module.

However, in terms of long-term reliability, the thermal filter extended the lifetime of a photovoltaic module by two years in Singapore and one year in Delft. Taking into account the degradation effects, the extended lifetime provided by the thermal filter in Singapore yields an overall positive result in terms of DC energy yield in both scenarios, with relative gains of 3.12%. The benefit provided by the filter is location dependent, as the overall effect of Delft was still negative, with a relative loss in the lifetime energy yield of 2.49%. Further improvements will be studied in later stages, but this solution ensures reliability and energy yield benefits in hot climates.

5.6. EXPERIMENTAL WORK AND MODEL VALIDATION

A test filter was manufactured by plasma-enhanced chemical vapor deposition (PECVD) with a flat glass as the substrate. The size of the glass was 15 cm by 15 cm. The details of the filter layout are found in Figure 5.15a. The coated glass was measured with the filter located on the backside (see Figure 5.15b). The predicted reflectance and the measured reflectance were compared to estimate the error of the optical model. The metrics used to estimate accuracy were the mean bias error (MBE), the mean absolute error (MAE), and the root mean square error (RMSE).

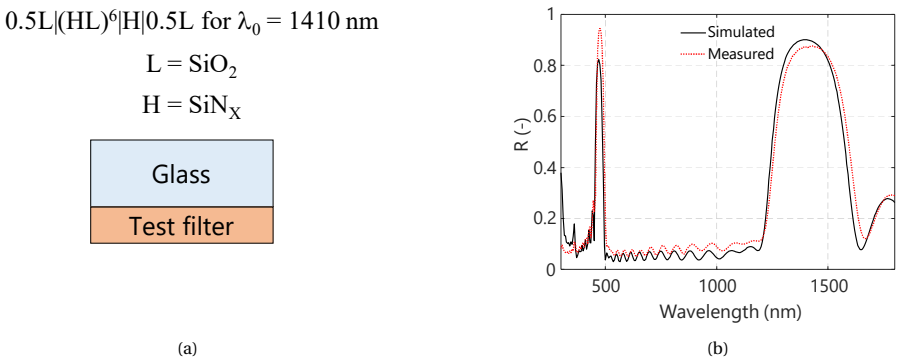

Figure 5.15: **(a)** Schematic of the test filter manufactured for the experimental study**(b)** Validation of the optical model of the test filter.

Table 5.6 presents the results of the validation procedure. The coated glass was then used as the top layer of a mini-PV module. The module consisted of an encapsulated SunPower Gen II solar cell. Another mini-module, without the thermal filter, was manufactured for comparison. Electrical measurements of both mini-modules were carried out under an AAA solar simulator under STC conditions, obtaining IV curves for both samples. The parameters for the electrical simulations were extracted using the equiva-

	Test filter
MAE	4.25%
MBE	1.49%
RMSE	6.59%

Table 5.6: MAE, MBE, and RMSE values for the assessment of the optical model accuracy.

lent circuit calculator from PV Lighthouse [152]. The ratio between the measured short circuit current from the mini-module with the filter with respect to its counterpart without the filter was used to scale down the irradiance value of the two-diode electrical model. The results show that this approach is very accurate in predicting the effect of the filter on the electrical performance of the mini-module, as shown in Figure 5.16a. The precision of the electrical model was evaluated by comparing the current values of the generated IV curve using the two-diode model with the measured values, producing an RMSE value of 0.05 A, as presented in Table 5.7.

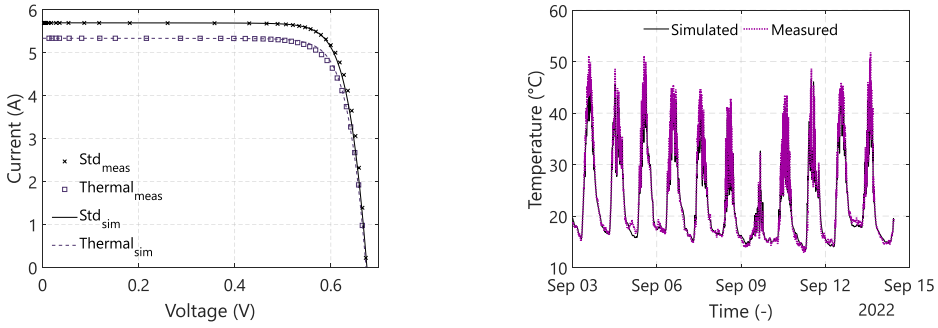

Figure 5.16: **(a)** Validation of the electrical model for a standard mini-module and a mini-module with a thermal filter **(b)** Thermal model validation for 11 consecutive days of measurements of the mini-module equipped with the thermal filter with a time resolution of 10 seconds.

After electrical measurements, both modules were taken for outdoor temperature measurements. The measurements were carried out for eleven consecutive days. A single T-type thermocouple was placed at the backside of each mini-module, and temperature measurements were taken every ten seconds. Both modules were in V_{OC} conditions. The evaluation of the thermal model shows that the predicted operating module temperature (backside value) was in very good agreement with the backside measurement, as shown in Figure 5.16b.

The model predicts the temperature of the backside of a mini-module with a thermal filter with an RMSE value of 1.44 °C for the entire range of measured values, as shown in Table 5.7. The time resolution for this simulation was twenty seconds to synchronize the temperature data with the measured irradiance data. The application of the thermal model for the case of the standard module produces slightly lower values of MAE, MBE, and RMSE. Figure 5.17a shows the measured and simulated values for the entire

	Electrical Model	Thermal model Standard	Thermal model Filter
MAE	0.03 A	0.87 °C	1.00 °C
MBE	0.01 A	0.34 °C	0.73 °C
RMSE	0.05 A	1.22 °C	1.44 °C

Table 5.7: Accuracy assessment of the electrical and thermal models used in this work for simulating the thermo-electrical performance of our mini modules. Numbers in the table refer to the case of a mini-module endowed with the thermal filter.

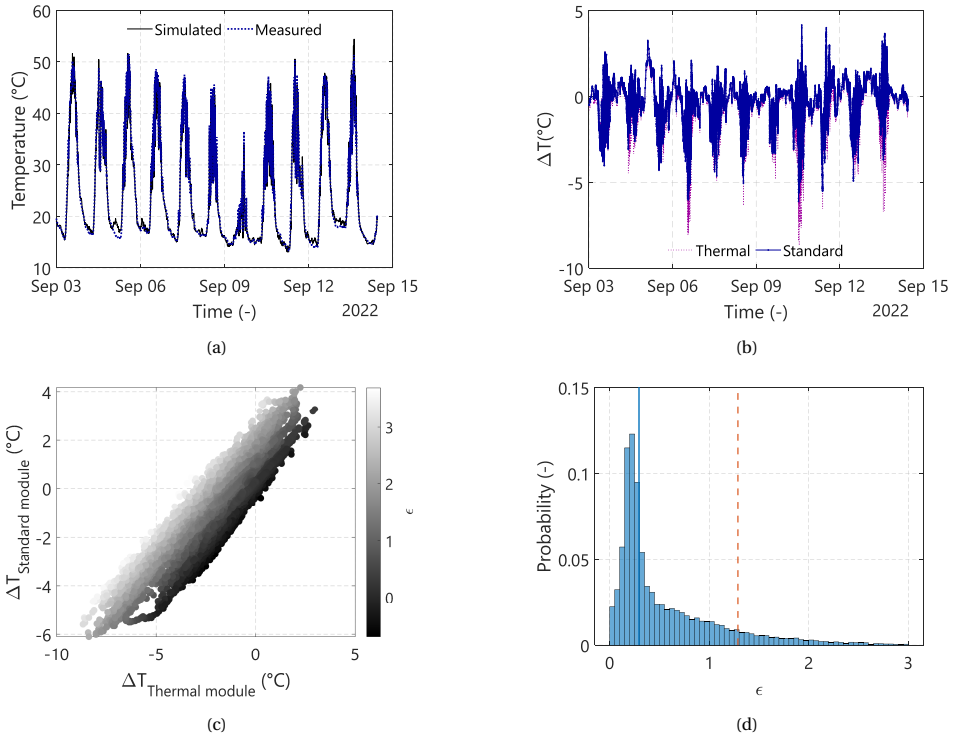

Figure 5.17: **(a)** Thermal model validation for the case of the standard mini-module for the same period of time and time resolution of the validation presented in Figure 5.16b. **(b)** Trends of the difference between the measured value and the predicted value for both mini modules. The trend observed is identical for both mini modules. **(c)** The analysis of the scatter plot of the parameter ϵ shows a strong correlation of the error between both mini modules, indicating that infrequent high discrepancies occur in both models. **(d)** Probability histogram of ϵ, showcasing only a marginal difference in the errors obtained on both simulations

measurement range for this latter case. The difference between these error values for both validations falls within the uncertainty of the measurement sensor (±0.5 °C). However, the values presented in Table 5.7, are calculated for the entire range of measurements. Analysis of the potential effect on model accuracy of the spectral approach is done by comparing the differences between the prediction of the standard mini-module and the mini-module with the implemented thermal filter. First, the difference between

the measured value and the simulated value for each case is defined as follows:

$$\Delta T_{module} = T_{measured} - T_{simulated} \tag{5.6}$$

Figure 5.17b shows the same trend for both mini-modules. However, there are differences in the values of ΔT, which sometimes present higher values for the case of the mini-module with the implemented thermal filter. Estimation of a new parameter, ϵ, defined by Equation 5.7, enables further analysis:

$$\epsilon = \Delta T_{standard} - \Delta T_{thermal} \tag{5.7}$$

Figure 5.17c indicates that, even though, on occasion, the value of ϵ is greater in the thermal model, the error trend strongly correlates with the error of the standard module. This correlation signifies that a potential error in the model affects both the thermal mini-module and the standard mini-module equally.

The probability histogram of ϵ, presented in Figure 5.17d, indicates only a marginal deviation of ϵ with a median value of 0.29 °C (solid blue line in Figure 5.17d) and a 90th percentile value of 1.29 °C (red dashed line). Therefore, it is unlikely that the infrequent differences in values of $\Delta T_{thermal}$ are related to the spectral thermal model.

6

THERMAL CONTROL: PHASE-CHANGE MATERIALS

This chapter is partially based on the following publication:

J.C. Ortiz Lizcano[1], H. Ziar, C. de Mooij, M.P.F Verheijen, C.v. Nierop & Sanchez, D. Ferlito, C. Connelli, A. Canino, M. Zeman, O. Isabella *Long-term experimental testing of phase change materials as cooling devices for photovoltaic modules*, Solar Energy Materials and Solar Cells, **277**, 113133 (2024).

This chapter presents the results of an experimental, interannual, and long-term study conducted at multiple locations. It studies the effects of phase change materials (PCMs) on the performance of photovoltaic modules by reducing their operational temperature. Two PV modules were manufactured so that the PCM slabs could be mechanically attached to their backside, ensuring contact with the related photovoltaic active area. The experiments were carried out in Delft, The Netherlands, from 2019 to 2021 and in Catania, Italy, during winter and the start of spring in 2023. The experiment also considered two installation layouts: building integrated (Delft) and standard rack-mounted (Catania). The measurements showed that PCM provides significant cooling in both locations, with a temperature reduction of up to 15 °C. In Delft, thermal control could be obtained for most of the sunny hours of the day, even during the summer months. In Catania, the PCM module occasionally showed higher temperatures than its standard counterpart, mainly because of winter-time environmental conditions. However, the PCM provided sufficient thermal control under all conditions, ensuring a higher energy yield. This increase ranged from 2.1 to 2.5% in Delft and from 1.3 to 1.6% in Italy.

[1] Candidate's contribution: Writing, coding work, experimental work, results analysis

6.1. INTRODUCTION

As discussed in Section 2.2 Thermal management is essential for photovoltaic system operation and maintenance. Heat generation in photovoltaic devices represents a significant loss in electrical efficiency. Moreover, high operating temperatures can also contribute to a significant reduction in the lifetime of photovoltaic modules [84]. The operating temperature of a module depends on multiple factors in addition to the environmental conditions under which they operate. The installation layout, for example, can reduce the cooling capacity of a photovoltaic module, particularly by affecting the convection mechanisms. This is the case of a photovoltaic module integrated into the building environment, where reduced convection leads to significant temperature increases compared to the same module operating on a rack-mounted layout [26]. Section 2.2 also summarized the technological developments aimed at reducing the operating temperature of PV modules that are frequently classified into passive techniques, such as spectral management [97], [205], [207] and active technologies [212].

Section 2.2.2 presented an overview of the different research efforts focused on using phase change materials (PCMs) as cooling devices and their potential application in photovoltaic systems. Given their potential to reduce the operational temperature of photovoltaic modules by tenths of degrees, they are considered one of the most promising solutions available.

The physical principles governing the way PCM acts as cooling devices are depicted in Figure 6.1.

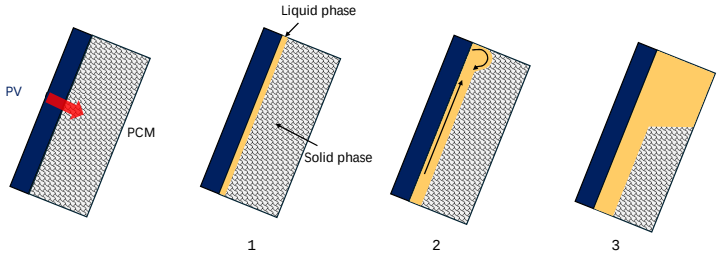

Figure 6.1: Physical mechanisms involved during the melting of a PCM: **1** Initial melting phase, governed by conduction. **2** Increased melting speed governed by natural convection which slows down as the PCM enters **3** the shrinking solid regime.

Once the PCM is mechanically attached to the backside of the photovoltaic module, the heat produced travels through the polymer encapsulation to the salt hydrate, which is in the solid phase. The initial heat transfer governing mechanism is conduction. A thin layer of solid PCM increases its temperature until it reaches its melting temperature (see **1** on Figure 6.1), and then the charge phase changes begin [213]. As PCM melts, the viscous forces begin to be surpassed by buoyancy forces [214], and a combination of conduction and convection governs heat transfer. The liquified PCM starts flowing, as the liquid phase of the PCM has a lower density than the solid phase, so the flow drifts upwards. Once the flow hits the upper surface of the casing, it is then directed to the boundary interface between the two phases, increasing the melting rate by creating convection cells (**2** on Figure 6.1). Under these conditions, the governing heat transfer

mechanism is natural convection. As the PCM melting fraction increases, the melting rate decreases, and the process enters the shrinking solid regime [215] (**3** on Figure 6.1).

Once the melting fraction reaches near unity, the thermal energy of the PV panel is stored in the liquid PCM as sensible heat [216]. Solidification occurs when heat begins to be extracted from the PCM because of cooling of the photovoltaic panel and reduction of the environmental temperature. During solidification, the governing heat transfer mechanism is almost exclusively conduction, since the thermal conductivity of the solid phase is higher than that of the liquid phase [217], [218], [219].

The time it takes to fully melt the PCM is dependent on many factors. The nature of the PCM itself, for example, determines its thermal conductivity, cinematic viscosity, and thermal diffusivity, and hence its Prandtl number. In materials with a high Prandtl number, the melting is limited by thermal transport, whereas in those with a low Prandtl number, the melting process is limited by their mass transport [214]. Furthermore, the geometry, orientation, and tilt angle also impact the time required to fully melt the material. For rectangular casings, decreasing the angle of tilt from fully vertical (90 °) to fully horizontal (0 °) increases the time it takes to melt the PCM [220], [221] . Likewise, the presence of internal fins [133], [222] and the addition of nanoparticles [223] can speed up the melting process by increasing heat transfer.

6.2. EXPERIMENTAL OVERVIEW

6.2.1. PHASE CHANGE MATERIAL SELECTION

The experimental works mentioned in section 2.2.2 of this document are usually limited to days up to a maximum of a year (in a single reported work) or indoor tests. No works study a multiannual multiple location test of a single type of PCM under different installation layouts. This work aims to provide insight into how a single type of PCM can provide cooling to PV modules working under the conditions of a BIPV system and a standard rack-mounted system in two climates. For the BIPV layout, the selected location was Delft in the Netherlands. This location has a moderate annual global horizontal irradiance of 2.95 kWh/m2 per day and an annual average ambient temperature of 10.8 °C [189]. BIPV systems are more likely to have operational temperatures that are higher than those of their rack-mounted counterparts in this location. Thus, cooling options are an attractive approach to BIPV systems. For the standard rack-mounted layout, the selected location was Catania, Italy. The location has a significantly higher average annual global horizontal irradiance of 4.82 kWh/m^2 per day and a higher annual average ambient temperature of 17.9 °C [189]. Here, the higher solar resource means that PCMs are attractive in potentially increasing large power plant yields. Furthermore, the data collected from both layouts is valuable for future modeling efforts.

The selected PCM compound was calcium chloride hexahydrate, the slabs have references CSP1900/CSP1575, which contain the same compound and melting temperature, but differ in case size. The numbers indicate the width of the casing; thus, CSP1575 is 15.75 cm wide and CSP1900 is 19 cm wide. These sizes were selected to fit the active area of the manufactured PV modules, as will be explained later. The main properties of the substance can be found in Table 6.1. The selected melting temperature of this PCM is 26 °C, with the purpose of testing if, under changing environmental conditions,

Figure 6.2: Selected Phase change material (PCM) encapsulated in a crystal storage panel made of high-density polyethylene. The panel is divided into 6 sections to avoid mixture separation

Property	Value
Dimensions (mm)	$(2 \cdot 157.5 + 190) \cdot 570 \cdot 13$
Type of filling	$CaCl_2$-6H_2O
Mass (kg)	1.8
Density ($kg \cdot dm^{-3}$)	1000
Melting temperature (°C)	26
Latent heat ($kJ \cdot kg^{-1}$)	310
Thermal conductivity (W/mK)	1.0
Kinematic viscosity (m^2/s)	$9.6 \cdot 10^6$
Thickness* (mm)	0.6
Heat transfer coefficient* (W/mK)	0.5

Table 6.1: Physical and thermal properties of the selected PCM (taken from [225]).*Indicates the values belong to the *casing* of the phase change material slab

the PV module could be (temperature-wise) controlled to perform close to standard test conditions (STC). The mixture is liquid and contained in a polymer casing in the shape of slabs with several grooves to avoid premature separation of the mixture, thus increasing the useful life of the PCM. The manufacturer of the PCM is Orange Climate Autarkis [224].

6.2.2. MODULE MANUFACTURING AND PCM INTEGRATION

To provide efficient thermal management to a PV module endowed with a PCM, the entire active area of the module must be in contact with the selected PCM. The manufacturing of two small photovoltaic modules followed the above-mentioned condition. Each module consists of sixteen IBC SunPower Maxeon^{TM} Gen II solar cells [194] connected in series. The encapsulation materials were a 60 cm x 60 cm PV glass sheet, 0.5 cm thick ethyl vinyl acrylate (EVA) and a 0.3 cm thick black PET back sheet. The complete layout of the module and the manufactured device is presented in Figure 6.3

To ensure that differences measured within the field experiments are due to the PCM, the current-voltage (IV) curves of both modules were characterized using a class AAA large area steady state solar simulator (LASS). In addition, electroluminescence (EL) tests were performed to verify the quality of manufacturing, thus avoiding potential unex-

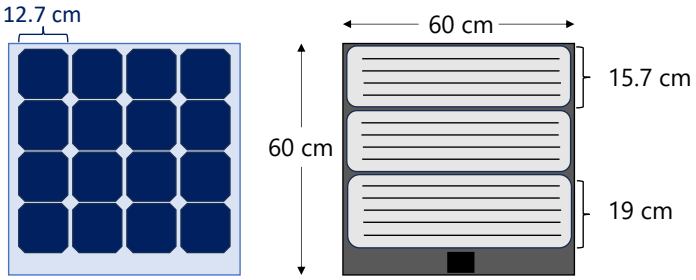

Figure 6.3: Layout of the manufactured PV module to ensure that the PCM slabs can be in contact with the entire active area of the PV module to secure optimal cooling: (left) front and (right) rear view of the PV-PCM module.

pected performance differences due to interconnection issues or cracks that could get worse as the module runs continuously. The result of the former is presented in Figure 6.4; while the latter can be found in the appendix 9. The electrical performance of both modules was found to be almost identical, with differences in power production under standard test conditions of 0.2%. The EL test showed that none of the modules had manufacturing differences that could produce different performance behaviors.

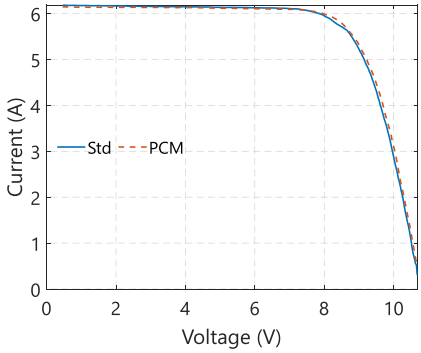

Figure 6.4: IV curves of the PV modules manufactured based on 16 IBC Maxeon Gen II solar cells connected in series.

Parameter	Standard	PCM
V_{OC} (V)	10.80	10.70
I_{SC} (V)	6.05	5.95
P_{mpp} (V)	48.70	48.60
η (%)	19.90	19.80

Table 6.2: Electrical parameters of the manufactured PV modules

For temperature measurement, 21 T-type thermocouples from RS components were calibrated by placing them inside an insulated chamber that was heated to a value of 27 °C. Seven selected thermocouples were attached to each module using 3M^{TM} thermally conductive adhesive transfer tape (8805); six of them were located behind selected solar cells and the seventh was placed close to the junction box. The selected distribution of the temperature sensors is shown in Figure 6.5a. The manufactured aluminum frames provided the mounting of the modules on the monitoring rack and the mounting of the PCM slabs to the back of the photovoltaic module, as shown in Figure 6.5a.

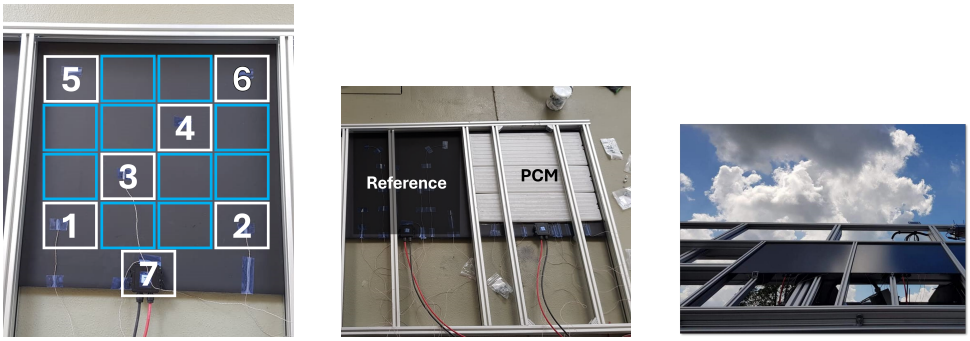

(a) (b) (c)

Figure 6.5: **(a)** Placement of the thermocouples on each of the manufactured modules; each square represents a solar cell within the PV module. The 7 thermocouples were attached using thermal tape. **(b)** The use of a tailored-made aluminum frame allowed mechanically attaching the PCM slabs on the backside of the PV module. **(c)** Both PV modules were installed on a fixed rack, oriented south, with a tilt angle of 35°. For clarity, in picture (c), cells 5 and 6 are the furthest from the base of the mounting rack.

6.2.3. EXPERIMENTAL WORK CARRIED OUT IN DELFT, NETHERLANDS

Both modules were mounted on a measurement rack located at the Delft University of Technology monitoring station (see Figure 6.5c). The premises are equipped with two measuring racks, a dual-axis tracking rack, and a manual rack that allows the selection of any desired azimuth for a fixed tilt. The latter was selected for experimental work. The rack has a 35° tilt and was oriented towards the south. Once the PCM slabs were mechanically attached to the backside of the PV module, a 19 mm thick Armaflex^{R} slab was adhered to each module, simulating an insulating backside condition frequently encountered in integrated building solutions. Temperature measurements were recorded using a Picolog^{R} datalogger and a Raspberry Pi device at 30-second intervals from July 2019 to February 2020. Electrical parameters were monitored and stored from July 2019 until August 2021. Other environmental parameters measured were ambient temperature, wind speed, global horizontal, diffuse horizontal, and direct normal irradiances (GHI, DHI and DNI, respectively). Table 6.3 provides information on the variables measured, related instruments, technical characteristics and uncertainty U of the measurements. For the case of the measured electrical power, the uncertainty is estimated using the following equation.

$$U_P = \sqrt{U_{Impp}^2 + U_{Vmpp}^2} \tag{6.1}$$

The measured data was initially filtered with a resolution of five minutes since the instruments could have differences in the time at which their respective measurement was recorded. Furthermore, potential outliers and erroneous data were filtered out by using a two-diode model of the selected PV modules. The measured values of plane of array irradiance (G_{POA}) and the module temperature (T_{PV}) were used as inputs for this model and then compared to the electrical parameters measured for the two PV modules. Any large deviation was considered an outlier and eliminated from the data. More details on this procedure can be found in Section 6.6. In total, 30% of the raw data measured during 2019 was filtered, 24% for the case of the data measured during 2020 and 15% from the one measured during 2021. Figures 6.6a to 6.6c present the results for both the standard photovoltaic module (blue circles) and the photovoltaic module with PCM slabs (orange squares). The data presented belong to measurements where the value of G_{POA} was greater than 20 $W \cdot m^{-2}$. The power correlates with the value of G_{POA} linearly with almost no outliers, indicating a good quality in the selected data.

Variable	Unit	Resolution	Uncertainty
Plane of array irradiance (G_{POA})	W/m^2	7.63 $\mu V/W/m^2$	$\pm 10\ \mu V$
DHI,GHI,DNI	W/m^2	7-14 $\mu V/W/m^2$	$\pm 7\ W/m^2$
V_{OC}, I_{SC}	V, A	3.8 mV, 15.2 μA	$\pm 0.1\ mV$, $\pm 0.2 \mu A$
PV temperature (T_{PV})	°C	0.01°C	±0.5°C or 0.4%
Wind speed (W_s)	m/s	0.1 m/s	$\pm 0.5\ m/s$
Ambient temperature (T_{amb})	°C	0.01°C	±0.5°C
MPPT Voltage	V	20 mV (0-81.9 V)	$\pm$ 0.1 mV, $\pm 0.2\ \mu A$
MPPT Current	A	2.5 mA (0-10.2 A)	
Max. module Power	W	Up to 300 W	$\pm 1 mW$

Table 6.3: Measured variables at the monitoring station in Delft, Netherlands. Irradiance on the plane of the array (G_{POA}), PV performance parameters and measurement of other environmental parameters were carried out using the LPVO MP1010F-1 [226] PV monitoring system. GHI, DHI, and DNI were measured using a Kipp & Zonen SOLYS2 [227] using SMP21 pyranometers and a SHP1 pyrheliometer. Thermocouples were RS PRO type T.The value of power is obtained from the multiplication of the maximum power point current and voltage. The uncertainty is estimated using equation 6.1

6.2.4. EXPERIMENTAL WORK CARRIED OUT AT CATANIA, ITALY

The experimental activities in Delft were finalized in August 2021, and the photovoltaic modules were removed from the monitoring station and characterized under the same LASS equipment used the previous time. EL imaging allowed inspection of potential damage from long-term activities. The results of these new measurements showed electrical parameters almost identical to those of the initial measurement. Furthermore, the EL images obtained showed that no damage was incurred during the testing period. Details of these tests are presented in the appendix 9.

The modules were shipped to ENEL facilities, located in Catania, Italy, at the end of September 2022. Figures 6.7a to 6.7c present photographs of the final setup.

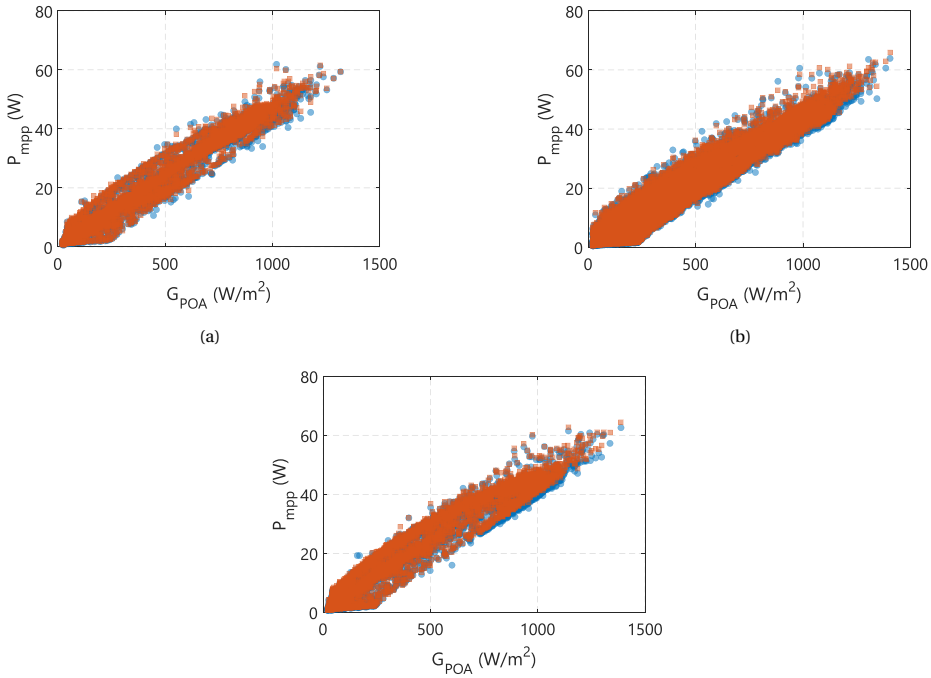

Figure 6.6: Measured instantaneous DC power related to the measured GPOA for the standard module (blue points) and the PV-PCM module (orange squares) in Delft for the period **(a)** 2019 (3908 data points), **(b)** 2020 (11719 data points) and **(c)** 2021 (36465 data points). All graphs present the final data after the elimination of outliers and desynchronized data that could potentially produce biases in the analysis. Additionally, the data presented here was compared to the resulting current, voltage, and power from a two-diode model to ensure good quality (see Table 6.5 and Section 6.6 for more information

Figure 6.7: Photographs of the installed PV modules at the facilities of ENEL, in Catania, Italy: **(a)** side by side view, with the PV-PCM module is on the right-hand side. **(b)** PV module rear view, and. **(c)** PV-PCM module rear view. The backside of the modules in this location was not insulated during the tests

The variables measured in the facilities are summarized in Table 6.4. The activities were carried out continuously from January until May 2023.

Variable	Unit	Resolution	Uncertainty
Plane of array irradiance (G_{POA})	W/m^2	8.5 $\mu V/W/m^2$	$\pm 10\ \mu V$
MPPT Voltage	V	1.0 mV	$\pm 0.025\ mV$
MPPT Current	A	1.0 mA	$\pm 0.1\ mA$
MPPT Power	W	-	$\pm 2.7 mW$
PV temperature (T_{PV})	°C	0.01 °C	±0.4 °C
Wind speed (W_s)	m/s	0.01 m/s	$\pm 0.4\ m/s$
Ambient temperature (T_{amb})	°C	0.01 °c	±0.4 °C

Table 6.4: Measured variables at Enel Facilities in Catania, Italy. The value of power is obtained from the multiplication of the maximum power point current and voltage. The uncertainty is estimated using equation 6.1

As in the case of the experiment in Delft, the data collected at ENEL facilities was filtered using a linear relationship between the value of G_{POA} and the maximum power point current (I_{mpp}), and a two-diode model to compare the power measurements. The data resulting used for the analysis is shown in Figure 6.8a for the case of the maximum power point current, and Figure 6.8b for the maximum power point voltage for both modules. In total, in Catania, 13550 data points were used for analysis, which represents nearly 1220 hours of operation from January to May 2023.

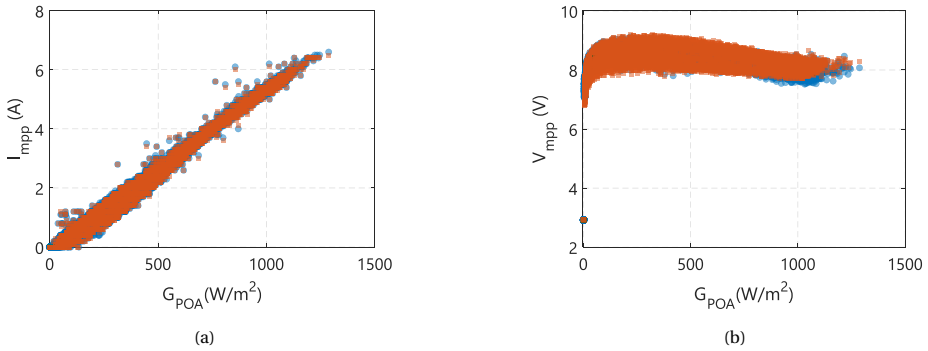

Figure 6.8: Measured (blue points) and filtered (orange points) data with respect to the measured GPOA for the tests carried out in Catania, Italy: **(a)** maximum power point current (I_{mpp}) and **(b)** maximum power point voltage (V_{mpp}).

6.3. EXPERIMENTAL RESULTS

The experiments carried out at both locations had differences in their installation layout due to the environmental conditions of each location. In addition, the number of measured variables was not the same due to technical differences between the facilities. The results of the measurements are therefore presented in two separate sections. Firstly, (i) the cooling that can be provided to a PV module by mechanically attaching PCM slabs at both locations, as well as (ii) the effect on it due to the environmental conditions and the installation layout of the PV module. Secondly, the effect on the electrical performance

for each case.

6.3.1. COOLING POTENTIAL PROVIDED TO THE PV MODULE BY THE PHASE CHANGE MATERIAL UNDER DIFFERENT ENVIRONMENTAL CONDITIONS AND INSTALLATION LAYOUTS

DELFT - PHOTOVOLTAIC MODULES WITH INSULATED BACKSIDE

Temperature measurements carried out in Delft consisted of monitoring the values sensed by T-Type thermocouples behind the six chosen solar cells, as shown in Figure 6.5a. The purpose of this placement is to analyze whether a homogeneous temperature profile could be obtained in the photovoltaic module by mechanically attaching the PCM slabs. The temperature data was recorded from July 2019 to February 2020. Due to a technical failure of the temperature measurement setup, from that point onward, it was only possible to monitor electrical parameters. The construction of temperature profiles for each module allows us to analyze the extent to which the PCM slabs can provide thermal management across the cells within the module. The profiles shown below correspond to the moment at which, each month, the standard photovoltaic module reaches its highest temperature. For the sake of brevity, only the profiles measured during the two warmest months are displayed in this document.

Figure 6.9a presents the temperature profile of the standard PV module during the month of July 2019. The highest recorded temperature value in this month was 78.69 °C in cell 3 (see Figure 6.5a for reference). The remaining cells had temperature values no lower than 73.53 °C (cell 2). In general, the highest temperature difference between cells within standard PV was 5.16 °C. At the same time, the PV-PCM module had a temperature profile as shown in Figure 6.9b. The outer cells (1, 2, 5 and 6) registered temperatures substantially lower than their counterparts in the standard module, with the largest difference measured at cell 5, 9.62 °C. However, the cells in the middle (3, 4), had a higher temperature value compared to 1, 2 5 and 6. Cell 4 had a temperature difference of only 0.77 °C compared to the same cell in the standard module, very close to the uncertainty of the thermocouple (± 0.5 °C), while cell 3 had a difference with respect to its counterpart in the standard PV module of 5.37 °C. Possible reasons for this inhomogeneity are explained in the next section.

Figures 6.10a and 6.10b present the same difference in the temperature profile for both modules at the highest recorded temperature in the standard photovoltaic module during the month of October 2019. For the case of the standard PV module (Figure 6.10a), the temperature profile follows the same pattern as for the month of July, with cell 3 presenting the highest value (52.72 °C) and cell 2 the lowest (48.16 °C), which means a maximum temperature difference between cells of 4.56 °C.

Figure 6.10b presents the temperature profile of the PV module with attached PCM slabs. At this moment in October 2019, the behavior of the PV module remains consistent with that of July. The outer cells present the lowest measured temperatures, whereas those in the middle registered the highest values. The difference between the warmest cell (cell 4 with 42.51 °C) and the coldest cell (cell 6 with 35.49 °C) in this month at this time is 7.02 °C, which is consistent with the difference observed during July (6.83 °C). The PV module with PCM attached always presents the largest gradient in its temperature profile, with cells 3 and 4 consistently being the warmest.

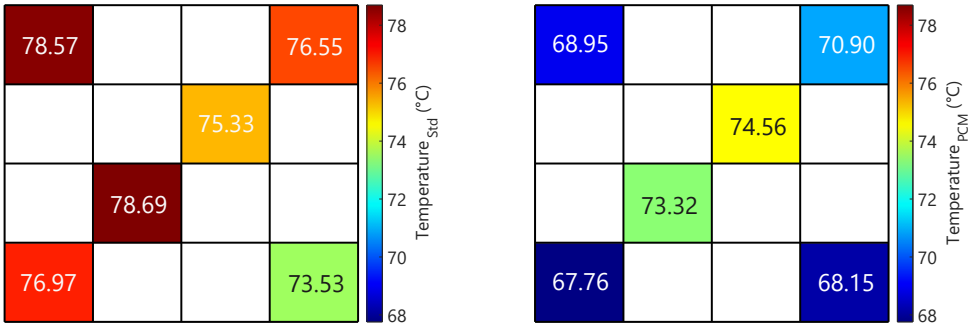

(a) (b)

Figure 6.9: **(a)** Temperature profile of a standard PV module at the highest value of temperature recorded during July 2019 in Delft. The squares describe the solar cell within the module following the same distribution and numbering presented in Figure 6.5a. The largest difference between the measured temperatures for this module was 5.16 °C. **(b)** Temperature profile of a PV module endowed with PCM slabs mechanically attached to its backside (PV-PCM module) for the same period as the case of **(a)**. The largest difference between the values of the measured temperatures in this case was 6.83 °C. The limits for the color graph were selected based on the lowest value of temperature recorded on **(b)** and the highest value recorded on **(a)**.

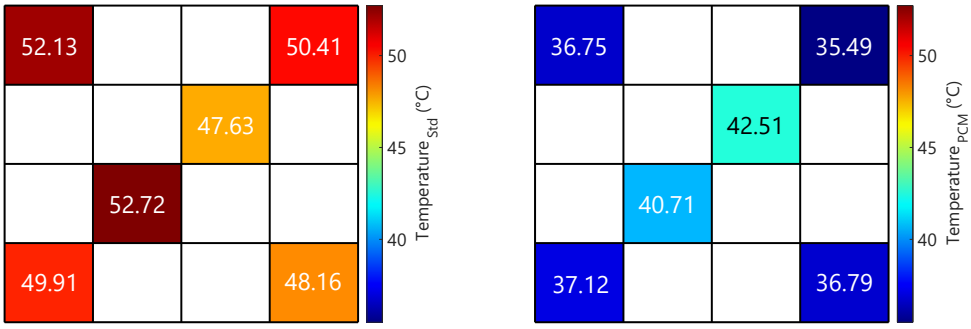

(a) (b)

Figure 6.10: **(a)** Temperature profile of a standard PV module at the highest value of temperature recorded during October 2019 in Delft. The squares describe the solar cell within the module following the same distribution and numbering presented in Figure 6.5a. The largest difference between the measured temperatures for this module was 4.56 °C. **(b)** Temperature profile of the PV-PCM module for the same period as the case of **(a)**. The largest difference between the values of the measured temperatures in this case was 7.02 °C. The limits for the color graph were selected based on the lowest value of temperature recorded on **(b)** and the highest value recorded on **(a)**.

The comparison between the profiles presented in Figures 6.10a and 6.10b indicates that the PCM slabs can provide substantial thermal control of the PV module. Cells 5 and 6 present temperature reductions of 14.92 °C and 15.38 °C, respectively. The figures presented above only show the moment when the standard photovoltaic module reaches its highest temperature. The behavior of both modules during these days is shown in Figure 6.11a and Figure 6.12a for July 2019 and October 2019, respectively, which depict the average temperature (mean measured value of cells 1 - 6) per hour. During the 30th

of July, the PCM slabs managed to reduce the average temperature of the PV module until 16:00 hours compared to the standard case. After 17:00 hours, the lowering of the ambient temperature and the irradiance cooled both modules. However, since the PCM slab presented the phase change (solid-to-liquid), the reverse process released the stored heat, which in turn heated the PV module, as seen later that day around 19:00 hours. During October 17th, the PCM slabs provided more consistent thermal management and the PV module with the attached slabs only showed higher operational temperatures after 17:00 hours.

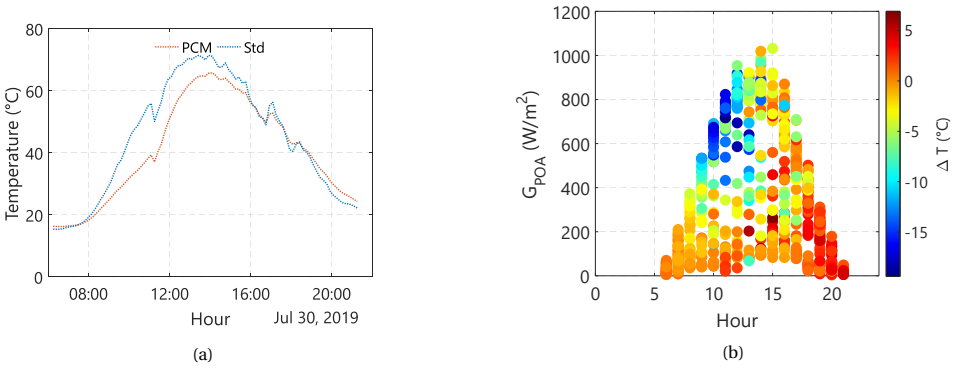

Figure 6.11: **(a)** Hourly average operational temperature of a PV module with (PCM) and without (Std) PCM slabs mechanically attached on the backside for a summer day in Delft. The PCM effectively reduces the operational temperature of the PV module with an insulated backside, particularly from the morning until early in the afternoon. Once the phase change takes place, and the ambient temperature starts cooling down, the release of heat from the PCM slabs keep the modules at a higher temperature compared to its standard counterpart. **(b)** Hourly average temperature difference between the standard PV module and the PV-PCM module related to the plane of array irradiance (G_{POA}) for the month of July. From 10 am until noon, the PCM slab can reduce the operational temperature of a PV module up to 15 °C. The cooling effect reduces overtime and after 15:00 hours the PV-PCM module presents higher operational temperature compared to the standard one.

The temperature difference between the average value measured from the six thermocouples on each PV module is denoted henceforth as ΔT, and mathematically defined as:

$$\Delta T(^{\circ}C) = \overline{T_{PV-PCM}} - \overline{T_{PV-Std}} \tag{6.2}$$

Negative values of ΔT indicate that PCM slabs thermally manage the photovoltaic module compared to the standard case. A positive value indicates that the module with the PCM slabs presents a higher operating temperature than the standard one. Figure 6.11b presents the calculated value of ΔT for every instant of time, grouped per hour of the day, and its relationship with the measured plane of array irradiance for the entire month of July 2019. The color code indicates the hour in which the PCM slabs provide cooling to the PV module (blue toward greens and yellow) and those in which that PV module presented a higher value of temperature compared to the standard one (orange toward reds). The general trend for the month follows that presented for the single day of the month in Figure 6.11a, where most of the cooling is provided around noon until 15:00 hours. From 9:00 to 10:00 hours, particularly at high G_{POA} values, the PCM provides cooling that consistently reduces the operating temperature of the photovoltaic

module between 10 °C and 15 °C. This effect is significantly lost later in the day, reaching a warming effect that produces a temperature difference of up to 5 °C more often observed after 17:00 hours. Figure 6.12b indicates that for the month of October, the PCM provides more consistent cooling to the PV module throughout most of the day, particularly at the hours of high values recorded G_{POA}. However, Figure 6.12b shows that during October, high values of G_{POA} were around 20% lower compared to July, leading to comparatively lower operating temperatures on both modules. However, the maximum temperature difference registered in terms of cooling was as in July, 15 °C. The warming effect, on the other hand, was greater during October, with measured differences up to 10 °C. However, these higher temperatures occurred only at low values of G_{POA} late in the day.

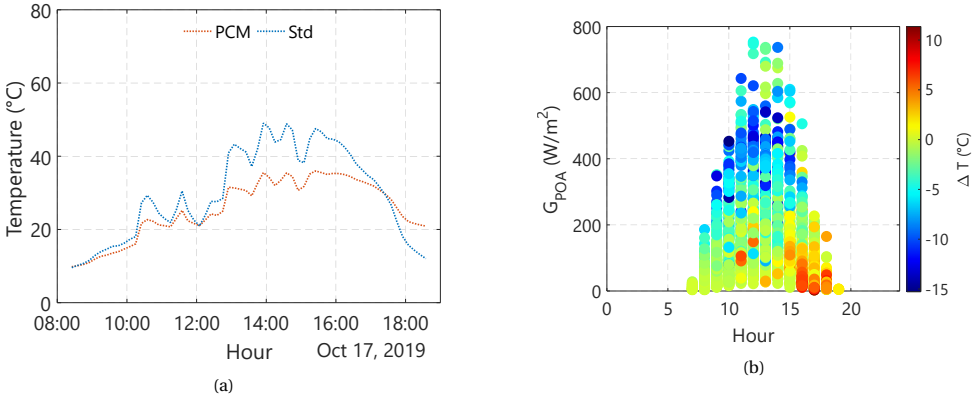

Figure 6.12: **(a)** Hourly average operational temperature of a PV module with (PCM) and without (Std) PCM slabs mechanically attached on the backside for an autumn day in Delft. Under this conditions, the PCM manages to provide cooling for most the day. The phase change is not completed and the PCM module only presents a higher value of operational temperature compared to the standard case at 17:00 hours. **(b)** Hourly average temperature difference between the standard PV module and the PV-PCM module related to the plane of array irradiance G_{POA} for the month of October. The lower values of G_{POA} compared to July (see Figure 6.11b) allow the PCM slabs to provide sufficient cooling capacity for almost the entire day to the PV module they are attached to

The thermal control provided by the PCM is greatly dependent on the amount of irradiance reaching the PV modules, as shown in Figure 6.11b and Figure 6.12b, but other environmental factors also contribute to the effectiveness of the PCM slabs. For this analysis, the average value of the temperature measured by the sensors in both modules was divided into calendar seasons. Summer of 2019 for example, covers the data ranging from July 24th (starting of the measurements) until September 21st. For fall, the data selection dates were 22nd in September until 21st of December. Lastly, winter encompasses the remaining data (measured until February 8th, 2020). Figures 6.13a to 6.13d present the histograms of the average recorded temperature of the PV module for summer (Figure 6.13a) and autumn (Figure 6.13b) for both the standard module and the PV-PCM module. To avoid populating the data measurements that occur very early or very late in the day, the data shown belong to the time of day when the measured irradiance was above 100 $W \cdot m^{-2}$ for each case. A different limit was set for the measurements of winter,

whose results are presented in the appendix 9 of this thesis.

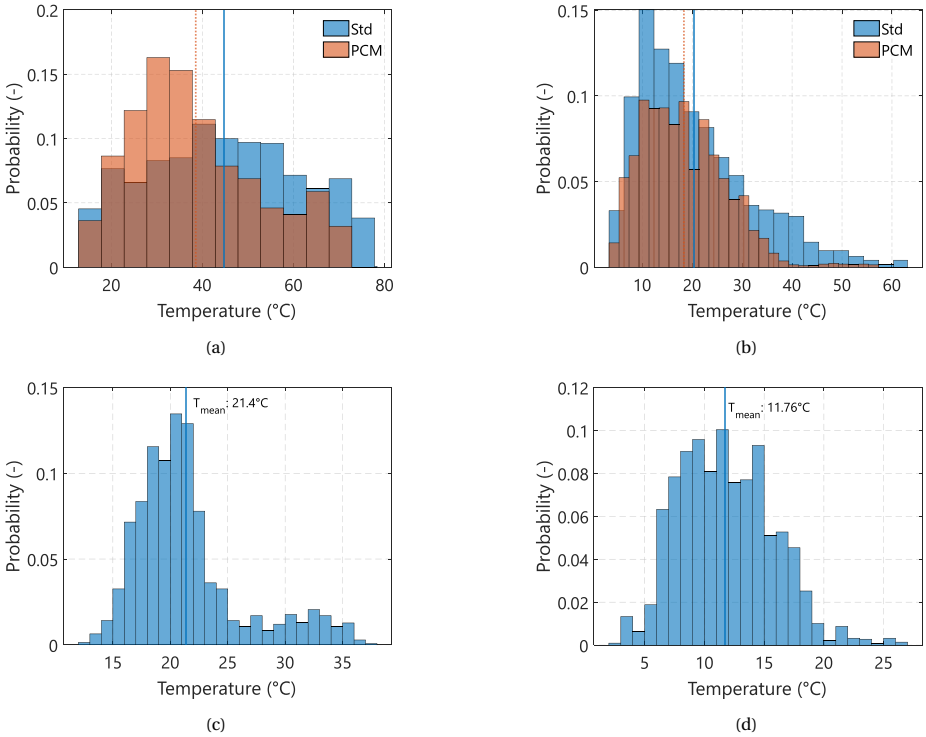

Figure 6.13: **(a)** Histogram of the measured operational temperature of the standard PV module (Std) and the PV-PCM module during the summer of 2019 (July 1 – September 21, 2019) between 10:00 and 17:00 hours. The vertical lines indicate the mean value of the measured temperature. During these hours, the PV-PCM module presented a mean measured value of 38.52 °C (dashed line). Compared to the value measured on the standard PV module (44.76 °C, continuous line), the PCM provides an average temperature reduction of 6.24 °C. **(b)** Histogram of the measured operational temperature of the standard PV module (Std) and the PV-PCM module during the autumn of 2019 (September 21 – December 21, 2019) between 10:00 and 17:00 hours. As presented in **(a)**, the mean values of temperature for the PV module with and without PCM are depicted by the vertical lines. **(c)** Complementary to **(a)**, histogram of the measured ambient temperature for the summer of 2019, showcasing a mean value of 21.40°C. **(d)** Complementary to **(b)**, histogram of the measured ambient temperature for the autumn of 2019, with a mean value of 11.76°C.

During summer, the average temperature reduction provided by the PCM slabs to the PV module was 6.24 °C. The calculated mean temperature in the standard module for this season was 44.76 °C, compared to 38.52 °C for the PV-PCM module. During the autumn, the mean recorded temperature in the standard module was 20.43 °C, while the PV-PCM module had a mean temperature of 18.34 °C, representing a temperature reduction of 2.09 °C. For these two seasons, the mean value of the recorded ambient temperature was 21.40 °C and 11.75 °C, respectively.

Figures 6.14a to 6.14d provides information on how the value of ΔT changes in relation with environmental factors. Figure 6.14a presents the relationship between ΔT,

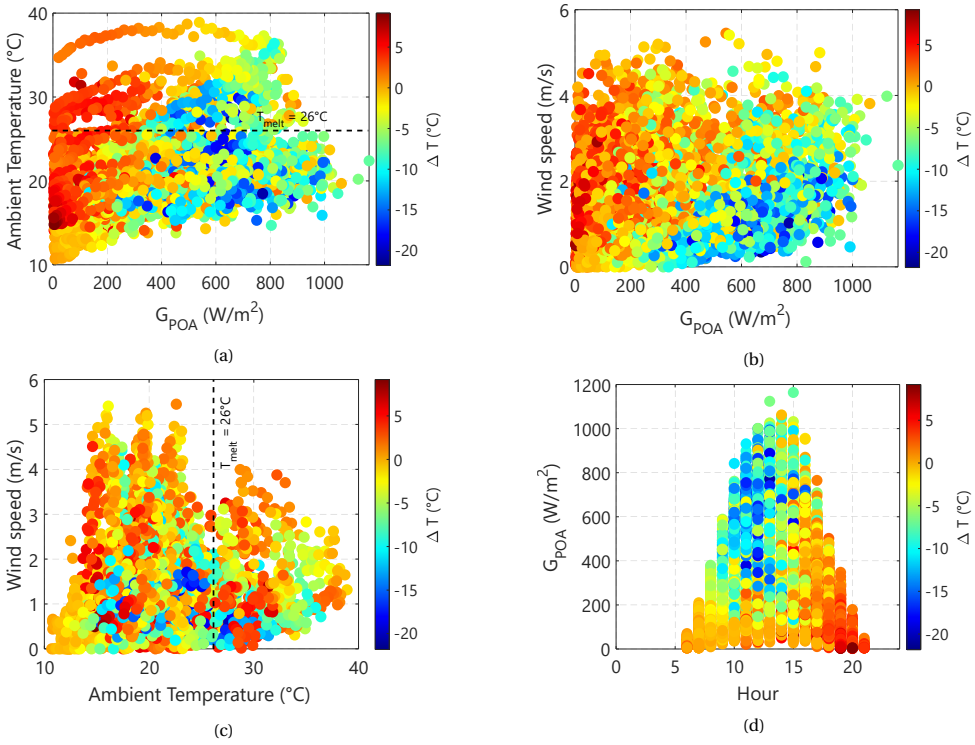

Figure 6.14: Influence of environmental conditions on the average temperature difference ΔT (°C) between PV-PCM and standard modules during summer 2019 in Delft: **(a)** effect of the ambient temperature related to the plane of array irradiance. The value of the melting temperature of the PCM is denoted by the dashed line; **(b)** effect of the wind speed related to the plane of array irradiance; **(c)** effect of the wind speed related to the ambient temperature; and **(d)** effect of the plane of array irradiance on the hourly temperature difference for the entire season

ambient temperature and G_{POA} during the summer of 2019 in Delft. The best cooling (denoted by blue to yellow colors) is provided at values of G_{POA} greater than 400 $W \cdot m^{-2}$ and lower values of ambient temperature, particularly when these are below the melting temperature of the chosen PCM slabs (26 °C). Nevertheless, the PCM slabs still manage to provide cooling at high ambient temperatures. The warming effect occurs mostly late in the day, when the density of red dots becomes more noticeable. The effect of wind speed and G_{POA} is presented in Figure 6.14b, which indicate that the best cooling is achieved at low values of wind speed (below 3 $m \cdot s^{-1}$) and high values of G_{POA}. It is important to highlight that in Delft, the backside of both PV modules was completely insulated. Higher wind speeds provide better cooling by convection mechanisms. An insulated backside reduces the effectiveness of convection, creating a more advantageous scenario for the PCM. However, even under this installation layout, high values of wind speed reduce the effectiveness of the PCM compared to the standard case, but the values of ΔT remain negative. Figure 6.14c presents the relationship between ΔT, wind speed and ambient temperature. In this case, the lowest values of ΔT are distributed mostly at

low values of wind speed (below 3 $m \cdot s^{-1}$) and values of ambient temperature below the melting temperature of the PCM slab. However, the effect of these environmental factors is not as acute as that of G_{POA}, as Figure 6.14d shows. During the summer of 2019, the PCM slabs were able to reduce the operating temperature of the PV module for most of the day, with the most reductions seen before 15:00 hours.

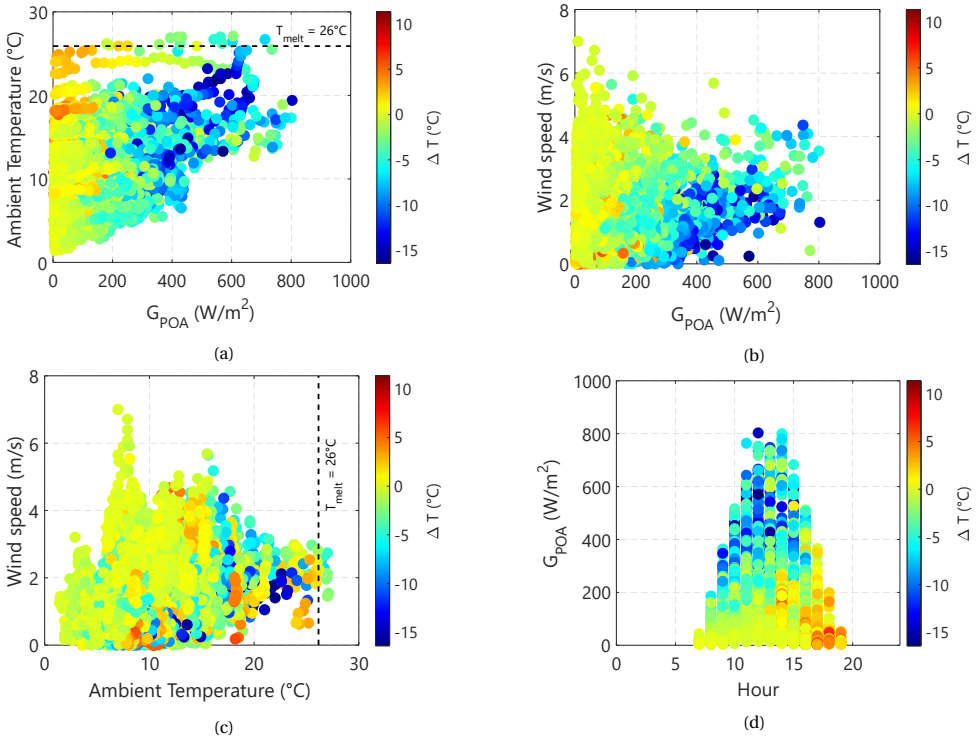

Figure 6.15: Influence of environmental conditions on the average temperature difference ΔT (°C) during autumn 2019 in Delft: **(a)** effect of the ambient temperature related to the plane of array irradiance. The value of the melting temperature of the PCM is denoted by the dashed line; **(b)** effect of the wind speed related to the plane of array irradiance; **(c)** effect of the wind speed related to the ambient temperature; and **(d)** effect of the plane of array irradiance on the hourly temperature difference for the entire season

Figures 6.15a to 6.15d is similar to Figures 6.14a to 6.14d but for a colder season, autumn. The lower values of G_{POA} and ambient temperature compared to summer help the PCM slabs to provide cooling for a wider range of values of G_{POA}. Particularly, this was because the measured ambient temperature values for this season were seldom above the melting point of the PCM. Notice that in Figure 6.15a to 6.15d, as opposed to Figure 6.14a, the color coding is slightly different. In the latter case, cooling was indicated by blue to orange colors, while warming was indicated by red colors. In Figure 6.15a, cooling is indicated by blue to green, whereas warming is indicated by yellow to red. This is because, during this season, the warming effect from the PCM slabs was higher compared to the summer, mostly due to lower measured ambient temperature during the evening. During solidification, the heat transferred from the PCM slabs to the

PV module maintains the temperature of the latter at significantly higher values than its standard counterpart, which cools down much faster due to the low values of ambient temperature. The warming effect, however, occurs at times when its impact on the overall electrical efficiency of the module is relatively low, as will be presented in the following section. During autumn, the measured values of wind speed were higher when compared to the summer, but high wind speed occurred at hours of low G_{POA}, as shown in Figure 6.15b. Also, during the autumn, the overall effect of ambient temperature and wind speed was not as significant as the effect produced by G_{POA}. Figure 6.15c indicates that during this season the values of ΔT that indicate better cooling happened at ambient temperatures lower than the melting temperature of the PCM, even during high wind speeds. Very low values of ambient temperatures and high values of wind speed resulted in a slight warming effect that never surpasses 5 °C. As in the case of summer, G_{POA} remains the most significant parameter (see Figure 6.15d). During autumn, the cooling potential provided by the PCM slabs had better consistency throughout the day compared to the summer.

CATANIA - PHOTOVOLTAIC MODULES WITH OPEN BACKSIDE

The experimental setup used in Catania contained the same standard and PV-PCM modules as those used in Delft. However, the methodology altered on the following aspects: (i) the PCM slabs were mechanically attached to the backside of the same PV module used for this purpose in Delft, but the backside of both modules was not insulated; (ii) the temperature of each module was measured utilizing one PT100 thermal sensor that was attached at their geometrical center. Lastly, the recorded electrical parameters were the maximum power point voltage (V_{mpp}) and maximum power point current (I_{mpp}) as opposed to the full IV curves measured in Delft. Results from the electrical measurements for each location are discussed in the previous section.

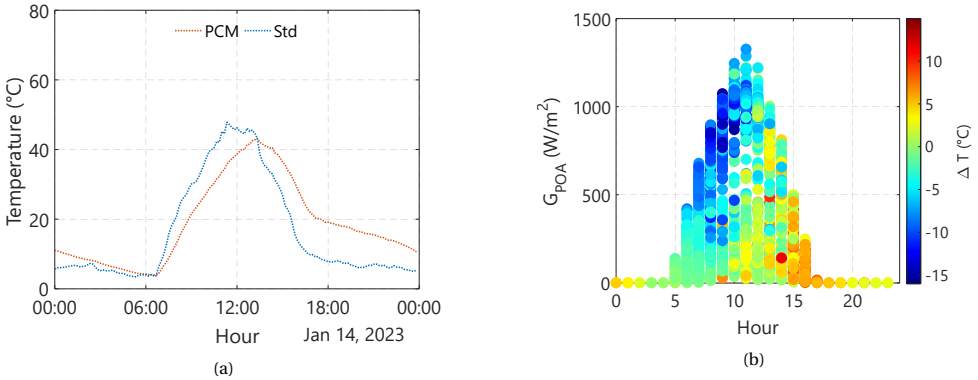

Figure 6.16: **(a)** Hourly operational temperature of the PV module with (PCM) and without (Std) PCM slabs attached to the backside with an open backside during a day in January 2023 in Catania, Italy. **(b)** Hourly average operational temperature difference for the entire month of January between the PV-PCM module and the standard counterpart. The PCM slabs allow the reduction of the temperature of the PV module consistently until 14:00 hours, covering the time of the highest irradiance values.

Figure 6.16a presents the hourly operating temperature of both standard and PV-

PCM modules during a day in January 2023 in Catania, Italy. Over the day, the operating temperature of the PV-PCM module is lower than that of the standard module. At around 14:00 hours, the standard module starts to cool down at a considerably higher rate than the module with the PCM. As a result, from 14:00 onwards, the overall effect from the PCM slabs is that of warming up of the module. As for the case of Delft, using the ΔT metric allows to assess the cooling provided by the PCM. Figure 6.16b presents the trend on the value of ΔT, per hour, as related to G_{POA} during the month of January. The best cooling happens from the early hours of the morning until 14:00 hours. Cooling is guaranteed during most of the hours of high values of G_{POA}. Notice that the limits depicted by the color code go from high cooling (blue, with a limiting value of -12 °C) to high warming (green towards reds, with a limiting value of 15 °C). The highest values of warming occur late in the day at low values of G_{POA}, which implies the potential negative effects on electrical performance are mostly avoided.

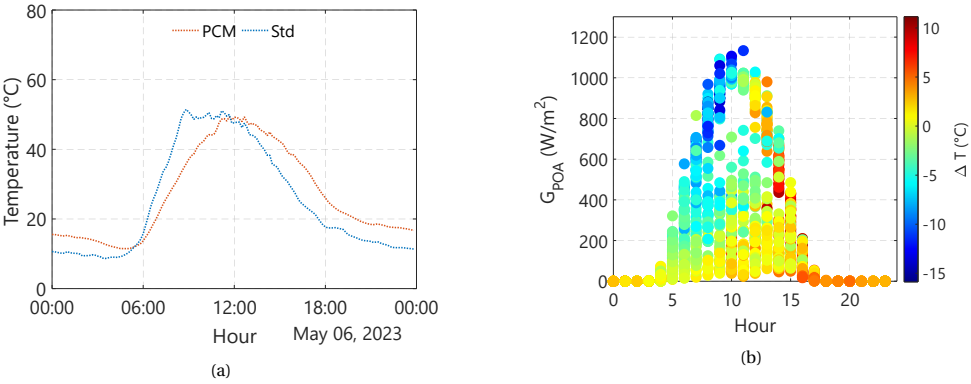

Figure 6.17: **(a)** Hourly operational temperature of the PV module with (PCM) and without (Std) PCM slabs attached to the backside with an open backside during a day in May 2023 in Catania, Italy. **(b)** Hourly average operational temperature difference for the entire month of May between the PV-PCM module and the standard counterpart. The PCM slabs allow the reduction of the temperature of the PV module consistently until 10:00 hours, covering some of the highest irradiance values.

In Catania, the cooling from the PCM slabs shift towards earlier hours of the day as ambient temperatures start to rise, similar to the behavior observed in Delft. Figure 6.17a shows that the photovoltaic module with the attached PCM slabs has a lower operating temperature compared to the standard case up to noon on a day in May 2023. Afterwards, the effect produced is a warming of the photovoltaic module until the end of the day. This trend is seen throughout the month of May, as seen in Figure 6.17b, where the maximum cooling is present between 9:00 and 11:00 hours, with ΔT values as low as -14 °C. During the afternoon, the warming of the module with the PCM can go as high as 10 °C compared to the standard module, and this warming occurs at G_{POA} values above 400 $W \cdot m^{-2}$, which leads to electrical performance losses. From a seasonal point of view, in Catania, both during winter and spring, the average temperature value for the PV-PCM module is higher than the value measured on the standard module. Figures 6.18a and 6.18b show the histograms of the measured temperatures for both modules during winter and spring, respectively. The values were filtered to those measured between 10:00

and 17:00 hours, which is the time frame at which high values of G_{POA} occur. During the winter months in Catania, the PV-PCM module had a mean measured temperature of 2.72 °C higher than the standard module with mean temperature values over a period of 26.98 °C against 24.26 °C, respectively. During spring, with measurements done between the 21st of March and the 16th of May 2023, the PV-PCM module also had a higher mean measured temperature (3.04 °C) compared to that of the standard module (31.64 °C vs 28.60 °C, respectively). These generally higher mean temperatures at the module level are correlated with the higher mean ambient temperature measured in Catania during spring (4.52 °C higher than during winter), as shown in Figures 6.18c and 6.18d.

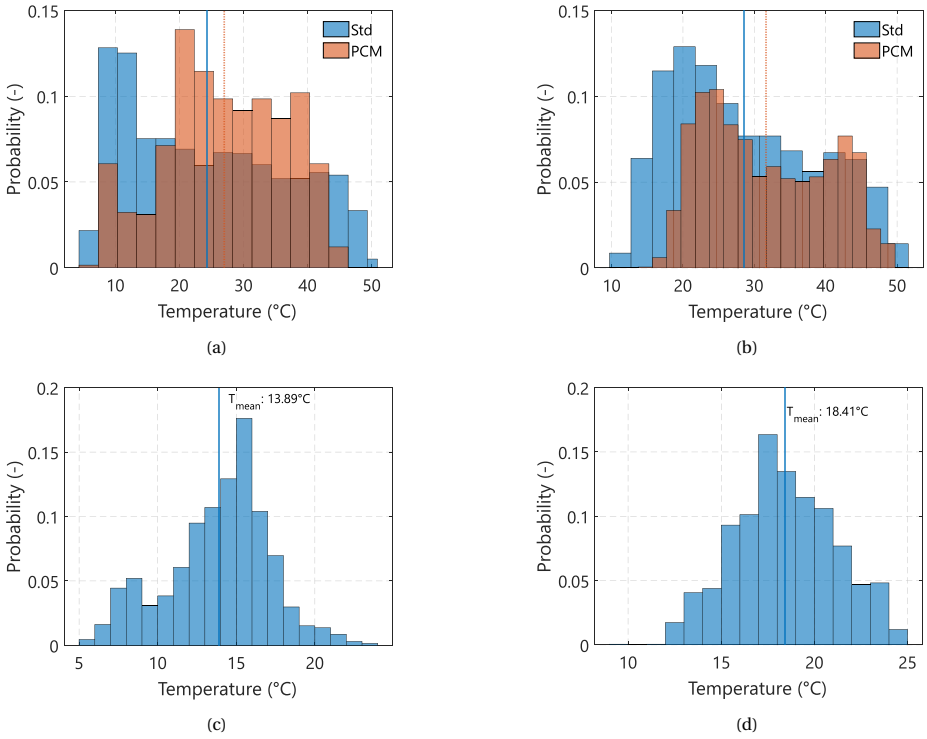

Figure 6.18: **(a)** Histogram of the measured operational temperature of the standard PV module (Std) and the PV-PCM module during winter 2023 (January 13 – March 21) between 10:00 and 17:00. The vertical lines indicate the mean value of the measured temperature. During these hours, the PV-PCM module is warmed up by the PCM, presenting a mean measured value of 26.98 °C (dashed line), 2.72 °C higher than that of the standard PV module (24.26 °C, continuous line). **(b)** Histogram of the measured operational temperature of the standard PV module (Std) and the PV-PCM module during the beginning of spring 2023 (March 21 – May 16) between 10:00 and 17:00. As presented in **(a)**, the mean values of temperature for the PV module with and without PCM are depicted by the vertical lines. **(c)** Complementary to **(a)**, histogram of the measured ambient temperature for the same period, showcasing a mean value of 13.89 °C. **(d)** Complementary to **(b)**, histogram of the measured ambient temperature for the spring of 2023, with a mean value of 18.41 °C.

Since the backside of both PV modules was left without insulation (as opposed to the experiments carried out in Delft), it is of interest to analyze how environmental con-

ditions impact, for this installation layout, the cooling potential provided by the PCM slabs. Given that most of the measurements performed in Catania were during the winter season (52% of the data points), Figures 6.19a to 6.19d show how the value of ΔT changes in relation to environmental factors. Figure 6.19a presents the relationship between G_{POA}, ambient temperature, and ΔT. An important aspect of this case is that the ambient temperature never had a value above the melting temperature of the PCM (26 °C). Given this condition, the cooling potential provided by the PCM (and represented by blue hues) increases with the value of G_{POA}. However, there are instances in which a warming effect was measured (represented by green to red hues) even at high G_{POA} values.

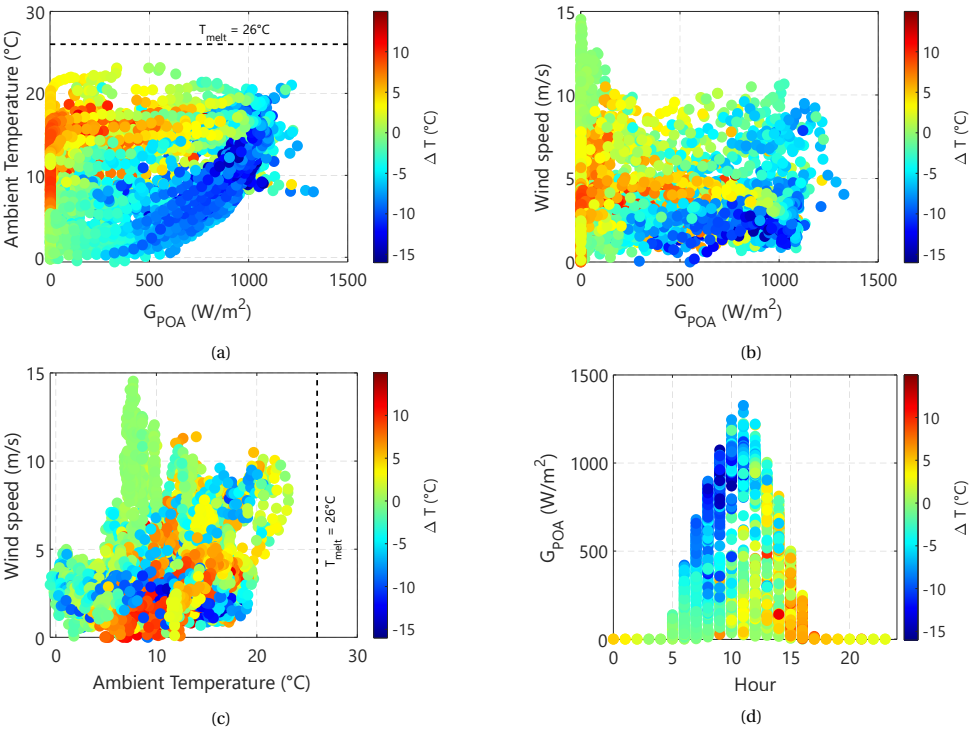

Figure 6.19: Influence of environmental conditions on the average temperature difference ΔT (°C) during the Winter of 2023 in Catania, Italy. **(a)** Effect of the ambient temperature related to the plane of array irradiance. The value of the melting temperature of the PCM is denoted by the dashed line; **(b)** Effect of the windspeed related to the plane of array irradiance. **(c)** Effect of the windspeed related to the ambient temperature. **(d)** Effect of the plane of array irradiance on the hourly temperature difference for the entire season.

The relationship between G_{POA}, wind speed conditions and ΔT is illustrated in Figure 6.19b. The best cooling provided by the PCM slabs is generally present at low values of wind speed for a wide range of irradiance conditions. However, even at high values of wind speed and high values of G_{POA}, PCM slabs still provide significant cooling. Most of the warming effect occurs during the afternoon hours, as shown in Figure 6.19d, which implies that the PCM is already saturated and the warming effect occurs. The high values

of the wind speed during this time increase the value of ΔT towards positive values, but its influence is less significant than that of the ambient temperature. Due to the very low ambient temperature, which never exceeded the melting temperature of the PCM, very little can be deduced from its relationship to the wind speed and ΔT (see Figure 6.19c). The ambient temperature remained stable during the first two months of spring (March through May), so the overall relationship between ΔT and the measured environmental parameters remained very similar to that of winter, as shown in the Appendix 9.

6.3.2. EFFECTS OF A PCM ON THE ELECTRICAL PERFORMANCE OF A PV MODULE

As explained in sections 6.2.3 and 6.2.4, both locations were equipped with devices that were able to monitor the electrical performance of both modules during the experiments. The instantaneous power produced by the modules was recorded and the data was synchronized with the remaining parameters (weather conditions, operational temperature, etc.). The data presented in this section have already been filtered using the methods explained in Section 6.6.

The PCM slabs, located on the backside of one of the PV modules, do not produce any optical loss. Its only effect is the reduction of the operating temperature by using the heat extracted from the module to create a phase change at a constant temperature. The main effect of this reduction is measured by an increased operating and open circuit voltage of the module, and a slight reduction in its current production. However, the latter effect is much lower than the former, and the overall result is an increased efficiency in electrical power production. Given the measured electrical parameters, the calculation of ΔP, defined as the difference between the instantaneous power produced by the standard module and that produced by the PV-PCM module, is mathematically expressed as follows:

$$\Delta P(W) = P_{PV-Std} - PV_{PV-PCM} \tag{6.3}$$

ΔP serves as a merit figure in analyzing the overall effect of the PCM on the electrical performance of a photovoltaic module in a way similar to its effect on the operating temperature presented in the previous section. A negative value of ΔP implies that the module with the PCM slabs produces more power than its standard opposite, whereas a positive value of ΔP means that is producing less power. Due to technical difficulties, maintenance procedures, and other scheduled activities carried out during the experimental work done in Delft, it was not possible to continually monitor the power production of the PV modules. As a result, some months have significantly more data than others. Reduction of potential biases regarding monthly energy yield calculations is done by calculating the energy production per hour measured in a month, which is defined as χ_{DC} and mathematically expressed as:

$$\chi_{DC}\left(\frac{W \cdot h}{hr - month}\right) = \frac{1}{N} \cdot \sum P_{PV} \tag{6.4}$$

Where N is the number of hours in which energy production was reliably measured at each month. The value of χ_{DC} is estimated separately for each module, and the relative energy gain or loss δ_{DC} is calculated as:

$$\delta_{DC}(\%) = \left(\frac{\chi_{PV-PCM} - \chi_{PV-Std}}{\chi_{PV-Std}} \right) \cdot 100 \tag{6.5}$$

The data presented based on the calculations performed using Equation 6.3 to Equation 6.5 have a time resolution of five minutes for the case of ΔP and monthly for the case of χ_{DC} and δ_{DC}.

DELFT, THE NETHERLANDS: PHOTOVOLTAIC MODULES WITH INSULATED BACKSIDE

The thermal control provided by the PCM causes a lower decrease in voltage compared to the standard case. Figure 6.20a presents the measured open circuit voltage (V_{OC}) of both modules during the same day of July as presented in Figure 6.11a). The V_{OC} value of the PV-PCM module remains higher compared to the standard module until 17:00 hours. This is the same time at which thermal control is lost and the warming effect starts. From this time of the day onward, the warming effect of the PCM slabs produces a lower value of V_{OC} on the module. However, this occurs at a time when G_{POA} is low and, consequently, the value of ΔP becomes *slightly positive*, meaning that the standard module produces *slightly* more power ($< 1\ W$) than the PV-PCM. This occurs in almost all instances of summer, as shown in Figure 6.20a, where most hours of the day with a high value of G_{POA} produce a higher power output in the case of the PV-PCM module.

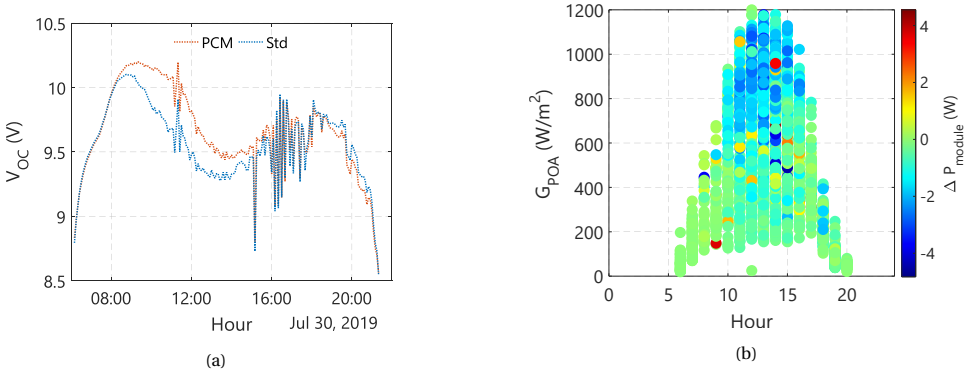

Figure 6.20: **(a)** Measured open circuit voltage of two PV modules, one with PCM slab attached on the backside (orange line) and a standard PV module during a day in July 2019 in Delft, Netherlands. In both cases, the backside of the PV modules was insulated with a 19-mm thick Armaflex® slab. **(b)** Difference in electrical power produced ΔP, as defined by Equation 6.3, per hour during the summer season (July – September 2019) in Delft. A negative value of ΔP means that the PV-PCM module produces more electrical power than its standard counterpart. This definition was decided to follow a similar color code as that presented to analyze the cooling potential in the previous section.

The thermal management provided by the PCM slabs during the summer of 2019 is maintained during the summers of 2020 and 2021 as shown in Figure 6.21a and Figure 6.21b , respectively. In both years, negative values of ΔP are achieved during most of the hours at which G_{POA} is above 600 $W \cdot m^{-2}$. Only occasionally, during these hours, ΔP has a positive value. Notice that, as expected, the behavior observed in Figure 6.20b and Figures 6.21a and 6.21b follow that of Figure 6.14d: the best observed improvements

in electrical performance happen when the PCM slabs provide substantial temperature reduction.

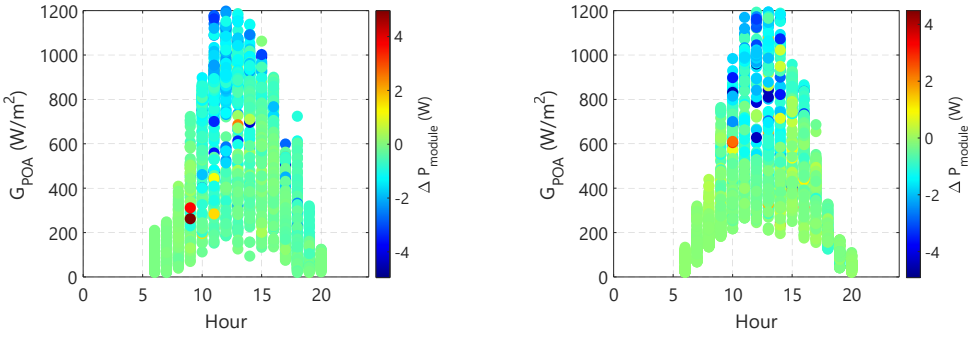

Figure 6.21: **(a)** Difference in electrical power produced ΔP, as defined by Equation 6.3, per hour for the summer season (July – September 2020) in Delft. A negative value of ΔP means that the PV-PCM module produces more electrical power than its standard counterpart. **(b)** The same relationship as presented in **(a)** but for the summer of 2021 in Delft.

Regarding the normalized energy yield, as defined by χ_{DC}, the PV-PCM module always had a higher value compared to the standard module. Even during the cold months of November and December, with limited solar resource, the PCM slabs manage to provide an overall positive effect, as shown in Figure 6.22a. The relative gain, expressed by δ_{DC}, is presented in Figure 6.22b. Relative gains during this year range from 1% in December to 4% in September.

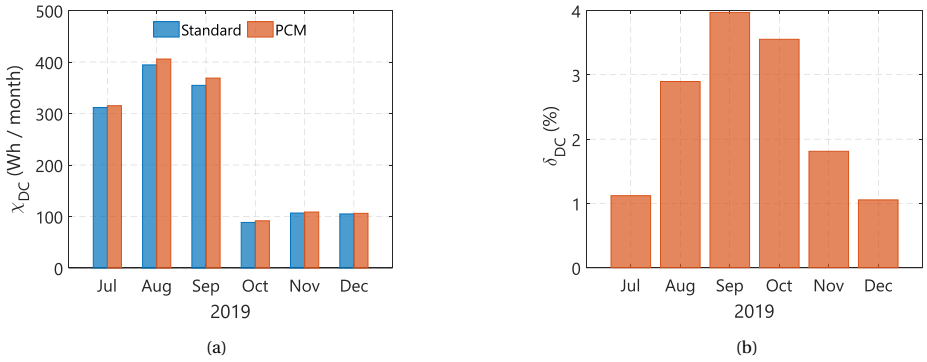

Figure 6.22: **(a)** Monthly values of χ_{DC} as defined by Equation 6.4, which represents the sum of energy divided by the amount of working hours during the month for each PV module. **(b)** Relative gain δ_{DC} demonstrates that the PCM slabs provided positive energy yield effects during all the measured months of 2019.

Data for 11 months in 2020 indicate that the implementation of PCM slabs provides increased energy yield production under all seasonal conditions, with the winter months of December and February indicating the lowest relative gain (see Figures 6.23a and

6.23b). During the spring and summer months, the relative gain ranges from 2.1% to 2.6%, which are lower values compared to 2019. During 2021, the relative gain was much more stable throughout all months, ranging from 2.1% to 2.6% from January towards July, as presented in Figures 6.23c and 6.23d.

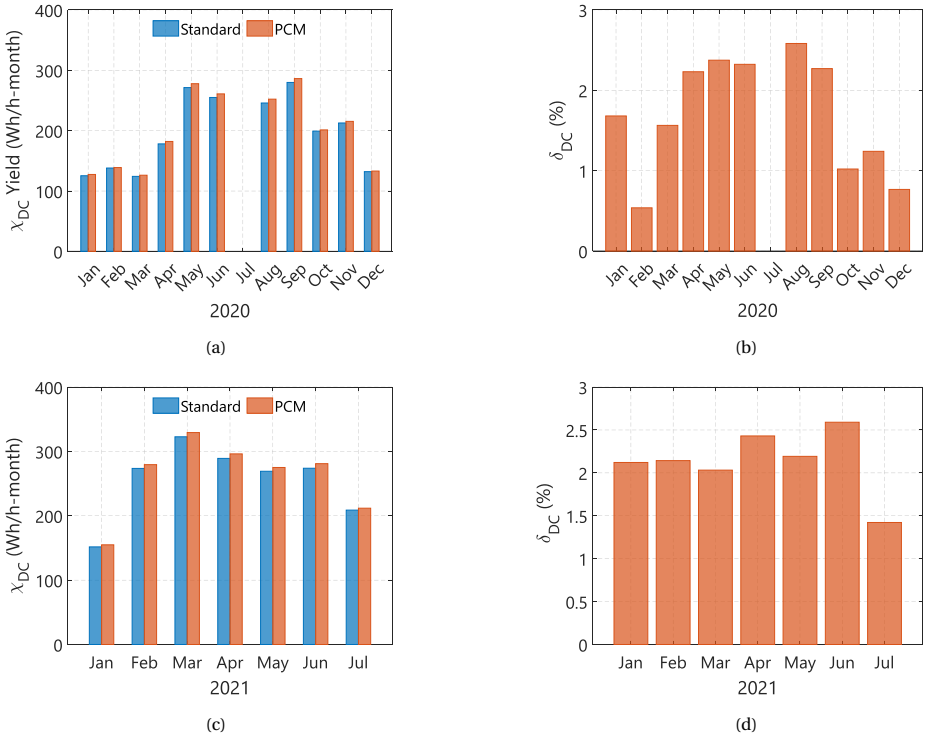

Figure 6.23: **(a)** Monthly values of χ_{DC} as defined by Equation 6.4, for the year 2020, representing the sum of energy divided by the amount of working hours during the month for each PV module. **(b)** Relative gain δ_{DC} evidence that the PCM slabs provided positive energy yield effects during all the measured months of 2020. Due to a failure in the system, no data was collected during July of this year. **(c)** Monthly values of χ_{DC} for the year 2021 and **(d)**relative gain δ_{DC} computed for all the measured months of 2021.

The variance in the relative gain observed in the PV-PCM module can mainly be attributed to the number of hours the modules worked during each month. For example, in July 2019, a total of 141.25 hours were recorded in both modules. During August, it was only possible to measure the electrical parameters for 56 hours. Given the dependence of the thermal management provided by the PCM on environmental factors, particularly irradiation, fewer hours of measurement can bias the relative gain in a positive or negative way. An example of each case is September 2019 (with 63 hours of measurements) and February 2020 (with 27 hours of measurements), where the gain is unusually high and unusually low, respectively. The months that had a substantial number of measurements were April, May, August, September 2020 and March, April, and June 2021 with measured hours ranging from 500 to 650 per month. During these months, the relative

gain is always estimated between 2.1% to 2.5%, thus providing a good indicator of the overall benefits of the monthly performance provided by the PCM slabs.

CATANIA, ITALY: PV MODULES WITH OPEN BACKSIDE

In Catania, the combination of high values of G_{POA} and low values of ambient temperature results in a gain in power production in the morning and a loss of power production in the afternoon when comparing the measurements of both modules and calculating ΔP, as shown in Figure 6.24b. These changes in the gain and loss of power from the PV module with PCM slabs compared to the standard module are caused by the effects on the voltage produced by the change of temperature (see Figure 6.24a).

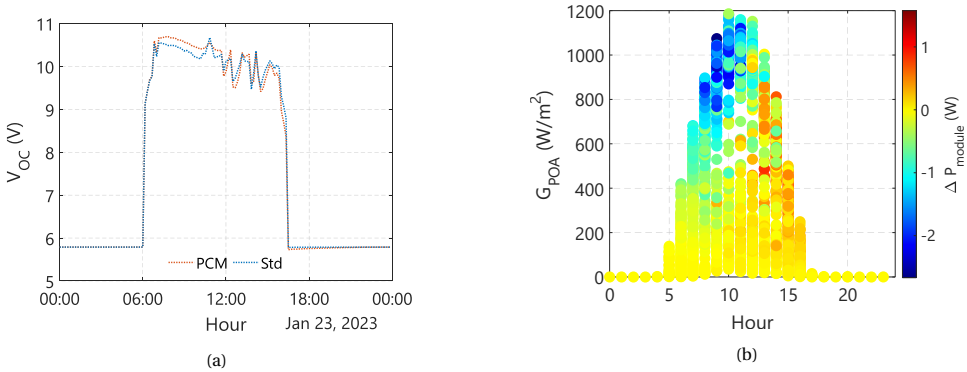

Figure 6.24: **(a)** Measured open circuit voltage of the two PV modules, the PV-PCM (orange dotted line) and the standard PV module (blue dotted line) during a day in January 2023 in Catania, Italy. In both cases, the installation layout was a rack mounted system with no obstruction on the backside. **(b)** Difference in electrical power produced ΔP, as defined by Equation 6.3, per hour for winter months of 2023 in Catania. A negative value of ΔP means that the PV-PCM module produces more electrical power than its standard counterpart.

In Delft, the value of ΔP was maintained negative for most of the day during summer. In Catania, this was not observed even during the winter months, where some losses were present just two hours after noon. One possible explanation for this observation is that the open backside of the standard photovoltaic module allows rapid cooling, aided by low ambient temperature and better convection mechanisms. In the PV-PCM module, low ambient temperatures cause a reversal of the phase change, meaning that heat is transferred from the slabs toward the module. Furthermore, the presence of the slabs itself reduces the effectiveness of the convection mechanisms on the backside of the module, which hinders cooling. Despite this, during the five months of measurements conducted in Catania, the overall effect of implementing the PCM slabs produced gains in the electrical energy yield of the PV module going from 1.3% in January to 1.6% in February (see Figure 6.25a). However, the relative gains are smaller than those measured in Delft. Like in the case of the experiment in Delft, it was not possible to monitor the electrical parameters throughout the months, so the gains presented in Figure 6.25b are an initial indicator of the relative potential benefits and the results might vary for the setup measured for longer periods.

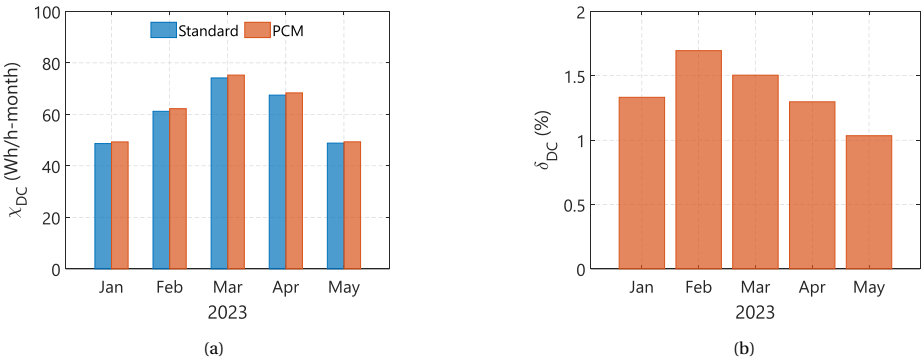

Figure 6.25: **(a)** Monthly values of χ_{DC}, as defined by Equation 6.4, for the year 2023 in Catania, Italy, representing the sum of energy divided by the amount of working hours during the month for each PV module. **(a)** Relative gain δ_{DC} denote that the PCM slabs provided positive energy yield effects during all the measured months of 2023.

6.4. DISCUSSION

From the data presented in the previous section, the following points of discussion are salient.

6.4.1. COOLING POTENTIAL AND TEMPERATURE HOMOGENEITY

In general, the implementation of the selected PCM slabs provides substantial cooling potential to PV modules simply by mechanically attaching them to the backside, with measured reductions of operational temperatures up to -15 °C in both locations, which are reductions in the range of those observed in other research work, as summarized in Section 6.2.1. The cooling could be provided for extended periods of time. In Delft, for example, the selected PCM slab could thermally manage the PV module for most of the day, even during the summer season (see Figure 6.12b and Figures 6.21a). In Catania, thermal control could not be secured throughout the day, even during the winter months of January to March 2023 (see Figure 6.19d). In the afternoon hours, the module with the PCM slabs had higher measure temperatures than the standard case. This led to lower comparative voltage values, thus indicating power losses. This shortcoming could be potentially avoided by choosing PCMs with different melting temperatures, depending on the average ambient temperature of the installation location. However, there are potential issues with temperature homogeneity. Figures 6.9a and 6.9b and Figures 6.10a and 6.10b show that a better contact is needed from the PCM slabs into the backside of the photovoltaic module. The temperature measurements done on the cells at the center of the module had values that differed from those at the edges by an amount larger than their counterparts in the standard PV module. This implies that contact with the PCM slabs in these cells is insufficient for efficient thermal management. The aluminum frame, as shown in Figure 6.5b provides sufficient contact at the edges, where the cooling from the PCM slabs is measured to be optimal. More options for ensuring sufficient contact need to be investigated.

6.4.2. EFFECTS OF ENVIRONMENTAL CONDITIONS AND INSTALLATION LAYOUT ON THE COOLING POTENTIAL AND ENERGY YIELD

Figures 6.14a to 6.14a, Figures 6.15a to 6.15d, and Figures 6.19a to 6.19d present the effect of the environmental parameters on the capacity of the PCM slabs to provide cooling (defined by the metric ΔT). The irradiance reaching the photovoltaic modules, G_{POA}, and the ambient temperature were found to be the most impacting factors. Wind conditions had a moderate effect, only negatively affecting ΔT at high wind speeds. The ambient temperature of the location is particularly important in relation to the melting temperature of the selected PCM. The best reduction in the operating temperature of the PV module occurs under conditions of high G_{POA} and ambient temperature lower than the aforementioned melting value. This is consistent with other published experimental works [228]. In both locations, the average ambient temperature is low enough to guarantee that most of the phase change occurs due to the heat extracted from the photovoltaic module.

Delft had the better conditions for the effectiveness of the selected PCM, in part because the backside of both PV modules was insulated. This hinders the cooling ability of the standard module by eliminating the convection heat transfer at the backside, producing operating temperatures during high irradiance that are higher than in the case of no insulation. The PCM slabs compensated for this by acting as heat sinks working at a much lower temperature. Thus, instantaneous differences in power production between both modules could reach 4.3 W (see Figure 6.20b) due to the higher operating voltage (Figure 6.20a). In general, in this installation layout, the PV-PCM module exhibited, on average, a normalized energy yield between 2.1% and 2.5% higher compared to its standard counterpart, accounting for all measurement years (see Figures 6.22a and 6.22b and Figures 6.23a to 6.23d).

However, the warming effect was greater in Catania than in Delft, also occurring during hours with high G_{POA}. This location not only has on average higher irradiance than Delft, but also presents on average more frequent clear skies, with a diffuse to global irradiance factor of 0.367 compared to Delft's 0.531 [189]. Even during the low ambient temperatures of winter, the warming effect in the afternoon was greater than that observed in Delft. A possible explanation for this is the installation layout selected for Catania. With no insulation on the backside, the standard module can cool more effectively. The PCM slabs provide thermal control if the material is in phase change; otherwise, it will act as additional thermal resistance that hinders the module's ability to cool down through the convection mechanisms on the backside. Furthermore, clear skies improve the radiative cooling of the module; as a consequence of this, the standard module begins to cool down quickly (see Figure 6.16a and Figure 6.17a). The PV-PCM module, under these conditions, starts to act as a heat sink for the PCM that will start to reverse the phase change, causing increased temperatures. In terms of the normalized energy yield, the relative gain was estimated to range from 1.3 to 1.6%.

Since the cooling potential provided by the PV module is very sensitive to the value of G_{POA}, the optimal melting temperature of the PCM oriented toward PV applications also depends on the tilt and orientation selected for the system. For example, a photovoltaic façade oriented toward the west in the northern hemisphere will have the highest values of G_{POA} during the afternoon. In addition, the values will be lower than the mod-

ules installed on a south facing façade. This sensitivity means that a PCM with a lower melting temperature will be more suitable for the modules oriented west. Optimizing the PCM parameters while considering the layout of the installation of the PV modules will provide better energy efficiency.

6.4.3. TECHNICAL ASPECTS OF IMPLEMENTATION

From a technical perspective, the implementation of PCM slabs in PV modules looks straightforward. Significant cooling is possible by mechanically attaching them to the backside. However, there are the following important considerations to optimize their benefit. The most important properties for selecting a PCM material for PV applications are its melting temperature and its latent heat (see the work of Verheijen [229]). The knowledge of manufacturers about tuning these properties is significant and it is a challenge for the designer to select the most appropriate PCM for its application. As shown in this work, the best match comes from a clear understanding of the environmental conditions of any given location and a careful consideration of the installation layout of the PV system. Integrated photovoltaic modules on façades, for example, will receive, on average, a lower irradiance. A PCM material with a melting temperature higher than the average ambient temperature during the warmest months will provide good thermal control to the photovoltaic modules throughout the year. For a given PCM material, the latent heat also improves thermal control but not to the same extent as the melting temperature.

Moreover, the tilt angle also influences the melting time of the PCM material. For a given PCM working under stable conditions, changing its tilt angle from 90° (vertical) to horizontal orientation increases the time it takes for the material to change phase. A PCM will melt slower on a façade system during summer in the northern hemisphere compared to one working under a tilted roof due to lower irradiance. However, for the same value of irradiance, the façade PCM will melt faster due to its tilt. In addition, the casing design of the PCM also impacts its performance. The casing of the product used in this work divides the slab into compartments, which can increase the melting rate by creating different buoyancy zones instead of one, as depicted in the experiments carried out by Kamkari and Shokouhmand [213]. However, the design differs from the study mentioned above on using grooves instead of fins, so the difference in the overall melting time and temperature profiles compared to a non-grooved casing is yet to be studied. Decreasing the melting time can be counterproductive, as it can translate into fewer hours of thermal control, particularly in the hours of high irradiance. All of these aspects need to be studied when designing and implementing PCM materials to provide cooling to PV systems.

Ensuring effective contact between the PCM slabs and the cells represents a different challenge. The PV modules manufactured for this project were designed so that the entire active area could be covered with PCM slabs. These might not be possible with standard full-cell PV modules, since the junction box is usually located at the back of one or two cells. This condition makes it impossible to cover the active area with PCM slabs. However, half-cell photovoltaic modules usually have a junction box in the middle of both groups of cells, without covering any active area. For these modules, PCM slabs are a particularly good option to provide thermal control.

The added weight is another important technical aspect regarding the PCM slabs used in this study. The addition of these devices can significantly increase the overall weight of the modules. Adding ten PCM slabs will increase the weight of the setup by 20 kg, which could become problematic for roof or façade installations. The high-density polymer (HDP) casing is designed to avoid mixture separation and leakage, ensuring higher reliability. Orange Climate Autarkis tested the PCM products mentioned above using the standardized test conducted by the PCM RAL Quality Association [230] (RAL-GZ 896 test). The results, according to the company, showed that the slabs can sustain more than 330,000 cycles of work. For a PV application that has one cycle per day, this number of cycles is translated into more than 80 years of service.

From an economic perspective, the addition of PCM slabs does not represent a substantial increase in the overall price of the photovoltaic system. Orange Climate Autarkis company estimates that, depending on the economy of scale and packaging, the costs of the PCM slabs could be in the range of 2 €/kg to 6 €/kg.

Reducing the operational temperature not only increases the electrical performance of a photovoltaic module but also has important benefits related to reliability. Studies have shown that, particularly in warm climates, operational temperature reductions can significantly extend the lifetime of a photovoltaic module. Furthermore, during the evening, the cooling of the PV module is slower as a result of the warming provided by the solidification of the PCM. This behavior could reduce the daily thermal gradient, which is the difference between the highest and lowest operating temperatures of a photovoltaic module on a given day. This thermal gradient also affects the reliability of the photovoltaic module. [211], [231], [24]. Studying this potential benefit can further increase the interest and economic viability of the implementation of these devices in photovoltaic systems.

6.5. CONCLUSIONS

This work presents a long-term study of the effect of adding phase change materials onto a 48.60 W_p PV module under different installation layouts and locations. It compares its performance to a 48.70 W_p PV module that works under the same conditions, but without PCM. The selected compound provided by Orange Climate Autarkis (phase change: solid to liquid) was Calcium Chloride Hexahydrate. The material was encased in high-density polymer within slabs and had a melting temperature of 26 °C with a latent heat of 300 kJ/l. The selected locations were Delft, The Netherlands, with moderate climatic conditions, frequently overcast days, and varied irradiation throughout the year. Measurements in this location started in 2019 and ended in 2021. Due to technical challenges and maintenance activities, the data collection was non-continuous, obtaining 4314 hours of operation after that filtering was applied to the collected data to ensure its quality. The second location was Catania, Italy. A location with frequent clear skies and high irradiance, even during winter. In this location, the experiments carried out during the winter and early spring months of 2023 allowed the measurement of 1220 hours of operation with a resolution of ten minutes. In Delft, both modules were insulated on the backside to mimic the condition of a building-integrated system. In Catania, the modules were kept with their backside open, representing the condition of a standard rack-mounted system.

The results of the experiments showed that the PCM slabs could consistently provide significant operational temperature reductions to the PV module. Under the tested building integrated layout in Delft, for example, during all the measured summer months of 2019, 2020, and 2021, the PV-PCM module presented temperature reductions of up to 15 °C compared to the standard module. In addition, thermal management was possible during most of the sunny hours in the summer days, with an average temperature reduction of 6.24 °C. The trend continued through the autumn months, where the average temperature reduction was 2.09 °C, mainly due to the lower irradiance available during that period. In general, the PCM provided thermal control during the sunny hours of all measured seasons.

In Catania, the trend was similar to that observed in Delft for the standard rack-mounted layout. However, the warming effect was more impactful due to the combination of lower ambient temperatures and high irradiance values. In the above-mentioned conditions, the standard module cools down quite rapidly late in the afternoon, aided by clear skies. The heat stored on the PCM starts to transfer to the PV module when the reverse phase change occurs (liquid to solid), thus warming the module. On average, the PV-PCM module in Catania had an average operating temperature slightly higher than its standard counterpart, by 2.72 °C in winter and 3.4 °C at the beginning of spring.

During all months measured at both locations, the PCM slabs provided sufficient thermal control to increase the energy yield of the PV module compared to the standard case. In Delft, the relative yield gain, normalized per hour of operation, was between 2.1 and 2.5% during the months with more recorded data. The benefit could be around 1% or 4% in months with less data, highlighting the importance of continuous long-term experimental work to have a fair assessment of the potential benefits of PCM. In Catania, the benefit provided by PCM was lower than that measured in Delft, with a relative increase in normalized energy yield between 1.3 and 1.6%.

The environmental parameters that affect the ability of the PCM to provide cooling are the combined effects of irradiance and ambient temperature. Under high ambient temperature and high irradiance conditions, the PCM is rapidly transitioned, reducing the time in which thermal control is achieved. Afterward, the PV-PCM module begins to present operational temperatures that are higher than those of its standard counterpart. Selecting a PCM with a higher melting temperature or latent heat value can reduce this condition. However, this could hinder potential benefits in the colder months. Therefore, a detailed analysis of the conditions under which a photovoltaic system will operate is necessary to select an appropriate PCM that ensures benefits under all conditions. Smith et al. [232] provide valuable insight into this matter.

6.6. METHODOLOGY FOR DATA FILTERING AND VALIDATION

The filtering of data for both locations consisted of comparing the measured electrical parameters of both PV modules with calculated values based on measurements of the irradiance plane of the array (G_{POA}) and the temperature of the PV module (T_{PV}). First, the measured short-circuit current was compared with a calculated one, denoted as (I_{SC_c}) and estimated using the following equation:

$$I_{SC_c}(A) = \frac{G_{POA}}{G_{STC}} \cdot I_{SC_{STC}} - \rho_{ISC} \cdot (T_{STC} - T_{PV}) \tag{6.6}$$

Here, G_{STC} and T_{STC} are the irradiance and temperature of the PV module that impinge under standard test conditions, respectively. ρ_{ISC} is the short-circuit current temperature coefficient of the PV module, which was assumed to be the same as that of the SunPower Maxeon^{TM}. Gen II solar cell (2.6 $mA/°C$).

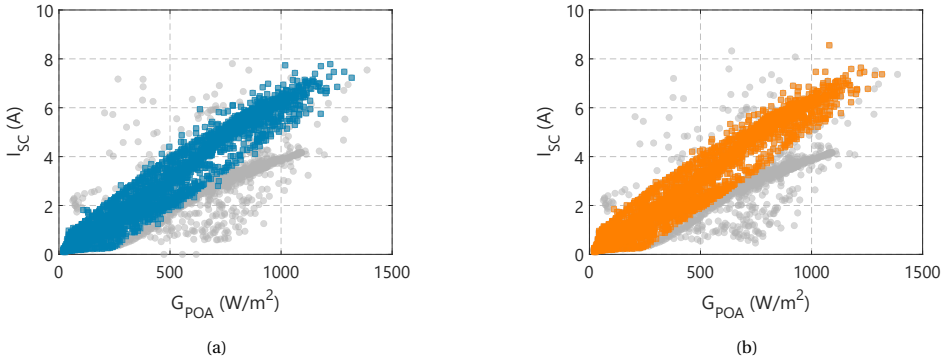

Figure 6.26: **(a)** Unfiltered (grey circles) and filtered (colored squares) data based on Equation 6.6 for the case of the standard PV module for year 2019 in Delft. **(b)** Unfiltered and filtered data based on Equation 6.6 for the case of the PV-PCM for the year 2019 in Delft.

To filter possible erroneous data, the calculation of the difference between the value of I_{SC_c} and the measured value of I_{SC} was compared with a limiting value of ±20% of $I_{SC_{STC}}$, following the recommendations provided in the literature [233]. Any value greater than or lower than this selected limit was considered unfit for analysis.

The second stage was to use a two-diode equivalent electrical circuit model to verify that the measured data was consistent with physical models and to avoid potential biases produced by out-of-synch measurements, accidental shading of pyranometers and modules, and other circumstances that might lead to measurement error. The parameters required for the equivalent circuit were extracted using the PV Lighthouse tool [152]. These values are presented in Table 6.5. The initial fitting considered a single encapsulated cell, which was extracted from the measurement of the PV module, and dividing its voltages by the number of cells in series (16). The final fitting shows good agreement with the measurement under STC conditions, as shown in Figure 6.27. Once validated, this physical model was used to estimate the power produced by the module under different climatic conditions. Notice that, since the initial fitting considered the cell already encapsulated, the optical losses produced by the front glass and the encapsulant were already accounted for. The values used as input on the two-diode model were measured G_{POA} and measured operational temperature (T_{PV}) for Catania and the average measured operational temperature ($\overline{T_{PV}}$), for validation of the data measured in Delft.

Figures 6.28a and 6.28b present the results of this procedure. For the case of the standard module, some measured power values deviate considerably from those estimated via the two-diode model. The same difference is not observed for the PV-PCM module,

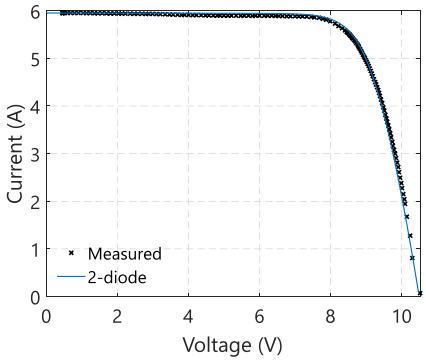

Figure 6.27: 2 Measured IV curve (denoted by X symbols), under STC conditions provided by the AAA class large area steady state (LASS) solar simulator. The module shown here would be then used to attach the PCM slabs on its backside (these laboratory measurements did not use any PCM). The two-diode equivalent circuit model use the parameters presented in Table A 1. The results show good agreement between the model and the measured module

Parameter			Value
Light collected current	(J_L)	$(mA \cdot cm^{-2})$	36.87
Saturation current 1	(J_1)	$(pA \cdot cm^{-2})$	0.38
Ideality factor 1	(m_1)	(-)	1.00
Saturation current 2	(J_2)	$(nA \cdot cm^{-}2)$	1.00
Ideality factor 2	(m_2)	(-)	2.00
Shunt resistance	(R_{SH})	$(k\Omega cm^2)$	10.00
Series Resistance	(R_S)	(Ωcm^2)	1.50

Table 6.5: Two-diode parameters used for simulations

whose measured power values match those estimated with the two-diode model. Problems with maximum power point tracking (MPPT) may be the reason for the discrepancy observed in the standard photovoltaic module.

A final filter calculated the difference between the estimated value of P_{max} from the two-diode model and the one measured from the MPPT tracking software. Any value greater than 2 W or less than -2 W was eliminated from both data sets (standard module and PCM module). In general, the errors obtained when comparing the modeled electrical parameters with the measured ones for the period July 2019 to February 2020 in Delft are as follows.

The data obtained in Catania, Italy, were subjected to the same approach.

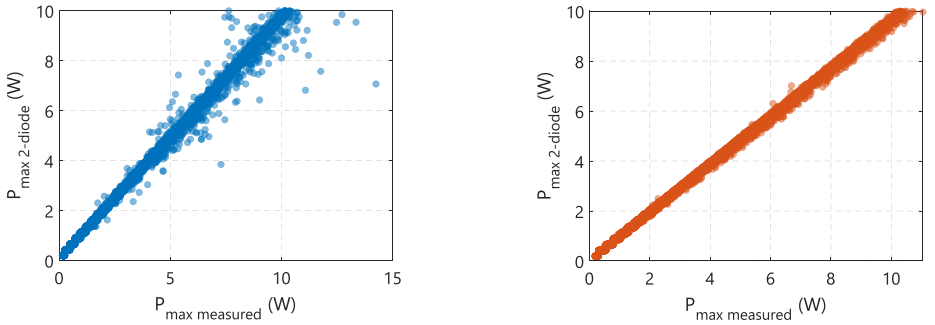

(a) (b)

Figure 6.28: **(a)** Measured and simulated value of the instantaneous maximum power of the standard PV module for the different environmental conditions (G_{POA} and ($\overline{T_{PV}}$) in Delft from July 2019 to February 2020. **(b)** Measured and simulated value of the instantaneous maximum power of the PV-PCM module for the different environmental conditions (G_{POA} and ($\overline{T_{PV}}$) in Delft from July 2019 to February 2020. Contrary to **(a)**, in this case the fit of the model shows very good agreement. The errors observed on the standard module are more likely due to errors in the maximum power point tracking algorithm.

Standard Module		PCM Module	
Parameter	Value	Parameter	Value
MAE	0.44	MAE	0.40
MBE	0.28	MBE	0.36
RMSE	1.11	RMSE	0.88

Table 6.6: Errors for the modeled instantaneous power (all values in W), via a two-diode model, compared to the measured values in Delft between July 2019 and February 2020.

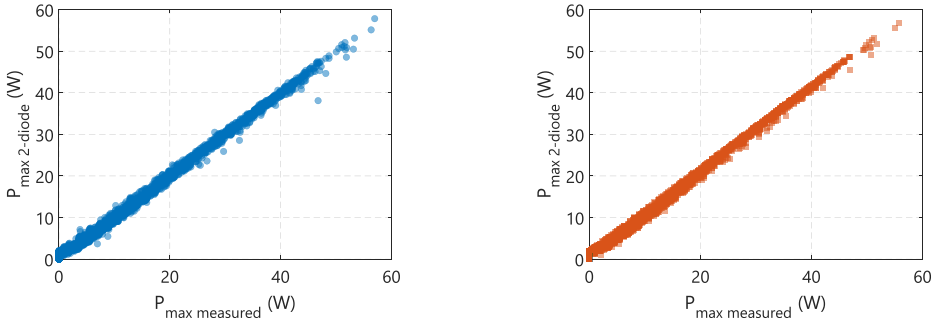

(a) (b)

Figure 6.29: **(a)** Measured and simulated value of the instantaneous maximum power of the standard PV module for the different environmental conditions (G_{POA} and T_{PV}) in Catania from January to May 2023. **(b)** Measured and simulated value of the instantaneous maximum power of the PV-PCM module for the different environmental conditions in Catania from January to May 2023.

Standard Module		PCM Module	
Parameter	Value	Parameter	Value
MAE	0.20	MAE	0.29
MBE	-0.05	MBE	-0.25
RMSE	0.45	RMSE	0.60

Table 6.7: Errors for the modeled instantaneous power (all values in W), via a two-diode model, compared to the measured values in Catania between January and May 2023.

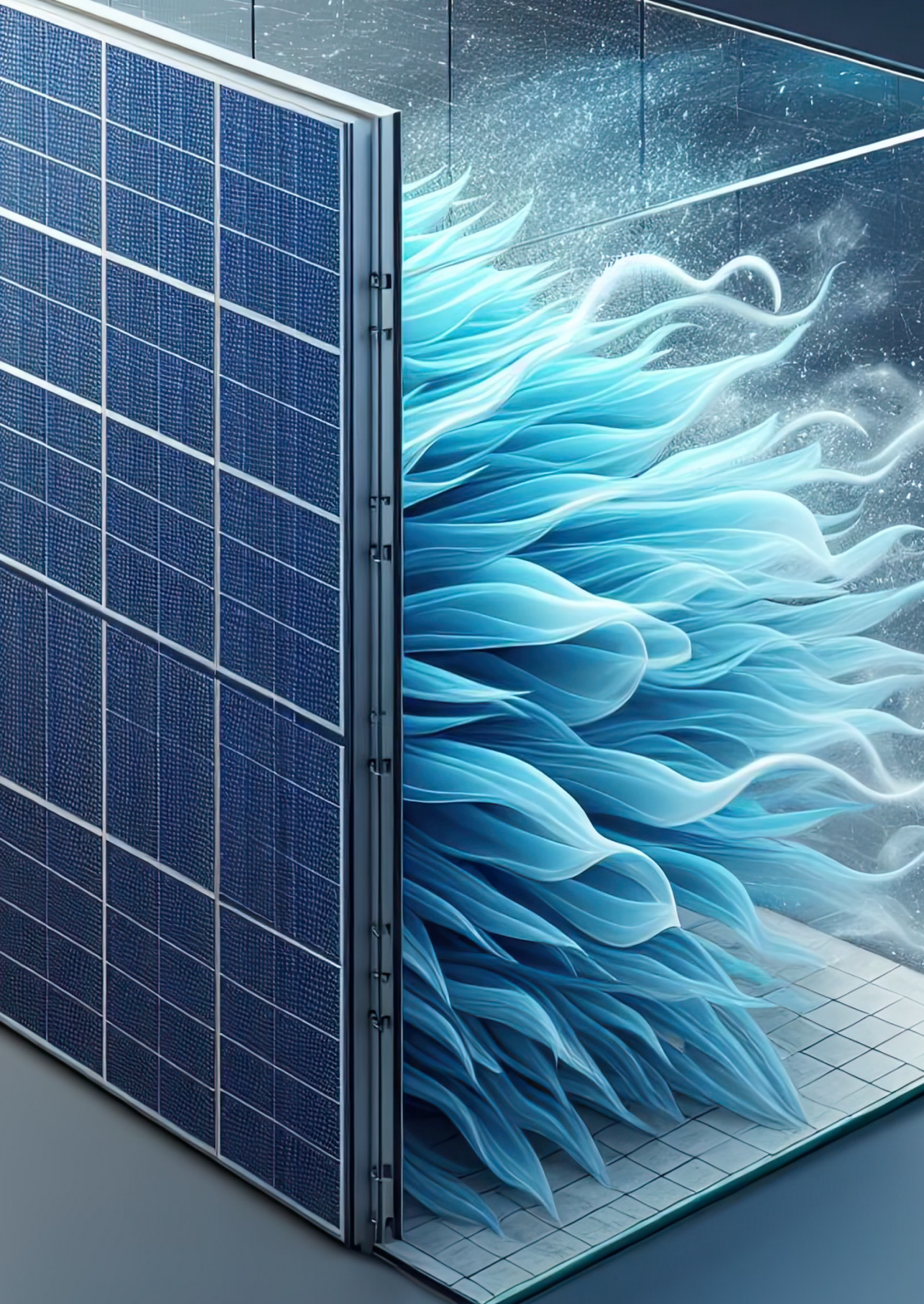

7

THERMAL MANAGEMENT: THE CONCEPT OF A PHOTOVOLTAIC CHIMNEY

This chapter is partially based on the following publication:

J.C. Ortiz Lizcano[1]**, Z. Haghighi, S. Wapperom**[2], C. Infante Ferreira, O. Isabella, A.v.d. Dobbelsteen, M. Zeman. *Photovoltaic chimney: Thermal modeling and demonstration of concept for integration in buildings.* Progress in Photovoltaics Research and Applications **28**, 465-482 (2020).

This work presents the concept of a photovoltaic solar chimney. The authors modeled and experimentally studied the integration of a photovoltaic (PV) system within a natural ventilated façade (NVF), trying to use the inherent cavity as a ventilation channel to transfer heat. Thermodynamic models were created to study the thermal and, therefore, the electrical performance of a photovoltaic system installed at different positions within the cavity of the NVF. An experimental photovoltaic chimney setup was manufactured to validate the computational models. The results show low RMSE values for the prediction of the mass flow and the temperature of the different materials considered in the chimney. A basic sensitivity analysis was performed to find the best position of the photovoltaic modules within the chimney for a three-story house in the Netherlands. Optimization showed that with a cavity depth of 0.2 m with PV modules located in the front layer, the annual electric yield is maximized. For the same cavity depth, placing the modules in the middle significantly increases heat flow production, albeit with a reduction in electrical performance.

[1] Candidate's contribution: Writing, simulation work, experimental work, results analysis
[2] The chapter is based on S. Waperom's work. He is considered an **equally** contributing author of this chapter

7.1. INTRODUCTION

During recent years, photovoltaics have experienced significant growth in technological development, installed capacity, and cost reduction. In terms of photovoltaic technology today, almost 20 different PV cell technologies are available and cell efficiency has reached 27.4% with monocrystalline silicon cells under standard test conditions [234]. This means that most of the absorbed irradiance is lost as heat. As explained in previous chapters, increasing operating temperatures have a significant impact on the electric yield of a photovoltaic module [235] and lead to faster degradation of photovoltaic cells and a reduction in service life.

Considering that the deployment of photovoltaic modules in urban environments has raised concerns about the topic of urban heat islands (UHI) [236], integrated photovoltaic heat management is essential. Modules placed in cities and an urban environment should be considered as a heat source in addition to electrical energy producing technology. This created a new trend: the development of hybrid applications with PV technology to extract heat from PV modules (e.g., PVT) [237].

High-rise buildings have become increasingly popular in the highly dense urban environment. Concern about climate change and the urgency to make the transition from fossil to renewable energy possible led to continuous efforts to achieve the nearly zero energy target in Europe. However, for a building of more than 3 stories, it is not feasible to rely solely on the limited roof area [238], [239]. International Energy Agency (IEA) indicates that incorporation of BIPV on building façades only may increase photovoltaic-suitable surfaces in buildings by approximately 35% [240].

Recently, an approach to producing natural ventilation from vertical surfaces, known as the Solar Chimney [241], is gaining popularity. The solar chimney has been tested and placed in many projects (ibid.) and is considered an effective passive heating, cooling, and ventilation approach for buildings.

The principle of operation of a solar chimney consists in creating a stack effect as a result of a density gradient in the air contained inside the chimney cavity. An absorber layer is used to collect the radiative energy of the sun and transfer it into the air in the form of heat. As air heats up, its density reduces, creating a draft. If the draft created within the cavity overcomes the pressure drop between the inlet and outlet ends of the chimney, then natural ventilation occurs [242]. Solar chimneys have been the subject of substantial research, both for large-scale energy production [243], [244] and for building applications [245]–[247].

Air flow layouts can vary according to the intended application. Some solar chimneys can collect cold air from living spaces or from the outside environment (see Figure 7.1). Other solutions place the chimney layout on the roof of a multi-story house, or a combined solar chimney layout that uses a vertical and a tilted cavity [246].

This work explores the idea of replacing the absorber layer of a solar chimney with photovoltaic modules. The heat extracted from the modules is used to create the required buoyancy effect. Furthermore, this work explores two potential cavity layouts, one that places the modules as the front layer of the cavity (PVF in Figure 7.1) and another that places the module at any place within the cavity itself (PVI in Figure 7.1). The thermodynamic behavior of these systems was modeled using MATLAB and validated with an experimental prototype. The model aims to simulate the performance of the

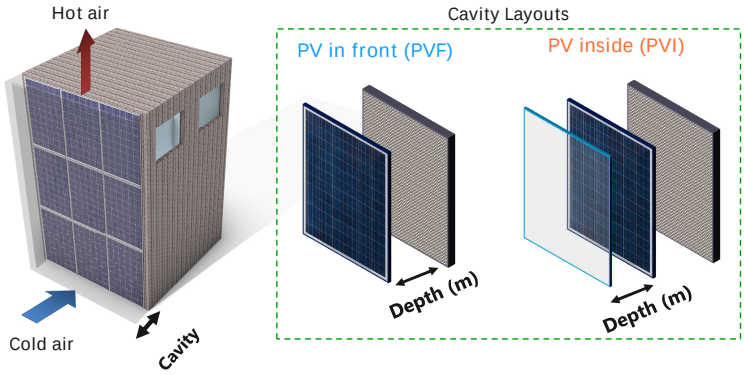

Figure 7.1: Sketch of the proposed photovoltaic chimney concept. The concept explores how the heat produced in the photovoltaic modules can be used to create natural ventilation of the air contained within the cavity. This work studies two different cavity configurations. First, placing the modules as the front layer of the cavity (PVF) and another that places the modules inside the cavity (PVI). In this second layout, the module can be placed attached to the building, or in any place inside the cavity.

system in different configurations, with the purpose of finding optimal geometries (cavity depth, height, and length) with respect to the energy performance of buildings, taking into account heating, ventilation, and electricity production.

7.2. MODELLING OF A PHOTOVOLTAIC CHIMNEY FAÇADE

During the last decade, different approaches have been proposed to model the behavior of a naturally ventilated façade. Analytical models such as the one by von Grabe [248], non-dimensional analysis done by Balocco [249], lumped one-dimensional element approach as described in Rheault and Bilgen[250], nodal network models as used by Gratia and Herde [251] and Ioannidis *et al.*[252], and computational fluid dynamics (CFD) methods such as those of DeGracia *et al.* [253].

As discussed briefly in the previous section, the principle of operation of the photovoltaic chimney consists of estimating the total radiative energy reaching its different layers. For both cavity configurations, the main absorber layer is the photovoltaic modules (middle layer in Figure 7.2). However, the glass layer also absorbs radiative energy, mainly in the ultraviolet range. In photovoltaic modules, part of the energy is transformed into electrical energy, and the remainder is dissipated as heat. Depending on their cavity layout (PVF or PVI) this heat is transferred to the air contained in both cavities (d_1 and d_2), for the case of PVI, as shown in Figure 7.2 or toward the environment and the cavity, for the case of PVF.

The system consists of one (PVF) or two heated surfaces that provide heat to the air contained within the cavity. This heat is used as input for the mass flow model. He *et al.* [254] highlight three different approaches to estimate this mass flow on solar chimneys. The single-zone model, which considers the cavity as a single zone in which temperature and density are evenly distributed. The stratified model, which considers the vertical variance of both temperature and density, and the plume model. This last ap-

proach is shown in Figure 7.2. The walls that are heated create thermal boundary layers of constant width δH. Inside the plume region (the colored columns in Figure 7.2) the stratified method is applied, outside of it, the air is considered to have the same properties as the ambient air entering the chimney. The main advantage of the plume model is that, since it considers horizontal variations on the properties of the air (one layer provides more heat than the other), it becomes valuable to find cavity depths that ensure maximum flow.

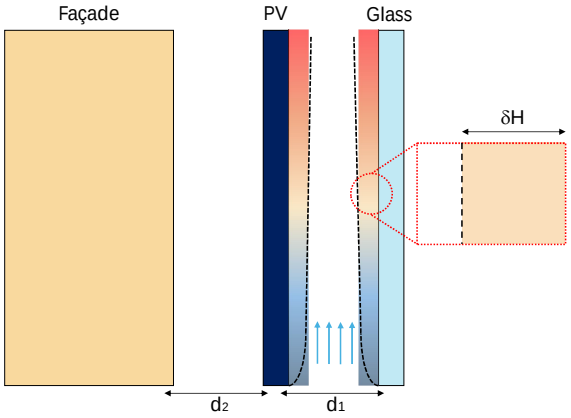

Figure 7.2: The photovoltaic chimney uses the heat produced by the photovoltaic panels and the front glass (for the case of a PVI layout) to heat up the air contain within the cavity. For simplicity, here only d_1. Two thermal boundaries, known as plume regions, are developed close to the heated surfaces. The flow and stack pressure of the air within the cavity is mainly driven by these plume zones. See [254] for an indepth mathematical explanation

This work uses a model based on a combination of a control volume model (CVM) and a plume zone analytic mass flow model created entirely in MATLAB. The input of the CVM user is meteorological data for location, chimney layout (height, width, depth, and building materials), total surface of the photovoltaic façade, specifications of the PV module and orientation in which the chimney is supposed to be installed. Given the overall layouts of NVF, all heat transfer mechanisms are described in two dimensions. It has been proven that such an approach produces accurate results for aspect ratios (height divided by depth) greater than 2. Wong *et al.* [255] demonstrated an error of 4% in 2D models that meet this condition compared to more sophisticated 3D models of the same geometry. In general terms, the model works as follows. To find the heat flux transferred to the airflow, the finite-volume method is used. The increase in surface temperature is found by estimating the total irradiance reaching the chimney. The combined convective heat transfer from the surfaces to the airflow is calculated and used as input in the mass flow model. Both models are solved by iteration.

7.2.1. IRRADIANCE MODEL

The model uses meteorological data as one of its main inputs. The user can provide a Typical Meteorological Year (TMY) file to provide hourly data of global horizontal irra-

diance (GHI), diffuse horizontal irradiance (DHI), and direct normal irradiance (DNI). The solar position is calculated using a MATLAB model following the method described in [256]. The contribution of each irradiance component in the plane of the irradiance array is calculated using the Perez model [148].

The contribution in the plain of the array irradiance on a vertical layer from the direct component of the irradiance is denoted by the equation 7.1.

$$G_L^{dir} = DNI \cdot cos(\theta) \tag{7.1}$$

where the cosine parameter represents the angle of incidence on the surface of the array, denoted by the equation 7.2.

$$cos(\theta) = cos(A_{TS}) \cdot cos(A_{ZL} - A_{ZS}) \tag{7.2}$$

The contribution of the diffuse irradiance component is calculated using Equation 7.3

$$G_L^{dif} = \frac{1}{2} \cdot DHI \tag{7.3}$$

This represents the contribution of the diffuse component for a free horizon on a vertical surface. The contribution of the ground irradiance was considered by:

$$G_L^{gr} = \frac{1}{2} \cdot (\Lambda) \cdot (GHI) \tag{7.4}$$

where Λ represents the value of the albedo of the ground. The sum of the values obtained from the equations 7.1, 7.3 and 7.4 gives the plane of irradiance of the array on a layer L in the chimney before the reflectance losses:

$$G_L^{POA} = G_L^{dir} + G_L^{dif} + G_L^{gr} \tag{7.5}$$

The notation presented in Equation 7.5 differs from that used in previous chapters, since it is estimated at the front layer L of a PV chimney. This front layer can be either a photovoltaic module or a glass layer.

7.2.2. CONTROL VOLUME METHOD

The model divides the geometry of the PV chimney into finite volumes. These are defined by the number of vertical volumes and the number of horizontal volumes per layer. Both can be defined by the chimney designer. The number of horizontal volumes on each layer must be equal for all layers. Air layers have only one horizontal control volume, given the nature of the mass flow model as described in the following section. An adjustable material database is included in the model. This database can be extended, and the user can choose any material present in the database to design the chimney.

An energy balance is created for each control volume and surface created in the model. Temperature calculations are performed by solving the energy equations at each layer using a first-order implicit central difference scheme. Since mass flow is considered as one-dimensional upward flow, a first-order upwind scheme is used for the calculation of heat transfer by the movement of air. Once all equations are obtained, a matrix A and

a vector C are created as described by equation 7.6. In this way, Gaussian elimination can be used to solve the set of equations and obtain the temperature at each control volume. Thus, a temperature profile was defined throughout the chimney.

$$[A] \cdot C = T \tag{7.6}$$

Figure 7.3 shows a schematic representation of how the model constructs the matrices to perform the iterative calculations used to find the heat fluxes and surface temperatures. The photovoltaic panel is considered to be installed inside the chimney cavity and its position will be moved to find the best energy performance for a given location and energy need.

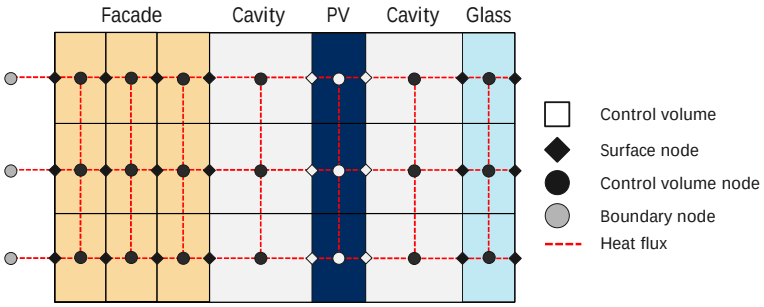

Figure 7.3: The user can define the amount of different vertical volumes and the horizontal control volumes per layer. The graph describes only 3 different vertical volumes and 1 horizontal volume per layer. Interaction between surface, centre and boundary nodes are also shown, as the modeled heat fluxes.

7

OPTICAL LOSSES AND PHOTOVOLTAIC POWER CALCULATION

The first calculations performed by the model are the optical losses of the incident irradiance in the first glass layer of the chimney. Solar radiation and gray-body radiation are treated separately.

The first reflection on the front glass is calculated considering the angle of incidence of light in the plane of the array (determined by equation 7.2) and the refractive index of the glass, here considered constant over all wavelengths and equal to 1.52 [257]. The backside reflectances are not considered in this model. Reflective losses are first found by averaging the reflectance of the perpendicular (r_p) and parallel (r_s) polarized light, described by the following equations.

$$r_s = \frac{ri_1 \cos\theta_i - ri_2 \cos\theta_t}{ri_1 \cos\theta_i + ri_2 \cos\theta_t} \tag{7.7}$$

$$r_{po} = \frac{ri_1 \cos\theta_t - ri_2 \cos\theta_i}{ri_1 \cos\theta_t + ri_2 \cos\theta_i} \tag{7.8}$$

where r_{i1} and r_{i2} are the refractive indices of the incident medium (air) and glass, respectively, and θ_t is the transmittance angle, which can be calculated by Snell's law:

$$\theta_t = \arcsin \cdot \left(\frac{ri_1}{ri_2} \sin\theta_i \right)$$

Lastly, the total reflectance is found using Equation 7.9:

$$R = 0.5 \cdot (r_s^2 + r_{po}^2) \tag{7.9}$$

Since the refractive index of air is considered equal outside and inside the chimney, the angle of incidence of light on the photovoltaic modules will be equal to the angle of incidence of light in the front glass. The effective irradiance reaching each layer is then defined by

$$I_{\mathrm{L}} = G_L^{POA} - R_L^{losses} \tag{7.10}$$

The absorbed irradiance is considered as a source of heat ($\dot{q}_{\mathrm{abs}}$) in each control volume (N) of the different layers. In general terms, this quantity is calculated by the following:

$$\dot{q}_{\mathrm{absN}} = I_{\mathrm{N}} \cdot \left(1 - \exp\left(-\alpha d\right)\right) \tag{7.11}$$

Where α is the extinction coefficient of the material (which for glass was considered constant and equal to $8.7 m^{-1}$) and d is the thickness of the layer, and in the model also equal to the depth of the control volume.

The transmitted irradiance that reaches the next control volume is calculated as follows:

$$I_{\mathrm{N_2}} = I_{\mathrm{N_1}} - \dot{q}_{\mathrm{absN_1}} \tag{7.12}$$

where the 1 and 2 subscripts denote two consecutive control volumes within any layer of the chimney. For the case of a layer, like the solar cells within the PV module located inside the cavity, this is expressed as:

$$I_{\mathrm{sc}} = I_{\mathrm{gl}} - \dot{q}_{\mathrm{absgl}} \tag{7.13}$$

Notice that this effective irradiance I_{sc} also considers the reflectance losses on the front surface of the module. Once its value is found, the model calculates the PV power. In this chapter, the photovoltaic module has the following characteristics: 1. The front and back layers are glass of 4 mm thickness. 2. Encapsulant (EVA) is assumed to be 1 mm thick and with the same optical and thermal characteristics of glass, and 15.24 cm mono-cSi solar cells with a standard test condition efficiency of 17 %.

The power delivered by the photovoltaic module is adjusted for different angles of incidence of light and different operating cell temperatures following the work of [258] and [259], respectively, by altering the efficiency η. The power is then calculated by the following.

$$P_{\mathrm{PV}} = I_{\mathrm{sc}} \cdot \eta \tag{7.14}$$

In the model, the PV module is divided into a number of control volumes equal to those chosen by the user. The middle volume is used to model the solar cells, and its considered as a perfect absorber, meaning that no irradiance reaches the building layer. The effective irradiance on the solar cell is given by equation 7.13. The heat flux on the solar cells ($\dot{q}_{\mathrm{sc}}$) is then defined as:

$$\dot{q}_{sc} = I_{sc} - P_{PV} \tag{7.15}$$

HEAT TRANSFER COEFFICIENT

Convection Convective heat transfer occurs on all the different layers of the Chimney. At the boundary between ambient air and the front glass, at the back boundary of the front glass and the air within the cavity, on both boundaries of the PV with the air within the cavity. The most suitable equations for the Nusselt number to model the air within the chimney were identified to be:

$$Nu_x = 0.406 \cdot Gr_x^{1/4} \qquad Gr_x < 10^9 \tag{7.16}$$

For laminar flow, and

$$Nu_x = 0.1 \cdot (Gr_x Pr)^{1/3} \qquad Gr_x \geq 10^9 \tag{7.17}$$

For turbulent flow. Where x is the vertical distance along the walls. The Grasshof number is calculated depending on the average temperature of the contained air and the boundary of the studied layer. The convective heat transfer coefficient is then calculated by:

$$h_c = \frac{Nu_x k}{x} \tag{7.18}$$

Where κ is the thermal conductivity of air. Once h_c is known, the heat flux from the boundary layer to the air is known, and the mass flow can be calculated. However, the mass flow also affects the convective heat transfer coefficient. Iteration is required to find the right value of h_c.

Radiation Since any object with a temperature above zero Kelvin irradiates heat, the model makes a distinction between solar radiation and grey body radiation. For the latter, the radiation transmitted to the environment is defined by:

$$Q_{12} = F_{12} \cdot A_1 \cdot \epsilon_1 \cdot \sigma \cdot \left(4\overline{T}^3\right)(T_1 - T_2) \tag{7.19}$$

Where, F_{12} is the view factor of layer 2 seen from layer 1. A_1 is the area of layer 1, ϵ_1 is the emissivity of the material and σ is the Stefaan-Boltzman constant. $\overline{T}$ is the average temperature of layer 1 and layer 2 and T_1 and T_2 are the temperatures of layers 1 and 2 respectively. The radiative heat transfer coefficient is therefore defined by:

$$h_r = F_{12} \cdot \sigma \cdot \epsilon \cdot \left(4\overline{T}^3\right) \tag{7.20}$$

To calculate the view factors, the following equation is used:

$$F_{12} = \left(1 + \left(\frac{d}{H}\right)^2\right)^{0.5} - \frac{d}{H} \tag{7.21}$$

Where d is the depth of the channel and H is the total height. In the model, the view factor is equally divided over the number of vertical control volumes as follows:

$$F_{1N} = \frac{F_{12}}{N_v} \tag{7.22}$$

The façade-to-environment view factor can be calculated by subtracting each layer view factor from the unity.

Conduction For conduction, 2D Fourier's law is used, which is defined by:

$$\rho \cdot c_p \cdot \frac{\partial T}{\partial t} = \frac{\partial}{\partial x}\left(k\frac{\partial T}{\partial x}\right) + \frac{\partial}{\partial y}\left(k\frac{\partial T}{\partial y}\right) + Q_{src} \tag{7.23}$$

Here, Q_{src} is the heat generated by a source. c_p is the specific heat, ρ is the density, and k is the thermal conductivity. In this model, the thermal properties of solids are considered constant.

MASS FLOW MODEL

There are three different analytical methods for calculating the mass flow. One that averages the temperature of the complete air channel, which is often referred to as the single-zone model. In this model, the pressure that drives the flow is calculated based on the difference between the channel temperature and the temperature of the contained air. The second model takes into account the variation of temperature with height and is known as the stratified model. The driving pressure difference is calculated by integrating the density over the height of the chimney [260]. The resulting difference in density is used to calculate the pressure difference that drives the flow. Lastly, the plume model considers both horizontal and vertical variations in temperature. The correction factors for this model were adjusted to increase accuracy and adopted in the current model. Compared to other works [260]–[265], this model has a better accuracy than its alternatives for similar cases.

The model assumes a constant plume depth. However, the temperature value within the plume varies, except for the air contained between the plumes, which is considered constant and equal to the ambient temperature. The model aims to solve the mechanical energy balance, as represented by equation 7.24 in its simplified form.

$$\left(\rho_{\mathrm{e}} - \rho_{\mathrm{ch}}\right) \cdot g \cdot H = \frac{\dot{m}^2}{2A} \cdot \left(\frac{K_{\mathrm{in}}}{\rho_{\mathrm{e}}} + \frac{K_{\mathrm{exit}}}{\rho_{\mathrm{p}}} + \frac{f \cdot H}{d_{\mathrm{h}} \cdot \rho_{\mathrm{ch}}}\right) \tag{7.24}$$

The right side of the equation depicts the pressure loss due to inlet, outlet and channel friction. The entrance and exit friction coefficients (K_{in} and K_{exit}) are equal to 0.5 and 0.88, respectively. The model considers all cavity areas as equal (inlet, outlet and shaft). The Darcy friction factor (f) is calculated as a function of the Reynolds number, the hydraulic diameter of the plume (d_{h}) and the channel area (A). The left side shows the pressure difference as a result from the variation in density.

Density at channel's exit (ρ_{e}), the plume density (ρ_p) and the mean channel density (ρ_{ch}) are calculated using equations 7.25-7.27. The Boussinesq approximation is used to calculate the density of the air in the channel and the resulting difference with the

ambient air. The ideal gas law is considered for the calculation of the plume density ($\rho = p/(RT)$). Finally, the channel depth ratio (ζ) and the weighted mean of the environmental and plume densities, allow to calculate the channel density.

$$\rho_{\text{exit}} = \rho_{\text{e}} \cdot \left(1 - \beta \cdot (T_{\text{exit}} - T_{\text{e}})\right) \tag{7.25}$$

$$\rho_{\text{p}} = \rho_{e} \cdot \frac{T_{\text{e}}}{T_{\text{exit}} - T_{\text{e}}} \cdot \log \cdot \frac{T_{\text{exit}}}{T_{\text{e}}} \tag{7.26}$$

$$\rho_{\text{ch}} = \zeta \cdot \rho_{\text{p}} + \rho_{\text{e}} \cdot (1 - \zeta) \tag{7.27}$$

The thermal boundary layer (δ_{H}, see Figure 7.2) is calculated using equation 7.28, where Ra_H is obtained by the heat flux ($\dot{q}$). The thermal boundary layer is then used to calculate the depth ratio of the plume to the depth of the channel as shown in the equation 7.29. In it, b is a correction factor that is empirically found and n are the expected boundary layers within the plume. In this work, n is always equal to 2, as the model considers each cavity of the chimney as a separate system with the middle layer (e.g., the photovoltaic module) being common for each case. The plume depth-to-channel ratio is used to calculate the channel density and the hydraulic diameter of the plume. Notice that, when this ratio is equal to 1, the plume model is equal to the stratified model.

$$\delta_{\text{H}} = 4.5 \cdot H \cdot \frac{\left(1 + \frac{\text{Pr}}{7.22}\right)^{0.9})^{\frac{2}{9}}}{(\text{Ra}_H \cdot \text{Pr})^{0.2}} \tag{7.28}$$

$$\zeta = n \cdot b \cdot \frac{\delta_{\text{H}}}{d} \tag{7.29}$$

Equations 7.30-7.32 show the correction factors. It can be seen that, for the case of laminar flow, no correction factor is needed. The change from laminar flow to turbulent flow occurs when the Reynolds number value is equal to or exceeds 2300. In his work, He et al. [254] proposed a number of correction factors; however, in this work, other values were deemed more suitable. These factors were optimized by reducing the RMSE between the experimental data and the model. An iterative process was used in which the correction factor started at a low value and was slightly increased until the RMSE reached a minimum.

$$b = 1, \qquad \text{Re}_{\text{ch}} < 2300 \tag{7.30}$$

$$b = 0.00042 \cdot \text{Re}_{\text{ch}}, \qquad Ra_H < 10^{14} \tag{7.31}$$

$$b = 0.000128 \cdot \text{Re}_{\text{ch}}, \qquad Ra_H \geq 10^{14} \tag{7.32}$$

7.3. EXPERIMENTAL SETUP & MEASUREMENT RESULTS

Figure 7.4 shows a sketch of the experimental setup without side material, sensors and without the large area steady-state solar simulator (LASS). The layers, from front to back, consist of glass, PV, and MDF with insulation material. This topology will be referred to as: 'PV Inside (PVI)' throughout the text. Another topology, without front glass, was also measured. This second layout will hence be referred to as: PV in front or PVF (see Figure 7.1). The frame is made of four cylindrical wooden poles that allow one to adjust the depth of the photovoltaic module. MDF extensions were added to the front layer. This was done to prevent irradiance from bypassing the first layer and directly reaching subsequent layers. The built-in setup is depicted in figure 7.5. The main measurements of the setup are listed below.

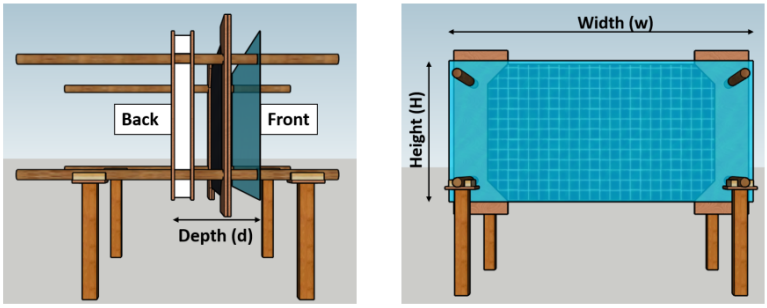

Figure 7.4: Sketch of the setup built for the validation of the mass flow and control volume models.

Figure 7.5: The built setup was built according to the physical properties of the PV module used. To the left, the set up without the front glass. The thermocouples were installed in the geometrical middle of the setup, as it is also shown in 7.6. To the right, the full setup with front glass and the plastic side coverage sheets.

1. The maximum width was determined by the size of the PV module which is 2 m
2. The inlet of the chimney had the same size of the cavity, which varied according to the layout studied
3. The inlet was located at 62.1 cm from the ground floor of the laboratory
4. The outlet of the chimney was located at 164.1 cm from the ground
5. The outlet had the same size as the cavity, and therefore, the inlet

6. The distance from the outlet to the ceiling of the laboratory was 52.8 cm

The frame width is an additional 0.1 m on both sides of the PV module, resulting in a total width of the structure of 2.2 m. Since other large-scale experiments with similar heights did not find an influence of the edges for widths of 1 m, a value of 2.2 m is considered safe from such influence [260]–[267].

The height affects both the mass flow and the temperature distribution of the concept. Ideally, the height is as high as the façade of a building. Therefore, a large height is recommended to reduce potential scaling errors. However, in the experiment, the height was limited to the dimensions of the LASS which stands in front of the test setup. The dimensions of the available photovoltaic modules were 1.02 m by 2 m, which were placed in the landscape position to ensure that the illumination of the LASS was as homogeneous as possible. This positioning limited the height of the remaining layers to 1.02 m, resulting in an aspect ratio of 0.5.

The channel depth was varied between 0.1 and 0.4 m in total, the aim of the experiment was to validate the model and then use it to predict the best location for a PV module.

Layer thicknesses were selected to be as close as possible to real applications. A glass-glass photovoltaic module of 8 mm thickness is used as front or middle layer. When the photovoltaic module is placed in the middle, a hardened glass sheet of 8 mm thickness is used as the front layer. Finally, the back layer consisted of 18 mm thick MDF plates insulated with 60 mm thick polystyrene to simulate an insulating building material.

The sides were closed with plastic sheets to prevent horizontal draft. The layers were placed as vertically as possible, and the inclination readers were taken at each new set of data collection.

7.3.1. MEASUREMENT SENSORS

Four variables were monitored using five different sensors. Their main characteristics are summarized in Table 7.1. Thermocouples of T-type PFA exposed welded tip from RS components were used to measure the temperatures of the front and back walls at each layer. A total of seven were used on each side to measure a temperature profile. Measurements were stored using a PicoLog TC-08 USB datalogger. The ambient temperature was also measured with a fully shaded thermocouple, which prevented any potential measurement bias.

Table 7.1: Sensors used in the experiment depicted with the range and accuracy provided by the manufacturer.

Sensor type	Range	Accuracy
Hot sphere anemometer	0 to 10 m/s	± (0.03 m/s + 5% of mv)
Hot sphere anemometer	-20 to 70°C	Not specified
Thermocouple T-type	-40 to 350°C	± 0.5 or ± 0.004T (°C)
GC-10 Eltek humidity sensor	0 to 100%	± 2%
GC-10 Eltek temperature sensor	-30 to 65	± 0.4 °C
Kipp & Zonen SPM10-A pyranometer	285 to 2800 nm	< 10 W/m^2

A hot sphere anemometer was used to measure both the temperature and velocity profile of the air. The latter was then used to calculate the mass flow. Both the temperature profile and the mass flow were used to estimate the convective heat flow. The sensor used was a Testo hot bulb probe with 3 mm of diameter (reference 0635 1049) alongside the Testo 445 multi-function instrument, which was used to log all the measurements.

A humidity sensor was used to measure humidity, as relative humidity could influence the Nusselt number by up to 2% and the Prandtl number by up to 5% under current test conditions [268]. Finally, a pyranometer was used to measure incident irradiance on both the front glass and the photovoltaic module of the experimental façade.

In total 42 thermocouples, 3 heat flux sensors, a humidity sensor, a pyranometer, and a hot-sphere anemometer were used for this experiment. All measurements were recorded using their corresponding manufacturer data logger.

7.3.2. SENSOR PLACEMENT

As mentioned above, seven thermocouples were used in each of the chimney layers to produce temperature profiles. Their distribution in each of the chimney layers is shown in Figure 7.6. In the last layer of the PV chimney structure (the building wall), two heat flux sensors were used, replacing 2 thermocouples, the top and bottom ones. The humidity sensor was attached to the structure and hidden from direct irradiance from the LASS. The anemometer was located 0.10 m below the exit of the air channel.

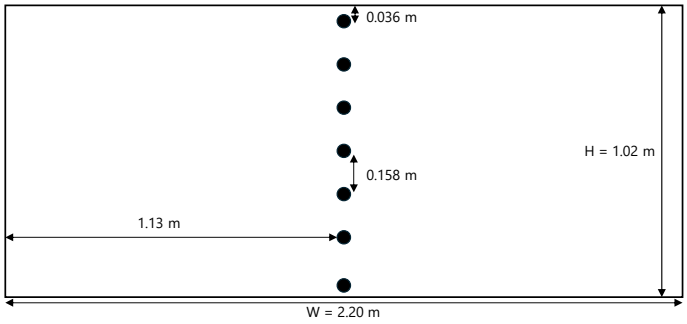

Figure 7.6: Thermocouple (depicted by the black dots) distribution on each of the layers of the Chimney, they were installed equidistant from one another, and located at the center of the layers

Before starting the complete set of measurements, three small experiments were conducted to increase accuracy and confirm initial assumptions in the model. First, since irradiance is the driving force behind the stack effect on the chimney, its impact on the measurement of air velocity was studied. Using a 20-second time scale in value averaging, the RMSE value was found to be below that of the equipment error. Second, the natural draught of the room was measured. It was found that values equal to or below 0.2 m/s could be caused by the room and not by the stack effect on the chimney. Lastly, measurements were performed to compare the inlet air temperature of the chimney with the ambient temperature of the room. It was confirmed that these values can be considered equal, as assumed by the thermal model.

7.3.3. TOPOLOGY MEASUREMENTS

Two main chimney topologies were considered for the measurements, as depicted in Figure 7.1. First, a layout which considers the photovoltaic module as the front layer of the cavity is henceforth known as (PVF). The second, which considers the photovoltaic located inside the cavity, is henceforth known as (PVI). The distances studied, which determine the main cavity of the facade (for the PVF case) and the two subcavities of the chimney (for the case of PVI), are summarized in Table 7.2.

Table 7.2: Topologies measured during the experiment. The second and third column show the depth of the different cavities when the PV is either at the front (PVF) or inside (PVI).d_1 and d_2 refer to the depth of the first and second cavity, respectively.

Topology	d_1	d_2	Measurements
PVF 0.1	0.1 m	-	3
PVF 0.2	0.2 m	-	3
PVF 0.4	0.4 m	-	4
PVI 0.1 - 0.1	0.1 m	0.1 m	2
PVI 0.2 - 0.2	0.2 m	0.2 m	2
PVI 0.3 - 0.1	0.3 m	0.1 m	2
PVI 0.1 - 0.3	0.1 m	0.3 m	2

7.3.4. UNCERTAINTY

Bias errors were reduced by using automated data loggers for all measurements, except air velocity. This value was taken once the new position of the probe reached steady state. The steady state was considered reached if the value did not change for more than 20 seconds. The data obtained did not show any sign of bias.

Random errors were quantified using the mean squared error value (RMSE) or the standard deviation, which is equal when the bias error is zero. Calculation of the RMSE error was done via:

$$RMSE = \sqrt{\frac{1}{N}\sum_{i=1}^{N}\left(e_i - \overline{e}\right)^2} \tag{7.33}$$

7.3.5. RESULTS AND ANALYSIS

IRRADIANCE MEASUREMENTS

Irradiance measurements were carried out on 24 different points on both the front PV module, for the case of the PVF, and on the front layer of both the glass and the PV module located inside the cavity, for the PVI. Measured values are summarized on Table 7.3. Irradiance values are not homogeneous across the front layer of the structure. The largest vertical deviation has a value of 147 $W \cdot m^{-2}$, and the largest horizontal deviation is 157 $W \cdot m^{-2}$.

Table 7.3: The measured irradiance including the RMSE ($W \cdot m^{-2}$) in front of the first layer. The distance from the top and the side for each measurement is shown on the left and upper column, respectively.

		Distance from the left side, viewed from the front					
		0.42 m	0.74 m	1.05 m	1.21 m	1.52 m	1.84 m
Dist. from top	0.11 m	1578 ± 7	1651 ± 15	1672 ± 17	1671 ± 5	1669 ± 8	1533 ± 11
	0.43 m	1603 ± 8	1702 ± 5	1710 ± 1	1725 ± 5	1705 ± 7	1569 ± 10
	0.59 m	1578 ± 8	1680 ± 5	1692 ± 7	1702 ± 10	1695 ± 4	1567 ± 17
	0.90 m	1442 ± 16	1578 ± 30	1568 ± 12	1536 ± 30	1574 ± 19	1491 ± 23

For the case of the PVI layout, the measured irradiance on the PV module located inside the cavity allowed the quantification of reflection and absorption losses on the front glass. Given that the layers had the same height and width, measurements were taken at the same locations. Table 7.4 shows the measured values. The average absorption in the glass was found to be 27%. This high value is explained by the amount of infrared radiation emitted by the LASS. For both the PVI and PVF layouts, the PV module was installed but not connected, modeling a condition V_{OC}.

Table 7.4: The measured irradiance including the RMSE ($W \cdot m^{-2}$), 65 mm behind the glass layer. The distance from the top and the side for each measurement is shown in the second column respectively the second row.

		Distance from the left side, viewed from the front					
		0.42 m	0.74 m	1.05 m	1.21 m	1.52 m	1.84 m
Dis. from top	0.11 m	1078 ± 46	1110 ± 6	1111 ± 38	1115 ± 11	1119 ± 11	1038 ± 27
	0.43 m	1179 ± 52	1238 ± 7	1224 ± 37	1259 ± 8	1244 ± 4	1113 ± 7
	0.59 m	1192 ± 55	1256 ± 7	1231 ± 48	1279 ± 9	1260 ± 8	1128 ± 12
	0.90 m	1169 ± 49	1213 ± 15	1183 ± 42	1236 ± 13	1235 ± 12	1099 ± 12

ENVIRONMENT AIR TEMPERATURE

Table 7.5 summarizes the average environmental temperature measured during the different layout setups. It can be seen that there is a maximum difference of 6 k between the measurement of the PVF layout with a cavity depth of 0.1 m and the PVI layout located in the middle of a 0.48 m chimney cavity. A lower ambient temperature increases the difference in temperature with respect to the air within the cavity. This results in higher mass flow. However, in the experiment this effect was found negligible compared to the effects of the cavity depth.

Table 7.5: Environment temperature and RMSE (°C) for all topologies. Where PVF means PV as front layer, and PVI means the PV located inside. The distances stand for the first respective second air channel depths.

Topology	Temperature (°C)
PVF, 0.4 m	29.8 ± 0.2
PVF, 0.2 m	29.6 ± 0.3
PVF, 0.1 m	32.8 ± 0.4
PVI, 0.1,0.1 m	28.9 ± 0.2
PVI, 0.2,0.2 m	27.9 ± 0.4
PVI, 0.3,0.1 m	29.4 ± 0.4
PVI, 0.1,0.3 m	26.9 ± 0.4

AIR HUMIDITY MEASUREMENTS

According to [268], the difference in the value of the Nusselt number for dry air contained within a channel at 77 °C average temperature, with 50 % humid air under the same conditions, is close to 1 %. As table 7.6 shows, such difference in humidity was never achieved, therefore, the effect on the Nusselt number can be considered negligible.

Table 7.6: Relative humidity and RMSE (%) of the environment air for all topologies. Where PVF and PVI follow the explanation found in table 7.5

Topology	Relative humidity (%)
PVF, 0.4 m	40.1 ± 0.7
PVF, 0.2 m	32.3 ± 0.8
PVF, 0.1 m	32.5 ± 0.8
PVI, 0.1,0.1 m	35.0 ± 0.4
PVI, 0.2,0.2 m	25.2 ± 0.4
PVI, 0.3,0.1 m	31.7 ± 0.5
PVI, 0.1,0.3 m	36.2 ± 0.5

ANEMOMETER TEMPERATURE PROFILES

Air temperature profiles across the cavity for both layouts were measured with the hot sphere anemometer and compared with the closest surface thermocouple. The cavity geometry, the layout of both configurations and the profiles obtained are reported in [269]. Thermal boundary layers were clearly visible on both cases. For the PVI layout, the air temperature at the middle of both cavities was higher than the air temperature at the middle of the PVF cavity. Lower air volume and higher surface temperatures on the surfaces forming channel 1 (front glass and PV) are the cause of this difference. In Channel 2 (PV and MDF), shows surface temperatures lower than the PVF case, but the horizontal temperature profile is higher. High velocity is the most likely reason behind this difference.

VELOCITY PROFILES

Velocity profile measurements are also reported in [269]. Centre velocity is larger in channel 1 when compared to the other cavities, and shows close symmetry in shape

with its temperature profile. It was observed that the higher the surface temperature on a layer, the higher the velocity of air near its boundary. The air velocity in channel 1 is almost 3 times that of channel 2, despite having the same depth, due to their difference in temperature.

SURFACE TEMPERATURES

For the sake of brevity, only two layouts will be discussed in this section. A PVF with 0.2 m cavity and a PVI with a PV module located in the middle of a 0.2 m cavity (i.e. two sub-cavities of 0.1 m each). Surface temperatures were measured and then averaged over the entire duration of the activity. The RMSE was calculated and analyzed to see the effect of the different layouts. Table 7.7 shows the temperatures of the PVF, on both the front layer (the PV module) and the back layer (the building material, here MDF). The seven temperatures belong to each thermocouple located on each layer as depicted by Figure 7.6.

Table 7.7: The average temperature (°C) readings of the thermocouples placed on the surface of each layer. The PV was located in front with a channel depth of 0.2 m. Readings were taken each second during all flow measurements. The RMSE of the readings are shown behind the plus minus symbol (±). The horizontal location of each thermocouple is depicted in figure 7.6.

Distance	PV		MDF	
from top (m)	Front T (°C)	Back T (°C)	Front T (°C)	Back T (°C)
0.04	113.1 ± 0.5	106.1 ± 0.6	61.6 ± 0.8	-
0.19	112.2 ± 0.7	108.2 ± 0.8	68.0 ± 0.8	31.0 ± 0.5
0.35	113.2 ± 0.8	107.0 ± 0.8	68.1 ± 0.8	31.1 ± 0.5
0.51	116.4 ± 0.6	106.8 ± 0.6	69.9 ± 0.8	30.6 ± 0.5
0.67	107.7 ± 0.5	103.7 ± 0.4	66.2 ± 0.7	30.0 ± 0.5
0.83	104.8 ± 0.4	97.5 ± 0.3	59.2 ± 0.6	29.2 ± 0.5
0.98	96.9 ± 0.7	87.0 ± 0.4	45.9 ± 0.4	-

A vertical gradient of temperatures (lower on the bottom, higher on the top) is expected. However, the non-homogeneous nature of the LASS irradiance, as shown in table 7.5, produces a similar pattern in temperatures on the front surface of the PV module as that of the irradiance measured.

For the case of the PVI with a 0.2 m cavity depth, the surface temperatures can be found on table 7.8. Similar to the PVF case, an increasing temperature gradient is formed from bottom to the top. Temperature of the PV module is lower than the case of the PVF. The reasons for this are the following: first, the LASS solar simulator produced a significant amount of infrared radiation (as discussed earlier). The front glass absorbs a relatively large quantity of it (27%). For the case of the PVF, all this radiation reaches directly the PV module. Second, the first layer on all the experiments was located very close to the LASS solar simulator, which produces higher radiative temperature from the environment, this condition will not occur under real ambient conditions.

Table 7.8: The average temperature (°C) readings of the thermocouples placed on the surface of each layer. The PV was located in the middle of a 0.2 m cavity producing two channels of 0.1 m. Readings were taken each second during all flow measurements. The RMSE of the readings are shown behind the plus minus symbol (±). The horizontal location of each thermocouple is depicted in figure 7.6

Distance	Glass		PV		MDF	
from top (m)	Front T (°C)	Back T (°C)	Front T (°C)	Back T (°C)	Front T (°C)	Back T (°C)
0.04	75.8 ± 0.2	88.0 ± 0.3	89.2 ± 0.2	88.1 ± 0.3	60.7 ± 0.3	-
0.19	81.1 ± 0.2	97.1 ± 0.3	101.1 ± 0.2	96.2 ± 0.3	66.1 ± 0.3	31.6 ± 0.2
0.35	84.2 ± 0.2	98.1 ± 0.4	100.9 ± 0.2	92.9 ± 0.3	63.5 ± 0.3	31.4 ± 0.2
0.51	88.4 ± 0.2	91.9 ± 0.3	97.3 ± 0.2	90.3 ± 0.3	61.4 ± 0.3	30.8 ± 0.2
0.67	84.1 ± 0.3	84.0 ± 0.3	90.4 ± 0.2	84.8 ± 0.2	56.1 ± 0.4	30.0 ± 0.2
0.83	72.8 ± 0.4	75.5 ± 0.3	79.9 ± 0.2	75.6 ± 0.2	48.2 ± 0.5	29.1 ± 0.2
0.98	66.0 ± 0.4	61.1 ± 0.3	65.8 ± 0.2	60.9 ± 0.3	45.6 ± 0.3	-

HEAT FLOW

Integrating the product of density, velocity, and temperature difference gives the convective heat flow through the channel. Due to the nature of the data, trapezoidal integration was used, and therefore the convective heat flow is given by Equation 7.34:

$$\dot{Q}' = c_p \sum_{i=1}^{N} \frac{\rho\left(T_{i-1}\right) v_{i-1}\left[T_{i-1} - T_e\right] + \rho\left(T_i\right) v_i\left[T_i - T_e\right]}{2} \Delta x_i \tag{7.34}$$

Thermophysical properties of air were obtained by linear interpolation on a lookup table similar to [250]. Given that humidity was considered negligible, dry air properties were used, specfic heat was assumed constant and equal to 1007 J/kg · K. The heatflow is unidirectional given that across the width of the layers all properties were considered constant. Table 7.9 show the results for all the topologies measured.

Table 7.9: The heat flow and respective progressed RMSE of different topologies. The values in red are physically impossible. It is assumed that the irradiance incident on the anemometer significantly increased its readings.

Topology	$\dot{Q}'$ channel 1 (W/m)	$\dot{Q}'$ channel 2 (W/m)	$\dot{Q}'$ total (W/m)
PVF 0.4 m	1592 ± 99	-	1592 ± 99
PVF 0.2 m	1396 ± 109	-	1396 ± 109
PVF 0.1 m	1411 ± 145	-	1411 ± 145
PVI 0.2, 0.2 m	3020 ± 162	457 ± 56	3476 ± 218
PVI 0.3, 0.1 m	2864 ± 114	686 ± 33	3550 ± 147
PVI 0.1, 0.3 m	4438 ± 47	394 ± 65	4832 ± 112
PVI 0.1, 0.1 m	4895 ± 64	750 ± 25	5646 ± 89

It can be observed that the incident heat, provided by the LASS solar simulator, is lower than the heat flux on channel 1. This is thermodynamically impossible. The reason for this discrepancy is the influence of direct irradiance on the anemometer. It can be seen that the values of heat flux on Channel 2 are far more consistent. In this channel the anemometer is completely hidden from irradiance coming from the LASS. Given this,

the values highlighted in red were discarded and not used for validation or analysis. The exit temperature for each channel depth is shown in Table 7.10

Table 7.10: The exit temperatures and the environmental temperature including the RMSE for all topologies.

Topology	T_{exit} channel 1 (°C)	T_{exit} channel 2 (°C)	T_e (°C)
PVF 0.4 m	37.0 ± 0.4	-	29.8 ± 0.2
PVF 0.2 m	40.8 ± 0.1	-	29.6 ± 0.3
PVF 0.1 m	48.0 ± 0.3	-	32.8 ± 0.4
PVI 0.2, 0.2 m	46.5 ± 1.9	37.1 ± 0.1	27.9 ± 0.4
PVI 0.3, 0.1 m	45.1 ± 1.4	43.5 ± 0.1	29.4 ± 0.4
PVI 0.1, 0.3 m	52.6 ± 0.7	35.4 ± 0.1	26.9 ± 0.4
PVI 0.1, 0.1 m	54.1 ± 1.0	44.1 ± 0.1	28.9 ± 0.2

MASS FLOW

Trapezoidal integration of the product of velocity and density yields the total mass flow:

$$\dot{m}' = \sum_{i=1}^{N} \frac{\rho\left(T_{i-1}\right) v_{i-1} + \rho\left(T_i\right) v_i}{2} \Delta x_i \tag{7.35}$$

The results are summarized on table 7.11 for all the topologies measured. The mass flow increases with the depth of the channel for the PVF topology. However, as mentioned before, a maximum draft of 0.2 m/s was measured in the room. The value measured for the case of a cavity of 0.4 m in the PVF was of 0.15 m/s. It cannot be concluded if this flow is the product of the draught in the room, or any effect caused by the PVF at such depth. This same condition appears on the PVI layout, where channel 1 has a depth of 0.1 and a channel 2 depth of 0.3. In this layout, the latter also produces a mass flow below the natural draught of the room.

Table 7.11: The mass flow per meter width and respective RMSE of different topologies. Channel 1 is the first channel from the front of the façade, channel 2 is the 2nd channel.

Topology	$\dot{m}'$ channel 1 (kg/(sm))	$\dot{m}'$ channel 2 (kg/(sm))	$\dot{m}'$ total (kg/(sm))
PVF 0.4 m	0.14 ± 0.00	-	0.14 ± 0.00
PVF 0.2 m	0.11 ± 0.01	-	0.11 ± 0.01
PVF 0.1 m	0.09 ± 0.01	-	0.09 ± 0.01
PVI 0.2, 0.2 m	0.14 ± 0.01	0.08 ± 0.00	0.23 ± 0.02
PVI 0.3, 0.1 m	0.15 ± 0.00	0.06 ± 0.00	0.21 ± 0.00
PVI 0.1, 0.3 m	0.17 ± 0.00	0.10 ± 0.00	0.26 ± 0.01
PVI 0.1, 0.1 m	0.17 ± 0.01	0.07 ± 0.00	0.24 ± 0.01

For the PVF layout, increasing the cavity depth from 0.1 m to 0.2 m has a very small effect on mass flow. However, using a similar depth and placing a PV module in the middle of the cavity more than doubles the flow. However, care should be taken as front-side measurements have been shown to be biased, as explained in Table 7.9. Looking only at channel 2 shows that the flow difference between both layouts is not large.

An analysis of the surface temperatures shows that, for the case of the PVI, the temperatures on both surfaces of the front glass and on the front surface of the PV module are larger than the back surface of the PV module and the MDF. This indicates that the mass flow on the first channel must be greater. Thus, the PVI layout yields a higher mass flow compared to the PVF.

PV TEMPERATURE

Given the important effect that temperature has on the performance of the PV modules, operating temperatures of the PV modules warrant a separate analysis. Table 7.12 shows the average temperatures and RSME values for all the measured layouts.

Table 7.12: The mean surface temperatures including the RMSE of the PV module for different topologies.

Topology	Mean PV front T (°C)	Mean PV back T (°C)
PVF 0.4 m	112.5 ± 0.8	103.0 ± 0.8
PVF 0.2 m	109.5 ± 0.6	102.8 ± 0.6
PVF 0.1 m	109.6 ± 0.3	108.0 ± 0.3
PVI 0.2, 0.2 m	83.8 ± 0.4	78.6 ± 0.4
PVI 0.3, 0.1 m	82.5 ± 0.3	78.3 ± 0.3
PVI 0.1, 0.3 m	85.7 ± 0.4	79.9 ± 0.5
PVI 0.1, 0.1 m	90.2 ± 0.2	84.9 ± 0.3

It can be seen that, as the cavity depth increases in the case of the PVF layout, the differences between the measured temperature at the front and back sides of the photovoltaic module also increase. Going from a depth of 0.2 m to 0.4 m, the variation of the back surface temperature in the photovoltaic module does not change significantly.

For the PVI layout, a trend seems to be clear: the closer the PV module is to the front glass, the higher its surface temperatures, both at the front and at the back. This applies to smaller depths on channel 1 more than on channel 2. In the latter case, since the MDF temperature is lower compared to the front glass temperature, the PV module temperature will be lower for smaller values of depth in channel 2.

It is important to note that the LASS used induces a bias in the measurements. The high infrared radiation and the very small distance between the LASS and the front layer cause a very high ambient temperature around the front layers, thus inducing effects not found in real-life applications.

7.4. VALIDATION OF THE COMPUTATIONAL MODEL

7.4.1. IRRADIANCE MODEL

The calculated incident irradiance was compared to a similar system using the System Advisor Model (SAM), a validated model created by NREL [270]. As can be seen in Figures 7.7a and 7.7b, both the direct and diffuse components on the plane of the array irradiance (G_{POA}) are in good agreement with the results obtained using SAM, which are models validated by NREL.

The root mean square difference of the model compared to SAM is of 0.4%.

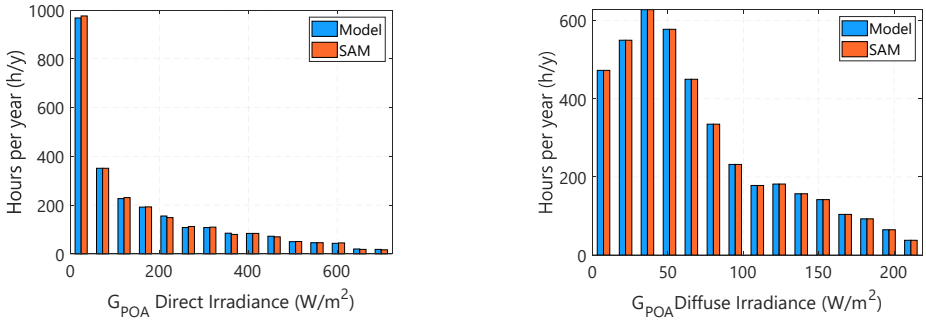

(a) (b)

Figure 7.7: A typical mean year weather file from weather station the Bilt in the Netherlands is used to model the expected direct **(a)** and diffuse **(b)** irradiance on a south oriented vertical wall. The results of the current model are compared with the results produced by the NREL-SAM using an equal orientation and the same weather file

7.4.2. CONTROL VOLUME MODEL AND MASS FLOW MODEL

Once the irradiance model was validated, the input from the experimental setup was used on the control model and the mass flow model to study their accuracy. The mean irradiance measured at the location of the thermocouples was used as input. Other relevant input variables are summarized in Table 7.13. The time taken by the setup to reach steady state was less than 3 hours.

Table 7.13: Input parameters used to model the experimental conditions.

Input variable	Value	Unit
Vertical control volumes	14	-
Horizontal control volumes / layer	5	-
Irradiance	1664.8	W/m^2
Angle of incidence	0	°
Roughness	0.0002	m
Time	3	h
Timestep	100	s

MASS FLOW MODEL

Given that the results for the PVF are calculated in a non-dimensional form, they are suitable for comparison with other studies with similar layouts. The ambient temperature was used to calculate all relevant properties of air. The modified Rayleigh number was obtained using Equation 7.36.

$$Ra^* = \left(\frac{g\beta H^4 q}{a\nu k}\right)\frac{d}{H} \tag{7.36}$$

With this modified Rayleigh number, the results were compared with those of other

relevant studies. The work of Liu et al. [265] was the only one of these in which an artificial light source is used. The results obtained are strongly correlated to those of Liu. Other data sets also show a strong correlation with the modified Rayleigh number, but their gradients change from one another. Figure 7.8 shows that the model can accurately model the mass flow of the PVF layout. It is important to note that, in Figure 7.8, the data from [265] was calculated with the correction factors presented in this work. Given that measurements for the layout of the PV module inside (PVI) produced a thermodynamically impossible scenario, due to the significant impact that the irradiance from the LASS had on the anemometer, the validation for this layout could not be carried out.

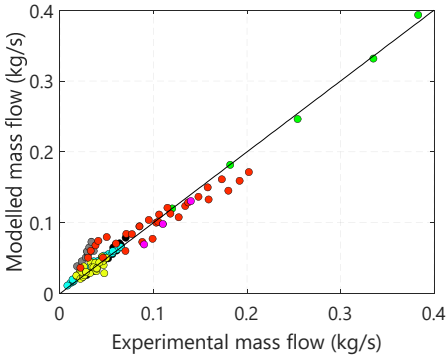

Figure 7.8: Modeled vs measured mass flow for multiple experimental data sets including the current research in kg/s. The current research values represent the PVF layout. The studies shown in this graph are: Green [262], grey [260], yellow [254], cyan [263], black [261]; red belongs to [265] with the *modified* correction presented on this work. Finally, magenta are the results of the experiments carried in this work

LOCAL SURFACE TEMPERATURE

Vertical temperature profiles were calculated for each layer and compared to the measurements obtained. Figure 7.9 and figure 7.10 show the vertical profiles for the PVF and PVI layout, respectively. In the former, the cavity depth was considered as 0.4 m. In the latter, the PV module was located at 0.1 m from the front glass and 0.3 m from the back surface. A good agreement for the temperature profiles of the back of the MDF surface and the front of the MDF surface on the PVI layout was observed for both experiments. The temperature of the front and back of the PV module is almost non-dependent on distance, whereas in the experiment a clear dependency is observed. This could be due to the simplification of the thermal resistance of the module, which is modeled by a single thermal resistance. Individual layer resistances were not considered. From the graphs, at 0.4 m from the bottom a concave behavior is observed, indicating the transition from laminar to turbulent flow. For the case of the PVI, front layer glass surface is plotted separately, and can be found on Figure 7.11.

Transient behavior was also compared for the different layouts. The model presents a good agreement with the front side of the PV module on the PVF case, an overestimation of the MDF front surface and a back MDF surface temperature difference that gets smaller with time (Figure 7.12). This last difference might be improved if the ambient

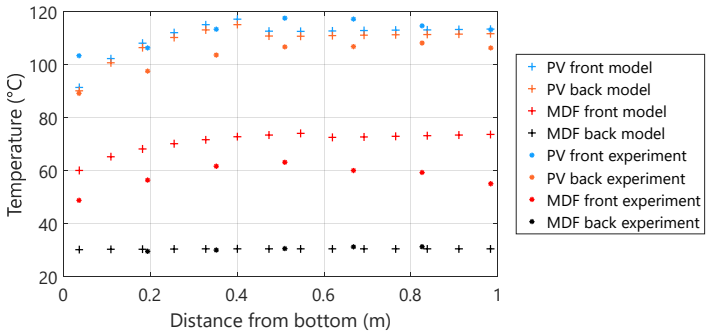

Figure 7.9: Local surface temperatures at each vertical position starting from the bottom for a PVF layout with a cavity depth of 0.4 m, modeled under homogeneous irradiance

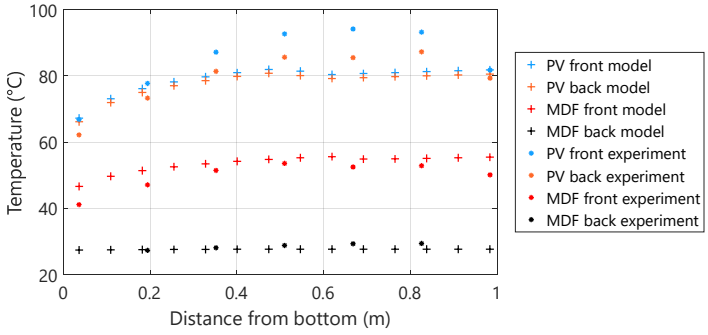

Figure 7.10: Local surface temperatures at each vertical position starting from the bottom for a PVI layout with channel depths of 0.1 m (channel 1) and 0.3 m (channel 2), modeled under homogeneous irradiance

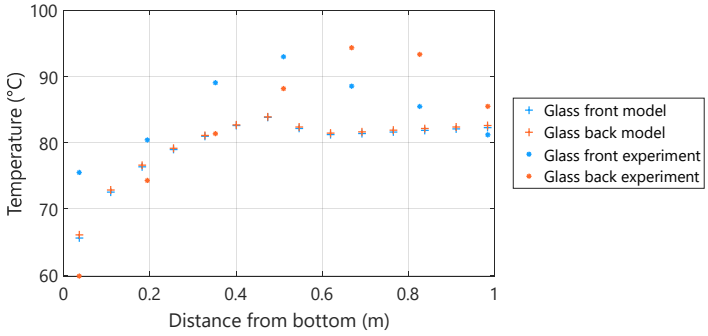

Figure 7.11: Local surface temperatures at each vertical position starting from the bottom for the front glass of the PVI layout, modeled under homogeneous irradiance

temperature is also varied with time, and not considered fixed as in the model. Given

the high power output of the LASS, the environmental temperature increased over time.

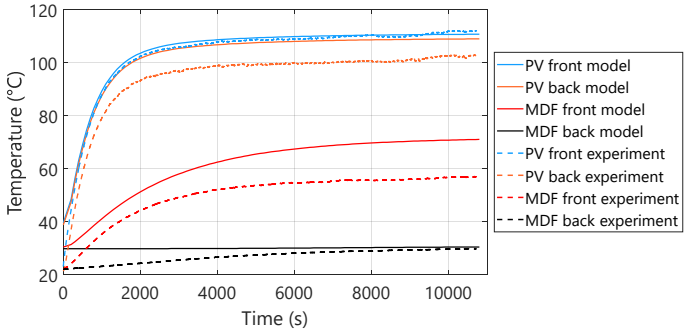

Figure 7.12: Transient behavior of the temperatures at the different surfaces on a PVF layout

For the PVI layout, an underestimation of the front PV temperature is observed and a better agreement of the front MDF front layer temperature, as depicted by Figure 7.13.

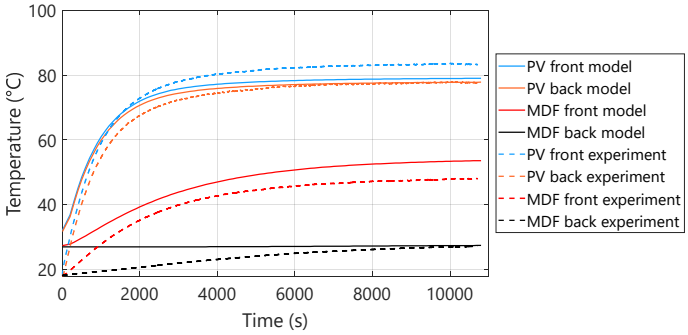

Figure 7.13: Transient behavior of the temperatures at the different surfaces on a PVI layout

AVERAGE VALUES AND RMSE

Convective heat flows were calculated by:

$$\dot{q} = c_p \left(T_{\text{exit}} - T_{\text{e}}\right) \dot{m} \tag{7.37}$$

All the results are summarized on Table 7.14.

Table 7.14: Model results of average surface temperatures, exit air flow temperatures, mass flows and heat flows per meter width. f stands for the front surface of the layer, b stands for the back surface, 1 stands for the front air channel and 2 stands for the back air channel.

Topology	T (°C) air 1	T (°C) air 2	T (°C) glass f	T (°C) glass b	T (°C) PV f	T (°C) PV b	T (°C) MDF f	T (°C) MDF b	$\dot{m}'$ (kg/sm) air 1	$\dot{m}'$ (kg/sm) air 2	$\dot{q}'$ (W/m) air 1	$\dot{q}'$ (W/m) air 2
PVF 0.4	36.1				110.7	108.9	71.0	30.4	0.14		886	
PVF 0.2	38.4				110.4	108.7	75.0	30.3	0.10		890	
PVF 0.1	47.1				115.3	113.7	83.2	33.6	0.06		882	
PVI 0.2,0.2	35.1	33.7	79.4	79.3	78.8	77.8	55.5	28.3	0.09	0.08	675	480
PVI 0.3,0.1	35.5	38.6	80.8	80.7	80.7	79.7	59.5	29.9	0.11	0.05	687	468
PVI 0.1,0.3	38.4	31.8	79.6	79.5	79.0	77.8	53.6	27.3	0.06	0.10	655	495
PVI 0.1,0.1	40.6	38.4	82.1	82.1	81.9	80.8	59.9	29.4	0.06	0.05	665	488

The differences between the model and the measurements for each layout are depicted in table 7.15.

Table 7.15: Model difference of average surface temperatures, exit air flow temperatures, mass flows and heat flows per meter width when compared with the experiment. f stands for the front surface of the layer, b stands for the back surface, 1 stands for the front air channel and 2 stands for the back air channel.

Topology	ΔT (K) air 1	ΔT (K) air 2	ΔT (K) glass f	ΔT (K) glass b	ΔT (K) PV f	ΔT (K) PV b	ΔT (K) MDF f	ΔT (K) MDF b	$\dot{m}'$ (kg/sm) air 1	$\dot{m}'$ (kg/sm) air 2	$\dot{q}'$ (W/m) air 1	$\dot{q}'$ (W/m) air 2
PVF 0.4	-0.9				-1.8	5.9	12.7	-0.1	-0.00		-705	
PVF 0.2	-2.4				0.9	5.9	11.5	0.0	-0.01		-506	
PVF 0.1	-0.9				5.7	5.7	18.2	0.7	-0.03		-529	
PVI 0.2,0.2		-3.4	-5.6	-0.3	-5.0	-0.8	3.9	-0.9		0.00		23
PVI 0.3,0.1		-4.9	-0.7	3.0	-1.8	1.4	5.4	-1.1		-0.01		-218
PVI 0.1,0.3		-3.6	-5.7	-3.7	-6.7	-2.1	3.4	-1.3		-0.00		102
PVI 0.1,0.1		-5.7	2.5	-3.9	-8.3	-4.1	2.2	-1.1		-0.02		-263

Relative RMSE values were obtained by dividing the absolute RMSE by the mean of the measurement values. RMSE for temperatures were calculated with the mean of the difference in temperature relative to environment. With respect to temperatures, the RMSE value is 5.27 °C. PV temperatures were 4.66 °C. The mass flow was 0.014 kg/s. Lastly, convective heat flow had the highest RMSE value, with 407 W. The models tend to underestimate the heat flow on both layouts.

7.5. PERFORMANCE OF A PV CHIMNEY: SENSITIVITY ANALYSIS

The performance of a PV chimney was carried out by comparing both topologies, PVF and PVI, for a three-story construction in Amsterdam, The Netherlands. The façade size, on both cases was assumed 10 m by 10 m, oriented toward the south. The input variables for the models are summarized in Table 7.16.

Table 7.16: Modeled input variables for a PVF and a PVI Chimney

Variable	PVF	PVI
Orientation	South (180°)	South (180°)
height	10 m	10 m
width	10 m	10 m
material 1	PV	glass
depth material 1	0.008 m	0.008 m
material 2	brick masonry	PV
depth material 2	0.1 m	0.008 m
material 3	mineral wool	brick masonry
depth 3	0.06 m	0.1 m
material 4	brick masonry	mineral wool
depth 4	0.1 m	0.06 m
material 5	-	brick masonry
depth 5	-	0.1 m

The model was used to perform a basic sensitivity analysis of the heat flow generation and electricity production for the PVF and PVI cases. The first step was to study the effect of the channel depth on both variables. The depth ranged from 0.2 m to 1.02 m in steps of 0.04 m. It was found that at smaller depths, the heat flow generation changed significantly until it reached a plateau at 0.2 m. From this depth on, the increase in heat flows grows slightly to a depth value of 0.4 m. The PVI, due to its configuration, has a higher heat flow than the PVF (see Figure 7.14a). However, the PV modules on the PVI layout work at higher temperatures compared to the PVF layout, reducing their electrical performance, as can be seen in Figure 7.14b.

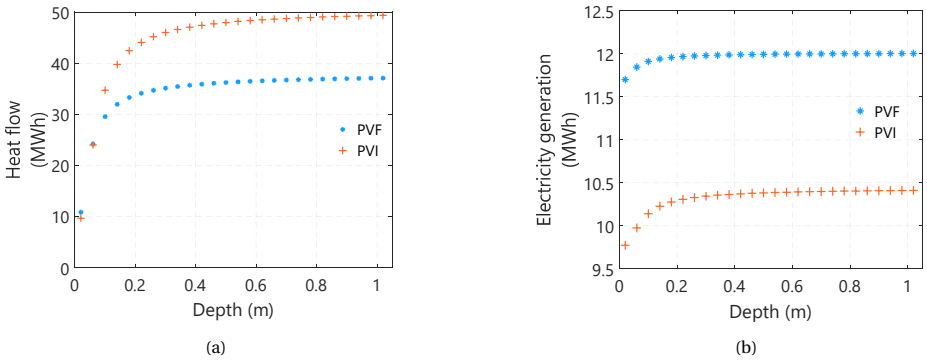

Figure 7.14: Yearly heat flow **(a)** and electricity **(b)** generation for a PVF and PVI as function of channel depth

For the PVI case, simulations were performed with the aim of finding the best position of the PV module inside the channel. As in the case of cavity depth, both yearly heat flow and electricity production were studied. The modules were located from 0.01

m from the front glass to 0.01 m from the masonry wall with steps of 0.01 m. An optimum for annual heat flow production was found when the PV modules were located near the middle of the cavity, slightly closer to the front glass (see figure 7.15a). To maximize yearly electricity production, the middle of the cavity also yields the highest values, slightly closer to the masonry wall (see figure 7.15b). In general, the optimal placement of the photovoltaic modules is in the middle of the cavity, at 0.1 m.

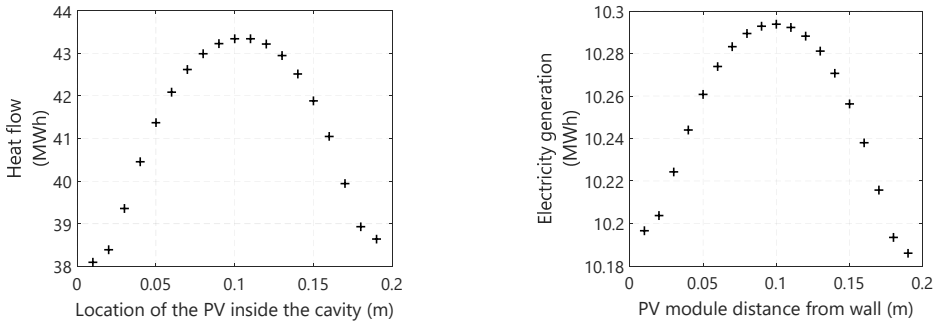

(a) (b)

Figure 7.15: Yearly heat flow **(a)** and electricity **(b)** generation for different locations of the PV module within the cavity depth for the PVI layout.

Further improvements for this model include: complete modeling of the electrical and heat demand of households as a function of their built areas. Inclusion of the effect of the wind speed in the air. Automatic optimization of a PVF or PVI that includes orientation, height, width, and cavity depth based on meteorological data for the location at which the technology will be implemented.

7.6. CONCLUSIONS

A new modeling method for the combination of two building energy methods, the PVF and the PVI of an integrated Chimney has been proposed and validated with experimental data. The user has the ability to provide input on the meteorological conditions of the desired location of installation, the materials to be used, the geometry of the double faç ade, and the specifications of the PV module chosen. The model calculates the resulting POA irradiance, temperature profiles, mass flow, and heat flow.

The relative RMSE of temperature, PV temperature, mass flow and heat flow were found to be 14.6, 7.3, 14.9 and 42.7 per cent respectively. Thus, it was found that both the PVF and the PVI layouts could be modeled by a 2D control volume thermal model. The heat flow could also be modeled, although care should be taken with respect to its accuracy.

A relative RMSD of 0.4% was found when comparing the irradiance model of this study with the irradiance model of SAM [270]. .

A sensitivity analysis was performed to find the effect of channel depth on the heat and electricity production of a PVF/PVI layout. An optimum cavity for the PVF layout is expected between 0 and 0.1 m. The generation of electricity and heat flow by pho-

tovoltaic modules within a PVI layout increased at positions closer to the building wall, reaching a plateau at cavity depths of around 0.2 m. The optimal location for the photovoltaic module in the channel for the base case (total channel depth of 0.2 m) was found in the middle, at 0.1 m.

8

CONCLUSIONS AND OUTLOOK

The works contained in this document were developed with the aim of contributing to the growing demands for accurate modeling and understanding of the particularities of building integrated photovoltaic (BIPV) solutions. Adapting standard photovoltaic modules to BIPV systems requires a number of technical challenges, particularly those of providing aesthetic versatility and providing reasonable electrical performance. To this end, the work developed in this book expands on the already substantial knowledge provided by previous research. The main contributions to the field of photovoltaic systems can be found in Section 1.3

8.1. CONCLUSIONS

8.1.1. ON IMPROVING AESTHETICS OF PHOTOVOLTAIC MODULES

In terms of aeshetics, **Chapter 2** provided an overview of the different coloring techniques, some of which have reached industrial-scale technological readiness, such as products based on microscopic ink patterns and interference structures. Alternatives, such as nanophotonic structures, still need significant technical development to reach this status, but their advantage of wavelength modulation with only one applied layer represents a promising approach for industrial applications. Similarly, using add-on layers (here called *intermezzo*) use established industrial processes and have the potential for rapid implementation.

The chapter concludes that more specific modeling tools are needed to aid in the design and performance estimation of colored photovoltaic modules. In particular, the spectral effects produced by the addition of color and its impact on the operating temperature for the variable real-world conditions will provide more valuable insight into the potential electrical output of these novel photovoltaic modules. A more accurate estimation of these parameters is essential for feasibility analysis and customer trust. This work (particularly in Chapters 3 to 5) provides the modeling framework that fulfills this requirement.

Chapter 3 introduces the base modeling approach to predict the effects on electrical

and thermal performance in a photovoltaic module induced by the addition of a color filter based on interference effects. The work demonstrates that this effect is accurately predicted using two scaling factors. The first is the factor of the color filter (CF), which accounts for the additional spectral optical loss generated by the color and its relationship not only with the spectral response of the solar cell but also with other optical losses such as those caused by the front glass sheet and the encapsulating material. The second factor is a modification of the angle-of-incidence (AOI) modifier, commonly used on standard photovoltaic models. This second factor, denoted j_{SC}, accounts for the additional optical loss produced by the spectral shift of the reflectance that occurs in the color filter at values of angle of incidence greater than zero degrees. Both CF and j_{SC} scale down the calculated plane of array irradiance, thus yielding an *effective* irradiance reaching the solar cell. Comparing the results of this approach to a more comprehensive device-level simulation using TCAD Sentaurus revealed an absolute error ranging from 0.2% at normal incidence, up to 2.0% at an angle of incidence equal to 80°.

The color filter analyzed in the chapter consisted of two different materials (SiN_x and SiO_2). Ten alternating layers of different thickness values of each of these materials produce colors with relatively high saturation but limited hues. This is due to the loss of color perception caused by the encapsulating material and the front glass. The loss in hue can be reduced to a limited extent by both texturing the front glass and increasing the difference between the refractive index of the materials (achieved here by increasing the value of SiN_x) and increasing the number of pairs.

Performance analysis of photovoltaic modules with colored cells operating in an integrated building layout (a 35° tilted roof and optimal azimuth) for two locations (Delft, NL and Alice Springs, AU) indicates that color provision can decrease the annual DC energy by up to 6.40% for colors of low saturation and up to 13.90% for those with higher saturation.

Given the aesthetic limitations of deposition of a color filter directly on the solar cell, **Chapter 4** explores the advantages of implementing it on the back side of the front glass sheet of a photovoltaic module. The deposition of the filter at this location protects it from environmental factors such as soiling, accidental scratches, humidity, etc. From an aesthetic perspective, this placement has significant improvements in terms of hue and saturation compared to the approach presented in Chapter 3. However, the color filter can cause significant glare and have poor color stability for the case of non-textured glass, conditions that are undesirable for integrated applications.

Glare is reduced by deposition of the color filter on a surface with a texture that induces significant haze, thus producing diffuse reflection. This approach is shown to completely eliminate glare, whilst still guaranteeing a wide range of hues. Stabilizing the color involves a more complex approach. It is argued that one of the methods to stabilize color lies in surface engineering. By changing the texturing pattern of the front glass and keeping the randomized texturing on the side where the color filter is deposited, it is possible to achieve reasonable color stability for a wide range of angles of incidence. This is demonstrated by the use of colormitery parameters, such as calculated values of luminance, chroma, and hue, but more importantly, by demonstrating how these parameters can help quantify the difference between colors. The parameter used in this work is the CIEDE2000 color difference formula ΔE_{00}. In this chapter, a value of ΔE_{00} below 2 con-

siders that the two compared colors are just differentiated under close inspection. If this condition is met, the color is considered stable.

The analysis of seven structures provided information on the geometries that perform better in terms of color stabilization. Hard-edged geometries, in particular inverted pyramids with depths of 250 μm and a pitch of 45°, show remarkable color stability even at angles of incidence as high as 70°. Furthermore, these same colorimetric approaches allow one to optimize the color filter design by reducing unnecessary optical losses, such as increased reflection of light at a wavelength in which high saturation is already perceived at a lower value. An additional advantage to this approach is the reduction of pairs of layers required for high color saturation, which simplifies the manufacturing of the filter.

In terms of energy performance, under the same conditions as those studied in Chapter 3, simulations showed that colored photovoltaic modules based on optical filters can achieve low relative energy losses compared to the standard case. Some green and blue hues presented relative yearly DC energy yield losses as low as 6%, brown hues can have losses of 9%, while purple hues can be achieved with losses as low as 11%. Given the efforts to stabilize the color, the relative losses barely changed for two different locations compared to their respective standard case. However, there are some hues that present limited reduction (less than 2%) due to a slightly better thermal performance in Alice Springs.

8.1.2. ON IMPROVING THERMAL PERFORMANCE OF PHOTOVOLTAIC MODULES

Chapter 2 detailed the spectrally resolved thermal model used for the simulation work carried out in the works discussed in Chapter 3 through Chapter 5. The initial validation was carried out using standard photovoltaic modules based on SunPower Maxeon Generation II solar cells. The modules were connected to a maximum power point tracking algorithm developed by the PVMD group. For these conditions, the thermal model predicted the measured temperature with a **daily** RMSE error of less than 2.5 °C for a time resolution of 1 min. In Chapter 4, the model was tested under open circuit voltage conditions for a single encapsulated cell with and without a color filter. The accuracy of the model remained consistent, with an RMSE error of 1.15 °C for both the standard case and the color case over a period of 11 days with a time resolution of 10 seconds. The work contained in Chapter 5 tested the accuracy of the model for a dual rejection of light at both short wavelengths and near-infrared wavelengths, with only a marginal increase in the RMSE error to 1.44 °C. This validated thermal modules represents a valuable contribution for future research related to spectral approaches aimed at thermal management of photovoltaic modules.

Chapter 4 discusses that the reflection of light to provide colors had the beneficial effect of reducing the operating temperature of the photovoltaic module. The main conclusion for the case of the different colors obtained was that the potential gain in electrical performance owing to lower operational temperature never compensated for the optical loss in providing color. This is one of the first works in the field to consider this effect when simulating the performance of a colored module under real-world conditions.

The thermal model allowed exploration of the use of optical filters for thermal man-

agement. **Chapter 5** presents a practical case of a simple filter based on two materials that was designed using the basic principle of quarter wavelength optical (QWOT) thickness approaches. The filter was designed to be used on solar cell architectures that have reduced heat generation due to subbandgap absorption, such as IBC solar cells. The method consisted in taking advantage of the harmonic reflectance that these designs present and placing such harmonic at a wavelength at which the thermalization losses of a c-Si solar cell were higher. The result was a simple filter that reflected light both in the near-infrared region (at a wavelength of 1350 nm) and in the violet region (at 450 nm). Second-order optimization algorithms helped in stabilizing the angular behavior of the filter and reducing its low-wavelenght relfectance peak. The final design consisted of a 15 layer stack that under nominal operating cell temperature conditions (NOCT) predicted a temperature reduction of 3.34 °C compared to the standard case.

The optimized design was simulated under the environmental conditions of two different locations, Delft, in the Netherlands, and Singapore. The initial finding predicts an average temperature reduction of 2.20 °C for Delft and 2.45 °C for Singapore. This temperature reduciton did not compensate for the optical loss produced by the reflectance peak at low wavelength values, and, overall, the annual losses on the DC energy yield for both locations were around 10%.

However, degradation models were used to study the effect of this temperature reduction on the lifetime of the module, showing promising results. In Singapore, an extended two-year lifetime not only eliminated the difference in total energy production between both cases (standard and thermal filter) but had a relative total gain in DC energy yield of 3.2%. The effect was found to be location dependent, as for the case of Delft, the extension was insufficient to bridge the energy yield gap created by the optical loss. This chapter emphasizes the importance of including degradation models when studying different cooling solutions tailored to photovoltaic modules.

Optical filters can be utilized to improve cooling in modules by spectral management and can work in conjunction with other passive approaches. Among the different passive approaches, phase change materials (PCM) represent one of the most promising candidates because of their versatility of design and exceptional cooling potential. **Chapter 6** presents one of the largest experimental works to date on the suitability of a given PCM when used for extended periods of time in different locations and different installation layouts. The work was carried out between 2019 and 2021 in Delft, The Netherlands and in the winter of 2022 and the early spring of 2023 in Catania, Italy. The PCM was a *calcium chloride hexahydrate* with a melting temperature of 26 °C encapsulated in polymer slabs, provided by the company Orange Climate Autarkis.

The PCM slabs were mechanically attached to the back of the customized photovoltaic modules, ensuring full coverage of their active area. In Delft, both the module with the attached slabs and its standard counterpart were covered in the back with insulating material to simulate an installation layout similar to an integrated building system. In Catania, both modules had their backside open to environmental conditions, thus studying the layout of a rack mounted system. The main finding of the experiment is that for both configurations in each location, the PCM slabs were able to provide substantial temperature reductions. The differences in measured temperatures between PV modules with PCM and their standard counterparts were up to 15 °C. Furthermore, the

PCM allowed for thermal management of the modules during the hours of the day when solar irradiance was highest.

The plane of array irradiance, in particular, was found to be the most influential environmental parameter affecting the time that the PCM material was able to provide cooling. On days with very high solar irradiance, the PCM could thermally manage the photovoltaic module for a limited number of hours. The melting of the PCM occurred faster during the summer than during the spring and autumn in Delft, indicating that a more consistent cooling was achieved in the latter seasons. The same behavior was observed in Catania. The second most influential environmental factor was the ambient temperature. Warm days contribute to shorter melting times, while during cold and sunny days the thermal management achieved was more consistent.

There were instances in which the PCM warmed the photovoltaic module to temperatures higher than the standard opposite. This condition occurred during hours of low ambient temperature and values of plane of array irradiance below 500 W/m^2. The warming occurs after the PCM is partially or fully melted, and in the experiments it only happened at later hours of the afternoon. However, avoiding such a condition must be taken into account when selecting an appropriate PCM for any given location. In general, for every month measured at both locations, the thermal management of the photovoltaic modules with the PCM slabs produced consistent increases in the normalized DC energy yield, with values ranging from 2.1% to 2.5% for Delft and 1.3% to 1.6% for Catania.

An alternative technology to thermal management consists of the use of the heat generated by the photovoltaic modules. **Chapter 7** presents an innovative design of a photovoltaic chimney. The chimney can be designed with up to three layers. A front layer, a cavity, a middle layer located at any point in this cavity, and a back layer. Photovoltaic modules can act as the front, back, or intermediate layer within the chimney cavity. A model combining mass flow calculations and photovoltaic heat generation allows prediction and optimization of the layout with better heat production, better electricity production, and the quality and potential use of the heat generated. The models were used to study the best cavity depth for each of the layouts mentioned above. Sensitivity analysis indicates that when the modules are placed in the front (referred to as PVF), a cavity depth range up to 0.1 m ensured optimal electrical output, while a cavity up to 0.2 m ensured more heat production. For the case of modules located inside the cavity, a depth of 0.2 m was found to be the most optimal configuration and placing the modules in the center of it. The quality of the heat generated was found to be insufficient for any meaningful direct use. However, the mass flow produced by the buoyancy effects has the potential to be used for ventilation purposes.

8.2. OUTLOOK

The results presented in this thesis document are to be considered only the initial steps to a more comprehensive body of research to improve upon it. In this regard, some salient aspects are listed below.

8.2.1. ON IMPROVING AESTHETICS OF PHOTOVOLTAIC MODULES

One of the most important improvements on the topic of color filters is to extend the modeling developed and incorporate new materials and design approaches that help reduce the number of layers required while still producing vibrant colors. The materials studied in this work were selected on the basis of technical constraints and the need to validate each step of the modeling process. Given their proximity to the refractive index value and their relative low thickness values (limited to 200 nm), the number of layers required to create highly saturated colors is significant. Other researchers (see, for example, [47], [198], [271]) have suggested combinations of materials and approaches that result in simpler designs, which are preferred to reach manufacturing on an industrial scale. Furthermore, these design methods have also been shown to be more proficient in obtaining colors with high purity while still maintaining relative losses below 5%, which are lower compared to the best performing filters obtained with the simple stack approach used in this book.

Further optimizations can be performed to expand the color potential of a given design while still ensuring color stability. An example of this is shown in Figures 8.1a and 8.1b. Reducing the depth and slope of the inverted pyramidal texture allows to obtain hues that are not feasible at greater depths, like yellows or red. However, this also entails a loss in color stability given by the steepness of the geometry. The surface engineering of the front glass can significantly expand the design options.

Figure 8.1: **(a)** Distribution of all obtained hues for different thickness combination of the SiO_2 and SiN_x layers when deposited on random textured surface (backside) and combined with an inverter pyramidal structure at the front side of the glass. The pyramids have a depth of 450 μm and a slope of 45°. **(b)** Improved hues by changing the geometry of the front surface to inverted pyramids of 100 μm of depth and a slope of 10°.

Alternately, the models presented in this work can be complemented by developing optimization methods like the needle technique, or Bayesian optimization to provide color stability to the color filter, thus avoiding the need of complex glass surface engineering. The advantage of these approaches is that, in addition to color stabilization, the layer count can also be optimized, thus ensuring simple and highly functional products.

In addition, integrating degradation models can help to better understand the potential benefit of the temperature reduction provided by the color filter. The potential lifetime improvement provided by this thermal benefit can bridge performance gaps to

the point to make colored photovoltaic modules the better option over standard ones for integrated systems.

8.2.2. ON THERMAL MANAGEMENT OF PHOTOVOLTAIC MODULES

Significant effort in the work of the spectral thermal filter involves stabilization of the reflectance at angles of incidence greater than 0°. The main reason was the limitation of considering the filter deposited on flat glass. The software used to deploy the second order optimization algorithm (needle technique) could not be used to study different texturing patterns. Other approaches like Bayesian optimization can be used to create alternative designs on texture that aid to stabilize reflection so that more focus is geared towards a balance between optical loss and thermal gain. Furthermore, it is paramount to include degradation effects and lifetime improvements, given its importance in studying the benefit of any cooling approach.

Given the location dependency of the benefit provided by spectral thermal filters, modeling suites should be able to provide global maps to pinpoint those locations where these solutions can provide the most benefits. An example of such a map is shown in Figure 8.2. The map showcases how dual perfect reflection of low wavelengths (450-500 nm) alongside near-infrared wavelengths (1350-1450 nm) can improve the lifetime of a standard PV module based on c-Si solar cells.

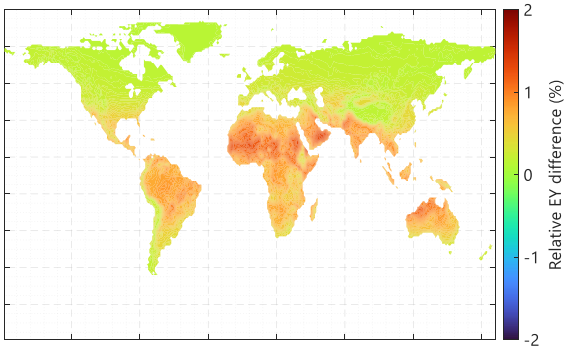

Figure 8.2: Example of the locations where full reflection of light at wavelengths between 450 - 500 nm and 1350 - 1450 nm provides the best potential for DC Energy gain by means of increased lifetime of a c-Si module. These results are preliminary, but provide an example of what modeling tools can deliver to optimize future designs of spectral thermal filters

The results are preliminary and are based on a simplified degradation model; however, they demonstrate how modeling tools can benefit from including more analysis for the design of spectral thermal management approaches.

A similar analysis can be applied to the suitability of a given phase-change material. In this sense, the finite-volume approach on which the current thermal model is based is very suitable for the addition of a phase-change material model. The main requirement is to ensure homogeneous cooling through the module to reduce the potential uncertainties of the modeling framework for validation. The experimental work carried out

demonstrated that the contact between the photovoltaic module and the PCM slab was insufficient and the cooling provided to cells on the edges of the module could not be guaranteed to those in the middle. This discrepancy in the measured temperatures hindered the completion of the model during this thesis work.

Finally, more experimental data are required to understand the potential of the PV chimney concept. As stated in Chapter 7, the large area steady state solar simulator had a disproportionate amount of infrared radiation that caused a temperature increase in the photovoltaic module (close to 80 °C). This, coupled to a rather limited height, can produce errors in the calculation of the mass flow obtained within the cavity. A more realistic demonstrator can reduce these uncertainties and better develop this promising concept.

9

APPENDICES

APPENDIX A

This is an appendix section that complements the information presented in Chapter 2. The complete set of equations for the twelve nodes shown in Figure 2.4 are presented below:

Node 1:

$$\frac{Q_{gen}\Delta_t}{\rho C_p} + T^p_{m,n} + 2Bi_c Fo_y T_a + 2Bi_R Fo_y T_s = T^{p+1}_{m,n}\left(1 + 2Fo_y + 2Fo_x + 2Bi_c Fo_y + 2Bi_R Fo_y\right) - 2Fo_y T^{p+1}_{m,n+1} - 2Fo_x T^{p+1}_{m+1,n}$$

Node 2:

$$\frac{Q_{gen}\Delta_t}{\rho C_p} + T^p_{m,n} + 2Bi_c Fo_y T_a + 2Bi_R Fo_y T_s = T^{p+1}_{m,n}\left(1 + 2Fo_y + 2Fo_x + 2Bi_c Fo_y + 2Bi_R Fo_y\right) - 2Fo_y T^{p+1}_{m,n+1} - Fo_x T^{p+1}_{m+1,n} - Fo_x T^{p+1}_{m-1,n}$$

Node 3:

$$\frac{Q_{gen}\Delta_t}{\rho C_p} + T^p_{m,n} + 2Bi_c Fo_y T_a + 2Bi_R Fo_y T_s = T^{p+1}_{m,n}\left(1 + 2Fo_y + 2Fo_x + 2Bi_c Fo_y + 2Bi_R Fo_y\right) - 2Fo_y T^{p+1}_{m,n+1} - 2Fo_x T^{p+1}_{m-1,n}$$

Node 4:

$$\frac{Q_{gen}\Delta_t}{\rho C_p} + T^p_{m,n} = T^{p+1}_{m,n}\left(1 + 2Fo_y + 2Fo_x\right) - Fo_y T^{p+1}_{m,n+1} - Fo_y T^{p+1}_{m,n-1} - 2Fo_x T^{p+1}_{m+1,n}$$

Node 5:

$$\frac{Q_{gen}\Delta_t}{\rho C_p} + T^p_{m,n} = T^{p+1}_{m,n}\left(1 + 2Fo_y + 2Fo_x\right) - Fo_y T^{p+1}_{m,n+1} - Fo_y T^{p+1}_{m,n-1} - Fo_x T^{p+1}_{m+1,n} - Fo_x T^{p+1}_{m-1,n}$$

Node 6:

$$\frac{Q_{gen}\Delta_t}{\rho C_p} + T^p_{m,n} = T^{p+1}_{m,n}\left(1 + 2Fo_y + 2Fo_x\right) - Fo_y T^{p+1}_{m,n+1} - Fo_y T^{p+1}_{m,n-1} - 2Fo_x T^{p+1}_{m-1,n}$$

Node 7:

$$Q_1 + Q_2 + T^p_{m,n} = T^{p+1}_{m,n}\left(1 + R_1 + R_2 + R_3 + R_4\right) - R_1 T^{p+1}_{m,n-1} - R_2 T^{p+1}_{m,n+1} - \left(R_3 + R_4\right) T^{p+1}_{m+1,n}$$

Node 8:

$$Q_1 + Q_2 + T^p_{m,n} = T^{p+1}_{m,n}\,(1 + R_1 + R_2 + 2R_3) - R_1\,T^{p+1}_{m,n-1} - R_2\,T^{p+1}_{m,n+1} - R_3\,T^{p+1}_{m+1,n} - R_3\,T^{p+1}_{m-1,n}$$

Node 9:

$$Q_1 + Q_2 + T^p_{m,n} = T^{p+1}_{m,n}\,(1 + R_1 + R_2 + R_3 + R_4) - R_1\,T^{p+1}_{m,n-1} - R_2\,T^{p+1}_{m,n+1} - (R_3 + R_4)\,T^{p+1}_{m-1,n}$$

Node 10:

$$\frac{Q_{gen}\Delta_t}{\rho C_p} + T^p_{m,n} + 2Bi_c Fo_y T_a + 2Bi_R Fo_y T_s = T^{p+1}_{m,n}\left(1 + 2Fo_y + 2Fo_x + 2Bi_c Fo_y + 2Bi_R Fo_y\right) - 2Fo_y T^{p+1}_{m,n-1} - 2Fo_x T^{p+1}_{m+1,n}$$

Node 11:

$$\frac{Q_{gen}\Delta_t}{\rho C_p} + T^p_{m,n} + 2Bi_c Fo_y T_a + 2Bi_R Fo_y T_s = T^{p+1}_{m,n}\left(1 + 2Fo_y + 2Fo_x + 2Bi_c Fo_y + 2Bi_R Fo_y\right) - 2Fo_y T^{p+1}_{m,n-1} - 2Fo_x T^{p+1}_{m+1,n}$$

Node 12:

$$\frac{Q_{gen}\Delta_t}{\rho C_p} + T^p_{m,n} + 2Bi_c Fo_y T_a + 2Bi_R Fo_y T_s = T^{p+1}_{m,n}\left(1 + 2Fo_y + 2Fo_x + 2Bi_c Fo_y + 2Bi_R Fo_y\right) - 2Fo_y T^{p+1}_{m,n-1} - 2Fo_x T^{p+1}_{m-1,n}$$

In the above equations, the values of R_{1-4} and Q_{1-2} are given by:

$$R_1 = \frac{2k_1\Delta_t}{\rho_1 C_{p_1}\Delta^2_{y_1} + \rho_2 C_{p_2}\Delta_{y_1}\Delta_{y_2}}$$

$$R_2 = \frac{2k_2\Delta_t}{\rho_1 C_{p_1}\Delta_{y_1}\Delta_{y_2} + \rho_2 C_{p_2}\Delta^2_{y_2}}$$

$$R_3 = \frac{2k_1\Delta_{y_1}\Delta_t}{\rho_1 C_{p_1}\Delta^2_x\Delta_{y_1} + \rho_2 C_{p_2}\Delta^2_x\Delta_{y_2}}$$

$$R_4 = \frac{2k_2\Delta_{y_2}\Delta_t}{\rho_1 C_{p_1}\Delta^2_x\Delta_{y_1} + \rho_2 C_{p_2}\Delta^2_x\Delta_{y_2}}$$

$$Q_1 = \frac{Q_{gen_1}\Delta_{y_1}\Delta_t}{\rho_1 C_{p_1}\Delta_{y_1} + \rho_2 C_{p_2}\Delta_{y_2}}$$

$$Q_2 = \frac{Q_{\text{gen}\,2}\Delta_{y_2}\Delta_t}{\rho_1 C_{p_1}\Delta_{y_1} + \rho_2 C_{p_2}\Delta_{y_2}}$$

Where the subscripts 1,2 belong to material 1 or 2 (for example, EVA / Solar Cell). A special case is Node 8, in which the value of R_3 is given by:

$$R_3 = \frac{2\Delta_t}{\rho_1 C_{p_1}\Delta^2_x\Delta_{y_1} + \rho_2 C_{p_2}\Delta^2_x\Delta_{y_2}}\left(\frac{k_1\Delta_{y_1}}{2} + \frac{k_2\Delta_{y_2}}{2}\right)$$

Since it depicts a node located at the centre of the module between two different materials. For more details on this approach, the interested reader is encouraged to consult the work of Aly *et al.* [150].

The heat generated by thermalization inside the cell was estimated under the following assumptions.

- The bandgap was assumed to be temperature independent and equal to 1100 nm
- Any photon absorbed above 1100 nm was considered a free carrier and was not taken into account as thermalization heat generation
- The relaxed carrier power was determined as $RC_p = \frac{\Phi_{c-si}\cdot h\cdot c}{\lambda_{c-si}}$ Where Φ_{c-si} represents the photon flux reaching the c-Si absorber, h is Planck's constant, c the speed of light and λ_{c-si} is the bandgap wavelength (1100 nm).

- The calculated thermalization is the difference between the total absorbed irradiance by the c-Si cell and the relaxed carrier power RC_p.

APPENDIX B

This is an appendix section that complements the information presented in Chapter 3.

OPTICAL PROPERTIES AND MANUFACTURING DETAILS

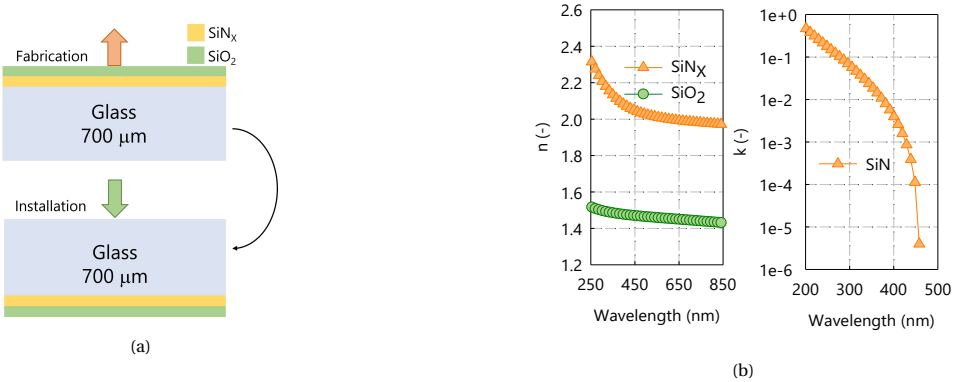

Figure 9.1: **(a)** Detail on the deposition direction and installation direction of the optical filters used in this work. The purpose of this strategy is to protect the filter from environmental hazard **(b)** Wavelength-dependent real (n) and imaginary part (k) of the complex refractive indexes of SiNx and SiO_2 used in this work. Measurements were carried out with a Woollam ellipsometer; $SiO_2$was found to be non-absorbing ($k = 0$) in the full wavelength range of interest.

The following are the deposition parameters for the color filter **Option 1**

Table 9.1: Deposition parameters of the color filter **Option 1**

Parameter	**SiO_2**	**SiN_x**
Temperature (°C)	300	300
Gas 1 flow (sccm)	SiH_4 = 1	SiH_4 = 2.5
Gas 2 flow (sccm)	CO_2 = 55	NH_3 = 47.5
Pressure (mbar)	1.40	0.80
Plasma power (W)	20	4
CTune (-)	26	26
CLoad (-)	53	53
Deposition rate on glass (nm/s)	0.44	0.30

For the case **Option 2** the following were the deposition parameters:

Table 9.2: Deposition parameters of the color filter **Option 2**

Parameter	**SiO_2**	**SiN_x**
Temperature (ºC)	300	300
Gas 1 flow (sccm)	SiH_4 = 8.5	SiH_4 = 20
Gas 2 flow (sccm)	N_2ON2O= 710	NH_3 = 20
Pressure (mbar)	1000	650
Plasma power (W)	20	20
Deposition rate on glass (nm/s)	1.20	0.21

VALIDATION OF THE SCALING FACTORS APPROACH

The following are the parameters used on the two-diode equivalent circuit model

Parameter			**Value**
Light collected current	(J_L)	$(mA \cdot cm^{-2})$	39.443
Saturation current 1	(J_1)	$(pA \cdot cm^{-2})$	83.650
Ideality factor 1	(m_1)	(-)	1.347
Saturation current 2	(J_2)	$(nA \cdot cm^{-}2)$	0.453
Ideality factor 2	(m_2)	(-)	2
Shunt resistance	(R_{SH})	$(k\Omega cm^2)$	23.570
Series Resistance	(R_S)	(Ωcm^2)	0.424

Table 9.3: Estimated two-diode parameters for the SunPower IBC solar cell

These results complement those presented in Chapter 3. For the case of color cells

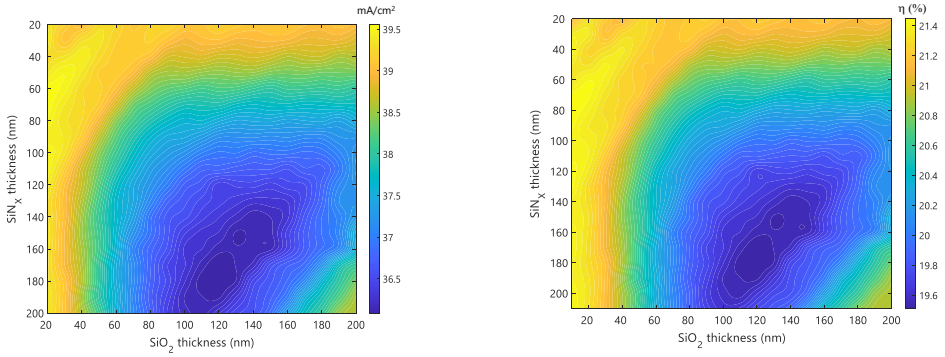

(a) (b)

Figure 9.2: **(a)** Value of J_{SC} for the different combinations of thickness of a color filter applied directly on a c-Si solar cell. **(b)** Value of η for the different combinations of thickness of a color filter applied directly on a c-Si solar cell

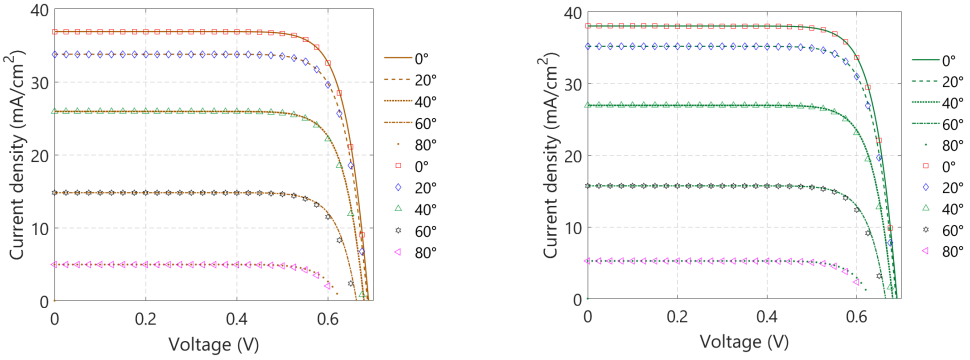

Figure 9.3: **(a)** Validation of the scaling factor approach when a brown color filter is applied directly on a solar cell. Simulations from the two-diode equivalent circuit model are presented in symbols and compared to those obtained via TCAD Sentaurus (lines) **(b)** The same validation for the case of a green color filter

ANGULAR BEHAVIOR ON TEXTURED SURFACES

To increase color saturation and brightness, the addition of a textured glass surface also has a significant impact on the value of the irradiance scaling factor j_{SC} for angles of incidences greater than the normal. Furthermore, each of the options of color filter presented in this work has a unique reflectance impact. We calculated the value of j_{SC} for each filter option, and for each combination of material thickness of the filter. In the figures below we show how texturing the surface of the front glass improves the angular performance of both the standard and the colored filter.

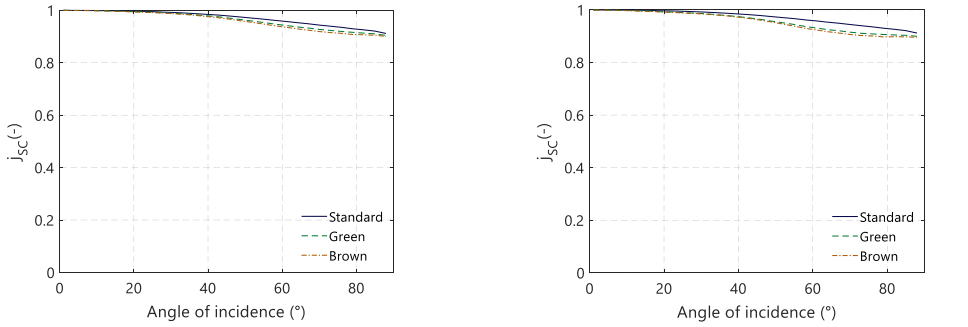

Figure 9.4: value of the angle of incidence modifier (j_{SC}) for an encapsulated colored and standard cell with textured glass: **(a)** for an encapsulated colored cell using filter Option 1; **(b)** for an encapsulated colored cell using filter Option 2. Improving saturation and color brightness increases the angular losses produced by the filter, as shown by the lower value of j_{SC} produced by the filter Option 2

Matrix of Temperatures and DC Energy yield

The following are the temperature and DC energy matrices for the different colors obtainable by the different thickness combinations of SiO_2 and SiN_X as presented in Chapter 3

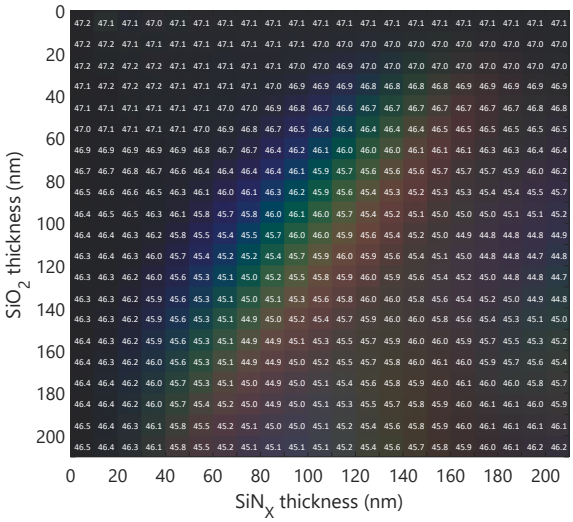

(a)

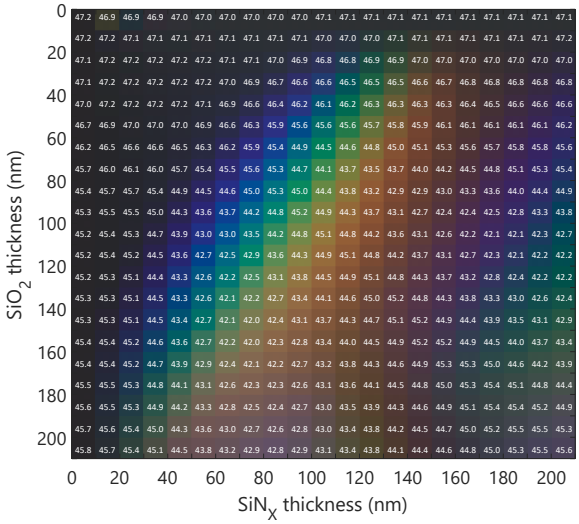

(b)

Figure 9.5: **(a)** Steady state temperature under NOCT conditions for the different colors obtainable with the color fitler **Option 1** (see Figure 3.13a) **(b)** Steady state temperature under NOCT conditions for the different colors obtainable with the color fitler **Option 2** (see Figure 3.14a)

The following are the DC Energy yield results for **Delft, NL**:

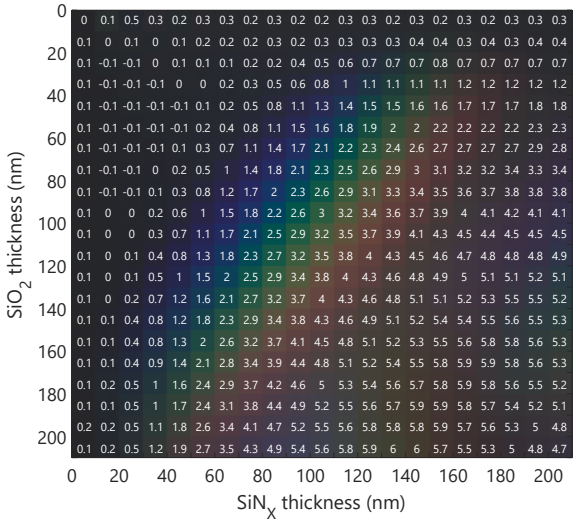

(a)

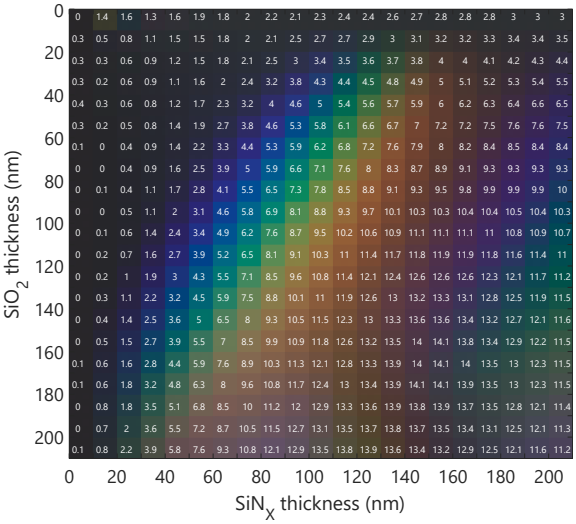

(b)

Figure 9.6: **(a)** Annual DC Energy yield for the different colors obtainable with the color fitler **Option 1** (see Figure 3.13a) for a system located in Delft **(b)** Annual DC Energy yield for the different colors obtainable with the color fitler **Option 1** (see Figure 3.13a)

The following are the DC Energy yield results for **Alice Springs, AU**:

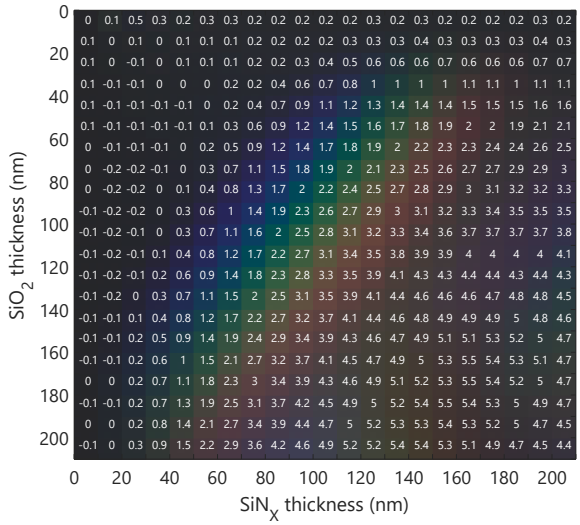

(a)

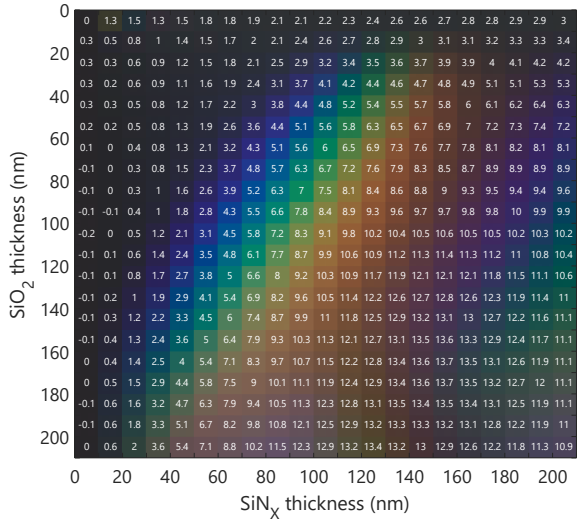

(b)

Figure 9.7: **(a)** Annual DC Energy yield for the different colors obtainable with the color fitler **Option 1** (see Figure 3.13a) for a system located in Alice Springs **(b)** Annual DC Energy yield for the different colors obtainable with the color fitler **Option 1** (see Figure 3.13a)

APPENDIX C

This is an appendix section that complements the information presented in Chapter 4.

OPTICAL PROPERTIES

The following are the optical properties of the materials contained in the optical filter:

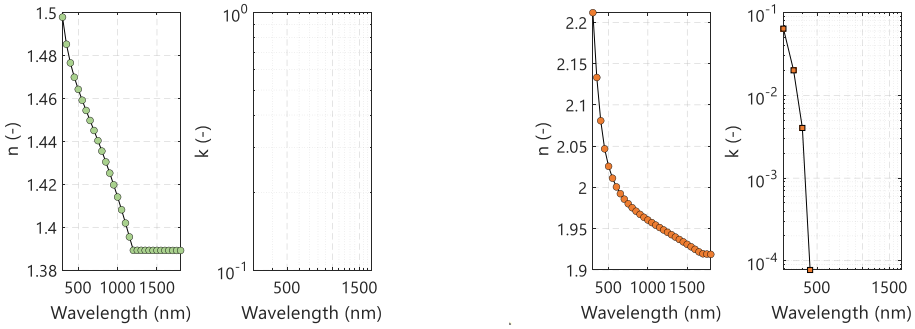

(a) (b)

Figure 9.8: Optical properties used in this work for silicon oxide, and silicon nitride, the data was obtained from measurements on a glass substrate via spectroscopic ellipsometry

The deposition parameters of this filter match those presented on the previous appendix for **Option 2**.

Details of the texturing layouts studied in Section 4.3 are presented below:

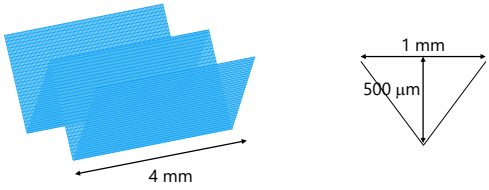

Figure 9.9: Schematics of a V-shaped glass texturing presented in Table 4.2. The texturing was created in MATLAB aiming to mimic the Albarino G series. The angle slope for this case is 45 °

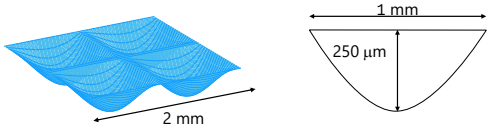

Figure 9.10: Schematics of a grooved glass texturing presented in Table 4.2. The texturing was created in MATLAB aiming to mimic the Albarino P series.

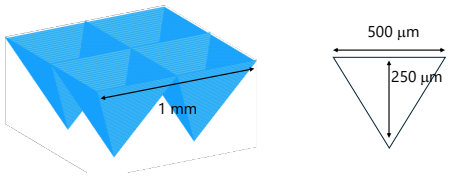

Figure 9.11: Schematics of an inverted glass texturing presented in Table 4.2. The texturing was created in MATLAB

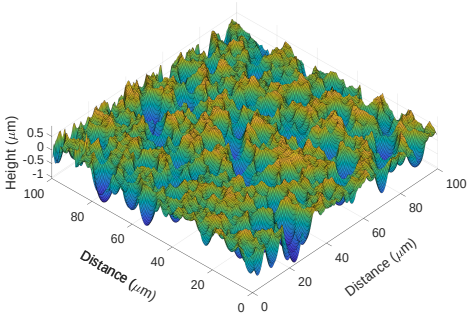

Figure 9.12: Atomic force microscope of the random texturing obtained after sputtering 200 nm of ITO and 30 minutes of etching. More details are depicted on [188]. The author claims that the distribution presents an equivalent diameter of less than $2\mu m$ with an average crater depth of $0.7\mu m$.

Each of the structures presented in Table 4.2 has a specific effect on the luminance of the different hues that can be produced. This effect is presented below:

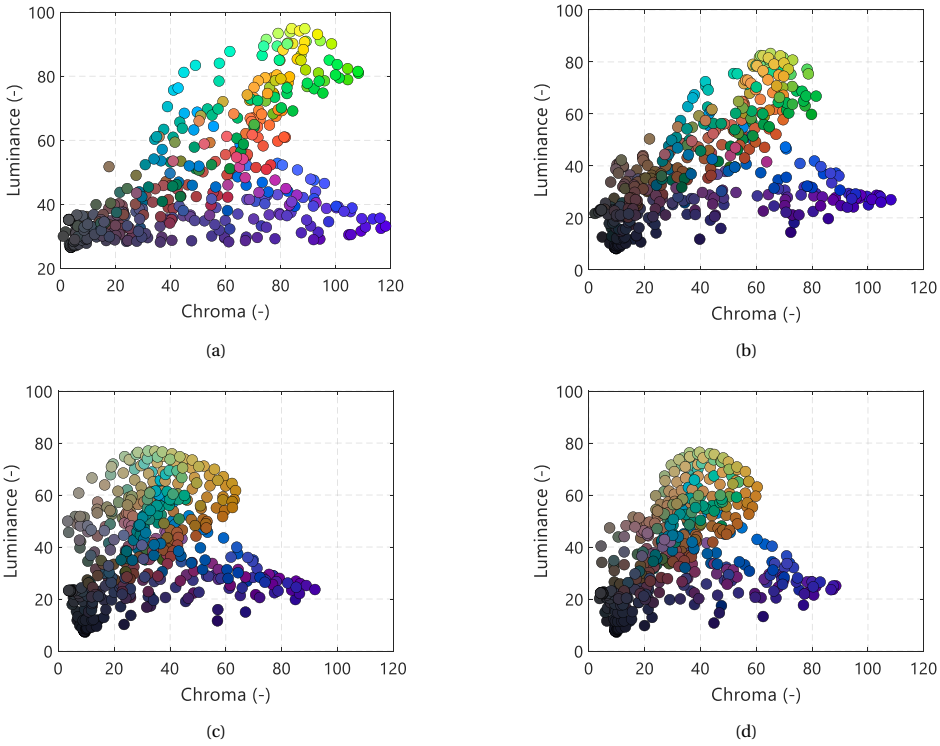

Figure 9.13: Chroma and luminance for the different colors produced under four different module structures (see Table 4.2): **(a)** Structure 1: flat | flat colored PV module. **(b)** Structure 4: V-shaped grooves | flat layout. **(c)** Structure 6: inverted pyramids | flat layout and **(d)** Structure 7: inverted pyramid | random texture layout.

APPENDIX D

This is an appendix section that complements the information presented in Chapter 5. The optical properties of the filter match those presented in Appendix C. Furthermore, the thermal and physical properties used in the thermal model were identical to those presented in Table 2.1.

The thickness values for each layer of the optimized design are found below.

Table 9.4: Thickness values and order of layers of the optimized optical filter. Notice that, to replicate the behavior shown in Figure 5.12a, the filter needs to be simulated working within the complete optical system described Figure 5.5 (i.e., considering the entire PV module layout)

Material	**Thickness (nm)**
$\mathbf{SiO_2}$	103
$\mathbf{SiN_x}$	163
$\mathbf{SiO_2}$	226
$\mathbf{SiN_x}$	176
$\mathbf{SiO_2}$	67
$\mathbf{SiN_x}$	16
$\mathbf{SiO_2}$	125
$\mathbf{SiN_x}$	169
$\mathbf{SiO_2}$	258
$\mathbf{SiN_x}$	16
$\mathbf{SiO_2}$	23
$\mathbf{SiN_x}$	151
$\mathbf{SiO_2}$	33
$\mathbf{SiN_x}$	17
$\mathbf{SiO_2}$	208

APPENDIX E

This appendix complements Chapter 6 and consists of additional results related to the experimental work with phase-change materials.
Results of the electroluminescence test:

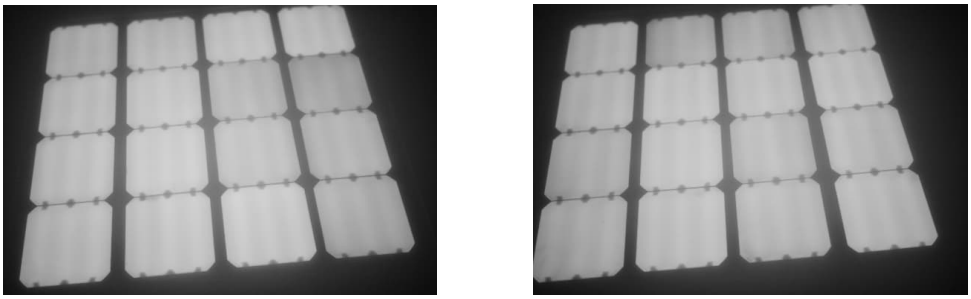

(a) (b)

Figure 9.14: **(a)** Electroluminescence image of the standard PV module after 3 years of operation without any maintenance. The images show no cracks or any other abnormalities on the module. **(b)** Similar to (a) for the case of the PV-PCM module, the integrity of the PV module was not hindered by the PCM slabs

Additional information of the cooling potential both in Delft and Catania

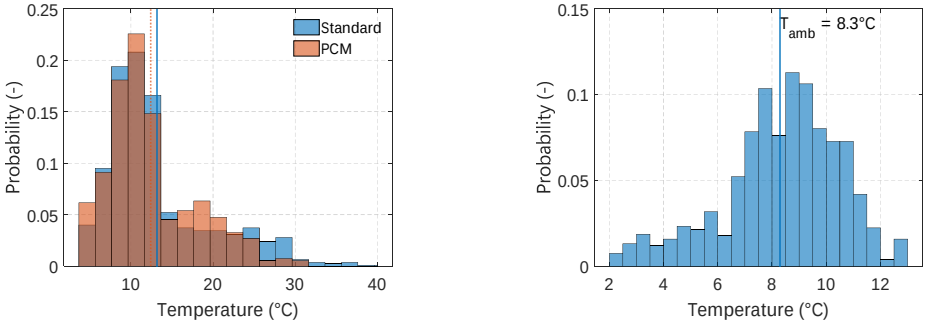

(a) (b)

Figure 9.15: **(a)** Histogram of the operational temperatures of the standard (Std) PV module and the PV-PCM module (PCM) for the winter days of 2019. (December 21, 2019, until February 8, 2020) between 9:00 and 15:00. The vertical lines indicate the mean values of the operating temperature of each module. Even during winter, the PV-PCM module presents lower operational temperatures. **(b)** Histogram of the measured ambient temperature for the same period described in (a).

Interannual climatic conditions in Delft and average climatic conditions in Catania

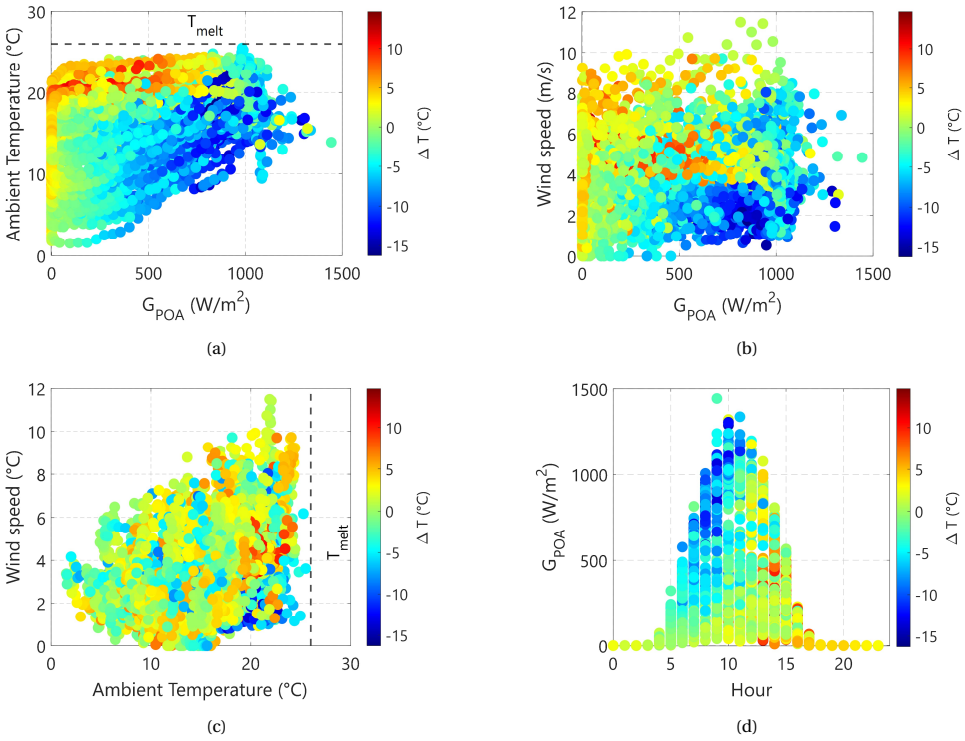

Figure 9.16: Influence of environmental conditions on the average temperature difference ΔT (°C) during spring 2023 in Catania, Italy: **(a)** Effect of the ambient temperature related to the plane of array irradiance. The value of the melting temperature of the PCM is denoted by the dashed line; **(b)** effect of the windspeed related to the plane of array irradiance. **(c)** effect of the windspeed related to the ambient temperature; and **(d)** effect of the plane of array irradiance on the hourly temperature difference for the entire season

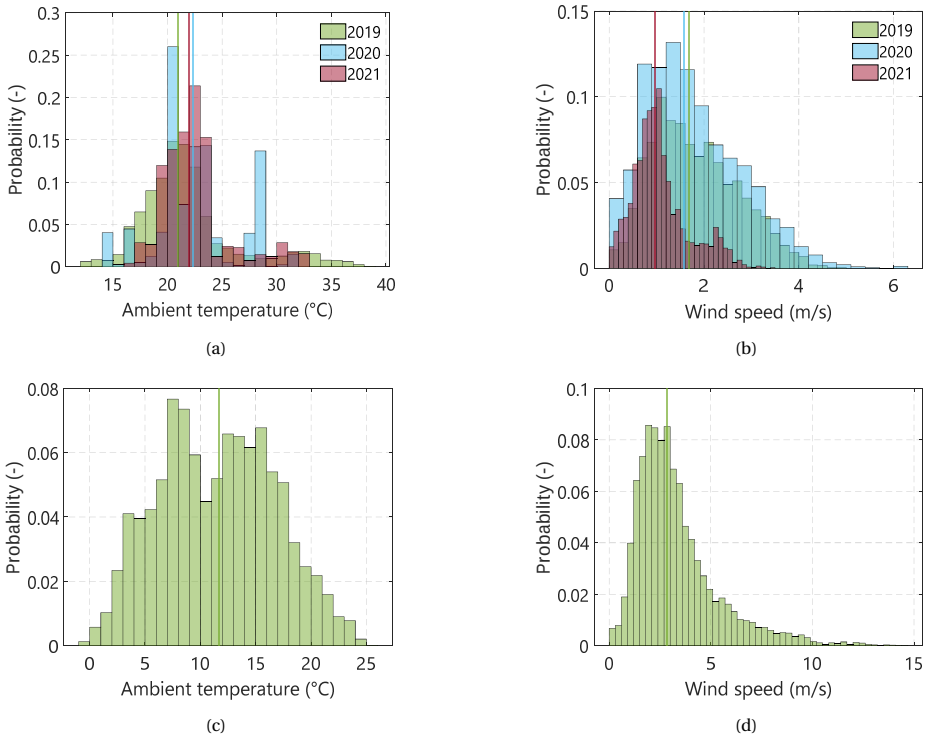

Figure 9.17: **(a)** Histogram of ambient temperatures measured during the summer of 2019, 2020 and 2021 in Delft. The mean values of the recorded ambient temperatures for all years remain close (21 °C in 2019, 22.3, °C in 2020 and 22.0 °C in 2021), which is consistent with the stable performance differences between both PV modules during these years. **(b)** Histogram of wind speed measured during the same season and years as (a). The data also reveals very high consistency between the years 2019 (1.67 m/s) and 2020 (1.58 m/s). During 2021, the mean measured windspeed was considerably lower (0.96 m/s). Nonetheless, the effect on overall energy yield was relatively small. **(c)** Histogram of ambient temperatures measured during the 2023 in Catania. The mean values of the recorded ambient temperatures were 12 °C. **(d)** Histogram of wind speed measured during the same season and years as **(c)** showcasing a mean value of 2.84 m/s. Even under these conditions, the PCM still provided benefit due to the high average irradiance reaching the panels.

ACKNOWLEDGEMENTS

A beautiful aspect of life lies in its unpredictability. As a mechanical engineer, my first interest in sustainable energy technology was wind energy. I came to Delft University of Technology to focus on this topic, but things changed abruptly, thanks to the lectures of Prof. Miro Zeman. His knowledge, enthusiasm, and passion for photovoltaics led me to pursue a master's thesis project in this field. During this search, I met Prof. Olindo Isabella, who showed me a list of available thesis projects and was particularly interested in finding a student to take on the topic of color photovoltaics. A mechanical engineer working on optics at an electrical engineering faculty seemed like a bit of a reach, so at first I was a bit reluctant to take on this task. Nevertheless, Prof. Isabella seemed more confident than me (by now, this has become a tradition) that things would turn out quite well, and they came to be. Miro and Olindo are the most influential people in my professional life. I will always be grateful for their continuous support, patience, and unnerving faith in our work during this Ph.D.; having them as promotors, is to me, an immense honor.

I also express my gratitude to this Ph.D. defense committee. Dr. Benedikt Bläsi, Prof. Dr. Martina Schmid, Prof. Dr. Kamel Hooman, Prof. Dr. Andy van den Dobbesteen, and Prof. Dr. Marko Topič. Your valuable insights and suggestions have improved the quality of this book and the way I communicate research. I am also very honored to have met you.

This book marks the conclusion of an exciting and sometimes challenging journey. One that would have been impossible for me to conclude without the support of my colleagues and friends. The PVMD group has a quality of people that is second to none. I owe a great deal of gratitude to the professors, associate professors, Ph.D. colleagues, technicians, and secretary staff for all their guidance, support, and patience they provided whenever I needed it. I apologize if my shy and reclusive nature made me seem aloof and distant. Please know that I greatly admire all of you and I cherished every moment, however brief, that you shared with me. To my office mates, Alba, David, Gianluca, Johan, and Reinder, I am sorry for being far from the best office partner, but be sure that I appreciate you dearly and will never forget you.

I want to highlight the enormous importance of Andrés Calcabrini, Carlos Ruiz Tobón, Paul Procel Moya, Yilong Zhou, Dr. Mirco Muttillo, Dr. Guangtao Yang, Dr. Rudi Santbergen, Dr. Hesan Ziar, Dr. Patrizio Manganiello, Robin Vismara, Manvika Singh, Martjin Tijssen, Stefaan Heirman, Daragh O'Connor and Dr. Zoheir Haghighi. Your guidance, advice, help, and faith in my work kept me motivated. Thank you to Andrés, Carlos, Yilong, Zoheir, and Paul, whose intelligence matches their good nature, friendships for which I will always be grateful.

I was also lucky to work with great MSc students during this journey, whose contributions were very important in all the works contained in this book. Patricia Seoane da Silva, the very first student I supervised, was very patient with my inexperience, some-

thing that I have always appreciated. It was a pleasure working with Chiraag Raja Reddy, Sander Wapperom, Simona Villa, Chris van Neirop y Sanchez, Mario Verheijen, Nitish Kumar Sinha, Cas de Mooij, Sukanya Prabudhesai, Kyriakos Vattis, Georgia Frantzi, Lyndon Wix, Mariana Cordoba Parra, Patrick Kwee and Manuel Dakessian. You made this journey much easier thanks to all your contributions, knowledge, and friendship. You helped shaping all the works contained here, and those who are not, it was due to lack of time. I hope to give them their due place further down the road. I will personally thank you for all you have done to help me. I have not forgotten Arturo Martinez Lopez, my MSc student, Ph.D. colleague, and dear, valuable friend; thank you, Arturo; it was very lucky for me to count on you.

To my dear friends outside academia, without you, I would not have the energy to endure the hard times of the pandemic, the loneliness, and the grief that came with it. I am forever grateful that you took the time to be there for me. Juan Camilo Ramirez, Maksymilian Szabunia, Sergio Moreno Wandurraga, Juan Sebastián Gelvez, Juan Camilo Cortés, Marco Garcia, Tatiana Suarez, Alba Pinto, Andrés Moreno Wandurraga. I hope to repay all your kindness. Sergio, thank you for being a fantastic friend, a patient roommate, and a challenging Wolfenstein E.T. foe. Juan Ramirez, Maks, and Andres, your friendship was one of the best things the Netherlands gave me. Marco, Tatiana, and Alba thank you for your support from the distance. Juan Sebastián and Juan Camilo Cortés, you have been my friends since the second grade; a true blessing to count on friends like you both. To all my friends in Colombia, I have never forgotten you, no matter the time since we last got in touch.

I also owe deep gratitude to Jenny Carolina Garcia Rangel, one of the most important people in my life. Your friendship, intelligence, kindness, and support were the highlight of these difficult years. I adore you beyond words and hope to give you back as much as you deserve. Thank you! from the bottom of my heart.

Last but not least, to my family, the greatest gift this life has given me. My parents, Omayra and Carlos Alberto, who were always supporting, believing in, and pushing me to keep trying. I am always in awe of your work ethic, character, and strong sense of justice, which have inspired me to be the best I can be. To my dear brother Carlos José, an exemplary professional, father, brother, and son. You have always helped me whenever I needed it, and I have always admired your leadership, intelligence, strength of character, and humility. To Yaneth Marcela, my dear sister, your support was essential during this last stage of this work. Above all, you have always impressed me with your intelligence, resilience, and dedication to those you love. To Maria Paula and Philipp, thank you for supporting my brother and sister, being part of my family, and continuously enriching our lives; we are blessed to have you. To Ana Sofía, your intelligence, joy, curiosity, and wit make me feel optimistic about our future. Finally, to Draco, and especially to *Murphy*, thank you for being in our lives, improving them with your company and love. *Los amo a montones!, gracias por toda la paciencia que han tenido conmigo*

Delft, 2025.


"Finally, from so little sleeping and so much reading, his brain dried up and he went completely out of his mind"
Miguel de Cervantes Saavedra - Don Quixote

BIBLIOGRAPHY

[1] Architecture2030.org, *Why the built environment*, Feb. 2023.

[2] International Energy Agency, "Technology and Innovation Pathways for Zero-carbon-ready Buildings by 2030", IEA, Paris, Tech. Rep., Feb. 2022.

[3] E. Ohene, A. P. Chan, and A. Darko, *Review of global research advances towards net-zero emissions buildings*, Jul. 2022. DOI: 10.1016/j.enbuild.2022.112142.

[4] A. Ahmed, T. Ge, J. Peng, W. C. Yan, B. T. Tee, and S. You, *Assessment of the renewable energy generation towards net-zero energy buildings: A review*, Feb. 2022. DOI: 10.1016/j.enbuild.2021.111755.

[5] M. K. Basher, M. Nur-E-Alam, M. M. Rahman, K. Alameh, and S. Hinckley, *Aesthetically Appealing Building Integrated Photovoltaic Systems for Net-Zero Energy Buildings. Current Status, Challenges, and Future Developments—A Review*, Apr. 2023. DOI: 10.3390/buildings13040863.

[6] D. J. Sailor, J. Anand, and R. R. King, "Photovoltaics in the built environment: A critical review", *Energy and Buildings*, vol. 253, Dec. 2021, ISSN: 03787788. DOI: 10.1016/j.enbuild.2021.111479.

[7] Grand View Research, "Building-integrated Photovoltaics Market Size, Share & Trends Analysis Report By Technology (Crystalline Silicon, Thin Film), By Application (Roof, Glass, Wall, Facade), By End-use, By Region, And Segment Forecasts, 2023 - 2030", Grand View Research, San Francisco, Tech. Rep., 2023, pp. 1–97.

[8] C. Ballif, L.-E. Perret-Aebi, S. Lufkin, and E. Rey, "Integrated thinking for photovoltaics in buildings", Tech. Rep., 2018. DOI: 10.1038/s41560-018-0176-2. [Online]. Available: http://www.kaleo-.

[9] S. A. Awuku, A. Bennadji, F. Muhammad-Sukki, and N. Sellami, "Myth or gold? The power of aesthetics in the adoption of building integrated photovoltaics (BIPVs)", *Energy Nexus*, vol. 4, Dec. 2021, ISSN: 27724271. DOI: 10.1016/j.nexus.2021.100021.

[10] J. S. Kumar, "The Psychology of Colour Influences Consumers' Buying Behaviour – A Diagnostic Study", *Ushus - Journal of Business Management*, vol. 16, no. 4, pp. 1–13, Oct. 2017, ISSN: 0975-3311. DOI: 10.12725/ujbm.41.1.

[11] S. L. Hille, H. C. Curtius, and R. Wüstenhagen, "Red is the new blue The role of color, building integration and country of origin in homeowners preferences for residential photovoltaics", *Energy and Buildings*, vol. 162, pp. 21–31, Mar. 2018, ISSN: 03787788. DOI: 10.1016/j.enbuild.2017.11.070.

[12] E. Lucchi, J. Adami, and A. E. Stawinoga, "Social acceptance of photovoltaic systems in heritage buildings and landscapes: Exploring barriers, benefits, drivers, and challenges for technical stakeholders in northern Italy", *Sustainable Energy Technologies and Assessments*, vol. 60, Dec. 2023, ISSN: 22131388. DOI: 10.1016/j.seta.2023.103544.

[13] P. López, "ACCEPTANCE OF BUILDING INTEGRATED PHOTOVOLTAIC (BIPV) IN HERITAGE BUILDINGS AND LANDSCAPES: POTENTIALS, BARRIER AND ASSESSMENT CRITERIA", Tech. Rep. [Online]. Available: http://www.supsi.ch.

[14] N. Sánchez-Pantoja, R. Vidal, and M. C. Pastor, *Aesthetic impact of solar energy systems*, Dec. 2018. DOI: 10.1016/j.rser.2018.09.021.

[15] P. Bonomo, G. Eder, N. M. Chivelet, *et al.*, *IEA PVPS Task 15 Categorization of BIPV applications*, P. Bonomo and G. Eder, Eds. 2021, ISBN: 9783907281215. [Online]. Available: www.iea-pvps.org.

[16] N. Martín-Chivelet, K. Kapsis, H. R. Wilson, *et al.*, "Building-Integrated Photovoltaic (BIPV) products and systems: A review of energy-related behavior", *Energy and Buildings*, vol. 262, May 2022, ISSN: 03787788. DOI: 10.1016/j.enbuild.2022.111998.

[17] G. Peharz and A. Ulm, "Quantifying the influence of colors on the performance of c-Si photovoltaic devices", *Renewable Energy*, vol. 129, pp. 299–308, Dec. 2018, ISSN: 18790682. DOI: 10.1016/j.renene.2018.05.068.

[18] F. Rosa, "Building-integrated photovoltaics (BIPV) in historical buildings: Opportunities and constraints", *Energies*, vol. 13, no. 14, Jul. 2020, ISSN: 19961073. DOI: 10.3390/en13143628.

[19] A. Morlier, B. Lim, S. Blankemeyer, *et al.*, "Photovoltaic Modules with the Look and Feel of a Stone Façade for Building Integration", *Solar RRL*, vol. 6, no. 5, May 2022, ISSN: 2367198X. DOI: 10.1002/solr.202100356.

[20] T. Rose and A. Wollert, "The dark side of photovoltaic - 3D simulation of glare assessing risk and discomfort", *Environmental Impact Assessment Review*, vol. 52, pp. 24–30, Apr. 2015, ISSN: 01959255. DOI: 10.1016/j.eiar.2014.08.005.

[21] H. Gholami, H. N. Røstvik, and D. Müller-Eie, "Holistic economic analysis of building integrated photovoltaics (BIPV) system: Case studies evaluation", *Energy and Buildings*, vol. 203, Nov. 2019, ISSN: 03787788. DOI: 10.1016/j.enbuild.2019.109461.

[22] H. Gholami and H. N. Røstvik, "Economic analysis of BIPV systems as a building envelope material for building skins in Europe", *Energy*, vol. 204, Aug. 2020, ISSN: 03605442. DOI: 10.1016/j.energy.2020.117931.

[23] R. Zimmerman, A. Panda, and V. Bulović, "Techno-economic assessment and deployment strategies for vertically-mounted photovoltaic panels", *Applied Energy*, vol. 276, Oct. 2020, ISSN: 03062619. DOI: 10.1016/j.apenergy.2020.115149.

[24] I. Kaaya, M. Koehl, A. P. Mehilli, S. De Cardona Mariano, and K. A. Weiss, "Modeling Outdoor Service Lifetime Prediction of PV Modules: Effects of Combined Climatic Stressors on PV Module Power Degradation", *IEEE Journal of Photovoltaics*, vol. 9, no. 4, pp. 1105–1112, 2019, ISSN: 21563403. DOI: 10.1109/JPHOTOV.2019.2916197.

[25] I. Kaaya, A. Alzade, S. Bouguerra, *et al.*, "A physics-based framework for modelling the performance and reliability of bipv systems", *Solar Energy*, vol. 277, p. 112 730, 2024, ISSN: 0038-092X. DOI: https://doi.org/10.1016/j.solener.2024.112730. [Online]. Available: https://www.sciencedirect.com/science/article/pii/S0038092X24004250.

[26] A. Gok, E. Ozkalay, G. Friesen, and F. Frontini, "The Influence of Operating Temperature on the Performance of BIPV Modules; The Influence of Operating Temperature on the Performance of BIPV Modules", *IEEE Journal of Photovoltaics*, vol. 10, no. 5, 2020. DOI: 10.1109/JPHOTOV.2020.3001181. [Online]. Available: https://www.ieee.org/publications/rights/index.html.

[27] T. Smith and J. Guild, "The C.I.E colorimetric standards and their use", *Transactions of the Optical Society*, vol. 33, no. 3, pp. 73–134, 1931.

[28] R. Granit, *Sensory Mechanisms of the Retina*. Hafner, 1963. [Online]. Available: https://books.google.nl/books?id=54gKAAAAMAAJ.

[29] D. B. Judd, D. L. Macadam, G. Wyszecki, *et al.*, "Spectral Distribution of Typical Daylight as a Function of Correlated Color Temperature WITH THE COLLABORATION OF", Tech. Rep., 1964.

[30] J. Lindon, J. Holmes, and G. Tranter, "Colorimetry , Theory", in *Encyclopedia of Spectroscopy and Spectrometry*, January 2000, 2019, pp. 337–343, ISBN: 0122266803.

[31] G. Sharma, W. Wu, and E. N. Dalal, "The CIEDE2000 color-difference formula: Implementation notes, supplementary test data, and mathematical observations", *Color Research and Application*, vol. 30, no. 1, pp. 21–30, 2005, ISSN: 03612317. DOI: 10.1002/col.20070.

[32] J. Halme and P. Mäkinen, "Theoretical efficiency limits of ideal coloured opaque photovoltaics", *Energy and Environmental Science*, vol. 12, no. 4, pp. 1274–1285, Apr. 2019, ISSN: 17545706. DOI: 10.1039/c8ee03161d.

[33] A. M. Shirazi, Z. S. Zomorodian, and M. Tahsildoost, "Techno-economic BIPV evaluation method in urban areas", *Renewable Energy*, vol. 143, pp. 1235–1246, Dec. 2019, ISSN: 18790682. DOI: 10.1016/j.renene.2019.05.105.

[34] C. Zomer, I. Custódio, A. Antoniolli, and R. Rüther, "Performance assessment of partially shaded building-integrated photovoltaic (BIPV) systems in a positive-energy solar energy laboratory building: Architecture perspectives", *Solar Energy*, vol. 211, pp. 879–896, Nov. 2020, ISSN: 0038092X. DOI: 10.1016/j.solener.2020.10.026.

[35] A. Calcabrini, R. Weegink, P. Manganiello, M. Zeman, and O. Isabella, "Simulation study of the electrical yield of various PV module topologies in partially shaded urban scenarios", *Solar Energy*, vol. 225, pp. 726–733, Sep. 2021, ISSN: 0038092X. DOI: 10.1016/j.solener.2021.07.061.

[36] P. Kozlovas, S. Gudzius, J. Ciurlionis, A. Jonaitis, I. Konstantinaviciute, and V. Bobinaite, "Assessment of Technical and Economic Potential of Urban Rooftop Solar Photovoltaic Systems in Lithuania", *Energies*, vol. 16, no. 14, Jul. 2023, ISSN: 19961073. DOI: 10.3390/en16145410.

[37] Y. Zhou, D. Wilmink, M. Zeman, O. Isabella, and H. Ziar, "A geographic information system-based large scale visibility assessment tool for multi-criteria photovoltaic planning on urban building roofs", *Renewable and Sustainable Energy Reviews*, vol. 188, Dec. 2023, ISSN: 18790690. DOI: 10.1016/j.rser.2023.113885.

[38] J. C. Ortiz Lizcano, S. Villa, Y. Zhou, *et al.*, "Optimal Design of Multilayer Optical Color Filters for Building-Integrated Photovoltaic (BIPV) Applications", *Solar RRL*, vol. 7, no. 19, Oct. 2023, ISSN: 2367198X. DOI: 10.1002/solr.202300256.

[39] H. Meddeb, M. Götz-Köhler, N. Neugebohrn, *et al.*, *Tunable Photovoltaics: Adapting Solar Cell Technologies to Versatile Applications*, Jul. 2022. DOI: 10.1002/aenm.202200713.

[40] P. Sehati, I. Malmros, S. Karlsson, and P. Kovacs, *BUILT ENVIRONMENT BUILDING TECHNOLOGY Aesthetically pleasing PV modules for the Built Environment*, ISBN: 9789188907301.

[41] Z. Li, T. Ma, H. Yang, L. Lu, and R. Wang, *Transparent and Colored Solar Photovoltaics for Building Integration*, Mar. 2021. DOI: 10.1002/solr.202000614.

[42] M. Pelle, F. Causone, L. Maturi, and D. Moser, *Opaque Coloured Building Integrated Photovoltaic (BIPV): A Review of Models and Simulation Frameworks for Performance Optimisation*, Feb. 2023. DOI: 10.3390/en16041991.

[43] C. Kutter, B. Bläsi, H. R. Wilson, *et al.*, "DECORATED BUILDING-INTEGRATED PHOTOVOLTAIC MODULES: POWER LOSS, COLOR APPEARANCE AND COST ANALYSIS", Tech. Rep.

[44] F. Lisco, G. Cattaneo, A. Virtuani, *et al.*, "Design and testing of a demonstrative BIPV façade manufactured with novel glass-free colored lightweight PV modules", in *2023 International Conference on Clean Electrical Power, ICCEP 2023*, Institute of Electrical and Electronics Engineers Inc., 2023, pp. 657–662, ISBN: 9798350348378. DOI: 10.1109/ICCEP57914.2023.10247449.

[45] T. Gewohn, M. R. Vogt, B. Lim, C. Schinke, and R. Brendel, "Postproduction Coloring of Photovoltaic Modules With Imprinted Textiles", *IEEE JOURNAL OF PHOTOVOLTAICS*, vol. 11, no. 1, 2021. DOI: 10.1109/JPHOTOV.2020.3034001. [Online]. Available: https://www.ieee.org/publications/rights/index.html.

[46] Kameleon Solar, *Portfolio*, Feb. 2024.

[47] B. Blasi, T. Kroyer, T. Kuhn, and O. Hohn, "The MorphoColor Concept for Colored Photovoltaic Modules", *IEEE Journal of Photovoltaics*, vol. 11, no. 5, pp. 1305–1311, Sep. 2021, ISSN: 21563403. DOI: 10.1109/JPHOTOV.2021.3090158.

[48] G. Peharz, K. Berger, B. Kubicek, *et al.*, "Application of plasmonic coloring for making building integrated PV modules comprising of green solar cells", *Renewable Energy*, vol. 109, pp. 542–550, 2017, ISSN: 18790682. DOI: 10.1016/j.renene.2017.03.068.

[49] A. Morlier, B. Lim, S. Blankemeyer, *et al.*, "Photovoltaic Modules with the Look and Feel of a Stone Façade for Building Integration", *Solar Rapid Resarch Letters*, no. 6, pp. 1–18, 2021. DOI: 10.1002/solr.202100356. [Online]. Available: https://doi.org/10.1002/solr.202100356..

[50] T. Masuda, Y. Kudo, and D. Banerjee, "Visually attractive and high-power-retention solar modules by coloring with automotive paints", *Coatings*, vol. 8, no. 8, Aug. 2018, ISSN: 20796412. DOI: 10.3390/coatings8080282.

[51] M. K. Basher, M. Nur-E-alam, M. M. Rahman, S. Hinckley, and K. Alameh, "Design, Development, and Characterization of Highly Efficient Colored Photovoltaic Module for Sustainable Buildings Applications", *Sustainability (Switzerland)*, vol. 14, no. 7, Apr. 2022, ISSN: 20711050. DOI: 10.3390/su14074278.

[52] W. G. Shin, J. Y. Shin, H. M. Hwang, C. H. Park, and S. W. Ko, "Power Generation Prediction of Building-Integrated Photovoltaic System with Colored Modules Using Machine Learning", *Energies*, vol. 15, no. 7, Apr. 2022, ISSN: 19961073. DOI: 10.3390/en15072589.

[53] B. Riedel, P. Messaoudi, Y. B. Assoa, *et al.*, "Color coated glazing for next generation BIPV: Performance vs aesthetics", *EPJ Photovoltaics*, vol. 12, 2021, ISSN: 21050716. DOI: 10.1051/epjpv/2021012.

[54] O. Isabella, "Light management in thin-film silicon solar cells", Ph.D. dissertation, Delft University of Technology, Delft, 2013.

[55] H. A. Macleod, *Thin-Film Optical Filters*, 5th ed., R. G. W. Brown and E. R. Pike, Eds. Boca Raton: Taylor & Francis Group, 2015, p. 696.

[56] A. Soman and A. Antony, "Colored solar cells with spectrally selective photonic crystal reflectors for application in building integrated photovoltaics", *Solar Energy*, vol. 181, pp. 1–8, Mar. 2019, ISSN: 0038092X. DOI: 10.1016/j.solener.2019.01.058.

[57] A. Røyset, T. Kolås, Ø. Nordseth, and C. C. You, "Optical interference coatings for coloured building integrated photovoltaic modules: Predicting and optimising visual properties and efficiency", *Energy and Buildings*, vol. 298, Nov. 2023, ISSN: 03787788. DOI: 10.1016/j.enbuild.2023.113517.

[58] A. Wessels, A. Callies, B. Bläsi, T. Kroyer, and O. Höhn, "Modeling the optical properties of Morpho-inspired thin-film interference filters on structured surfaces", *Optics Express*, vol. 30, no. 9, p. 14 586, 2022, ISSN: 10944087. DOI: 10.1364/oe.455776.

[59] A. Ingenito, J. C. O. Lizcano, S. L. Luxembourg, *et al.*, "Optimized back Reflectors for Rear Diffused c-Si Solar Cells", *Energy Procedia*, vol. 55, pp. 94–100, Jan. 2014, ISSN: 1876-6102. DOI: 10.1016/J.EGYPRO.2014.08.085.

[60] LOF Solar, *Commercial Projects*, Feb. 2024.

[61] Soluxa, *Our Projects*, Feb. 2024.

[62] Kromatix, *References*, Feb. 2024.

[63] Megasol, *SolarColor Morpho*, Mar. 2024.

[64] N. Jolissaint, R. Hanbali, J. C. Hadorn, and A. Schüler, "Colored solar façades for buildings", in *Energy Procedia*, vol. 122, Elsevier Ltd, 2017, pp. 175–180. DOI: 10.1016/j.egypro.2017.07.340.

[65] M. Rudzikas, J. Donėlienė, E. Bužavaitė-Vertelienė, Z. Balevičius, C. Leuvrey, and A. Šetkus, "Design and investigation of 1D photonic crystal based structures for BIPV cell colorization by sol-gel dipping technology", *Solar Energy*, vol. 250, pp. 285-294, Jan. 2023, ISSN: 0038092X. DOI: 10.1016/j.solener.2022.12.028.

[66] Z. Xu, T. Matsui, K. Matsubara, and H. Sai, "Tunable and angle-insensitive structural coloring of solar cell modules for high performance building-integrated photovoltaic application", *Solar Energy Materials and Solar Cells*, vol. 247, Oct. 2022, ISSN: 09270248. DOI: 10.1016/j.solmat.2022.111952.

[67] V. Neder, S. L. Luxembourg, and A. Polman, "Efficient colored silicon solar modules using integrated resonant dielectric nanoscatterers", *Applied Physics Letters*, vol. 111, no. 7, Aug. 2017, ISSN: 00036951. DOI: 10.1063/1.4986796.

[68] F. Uleman, V. Neder, A. Cordaro, A. Alù, and A. Polman, "Resonant Metagratings for Spectral and Angular Control of Light for Colored Rooftop Photovoltaics", *ACS Applied Energy Materials*, vol. 3, no. 4, pp. 3150–3156, Apr. 2020, ISSN: 25740962. DOI: 10.1021/acsaem.0c00027.

[69] Y. Zhou, C. Jia, K. Lu, C. Wang, L. Ma, and L. Liu, "Energy-efficient colorful silicon photovoltaic modules driven by transparent-colored radiative cooling", *Solar Energy Materials and Solar Cells*, vol. 259, Aug. 2023, ISSN: 09270248. DOI: 10.1016/j.solmat.2023.112459.

[70] Z. Li, T. Ma, S. Li, *et al.*, "High-Efficiency, Mass-Producible, and Colored Solar Photovoltaics Enabled by Self-Assembled Photonic Glass", *ACS Nano*, vol. 16, pp. 11 473–11 482, 2022. DOI: 10.1021/acsnano.2c05840. [Online]. Available: https: //doi.org/10.1021/acsnano.2c05840.

[71] Y. Wu, Y. Chen, Q. Song, and S. Xiao, *Dynamic Structural Colors Based on All-Dielectric Mie Resonators*, Jun. 2021. DOI: 10.1002/adom.202002126.

[72] M. Schmid, P. Andrae, and P. Manley, "Plasmonic and photonic scattering and near fields of nanoparticles", Tech. Rep., 2014. [Online]. Available: http://www.nanoscalereslett.com/content/9/1/50.

[73] T. Das Gupta, L. Martin-Monier, W. Yan, *et al.*, "Self-assembly of nanostructured glass metasurfaces via templated fluid instabilities", *Nature Nanotechnology*, vol. 14, no. 4, pp. 320–327, Apr. 2019, ISSN: 17483395. DOI: 10.1038/s41565-019-0362-9.

[74] A. Ghosh, S. Sundaram, and T. K. Mallick, "Colour properties and glazing factors evaluation of multicrystalline based semi-transparent Photovoltaic-vacuum glazing for BIPV application", *Renewable Energy*, vol. 131, pp. 730–736, Feb. 2019, ISSN: 18790682. DOI: 10.1016/j.renene.2018.07.088.

[75] W. J. Kim, D. H. Cho, S. H. Hong, *et al.*, "Implementation of various colors in Cu(In,Ga)Se2 thin-film solar cells by diffractive nanostructures", *Solar Energy Materials and Solar Cells*, vol. 257, Aug. 2023, ISSN: 09270248. DOI: 10.1016/j.solmat.2023.112392.

[76] G. Y. Yoo, J. S. Jeong, S. Lee, *et al.*, "Multiple-Color-Generating Cu(In,Ga)(S,Se)2 Thin-Film Solar Cells via Dichroic Film Incorporation for Power-Generating Window Applications", *ACS Applied Materials and Interfaces*, vol. 9, no. 17, pp. 14 817–14 826, May 2017, ISSN: 19448252. DOI: 10.1021/acsami.7b01416.

[77] S. H. Lee, S. J. Yun, M. Shin, and J. W. Lim, "Cu2O thin films as the color-adjusting layer in semi-transparent a-Si:H solar cells", *Solar Energy Materials and Solar Cells*, vol. 117, pp. 519–525, 2013, ISSN: 09270248. DOI: 10.1016/j.solmat.2013.07.029.

[78] S. Yeop Myong and S. Won Jeon, "Design of esthetic color for thin-film silicon semi-transparent photovoltaic modules", *Solar Energy Materials and Solar Cells*, vol. 143, pp. 442–449, 2015, ISSN: 09270248. DOI: 10.1016/j.solmat.2015.07.042. [Online]. Available: http://dx.doi.org/10.1016/j.solmat.2015.07.042.

[79] N. Neugebohrn, K. Gehrke, K. Brucke, M. Götz, and M. Vehse, "Multifunctional metal oxide electrodes: Colour for thin film solar cells", *Thin Solid Films*, vol. 685, pp. 131–135, Sep. 2019, ISSN: 00406090. DOI: 10.1016/j.tsf.2019.06.012.

[80] Onyx Solar, *Projects*, Feb. 2024.

[81] C. Nan, Y. Hao, X. Huang, H. Wang, and H. Yang, "Investigation on temperature dependence of recent high-efficiency silicon solar modules", *Solar Energy Materials and Solar Cells*, vol. 266, p. 112 649, 2024, ISSN: 0927-0248. DOI: https://doi.org/10.1016/j.solmat.2023.112649. [Online]. Available: https://www.sciencedirect.com/science/article/pii/S0927024823004701.

[82] P. Singh and N. M. Ravindra, "Temperature dependence of solar cell performance - An analysis", *Solar Energy Materials and Solar Cells*, vol. 101, pp. 36–45, 2012, ISSN: 09270248. DOI: 10.1016/j.solmat.2012.02.019. [Online]. Available: http://dx.doi.org/10.1016/j.solmat.2012.02.019.

[83] J. Ascencio-Vásquez, I. Kaaya, K. Brecl, K. A. Weiss, and M. Topič, "Global climate data processing and mapping of degradation mechanisms and degradation rates of PV modules", *Energies*, vol. 12, no. 24, pp. 1–16, 2019, ISSN: 19961073. DOI: 10.3390/en12244749.

[84] I. Kaaya, J. Ascencio-Vásquez, K. A. Weiss, and M. Topič, "Assessment of uncertainties and variations in PV modules degradation rates and lifetime predictions using physical models", *Solar Energy*, vol. 218, no. June 2020, pp. 354–367, 2021, ISSN: 0038092X. DOI: 10.1016/j.solener.2021.01.071.

[85] A. A. r. Amr, A. A. Hassan, M. Abdel-Salam, and A. H. M. El-Sayed, "Enhancement of photovoltaic system performance via passive cooling: Theory versus experiment", *Renewable Energy*, vol. 140, pp. 88–103, 2019, ISSN: 18790682. DOI: 10.1016/j.renene.2019.03.048. [Online]. Available: https://doi.org/10.1016/j.renene.2019.03.048.

[86] E. Z. Ahmad, K. Sopian, H. Jarimi, *et al.*, "Recent advances in passive cooling methods for photovoltaic performance enhancement", *International Journal of Electrical and Computer Engineering*, vol. 11, no. 1, pp. 146–154, 2021, ISSN: 20888708. DOI: 10.11591/ijece.v11i1.pp146-154.

[87] S. Siah Chehreh Ghadikolaei, "Solar photovoltaic cells performance improvement by cooling technology: An overall review", *International Journal of Hydrogen Energy*, vol. 46, no. 18, pp. 10 939–10 972, 2021, ISSN: 03603199. DOI: 10.1016/j.ijhydene.2020.12.164. [Online]. Available: https://doi.org/10.1016/j.ijhydene.2020.12.164.

[88] R. Harahap and S. Suherman, "Active Versus Passive Cooling Systems In Increasing Solar Panel Output", *Procedia Environmental Science, Engineering and Management*, vol. 8, no. 1, pp. 157–166, 2021, ISSN: 23929545.

[89] S. Nižetić, E. Giama, and A. M. Papadopoulos, "Comprehensive analysis and general economic-environmental evaluation of cooling techniques for photovoltaic panels, Part II: Active cooling techniques", *Energy Conversion and Management*, vol. 155, pp. 301–323, Jan. 2018, ISSN: 0196-8904. DOI: 10.1016/J.ENCONMAN.2017.10.071.

[90] H. M. Maghrabie, A. S. A. Mohamed, A. M. Fahmy, and A. A. A. Samee, "Performance augmentation of PV panels using phase change material cooling technique: A review", *SVU-International Journal of Engineering Sciences and Applications*, vol. 2, no. 2, pp. 1–13, 2021, ISSN: 2735-4571. DOI: 10.21608/SVUIJESA.2021.87202.1013.

[91] H. M. Ali, *Recent advancements in PV cooling and efficiency enhancement integrating phase change materials based systems – A comprehensive review*, Feb. 2020. DOI: 10.1016/j.solener.2019.11.075.

[92] B. Zhao, M. Hu, X. Ao, Q. Xuan, and G. Pei, "Spectrally selective approaches for passive cooling of solar cells: A review", *Applied Energy*, vol. 262, no. October 2019, p. 114 548, 2020, ISSN: 03062619. DOI: 10.1016/j.apenergy.2020.114548. [Online]. Available: https://doi.org/10.1016/j.apenergy.2020.114548.

[93] L. Zhu, A. Raman, K. X. Wang, M. A. Anoma, and S. Fan, "Radiative cooling of solar cells", *Optica*, vol. 1, no. 1, p. 32, Jul. 2014, ISSN: 23342536. DOI: 10.1364/optica.1.000032.

[94] B. Zhao, M. Hu, X. Ao, and G. Pei, "Performance analysis of enhanced radiative cooling of solar cells based on a commercial silicon photovoltaic module", *Solar Energy*, vol. 176, pp. 248–255, Dec. 2018, ISSN: 0038092X. DOI: 10.1016/j.solener.2018.10.043.

[95] T. S. Safi and J. N. Munday, "Improving photovoltaic performance through radiative cooling in both terrestrial and extraterrestrial environments", *Optics Express*, vol. 23, no. 19, A1120, Sep. 2015, ISSN: 10944087. DOI: 10.1364/oe.23.0a1120.

[96] B. Zhao, M. Hu, X. Ao, X. Huang, X. Ren, and G. Pei, "Conventional photovoltaic panel for nocturnal radiative cooling and preliminary performance analysis", *Energy*, vol. 175, pp. 677–686, May 2019, ISSN: 03605442. DOI: 10.1016/j.energy.2019.03.106.

[97] D. Sato and N. Yamada, "Review of photovoltaic module cooling methods and performance evaluation of the radiative cooling method", *Renewable and Sustainable Energy Reviews*, vol. 104, no. December 2018, pp. 151–166, 2019, ISSN: 18790690. DOI: 10.1016/j.rser.2018.12.051. [Online]. Available: https://doi.org/10.1016/j.rser.2018.12.051.

[98] M. Hu, B. Zhao, Suhendri, *et al.*, *Applications of radiative sky cooling in solar energy systems: Progress, challenges, and prospects*, May 2022. DOI: 10.1016/j.rser.2022.112304.

[99] N. Khorrami, M. Rajabi Zargarabadi, and M. Dehghan, "A novel spectrally selective radiation shield for cooling a photovoltaic module", *Sustainable Energy Technologies and Assessments*, vol. 46, no. April, p. 101 269, 2021, ISSN: 22131388. DOI: 10.1016/j.seta.2021.101269. [Online]. Available: https://doi.org/10.1016/j.seta.2021.101269.

[100] R. Vaillon, O. Dupré, R. B. Cal, and M. Calaf, "Pathways for mitigating thermal losses in solar photovoltaics", *Scientific Reports*, vol. 8, no. 1, Dec. 2018, ISSN: 20452322. DOI: 10.1038/s41598-018-31257-0.

[101] X. Sun, T. J. Silverman, Z. Zhou, M. R. Khan, P. Bermel, and M. A. Alam, "An Optics-Based Approach to Thermal Management of Photovoltaics: Selective-Spectral and Radiative Cooling", Tech. Rep.

[102] R. B. Heideier, A. L. Gimenes, M. E. Udaeta, and M. A. Saidel, "Optical filter design applied to photovoltaic modules to maximize energy production", *Solar Energy*, vol. 159, pp. 908–913, Jan. 2018, ISSN: 0038092X. DOI: 10.1016/j.solener.2017.10.013.

[103] Y. Lu, Z. Chen, L. Ai, *et al.*, "A Universal Route to Realize Radiative Cooling and Light Management in Photovoltaic Modules", *Solar RRL*, vol. 1, no. 10, Oct. 2017, ISSN: 2367198X. DOI: 10.1002/solr.201700084.

[104] S. Lin, L. Ai, J. Zhang, *et al.*, "Silver ants-inspired flexible photonic architectures with improved transparency and heat radiation for photovoltaic devices", *Solar Energy Materials and Solar Cells*, vol. 203, Dec. 2019, ISSN: 09270248. DOI: 10.1016/j.solmat.2019.110135.

[105] X. Cui, X. Sun, L. Zhou, and X. Wei, "Thermal and electrical performance analysis of monofacial double-glass photovoltaic module with radiative cooling coating on the rear surface", *Solar Energy*, vol. 264, Nov. 2023, ISSN: 0038092X. DOI: 10.1016/j.solener.2023.111986.

[106] A. Ingenito, S. Luxembourg, P. Spinelli, A. Weeber, O. Isabella, and M. Zeman, "Optimized metal free back reflectors for high efficiency open rear c-Si solar cells", in *2015 IEEE 42nd Photovoltaic Specialist Conference, PVSC 2015*, Institute of Electrical and Electronics Engineers Inc., Dec. 2015, ISBN: 9781479979448. DOI: 10.1109/PVSC.2015.7356157.

[107] O. Isabella, S. Dobrovolskiy, G. Kroon, and M. Zeman, "Design and application of dielectric distributed Bragg back reflector in thin-film silicon solar cells", *Journal of non-crystalline solids*, vol. 358, no. 17, pp. 2295–2298, 2012.

[108] L. Adachi, G. Hanashi, S. Kubota, *et al.*, "Highly efficient color-control technique for building-integrated photovoltaics using optical dielectric thin film", *Japanese Journal of Applied Physics*, vol. 62, no. SL, Aug. 2023, ISSN: 13474065. DOI: 10.35848/1347-4065/acc594.

[109] Y. An, C. Sheng, and X. Li, "Radiative cooling of solar cells: Opto-electro-thermal physics and modeling", *Nanoscale*, vol. 11, no. 36, pp. 17 073–17 083, Sep. 2019, ISSN: 20403372. DOI: 10.1039/c9nr04110a.

[110] E. Akerboom, T. Veeken, C. Hecker, J. Van De Groep, and A. Polman, "Passive Radiative Cooling of Silicon Solar Modules with Photonic Silica Microcylinders", *ACS Photonics*, vol. 9, no. 12, pp. 3831–3840, Dec. 2022, ISSN: 23304022. DOI: 10.1021/acsphotonics.2c01389.

[111] B. Zhao, M. Hu, X. Ao, Q. Xuan, and G. Pei, "Comprehensive photonic approach for diurnal photovoltaic and nocturnal radiative cooling", *Solar Energy Materials and Solar Cells*, vol. 178, pp. 266–272, May 2018, ISSN: 09270248. DOI: 10.1016/j.solmat.2018.01.023.

[112] G. Perrakis, A. C. Tasolamprou, G. Kenanakis, E. N. Economou, S. Tzortzakis, and M. Kafesaki, "Combined nano and micro structuring for enhanced radiative cooling and efficiency of photovoltaic cells", *Scientific Reports*, vol. 11, no. 1, Dec. 2021, ISSN: 20452322. DOI: 10.1038/s41598-021-91061-1.

[113] G. Perrakis, A. C. Tasolamprou, G. Kenanakis, E. N. Economou, S. Tzortzakis, and M. Kafesaki, "Passive radiative cooling and other photonic approaches for the temperature control of photovoltaics: a comparative study for crystalline silicon-based architectures", *Optics Express*, vol. 28, no. 13, p. 18 548, Jun. 2020, ISSN: 10944087. DOI: 10.1364/oe.388208.

[114] G. Fan, B. Duan, Y. Zhang, X. Li, and X. Ji, "Full-spectrum selective thin film based photonic cooler for solar cells of space solar power station", *Acta Astronautica*, vol. 180, pp. 196–204, Mar. 2021, ISSN: 00945765. DOI: 10.1016/j.actaastro.2020.12.035.

[115] I. M. Slauch, M. G. Deceglie, T. J. Silverman, and V. E. Ferry, "Spectrally Selective Mirrors with Combined Optical and Thermal Benefit for Photovoltaic Module Thermal Management", *ACS Photonics*, vol. 5, no. 4, pp. 1528–1538, Apr. 2018, ISSN: 23304022. DOI: 10.1021/acsphotonics.7b01586.

[116] W. Li, Y. Shi, K. Chen, L. Zhu, and S. Fan, "A Comprehensive Photonic Approach for Solar Cell Cooling", *ACS Photonics*, vol. 4, no. 4, pp. 774–782, Apr. 2017, ISSN: 23304022. DOI: 10.1021/acsphotonics.7b00089.

[117] V. Tyagi, K. Chopra, R. Sharma, *et al.*, "A comprehensive review on phase change materials for heat storage applications: Development, characterization, thermal and chemical stability", *Solar Energy Materials and Solar Cells*, vol. 234, p. 111 392, 2022, ISSN: 0927-0248. DOI: https://doi.org/10.1016/j.solmat.2021.111392.

[118] P. Zhang, X. Xiao, and Z. W. Ma, *A review of the composite phase change materials: Fabrication, characterization, mathematical modeling and application to performance enhancement*, Mar. 2016. DOI: 10.1016/j.apenergy.2015.12.043.

[119] I. Shamseddine, F. Pennec, P. Biwole, and F. Fardoun, "Supercooling of phase change materials: A review", *Renewable and Sustainable Energy Reviews*, vol. 158, p. 112 172, 2022, ISSN: 1364-0321. DOI: https://doi.org/10.1016/j.rser.2022.112172. [Online]. Available: https://www.sciencedirect.com/science/article/pii/S1364032122000995.

[120] E. Japs, G. Sonnenrein, J. Steube, J. Vrabec, E. Kenig, and S. Krauter, "Technical Investigation of Photovoltaic module with integrated improved phase change material", in *28th European Photovoltaic Solar Energy Conference and Exhibition*, EUPVSEC, 2013, pp. 500–502.

[121] S. Maiti, S. Banerjee, K. Vyas, P. Patel, and P. K. Ghosh, "Self regulation of photovoltaic module temperature in V-trough using a metal-wax composite phase change matrix", *Solar Energy*, vol. 85, no. 9, pp. 1805–1816, 2011, ISSN: 0038092X. DOI: 10.1016/j.solener.2011.04.021. [Online]. Available: http://dx.doi.org/10.1016/j.solener.2011.04.021.

[122] S. Sharma, L. Micheli, W. Chang, A. A. Tahir, K. S. Reddy, and T. K. Mallick, "Nano-enhanced Phase Change Material for thermal management of BICPV", *Applied Energy*, vol. 208, pp. 719–733, Dec. 2017, ISSN: 03062619. DOI: 10.1016/j.apenergy.2017.09.076.

[123] A. Hasan, J. Sarwar, H. Alnoman, and S. Abdelbaqi, "Yearly energy performance of a photovoltaic-phase change material (PV-PCM) system in hot climate", *Solar Energy*, vol. 146, pp. 417–429, 2017, ISSN: 0038092X. DOI: 10.1016/j.solener.2017.01.070.

[124] R. Stropnik and U. Stritih, "Increasing the efficiency of PV panel with the use of PCM", *Renewable Energy*, vol. 97, pp. 671–679, Nov. 2016, ISSN: 18790682. DOI: 10.1016/j.renene.2016.06.011.

[125] R. Madurai Elavarasan, M. Nadarajah, R. Pugazhendhi, and S. Gangatharan, "An experimental investigation on coalescing the potentiality of PCM, fins and water to achieve sturdy cooling effect on PV panels", *Applied Energy*, vol. 356, Feb. 2024, ISSN: 03062619. DOI: 10.1016/j.apenergy.2023.122371.

[126] K. Senthil Kumar, S. Revanth, D. Sanjeev, P. Sabesh Kumar, and P. Surya, "Experimental investigation of improving the energy conversion efficiency of pv cell by integrating with pcm", *Materials Today: Proceedings*, vol. 37, pp. 712–716, 2021, International Conference on Newer Trends and Innovation in Mechanical Engineering: Materials Science, ISSN: 2214-7853. DOI: https://doi.org/10.1016/j.matpr.2020.05.723. [Online]. Available: https://www.sciencedirect.com/science/article/pii/S2214785320343352.

[127] A. Karthick, K. Kalidasa Murugavel, A. Ghosh, K. Sudhakar, and P. Ramanan, "Investigation of a binary eutectic mixture of phase change material for building integrated photovoltaic (bipv) system", *Solar Energy Materials and Solar Cells*, vol. 207, p. 110 360, 2020, ISSN: 0927-0248. DOI: https://doi.org/10.1016/j.solmat.2019.110360. [Online]. Available: https://www.sciencedirect.com/science/article/pii/S0927024819306865.

[128] A. Singh, V. Umakanth, N. Tyagi, and S. Kumar, "A comparative study of different polymer materials for the development of flexible crystalline silicon modules", *Solar Energy Materials and Solar Cells*, vol. 255, Jun. 2023, ISSN: 09270248. DOI: 10.1016/j.solmat.2023.112259.

[129] T. Wongwuttanasatian, T. Sarikarin, and A. Suksri, "Performance enhancement of a photovoltaic module by passive cooling using phase change material in a finned container heat sink", *Solar Energy*, vol. 195, pp. 47–53, 2020, ISSN: 0038-092X. DOI: https://doi.org/10.1016/j.solener.2019.11.053. [Online]. Available: https://www.sciencedirect.com/science/article/pii/S0038092X19311533.

[130] N. Choubineh, H. Jannesari, and A. Kasaeian, "Experimental study of the effect of using phase change materials on the performance of an air-cooled photovoltaic system", *Renewable and Sustainable Energy Reviews*, vol. 101, pp. 103–111, 2019, ISSN: 1364-0321. DOI: https://doi.org/10.1016/j.rser.2018.11.001. [Online]. Available: https://www.sciencedirect.com/science/article/pii/S1364032118307330.

[131] F. Rajaee, M. A. V. Rad, A. Kasaeian, O. Mahian, and W. M. Yan, "Experimental analysis of a photovoltaic/thermoelectric generator using cobalt oxide nanofluid and phase change material heat sink", *Energy Conversion and Management*, vol. 212, May 2020, ISSN: 01968904. DOI: 10.1016/j.enconman.2020.112780.

[132] E. Klugmann-Radziemska and P. Wcisło-Kucharek, "Photovoltaic module temperature stabilization with the use of phase change materials", *Solar Energy*, vol. 150, pp. 538–545, 2017, ISSN: 0038-092X. DOI: https://doi.org/10.1016/j.solener.2017. 05.016. [Online]. Available: https://www.sciencedirect.com/science/article/pii/S0038092X17303936.

[133] P. H. Biwole, P. Eclache, and F. Kuznik, "Phase-change materials to improve solar panel's performance", *Energy and Buildings*, vol. 62, pp. 59–67, 2013, ISSN: 03787788. DOI: 10.1016/j.enbuild.2013.02.059.

[134] Y. Dutil, D. R. Rousse, N. B. Salah, S. Lassue, and L. Zalewski, *A review on phase-change materials: Mathematical modeling and simulations*, Jan. 2011. DOI: 10.1016/j.rser.2010.06.011.

[135] M. J. Huang, P. C. Eames, and B. Norton, "Thermal regulation of building-integrated photovoltaics using phase change materials", *International Journal of Heat and Mass Transfer*, vol. 47, no. 12-13, pp. 2715–2733, Jun. 2004, ISSN: 00179310. DOI: 10.1016/j.ijheatmasstransfer.2003.11.015.

[136] K. Kant, A. Shukla, A. Sharma, and P. H. Biwole, "Heat transfer studies of photovoltaic panel coupled with phase change material", *Solar Energy*, vol. 140, pp. 151–161, Dec. 2016, ISSN: 0038092X. DOI: 10.1016/j.solener.2016.11.006.

[137] S. Khanna, K. S. Reddy, and T. K. Mallick, "Optimization of finned solar photovoltaic phase change material (finned pv pcm) system", *International Journal of Thermal Sciences*, vol. 130, pp. 313–322, Aug. 2018, ISSN: 12900729. DOI: 10.1016/j.ijthermalsci.2018.04.033.

[138] M. Tao, L. Zhenpeng, and Z. Jiaxin, *Photovoltaic panel integrated with phase change materials (PV-PCM): technology overview and materials selection*, Dec. 2019. DOI: 10.1016/j.rser.2019.109406.

[139] S. Preet, *A review on the outlook of thermal management of photovoltaic panel using phase change material*, Dec. 2021. DOI: 10.1016/j.egycc.2021.100033.

[140] R. Santbergen, T. Meguro, T. Suezaki, G. Koizumi, K. Yamamoto, and M. Zeman, "GenPro4 Optical Model for Solar Cell Simulation and Its Application to Multi-junction Solar Cells", *IEEE Journal of Photovoltaics*, vol. 7, no. 3, pp. 919–926, May 2017, ISSN: 21563381. DOI: 10.1109/JPHOTOV.2017.2669640.

[141] D.-P. H. Holst, "Development and application of a modular ray tracing framework to multi-scale simulations in photovoltaics", Ph.D. dissertation, Gottfried Wilhelm Leibniz Universitat Hannover, Hannover, 2015, pp. 1–139.

[142] N. Tucher, J. Eisenlohr, H. Gebrewold, *et al.*, "Optical simulation of photovoltaic modules with multiple textured interfaces using the matrix-based formalism OPTOS", *Optics Express*, vol. 24, no. 14, A1083, Jul. 2016, ISSN: 1094-4087. DOI: 10.1364/oe.24.0a1083.

[143] P. Tillmann, K. Jäger, A. Karsenti, L. Kreinin, and C. Becker, "Model-chain validation for estimating the energy yield of bifacial perovskite/silicon tandem solar cells", *Solar RRL*, vol. 6, no. 9, p. 2 200 079, 2022. DOI: https://doi.org/10.1002/solr.202200079. eprint: https://onlinelibrary.wiley.com/doi/pdf/10.1002/solr.202200079. [Online]. Available: https://onlinelibrary.wiley.com/doi/abs/10.1002/solr.202200079.

[144] A. Wessels, L. Christen, A. Callies, T. Kroyer, O. Höhn, and B. Bläsi, "Modeling of thin-film interference filters on structured substrates: Microfacet-based bsdf versus ray tracing", *Opt. Express*, vol. 31, no. 12, pp. 20 102–20 111, Jun. 2023. DOI: 10.1364/OE.489221. [Online]. Available: https://opg.optica.org/oe/abstract.cfm?URI=oe-31-12-20102.

[145] A. V. Tikhonravov, "Needle optimization technique: the history and the future", *Optical Thin Films V: New Developments*, vol. 3133, p. 2, 1997, ISSN: 0277786X. DOI: 10.1117/12.290180.

[146] A. Borja Block, J. Escarre Palou, A. Faes, A. Virtuani, and C. Ballif, "Accurate color characterization of solar photovoltaic modules for building integration", *Solar Energy*, vol. 267, Jan. 2024, ISSN: 0038092X. DOI: 10.1016/j.solener.2023.112227.

[147] C. A. Gueymard, "The SMARTS spectral irradiance model after 25 years: New developments and validation of reference spectra", *Solar Energy*, vol. 187, pp. 233–253, Jul. 2019, ISSN: 0038-092X. DOI: 10.1016/J.SOLENER.2019.05.048.

[148] R. Perez, P. Ineichen, R. Seals, J. Michalsky, and R. Stewart, "Modeling daylight availability and irradiance components from direct and global irradiance", *Solar Energy*, vol. 44, no. 5, pp. 271–289, 1990, ISSN: 0038-092X. DOI: https://doi.org/10.1016/0038-092X(90)90055-H. [Online]. Available: https://www.sciencedirect.com/science/article/pii/0038092X9090055H.

[149] L. Xu, W. Liu, H. Liu, *et al.*, "Heat generation and mitigation in silicon solar cells and modules", *Joule*, vol. 5, no. 3, pp. 631–645, Mar. 2021, ISSN: 25424351. DOI: 10.1016/j.joule.2021.01.012.

[150] S. P. Aly, S. Ahzi, N. Barth, and B. W. Figgis, "Two-dimensional finite difference-based model for coupled irradiation and heat transfer in photovoltaic modules", *Solar Energy Materials and Solar Cells*, vol. 180, pp. 289–302, Jun. 2018, ISSN: 0927-0248. DOI: 10.1016/J.SOLMAT.2017.06.055.

[151] T. Bergman, A. Lavine, and F. Incropera, *Fundamentals of Heat and Mass Transfer, 7th Edition*. John Wiley & Sons, Incorporated, 2011, ISBN: 9781118137253. [Online]. Available: https://books.google.nl/books?id=5cgbAAAAQBAJ.

[152] P. Lighthouse, *PV Lighthouse: Equivalent-circuit calculator*. [Online]. Available: https://www.pvlighthouse.com.au.

[153] K. Yoshikawa, W. Yoshida, T. Irie, *et al.*, "Exceeding conversion efficiency of 26% by heterojunction interdigitated back contact solar cell with thin film si technology", *Solar Energy Materials and Solar Cells*, vol. 173, pp. 37–42, 2017, Proceedings of the 7th international conference on Crystalline Silicon Photovoltaics, ISSN: 0927-0248. DOI: https://doi.org/10.1016/j.solmat.2017.06.024.

[154] P. Cousins, D. Smith, H.-C. Luan, *et al.*, "Generation 3: Improved performance at lower cost", 2010, pp. 275–278. DOI: 10.1109/PVSC.2010.5615850.

[155] C. Oleari, "Chapter 9 - color in optical coatings", in *Optical Thin Films and Coatings (Second Edition)*, ser. Woodhead Publishing Series in Electronic and Optical Materials, A. Piegari and F. Flory, Eds., Second Edition, Woodhead Publishing, 2018, pp. 389–421, ISBN: 978-0-08-102073-9. DOI: https://doi.org/10.1016/B978-0-08-102073-9.00009-6. [Online]. Available: https://www.sciencedirect.com/science/article/pii/B9780081020739000096.

[156] J. Kvavle, C. Bell, J. Henrie, S. Schultz, and A. Hawkins, "Improvement to reflective dielectric film color pictures", *Optics Express*, vol. 12, no. 23, pp. 5789–5794, 2004. DOI: 10.1364/OPEX.12.005789.

[157] E. Schneiderlochner, J. Bruckner, and R. Biedermann, "High throughput magnetron sputtering technology at 10,000 wafers per hour cost-competitive manufacturing of transparent conductive oxides (tco)", *3rd International workshop on SHJ Solar Cells*, pp. 1–17, 2020.

[158] P. Kelly and R. Arnell, "Magnetron sputtering: A review of recent developments and applications", *Vacuum*, vol. 56, no. 3, pp. 159–172, 2000. DOI: 10.1016/S0042-207X(99)00189-X.

[159] A. Ingenito, O. Isabella, and M. Zeman, "Experimental demonstration of 4n 2 classical absorption limit in nanotextured ultrathin solar cells with dielectric omnidirectional back reflector", *ACS Photonics*, vol. 1, no. 3, pp. 270–278, 2014. DOI: 10.1021/ph4001586.

[160] M. Lumb, W. Yoon, C. Bailey, D. Scheiman, J. Tischler, and R. Walters, "Modeling and analysis of high-performance, multicolored anti-reflection coatings for solar cells", *Optics Express*, vol. 21, no. 104, A585–A594, 2013. DOI: 10.1364/OE.21.00A585.

[161] B. Conway, "Neural mechanisms of color vision: Double-opponent cells in the visual cortex", *Neural Mechanisms of Color Vision*, 2002.

[162] M. Nadenau, S. Winkler, D. Alleysson, and M. Kunt, "Human vision models for perceptually optimized image processing - a review", *Proceedings of the IEEE*, 2000.

[163] N. Ibraheem, M. Hasan, R. Khan, and P. Mishra, "Understanding color models: A review", *ARPN Journal of Science and Technology*, vol. 2, no. 3, pp. 265–275, 2012.

[164] J. Schanda, *Colorimetry: Understanding the CIE System*. 2007, pp. 1–459. DOI: 10.1002/9780470175637.

[165] R. Paschotta, *Cie standard illuminants*, RP Photonics Encyclopedia. DOI: 10.61835/6ho. [Online]. Available: https://www.rp-photonics.com/cie_standard_illuminants.html (visited on 05/22/2024).

[166] F. W. Billmeyer Jr., "Measuring colour, by r. w. g. hunt, ellis horwood, ltd, chichester, 1987; distributed by halsted press, div. john wiley & sons, new york, 221 pp.", *Color Research & Application*, vol. 13, no. 5, pp. 332–333, 1988. DOI: https://doi.org/10.1002/col.5080130511. eprint: https://onlinelibrary.wiley.com/doi/pdf/10.1002/col.5080130511. [Online]. Available: https://onlinelibrary.wiley.com/doi/abs/10.1002/col.5080130511.

[167] G. W. Meyer and D. P. Greenberg, "Perceptual color spaces for computer graphics", *SIGGRAPH Comput. Graph.*, vol. 14, no. 3, pp. 254–261, Jul. 1980, ISSN: 0097-8930. DOI: 10.1145/965105.807502. [Online]. Available: https://doi.org/10.1145/965105.807502.

[168] B. Lindbloom, *Rgb and xyz matrices*, Bruce Justin Lindbloom, 2017. [Online]. Available: http://www.brucelindbloom.com/index.html?Eqn_RGB_XYZ_Matrix.html (visited on 05/22/2024).

[169] G. Saravanan, G. Yamuna, and S. Nandhini, "Real time implementation of rgb to hsv/hsi/hsl and its reverse color space models", in *2016 International Conference on Communication and Signal Processing (ICCSP)*, 2016, pp. 0462–0466. DOI: 10.1109/ICCSP.2016.7754179.

[170] Y.-I. Ohta, T. Kanade, and T. Sakai, "Color information for region segmentation.", *Computer Graphics & Image Processing*, vol. 13, no. 3, pp. 222–241, 1980. DOI: 10.1016/0146-664X(80)90047-7.

[171] M. D. Fairchild, "Color appearance terminology", in *Color Appearance Models*. John Wiley and Sons, Ltd, 2013, ch. 4, pp. 85–96, ISBN: 9781118653128. DOI: https://doi.org/10.1002/9781118653128.ch4. eprint: https://onlinelibrary.wiley.com/doi/pdf/10.1002/9781118653128.ch4. [Online]. Available: https://onlinelibrary.wiley.com/doi/abs/10.1002/9781118653128.ch4.

[172] G. Yang, A. Ingenito, N. Van Hameren, O. Isabella, and M. Zeman, "Design and application of ion-implanted polysi passivating contacts for interdigitated back contact c-si solar cells", *Applied Physics Letters*, vol. 108, no. 3, 2016. DOI: 10.1063/1.4940364.

[173] G. Yang, A. Ingenito, O. Isabella, and M. Zeman, "Ibc c-si solar cells based on ion-implanted poly-silicon passivating contacts", *Solar Energy Materials and Solar Cells*, vol. 158, pp. 84–90, 2016. DOI: 10.1016/j.solmat.2016.05.041.

[174] P. Procel, A. Ingenito, R. De Rose, *et al.*, "Opto-electrical modelling and optimization study of a novel ibc c-si solar cell", *Progress in Photovoltaics: Research and Applications*, vol. 25, no. 6, pp. 452–469, 2017. DOI: 10.1002/pip.2874.

[175] P. Procel, G. Yang, O. Isabella, and M. Zeman, "Numerical simulations of ibc solar cells based on poly-si carrier-selective passivating contacts", *IEEE Journal of Photovoltaics*, vol. 9, no. 2, pp. 374–384, 2019. DOI: 10.1109/JPHOTOV.2019.2892527.

[176] M. Wolf, G. Noel, and R. Stirn, "Investigation of the double exponential in the current-voltage characteristics of silicon solar cells", *IEEE Transactions on Electron Devices*, vol. ED-24, no. 4, pp. 419–428, 1977. DOI: 10.1109/T-ED.1977.18750.

[177] J. Pcharles, G. Bordure, A. Khoury, and P. Mialhe, "Consistency of the double exponential model with physical mechanisms of conduction for a solar cell under illumination", *Journal of Physics D: Applied Physics*, vol. 18, no. 11, pp. 2261–2268, 1985. DOI: 10.1088/0022-3727/18/11/015.

[178] S. P. Coorporation, "MAXEON ™ GEN III SOLAR CELLS Electrical Characteristics of a typical Maxeon Gen III Cell", pp. 3–4, 2017.

[179] S. Villa, "Colored PV modules based on Interference Filters", Ph.D. dissertation, Delft University of Technology, Delft, 2018.

[180] J. Balenzategui and F. Chenlo, "Measurement and analysis of angular response of bare and encapsulated silicon solar cells", *Solar Energy Materials and Solar Cells*, vol. 86, no. 1, pp. 53–83, 2005. DOI: 10.1016/j.solmat.2004.06.007.

[181] E. Sjerps-Koomen, E. Alsema, and W. Turkenburg, "A simple model for pv module reflection losses under field conditions", *Solar Energy*, vol. 57, no. 6, pp. 421–432, 1996. DOI: 10.1016/S0038-092X(96)00137-5.

[182] B. Knisely, S. Janakeeraman, J. Kuitche, and G. Tamizhmani, *Validation of Draft International Electrotechnical Commission 61853-2 Standard: Angle of Incidence Effect on Photovoltaic Modules*, 2013.

[183] N. Martin and J. Ruiz, "Calculation of the pv modules angular losses under field conditions by means of an analytical model", *Solar Energy Materials and Solar Cells*, vol. 70, no. 1, pp. 25–38, 2001. DOI: 10.1016/S0927-0248(00)00408-6.

[184] B. Marion, "Numerical method for angle-of-incidence correction factors for diffuse radiation incident photovoltaic modules", *Solar Energy*, vol. 147, pp. 344–348, 2017. DOI: 10.1016/j.solener.2017.03.027.

[185] H. Tan, E. Psomadaki, O. Isabella, *et al.*, "Micro-textures for efficient light trapping and improved electrical performance in thin-film nanocrystalline silicon solar cells", *Applied Physics Letters*, vol. 103, no. 17, 2013. DOI: 10.1063/1.4826639.

[186] G. Yang, R. Van Swaaij, O. Isabella, and M. Zeman, "A novel way of texturing glass for microcrystalline silicon thin film solar cells application", *Progress in Photovoltaics: Research and Applications*, vol. 23, no. 10, pp. 1283–1290, 2015. DOI: 10.1002/pip.2550.

[187] G. Yang, R. Van Swaaij, H. Tan, O. Isabella, and M. Zeman, "Modulated surface textured glass as substrate for high efficiency microcrystalline silicon solar cells", *Solar Energy Materials and Solar Cells*, vol. 133, pp. 156–162, 2015. DOI: 10.1016/j.solmat.2014.11.013.

[188] T. C. Loef, "Periodic-Random Modulated Surface Textures", M.S. thesis, Delft University of Technology, Delft, 2018.

[189] SOLARGIS, *SOLARGIS Prospect*, Dec. 2023.

[190] J. Remund, S. Müller, M. Schmutz, and P. Graf, "Meteonorm version 8", 2020. [Online]. Available: METEOTEST%20(www.%20meteotest.%20com).

[191] H. Kawamura, K. Naka, N. Yonekura, *et al.*, "Simulation of I-V characteristics of a PV module with shaded PV cells", *Solar Energy Materials and Solar Cells*, vol. 75, no. 3-4, pp. 613–621, 2003, ISSN: 09270248. DOI: 10.1016/S0927-0248(02)00134-4.

[192] A. Zeileis, K. Hornik, and P. Murrell, "Escaping RGBland: Selecting colors for statistical graphics", *Computational Statistics and Data Analysis*, vol. 53, no. 9, pp. 3259–3270, 2009, ISSN: 01679473. DOI: 10.1016/j.csda.2008.11.033.

[193] D. Ristau and H. Ehlers, *Thin film optical coatings*. 2012, pp. 401–424, ISBN: 978-36-4219-409-2. DOI: 10.1007/978-3-642-19409-2{_}6.

[194] SunPower, "MAXEON™ GEN III SOLAR CELLS Positive Electrical Grounding Interconnect Tab and Process Recommendations Cell Physical Characteristics", *Photovoltaics: Research and Applications*, no. 5, pp. 46–352, 2010. [Online]. Available: http://us.sunpower.com/about/sunpower-technology/patents/.

[195] M. R. Vogt, H. Hahn, H. Holst, *et al.*, "Measurement of the optical constants of soda-lime glasses in dependence of iron content and modeling of iron-related power losses in crystalline si solar cell modules", *IEEE Journal of Photovoltaics*, vol. 6, no. 1, pp. 111–118, Jan. 2016, ISSN: 21563381. DOI: 10.1109/JPHOTOV.2015.2498043.

[196] M. R. Vogt, H. Holst, H. Schulte-Huxel, *et al.*, "Optical Constants of UV Transparent EVA and the Impact on the PV Module Output Power under Realistic Irradiation", *Energy Procedia*, vol. 92, pp. 523–530, Aug. 2016, ISSN: 1876-6102. DOI: 10.1016/J.EGYPRO.2016.07.136.

[197] Saint-Gobain Glass - Business Unit Photovoltaics, "SGG ALBARINO High energy transmittance extra-white patterned glass for the photovoltaic and solar thermal industry. ® SAINT-GOBAIN GLASS VISION", France, Tech. Rep., 2017. [Online]. Available: https://glassolutions.sk/sites/glassolutions.eu/files/2017-08/sgg-albarino-prospekt.pdf.

[198] T. He, T. Ma, B. Bläsi, Z. Li, S. Li, and Y. Chen, "Design of periodic dielectric multilayer thin films for colorizing pv panels", *Solar Energy*, vol. 278, p. 112 655, 2024, ISSN: 0038-092X. DOI: https://doi.org/10.1016/j.solener.2024.112655.

[199] P. A. Van Nijnatten, "An automated directional reflectance/transmittance analyser for coating analysis", in *Thin Solid Films*, vol. 442, Oct. 2003, pp. 74–79. DOI: 10.1016/S0040-6090(03)00947-7.

[200] K. Jäger, O. Isabella, L. Zhao, and M. Zeman, "Light scattering properties of surface-textured substrates", in *Current Topics in Solid State Physics*, vol. 7, 2010, pp. 945–948. DOI: 10.1002/pssc.200982695.

[201] K. Jäger, O. Isabella, R. A. Van Swaaij, and M. Zeman, "Angular resolved scattering measurements of nano-textured substrates in a broad wavelength range", *Measurement Science and Technology*, vol. 22, no. 10, 2011, ISSN: 13616501. DOI: 10.1088/0957-0233/22/10/105601.

[202] K. Pfeiffer, U. Schulz, A. Tünnermann, and A. Szeghalmi, "Antireflection Coatings for Strongly Curved Glass Lenses by Atomic Layer Deposition", *Coatings 2017, Vol. 7, Page 118*, vol. 7, no. 8, p. 118, Aug. 2017, ISSN: 2079-6412. DOI: 10.3390/COATINGS7080118. [Online]. Available: https://www.mdpi.com/2079-6412/7/8/118/htm%20https://www.mdpi.com/2079-6412/7/8/118.

[203] J. C. Ortiz Lizcano, P. Procel, A. Calcabrini, *et al.*, "Colored optic filters on c-Si IBC solar cells for building integrated photovoltaic applications", *Progress in Photovoltaics: Research and Applications*, vol. 30, no. 4, pp. 401–435, Apr. 2022, ISSN: 1099159X. DOI: 10.1002/PIP.3504.

[204] A. V. Tikhonravov and M. K. Trubetskov, "Development of the needle optimization technique and new features of OptiLayer design software", *Optical Interference Coatings*, vol. 2253, no. November 1994, p. 10, 1994, ISSN: 1996756X. DOI: 10.1117/12.192109.

[205] J. C. Ortiz Lizcano, I. Kaaya, H. Ziar, *et al.*, "Practical Design of an Optical Filter for Thermal Management of Photovoltaic Modules", *Progress in Photovoltaics, Research and Applications*, 2024.

[206] M. R. Vogt, H. Schulte-Huxel, M. Offer, *et al.*, "Reduced Module Operating Temperature and Increased Yield of Modules with PERC Instead of Al-BSF Solar Cells", *IEEE Journal of Photovoltaics*, vol. 7, no. 1, pp. 44–50, Jan. 2017, ISSN: 21563381. DOI: 10.1109/JPHOTOV.2016.2616191.

[207] P. Seoane da Silva, "Infrared optical filters for passive cooling of c-Si solar modules", Ph.D. dissertation, Delft University of Technology, Delft.

[208] A. V. Tikhonravov, M. K. Trubetskov, and G. W. DeBell, "Optical coating design approaches based on the needle optimization technique", *Applied Optics*, vol. 46, no. 5, pp. 704–710, 2007, ISSN: 15394522. DOI: 10.1364/AO.46.000704.

[209] M. K. Trubetskov and A. V. Tikhonravov, "Modern design tools and a new paradigm in optical coating design", *Applied Optics, Vol. 51, Issue 30, pp. 7319-7332*, vol. 51, no. 30, pp. 7319–7332, Oct. 2012, ISSN: 2155-3165. DOI: 10.1364/AO.51.007319.

[210] M. Šúri, T. A. Huld, and E. D. Dunlop, "PV-GIS: A web-based solar radiation database for the calculation of PV potential in Europe", *International Journal of Sustainable Energy*, vol. 24, no. 2, pp. 55–67, 2005, ISSN: 1478646X.

[211] I. Kaaya, A. Alzade, A. Tuomiranta, J. Ascencio-Vásquez, D. Saelens, and I. Gordon, "Lifetime Prediction of Photovoltaic Modules: Towards a Generalized Physics-Based Approach", in *8th World Conference on Photovoltaic Energy Conversion*, Milan, 2022.

[212] S. Nižetić, A. M. Papadopoulos, and E. Giama, "Comprehensive analysis and general economic-environmental evaluation of cooling techniques for photovoltaic panels, Part I: Passive cooling techniques", *Energy Conversion and Management*, vol. 149, pp. 334–354, 2017, ISSN: 01968904. DOI: 10.1016/j.enconman.2017.07.022.

[213] B. Kamkari and H. Shokouhmand, "Experimental investigation of phase change material melting in rectangular enclosures with horizontal partial fins", *International Journal of Heat and Mass Transfer*, vol. 78, pp. 839–851, 2014, ISSN: 00179310. DOI: 10.1016/j.ijheatmasstransfer.2014.07.056.

[214] M. Fadl and P. Eames, "A numerical investigation into the heat transfer and melting process of lauric acid in a rectangular enclosure with three values of wall heat flux", vol. 158, Elsevier Ltd, 2019, pp. 4502–4509. DOI: 10.1016/j.egypro.2019.01.761.

[215] N. Mallya and S. Haussener, "Buoyancy-driven melting and solidification heat transfer analysis in encapsulated phase change materials", *International Journal of Heat and Mass Transfer*, vol. 164, Jan. 2021, ISSN: 00179310. DOI: 10.1016/j.ijheatmasstransfer.2020.120525.

[216] K. Kant, A. Shukla, A. Sharma, and P. H. Biwole, "Heat transfer studies of photovoltaic panel coupled with phase change material", *Solar Energy*, vol. 140, pp. 151–161, Dec. 2016, ISSN: 0038092X. DOI: 10.1016/j.solener.2016.11.006.

[217] K. Kant, R. Pitchumani, A. Shukla, and A. Sharma, "Analysis and design of air ventilated building integrated photovoltaic (bipv) system incorporating phase change materials", *Energy Conversion and Management*, vol. 196, pp. 149–164, Sep. 2019, ISSN: 01968904. DOI: 10.1016/j.enconman.2019.05.073.

[218] A. Shukla, K. Kant, P. H. Biwole, R. Pitchumani, and A. Sharma, "Melting and solidification of a phase change material with constructal tree-shaped fins for thermal energy storage", *Journal of Energy Storage*, vol. 53, Sep. 2022, ISSN: 2352152X. DOI: 10.1016/j.est.2022.105158.

[219] J. Sutradhar, R. Kothari, and S. K. Sahu, "Solidification and melting model of phase change material with volumetric shrinkage/expansion void in an annulus", *Applied Thermal Engineering*, vol. 195, Aug. 2021, ISSN: 13594311. DOI: 10.1016/j.applthermaleng.2021.117202.

[220] T. Sathe and A. S. Dhoble, "Thermal analysis of an inclined heat sink with finned pcm container for solar applications", *International Journal of Heat and Mass Transfer*, vol. 144, Dec. 2019, ISSN: 00179310. DOI: 10.1016/j.ijheatmasstransfer.2019.118679.

[221] Y. Hong, W. B. Ye, S. M. Huang, M. Yang, and J. Du, "Thermal storage characteristics for rectangular cavity with partially active walls", *International Journal of Heat and Mass Transfer*, vol. 126, pp. 683–702, Nov. 2018, ISSN: 00179310. DOI: 10.1016/j.ijheatmasstransfer.2018.05.005.

[222] V. Joshi and M. K. Rathod, "Constructal enhancement of thermal transport in latent heat storage systems assisted with fins", *International Journal of Thermal Sciences*, vol. 145, Nov. 2019, ISSN: 12900729. DOI: 10.1016/j.ijthermalsci.2019.105984.

[223] S. L. Tariq, H. M. Ali, M. A. Akram, M. M. Janjua, and M. Ahmadlouydarab, *Nanoparticles enhanced phase change materials (NePCMs)-A recent review*, Jul. 2020. DOI: 10.1016/j.applthermaleng.2020.115305.

[224] Orange Climate Autarkis, *Phase Transition Heat Storage*, Jul. 2023.

[225] P. van den Engel, M. Malin, N. K. Venkatesh, and L. A. de Araujo Passos, "Performance of a Phase Change Material Battery in a Transparent Building", *Fluid Dynamics and Materials Processing*, vol. 19, no. 3, pp. 783–805, 2023, ISSN: 15552578. DOI: 10.32604/fdmp.2022.021962.

[226] U. o. L. LPVO, "PV monitoring solutions", University of Ljubljana, Ljubljana, Tech. Rep., 2023.

[227] Kipp and Zonen, *SOLYS2 Sun Tracker*, Dec. 2023.

[228] Sarwar J, McCormack S, Huang MJ, and Norton B, "Experimental validation of CFD modelling for thermal regulation of Photovoltaic panels using phase change material", in *International Conference for Sustainable Energy Storage*, Belfast, Feb. 2011.

[229] M. Verheijen, "Thermal management of photovoltaics using phase change materials", Ph.D. dissertation, Delft University of Technology, Delft, Aug. 2019.

[230] Gütegemeinschaft PCM e.V., *Quality Association PCM*, Jan. 2024.

[231] I. Kaaya, S. Lindig, K. A. Weiss, A. Virtuani, M. Sidrach de Cardona Ortin, and D. Moser, "Photovoltaic lifetime forecast model based on degradation patterns", *Progress in Photovoltaics: Research and Applications*, vol. 28, no. 10, pp. 979–992, 2020, ISSN: 1099159X. DOI: 10.1002/pip.3280.

[232] C. J. Smith, P. M. Forster, and R. Crook, "Global analysis of photovoltaic energy output enhanced by phase change material cooling", *Applied Energy*, vol. 126, pp. 21–28, Aug. 2014, ISSN: 03062619. DOI: 10.1016/j.apenergy.2014.03.083.

[233] A. Livera, M. Theristis, E. Koumpli, *et al.*, "Data processing and quality verification for improved photovoltaic performance and reliability analytics", *Progress in Photovoltaics: Research and Applications*, vol. 29, no. 2, pp. 143–158, Feb. 2021, ISSN: 1099159X. DOI: 10.1002/pip.3349.

[234] M. A. Green, E. D. Dunlop, M. Yoshita, *et al.*, "Solar cell efficiency tables (version 65)", *Progress in Photovoltaics: Research and Applications*, vol. 33, no. 1, pp. 3–15, 2025. DOI: https://doi.org/10.1002/pip.3867. eprint: https://onlinelibrary.wiley.com/doi/pdf/10.1002/pip.3867. [Online]. Available: https://onlinelibrary.wiley.com/doi/abs/10.1002/pip.3867.

[235] L. Maturi, G. Belluardo, D. Moser, and M. Del Buono, "Bipv system performance and efficiency drops: Overview on pv module temperature conditions of different module types", *Energy Procedia*, vol. 48, pp. 1311–1319, 2014.

[236] T. S. Elhabodi, S. Yang, J. Parker, S. Khattak, B.-J. He, and S. Attia, "A review on bipv-induced temperature effects on urban heat islands", *Urban Climate*, vol. 50, p. 101 592, 2023, ISSN: 2212-0955. DOI: https://doi.org/10.1016/j.uclim.2023.101592. [Online]. Available: https://www.sciencedirect.com/science/article/pii/S2212095523001864.

[237] A. S. Abdelrazik, F. Al-Sulaiman, R. Saidur, and R. Ben-Mansour, "A review on recent development for the design and packaging of hybrid photovoltaic/thermal (pv/t) solar systems", *Renewable and Sustainable Energy Reviews*, vol. 95, pp. 110–129, 2018.

[238] K. Farkas, M. C. Munari Probst, and M. Horvat, "Barriers and needs for building integration of solar thermal and photovoltaics", 2010. [Online]. Available: http://infoscience.epfl.ch/record/162426.

[239] A. Scognamiglio and H. N. Røstvik, "Photovoltaics and zero energy buildings: A new opportunity and challenge for design", *Progress in Photovoltaics: Research and applications*, vol. 21, no. 6, pp. 1319–1336, 2013.

[240] S. Nowak, M. Gutschner, D. Ruoss, P. Togweiler, and T. Schoen, "Potential for building integrated photovoltaics", *Report IEA-PVPS T7-4*, 2002.

[241] D. Harris and N. Helwig, "Solar chimney and building ventilation", *Applied Energy*, vol. 84, no. 2, pp. 135–146, 2007.

[242] L. Mullett, "The solar chimney—overall efficiency, design and performance", *International journal of ambient energy*, vol. 8, no. 1, pp. 35–40, 1987.

[243] A. Kasaeian, S. Molana, K. Rahmani, and D. Wen, "A review on solar chimney systems", *Renewable and Sustainable Energy Reviews*, vol. 67, pp. 954–987, 2017, ISSN: 1364-0321. DOI: https://doi.org/10.1016/j.rser.2016.09.081. [Online]. Available: https://www.sciencedirect.com/science/article/pii/S1364032116305718.

[244] E. Cuce, P. M. Cuce, S. Carlucci, *et al.*, "Solar chimney power plants: A review of the concepts, designs and performances", *Sustainability*, vol. 14, no. 3, 2022, ISSN: 2071-1050. DOI: 10.3390/su14031450. [Online]. Available: https://www.mdpi.com/2071-1050/14/3/1450.

[245] N. Monghasemi and A. Vadiee, "A review of solar chimney integrated systems for space heating and cooling application", *Renewable and Sustainable Energy Reviews*, vol. 81, pp. 2714–2730, 2018, ISSN: 1364-0321. DOI: https://doi.org/10.1016/j.rser.2017.06.078. [Online]. Available: https://www.sciencedirect.com/science/article/pii/S1364032117310225.

[246] M. Khosravi, F. Fazelpour, and M. A. Rosen, "Improved application of a solar chimney concept in a two-story building: An enhanced geometry through a numerical approach", *Renewable Energy*, vol. 143, pp. 569–585, 2019, ISSN: 0960-1481. DOI: https://doi.org/10.1016/j.renene.2019.05.042. [Online]. Available: https://www.sciencedirect.com/science/article/pii/S0960148119307025.

[247] E. Oesterle, Lieb, Lutz, and Heusler, *Double-Skin Facades*, Illustrate. Prestel, 2001, p. 207, ISBN: 3791325043.

[248] J. Von Grabe, "Flow resistance for different types of windows in the case of buoyancy ventilation", *Energy and Buildings*, vol. 65, pp. 516–522, 2013, ISSN: 03787788. DOI: 10.1016/j.enbuild.2013.06.035. [Online]. Available: http://dx.doi.org/10.1016/j.enbuild.2013.06.035.

[249] C. Balocco, "A non-dimensional analysis of a ventilated double facade energy performance", *Energy and Buildings*, vol. 36, no. 1, pp. 35–40, 2004, ISSN: 03787788. DOI: 10.1016/S0378-7788(03)00086-0.

[250] S. Rheault and E. Bilgen, "Heat Transfer Analysis in an Automated Venetian Blind Window System", *Journal of Solar Energy Engineering*, vol. 111, no. 1, p. 89, Feb. 1989, ISSN: 01996231. DOI: 10.1115/1.3268291.

[251] E. Gratia and A. De Herde, "Greenhouse effect in double-skin facade", *Energy and Buildings*, vol. 39, no. 2, pp. 199–211, 2007, ISSN: 03787788. DOI: 10.1016/j.enbuild.2006.06.004.

[252] Z. Ioannidis, A. Buonomano, A. Athienitis, and T. Stathopoulos, "Modeling of Double Skin Façades Integrating Photovoltaic Panels and automated roller shades: Analysis of the Thermal and Electrical Performance", *Energy and Buildings*, vol. 154, pp. 618–632, 2017, ISSN: 03787788. DOI: 10.1016/j.enbuild.2017.08.046. [Online]. Available: http://linkinghub.elsevier.com/retrieve/pii/S0378778817317851.

[253] A. De Gracia, A. Castell, L. Navarro, E. Oró, and L. F. Cabeza, "Numerical modelling of ventilated facades: A review", *Renewable and Sustainable Energy Reviews*, vol. 22, pp. 539–549, 2013, ISSN: 13640321. DOI: 10.1016/j.rser.2013.02.029.

[254] G. He, J. Zhang, and S. Hong, "A new analytical model for airflow in solar chimneys based on thermal boundary layers", *Solar Energy*, vol. 136, pp. 614–621, Oct. 2016, ISSN: 0038092X. DOI: 10.1016/j.solener.2016.07.041. [Online]. Available: http://dx.doi.org/10.1016/j.solener.2016.07.041%20http://linkinghub.elsevier.com/retrieve/pii/S0038092X16302997.

[255] S. C. Wong, S. H. Chu, and M. H. Ai, "Revisit on natural convection from vertical isothermal plate arrays II—3-D plume buoyancy effects", *International Journal of Thermal Sciences*, vol. 126, no. January, pp. 205–217, 2018, ISSN: 12900729. DOI: 10.1016/j.ijthermalsci.2018.01.008. [Online]. Available: https://doi.org/10.1016/j.ijthermalsci.2018.01.008.

[256] A. H. Smets, O. Isabella, M. Zeman, *et al.*, *Solar energy: the physics and engineering of photovoltaic conversion technologies and systems*. UIT, 2016.

[257] J. Shelby, *Introduction to glass science and technology*. RSC Publishing, 2005, p. 291, ISBN: 2013436106. DOI: 10.1360/zd-2013-43-6-1064.

[258] I. Haedrich, S. Surve, and A. Thomson, "Cell to module (CTM) ratios for varying industrial cell types", *2015 Asia pacific Solar research conference*, pp. 1–6, 2015. [Online]. Available: http://apvi.org.au/solar-research-conference/wp-content/uploads/2015/12/I-Haedrich_Peer-Reviewed_FINAL.pdf.

[259] D. T. Cotfas, P. A. Cotfas, and O. M. Machidon, "Study of Temperature Coefficients for Parameters of Photovoltaic Cells", *International Journal of Photoenergy*, vol. 2018, no. 4, pp. 1–12, 2018. DOI: 10.1155/2018/5945602. [Online]. Available: https://doi.org/10.1155/2018/5945602.

[260] Z. D. Chen, P. Bandopadhayay, J. Halldorsson, C. Byrjalsen, P. Heiselberg, and Y. Li, "An experimental investigation of a solar chimney model with uniform wall heat flux", *Building and Environment*, vol. 38, no. 7, Moshfegh, B., & Sandberg, M. (1998). Flow and heat, 2003, ISSN: 03601323. DOI: 10.1016/S0360-1323(03)00057-X.

[261] A. La Pica, G. Rodonò, and R. Volpes, "An experimental investigation on natural convection of air in a vertical channel", *International Journal of Heat and Mass Transfer*, vol. 36, no. 3, Moshfegh, B., & Sandberg, M. (1998). Flow and heat, 1993, ISSN: 00179310. DOI: 10.1016/0017-9310(93)80036-T.

[262] B. Moshfegh and M. Sandberg, "Flow and heat transfer in the air gap behind photovoltaic panels", *Renewable & Sustainable Energy Reviews*, vol. 2, Moshfegh, B., & Sandberg, M. (1998). Flow and heat, 1998, ISSN: 13640321. DOI: 10.1016/S1364-0321(98)00005-7. [Online]. Available: http://dx.doi.org/10.1016/S1364-0321(98)00005-7.

[263] S. A. Burek and A. Habeb, "Air flow and thermal efficiency characteristics in solar chimneys and Trombe Walls", *Energy and Buildings*, vol. 39, no. 2, Moshfegh, B., & Sandberg, M. (1998). Flow and heat, 2007, ISSN: 03787788. DOI: 10.1016/j.enbuild.2006.04.015.

[264] J. Mathur, N. K. Bansal, S. Mathur, M. Jain, and Anupma, "Experimental investigations on solar chimney for room ventilation", *Solar Energy*, vol. 80, no. 8, Moshfegh, B., & Sandberg, M. (1998). Flow and heat, 2006, ISSN: 0038092X. DOI: 10.1016/j.solener.2005.08.008.

[265] B. Liu, X. Ma, X. Wang, C. Dang, Q. Wang, and R. Bennacer, "Experimental study of the chimney effect in a solar hybrid double wall", *Solar Energy*, vol. 115, Moshfegh, B., & Sandberg, M. (1998). Flow and heat, 2015, ISSN: 0038092X. DOI: 10.1016/j.solener.2015.02.012. [Online]. Available: http://dx.doi.org/10.1016/j.solener.2015.02.012.

[266] D. Ryan and S. A. Burek, "Experimental study of the influence of collector height on the steady state performance of a passive solar air heater", *Solar Energy*, vol. 84, no. 9, Moshfegh, B., & Sandberg, M. (1998). Flow and heat, 2010, ISSN: 0038092X. DOI: 10.1016/j.solener.2010.05.018. [Online]. Available: http://dx.doi.org/10.1016/j.solener.2010.05.018.

[267] T. F. Ayinde, S. A. M. Said, and M. A. Habib, "Experimental investigation of turbulent natural convection flow in a channel", *Heat and Mass Transfer*, vol. 42, no. 3, Moshfegh, B., & Sandberg, M. (1998). Flow and heat, 2006, ISSN: 0947-7411. DOI: 10.1007/s00231-005-0017-2. [Online]. Available: http://link.springer.com/10.1007/s00231-005-0017-2.

[268] J. Zhang, A. Gupta, and J. Baker, "Effect of Relative Humidity on the Prediction of Natural Convection Heat Transfer Coefficients", *Heat Transfer Engineering*, vol. 28, no. 4, pp. 335–342, Apr. 2007, ISSN: 0145-7632. DOI: 10.1080/01457630601122823.

[269] J. C. Ortiz Lizcano, Z. Haghighi, S. Wapperom, *et al.*, "Photovoltaic chimney: Thermal modeling and concept demonstration for integration in buildings", *Progress in Photovoltaics: Research and Applications*, vol. 28, no. 6, pp. 465–482, 2020. DOI: https://doi.org/10.1002/pip.3194. eprint: https://onlinelibrary.wiley.com/doi/pdf/10.1002/pip.3194. [Online]. Available: https://onlinelibrary.wiley.com/doi/abs/10.1002/pip.3194.

[270] P. Gilman, "Sam photovoltaic model technical reference", National Renewable Energy Lab.(NREL), Golden, CO (United States), Tech. Rep. NREL/TP -6A20- 64102, 2015.

[271] J. Schaible, H. Winarto, V. Škorjanc, *et al.*, "Optimizing aesthetic appearance of perovskite solar cells using color filters", *Solar RRL*, vol. 9, no. 2, p. 2 400 627, 2025. DOI: https://doi.org/10.1002/solr.202400627. eprint: https://onlinelibrary.wiley.com/doi/pdf/10.1002/solr.202400627. [Online]. Available: https://onlinelibrary.wiley.com/doi/abs/10.1002/solr.202400627.

LIST OF PUBLICATIONS

PEER-REVIEWED PUBLICATIONS

1. **J.C. Ortiz Lizcano, Z. Haghighi, S. Wapperom**, C. Infante Ferreira, O. Isabella, A.v.d. Dobbelsteen, M. Zeman. *Photovoltaic chimney: Thermal modeling and concept demonstration for integration in buildings.* Progress in Photovoltaics Research and Applications **28**, 465-482 (2020).

2. **J.C. Ortiz Lizcano**, P. Procel, A. Calcabrini, G. Yang, A. Ingenito, R. Santbergen, M. Zeman, O. Isabella, *Colored optic filters on c-Si IBC solar cells for building integrated photovoltaic applications*, Progress in Photovoltaics Research and Applications, **30**(4), 401-435 (2021).

3. **J.C. Ortiz Lizcano**, S. Villa, Y. Zhou, G. Frantzi, K. Vattis, A. Calcabrini, G. Yang, M. Zeman, O. Isabella *Optimal Design of Multilayer Optical Color Filters for Building-Integrated Photovoltaic (BIPV) Applications*, Solar RRL, **7**, 2300256 (2023).

4. **J.C. Ortiz Lizcano**, I. Kaaya, H. Ziar, P.S da Silva, Y. Zhou, M. Zeman, O. Isabella *Practical Design of an Optical Filter for Thermal Management of Photovoltaic Modules*, Progress in Photovoltaics Research and Applications, **32**(11), 753-773 (2024).

5. **J.C. Ortiz Lizcano**, H. Ziar, C. de Mooij, M.P.F Verheijen, C.v. Nierop & Sanchez, D. Ferlito, C. Connelli, A. Canino, M. Zeman, O. Isabella *Long-term experimental testing of phase change materials as cooling devices for photovoltaic modules*, Solar Energy Materials and Solar Cells, **277**, 113133 (2024).

6. **J.C. Ortiz Lizcano**, O. Isabella, B.Bläsi, M. Schmid *Chapter 11: Color and aesthetics of photovoltaic modules*, from *Optics for Terawatt-Scale Photovoltaics: Review and Perspectives* by K. Jäger *et al.* Advances in Optics and Photonics, (2025).

CONFERENCE CONTRIBUTIONS

1. K. Jäger, S. Burger, U. Aeberhard, E. Llado, B. Bläsi, B. Ehrler, W. Favre, A. Fejfar, T. Gageot, I. Gordon, H. Helmers, O. Höhn, O. Isabella, M. Jošt, M. Ledinský, J. Mandal, P. Manley, D. Munoz, **J. C Ortiz Lizcano**, U. Paetzold, A. Raman, H. Sai, R. Saive, M. Schmid, E. Yablonovitch, and C. Becker, *A Roadmap on Optics for Terawatt Scale Photovoltaics*, in Advanced Photonics Congress 2024, Technical Digest Series (Optica Publishing Group, 2024), **paper STu2G.5**.

2. **J.C. Ortiz Lizcano**, A. Calcabrini, R. Santbergen, P. Procel Mota, M. Zeman, O. Isabella, *Concepts for heat utilization and passive cooling techniques to improve reliability and performance of Building Integrated Photovoltaics (BIPV)*, IOP Conf. Ser.: Earth Environ. Sci., 2022, 1085 012002

3. O. Isabella, R. Santbergen, H. Ziar, A. Calcabrini, **J.C. Ortiz Lizcano**, E. Garcia Goma, P. Nepal, V. Schepel, M. Zeman, *Advanced modeling of E/UIPV systems from location to load*, 2018 IEEE 7th World Conference on Photovoltaic Energy Conversion (WCPEC) (A Joint Conference of 45th IEEE PVSC, 28th PVSEC & 34th EU PVSEC), Waikoloa, HI, USA, 2018, pp. 2691-2696.

4. **J.C Ortiz Lizcano**, G. Yang, S. Villa, O. Isabella, M. Zeman *Design of colored Bragg reflectors with heating reduction capability for BIPV applications.*, 35th EUPVSEC **1CO.2.3**, (2018).

5. **J.C Ortiz Lizcano**, M. Verheijen, C.v. Nierop & Sanchez, P. Luscuere, O. Isabella, M. Zeman *Thermal Management of PV modules with Phase Change Materials*, 36th EUPVSEC **1BO.9.6**, (2019).

6. **J.C Ortiz Lizcano**, Z. Haghighi, S. Wapperom, C. Infante Ferreira, O. Isabella, A.v.d. Dobbelsteen, M. Zeman *Photovoltaic Chimney: Thermal modeling and concept demonstration for integration in buildings*, 36th EUPVSEC **6BO.8.3**, (2019).

7. **J.C Ortiz Lizcano**, P.S. da Silva, G. Yang, M. Verheijen, C.v. Nierop & Sanchez, O. Isabella, M. Zeman *Passive cooling techniques for BIPV systems.*, 29th PVSEC **10THO4**, (2019)

8. **J.C Ortiz Lizcano**, G. Frantzi, A. Calcabrini, S. Villa, G. Yang, O. Isabella, *Optic filters as multi-purpose devices for photovoltaic applications: Models for a full performance assessment and optimized design*, 38th EUPVSEC **1BO.16.2**, (2021).

PATENTS

1. **J.C Ortiz Lizcano**, H. Ziar, M. Dakessian, O. Isabella, *Integrated internal heat sink for passively cooling photovoltaic modules*, **IPC H01L**, Patent number **OCT-22-055** (2022).

2. **J.C Ortiz Lizcano**, A.V. Martinez Lopez, O. Isabella, *Miura-Ori Photovoltaic module*, **IPC H02S**, Patent number **OCT-19-065** (2021).

3. Z. Haghighi, **J.C Ortiz Lizcano**, O. Isabella, M. Zeman, A.v.d. Dobbelsteen *Photovoltaic Chimney*, **IPC F24S, H02S**, Patent number **OCT-18-075** (2020).

CURRICULUM VITÆ

Juan Camilo ORTIZ LIZCANO

EDUCATION

2001–2007	B.Sc in Mechanical Engineering Universidad Industrial de Santander
2012–2014	M.Sc in Sustainable Energy Technologies Delft University of Technology
2017–2024	PhD. Candidate Delft University of Technology *Thesis:* Improving aesthetics and energy performance of photovoltaics for the building environment *Promotor:* Prof. dr. Ir. O. Isabella Prof. dr. Ir. M. Zeman


TUDelft